Experimental Characterization of Advanced Composite Materials

Third Edition

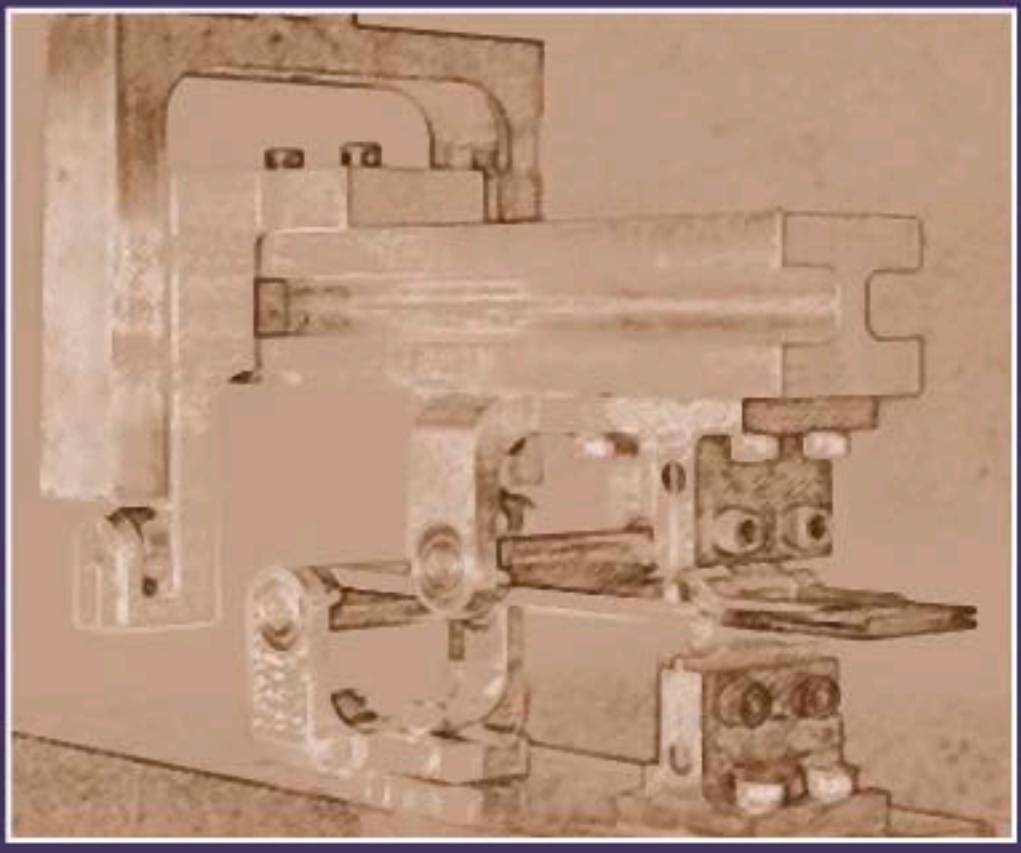

Donald F. Adams • Leif A. Carlsson • R. Byron Pipes

CRC PRESS

Experimental Characterization of Advanced Composite Materials Third Edition

Experimental Characterization of Advanced Composite Materials Third Edition

Donald F. Adams • Leif A. Carlsson • R. Byron Pipes

CRC PRESS

Boca Raton London New York Washington, D.C.

Library of Congress Cataloging-in-Publication Data

Carlsson, Leif A., 1952–
Experimental characterization of advanced composite materials / Leif Carlsson, Donald F. Adams, R. Byron Pipes. — 3rd ed.
p. cm.
Includes bibliographical references and index.
ISBN 1-58716-100-1
1. Composite materials—Testing. I. Adams, Donald Frederick, 1935– II. Pipes, R. Byron. III. Title.

TA418.9.C6 C324 2002
620.1'18'0287—dc21

2002073579
CIP

International Standard Book Number 1-58716-100-1
Library of Congress Card Number 2002073579
Printed in the United States of America 1 2 3 4 5 6 7 8 9 0
Printed on acid-free paper

Dedications

D.F.A.: To my wife and very best friend, Roberta,

mother of our four children, Dave, Dan, Doug, and Jayne

L.A.C.: To the memory of Dr. Alf de Ruvo,

coadvisor of my Ph.D. dissertation and long-time friend.

R.B.P.: To the memory of Professor Roy McCullough

for his three decades of warm and supportive friendship.

Preface

The experimental characterization of composite materials has been an elusive topic, because it has been a continually evolving one. As new types of composites have been developed and new applications found, new testing challenges have continually evolved. For example, in the 1960s the primary structural composite material available to compete with metals consisted of carbon fiber in a brittle epoxy matrix, a material of relatively low toughness. Thus, toughness as a property was de-emphasized by the composite materials community. However, by the beginning of the 1980s, many new matrix materials, e.g., toughened epoxies and high-temperature thermoplastics, were being incorporated to produce toughened composites. Obviously, the need quickly arose to develop test methods for ranking the relative toughness of composite materials. But there are multiple definitions of toughness, damage tolerance, and the effect of defects. Soon many test methods not previously applied to composites were being proposed, including Mode I, II, and mixed-mode fracture mechanics, beam and plate impact, compression after plate impact, and open-hole tension and compression.

This evolution of test methods to meet new demands has continued over the years as additional aspects have risen in importance; e.g., influences of temperature, moisture, solvents, and other factors affecting durability. Improvements in fiber–matrix interfacial bonding, the introduction of organic fibers such as aramid, polyethylene, liquid crystal polymer, and natural forms such as hemp and jute, and ultrahigh modulus inorganic fibers, particularly carbon, also have occurred. Likewise, new classes of matrix materials such as bismalimides, polyimides, and many others have necessitated still more test methods, or revisions of existing ones.

As we now enter the 21st century, applications of all types of composite materials to commercial products are being emphasized. In anticipation of this development, the 1990s were a period of consolidation of test methods, and attempts to better understand those methods being used. Thus, the present text comes at an opportune time, i.e., when the evolution of test methods is in a relatively stable period and definitive recommendations can be made. The goal of this text is to present primarily only those mechanical test methods that have achieved some consensus as being the best presently available, recognizing that "best" is often subjective.

The primary audience for this text will be university, junior college, and technical school undergraduate students, and beginning university graduate students, taking a course in experimental mechanics of composite materials.

However, this text also addresses a much larger audience. Quite frequently, engineers and technicians in industry and government laboratories are

assigned composite material testing responsibilities, but have little or no prior experience. These individuals are associated with a wide range of organizations, including corporate research, federal laboratories, university research, material suppliers, contract design organizations, and custom fabrication shops. They need to choose among competing test methods, to perform or supervise the performance of mechanical testing, and then interpret the experimental data obtained. In this sense this text complements American Society for Testing and Materials (ASTM) and other standards. This text is sufficiently straightforward and concise in its presentation to appeal to this group if individuals who need a quick start.

Another potential audience includes those who attend composite material characterization short courses and tutorials. The present text, because of its concise wording and numerous figures and tables, will serve both as a set of course notes and a permanent reference source of topics covered.

The 14 chapters of the text are organized to meet the class laboratory schedule needs of a one-semester or one-quarter course. Specific topics (chapters) can be deleted as required to fit the actual time available. The text is intended to be self-contained, with no reference texts required.

The first four chapters provide an introduction to the special terminology and conventions that have evolved related to composite materials (Chapter 1), a summary of the unique analysis methods and data reduction formulas required (Chapter 2), sufficient laminate processing information to permit the reader to fabricate his or her own composites for testing (Chapter 3), and details of specimen preparation and testing equipment required (Chapter 4).

Chapters 5 through 10 each cover a specific aspect of lamina testing, including tension, compression, shear, flexure, off-axis tension, and thermoelastic response. Extensions of these principles to laminate mechanical and thermoelastic response are covered in Chapters 11 and 12, respectively. The composite durability issues referred to previously are detailed in Chapter 13 (effects of defects) and Chapter 14 (fracture mechanics). Of particular note among the appendices is Appendix C, which contains a sample laboratory report. This is intended to serve as a guide for the reader in the preparation of an acceptable form of data analysis and presentation.

D.F.A., Laramie, WY

L.A.C., Boca Raton, FL

R.B.P., Akron, OH

Acknowledgments

We are indebted to many people who have contributed to and supported the three editions of this text. Seija Carlsson prepared the manuscript for the first edition. Rosemarie Chiucchi and Teresa Perez prepared the revised manuscript for this second edition, and Teresa Perez assisted the authors in the preparation of Chapters 2, 9, 10, 12, and 14 for the third edition. We would also like to thank Touy Thiravong for help in clarifying many technical details related to testing and preparation of specimens; Dr. John W. Gillespie, Jr., Dale W. Wilson, and William A. Dick for reviewing the manuscript for the first edition; and Dr. Anthony Smiley, Dr. William Sanford, and Rod Don, who shared their knowledge of processing of thermoplastic and thermoset composites. We acknowledge Dr. Pascal Hubert, Prof. Anoush Poursartip, and his research students at the University of British Columbia for their contributions to Chapter 3 of the third edition.

We would also like to thank the late Woody Snyder, who supplied many of the photographs in this book. Thanks are due to Judy Joos, Mark Deshon, Shawn Pennell, Sherri VonHartman, and Jeffrey Weinraub for the artwork. Dr. James R. Reeder of the National Aeronautics and Space Administration (NASA) Langley Research Center kindly supplied information on the mixed-mode bending (MMB) test. Dr. Shaw Ming Lee of Hexcel Corporation provided much useful information on the edge crack torsion (ECT) specimen, and Prof. Barry Davidson of Syracuse University shared many of his papers on the four-point bend end-notched flexure (4ENF) specimen. Dr. Xiaoming Li of University of Tennessee provided test data generated on the ECT specimen. Students who scrutinized parts of the text and suggested improvements were Robert Rothschilds, Bruce Trethewey, Gary Becht, Ellen Brady, and James Newill. Finally, we thank the many students for providing the test results presented in numerous graphs throughout all three editions of the text. Of those, we single out Robert Jurf, Thomas Chapman, David Adkins, Richard Givler, Robert Wetherhold, Richard Walsh, Nicolass Ballityn, Bruce Yost, James York, Yong-Zhen Chen, Uday Kashalikar, and Mark Cirino.

Authors

Donald F. Adams, Ph.D., is the founder and president of Wyoming Test Fixtures, Inc., a company specializing in the design and fabrication of mechanical test fixtures for the composite materials community since 1988. He is also emeritus professor of mechanical engineering at the University of Wyoming, where he was director of the Composite Materials Research Group for 27 years.

Dr. Adams received his B.S. in mechanical engineering from the University of Illinois (1957), his M.S. in mechanical engineering from the University of Southern California (1960), and his Ph.D. in theoretical and applied mechanics from the University of Illinois (1963).

His industry experience was with Northrop Aircraft Corporation, Hawthorne, CA (3 years), the Aeronutronic Division of Ford Motor Company, Newport Beach, CA (4 years), and the Rand Corporation, Santa Monica, CA (5 years). He joined the University of Wyoming in 1972.

Dr. Adams has been involved full time in composite materials analysis, testing, and design for 40 years. He headed a very active interdisciplinary composite materials research group at the University of Wyoming for many years, which was involved in a broad range of government and industry programs. Dr. Adams continues to serve on a number of national committees and review boards, and is a member of the editorial boards of four prominent composite materials journals. He is very active in the test methods committees of American Society for Testing and Materials (ASTM) and MIL-HDBK-17. He regularly presents seminars and short courses both in the U.S. and elsewhere, and has published extensively in the journal literature.

Leif A. Carlsson, Ph.D., received his advanced degrees from Uppsala University and Chalmers University of Technology in Sweden. After completion of his formal education, he spent a postdoctoral year at Rensselaer Polytechnic Institute in Troy, New York. He then returned to Sweden and served as head of the composites section at the Aeronautical Research Institute of Sweden (FFA). When he returned to the U.S., he assumed a visiting position at the Center for Composite Materials at the University of Delaware, after which he joined the faculty of mechanical engineering at Florida Atlantic University. Dr. Carlsson has published extensively in the areas of mechanics and fracture mechanics of composite materials and sandwich structures.

R. Byron Pipes, N.A.E., Goodyear Professor of Polymer Engineering (Effective December 1, 2001) served as president, Rensselaer Polytechnic Institute from 1993 to 1998. As Distinguished Visiting Scholar at the College of William and

Mary, he pursued research at the National Aeronautics and Space Administration (NASA) Langley Research Center in the field of carbon nanotechnology during 1999 to 2001. He was provost and vice president for academic affairs at the University of Delaware from 1991 to 1993 and served as dean of the College of Engineering and director of the Center for Composite Materials during 1977 to 1991 at the same institution. Dr. Pipes was elected to the National Academy of Engineering in 1987 and the Royal Swedish Academy of Engineering Sciences in 1993. He was appointed Robert L. Spencer Professor of Engineering in 1986 in recognition of his outstanding scholarship in the field of polymer composite materials ranging over the subject areas of advanced manufacturing science, durability, design, and characterization. He is the author of more than 100 archival publications, including four books, and has served on the editorial boards of four journals in his field. Dr. Pipes has been recognized for his leadership in creating partnerships for university research with the private sector, government, and academia. He served as one of the first six directors of National Engineering Research Centers of the National Science Foundation (NSF). Dr. Pipes received his doctoral degree in mechanical engineering from the University of Texas and the M.S.E. from Princeton University. He is the recipient of the Gustus L. Larson Award of Pi Tau Sigma and the Chaire Francqui, Distinguished Faculty Scholar Award in Belgium. He holds fellow rank in ASC, American Society of Mechanical Engineers (ASME), and SAMPE. Dr. Pipes has served on a number of National Research Council panels as both member and chair, and served two terms on the National Materials Advisory Board.

Table of Contents

1 Introduction 1
1.1 Background 2
1.2 Laminate Orientation Code 3
1.2.1 Standard Laminate Code 4
1.2.2 Basic Condensed Code 5
1.2.3 Specific Condensed Code 6
1.2.4 Summary 6
1.3 Influences of Material Orthotropy on Experimental Characterization 6
1.3.1 Material and Geometric Coordinates 6
1.3.2 Stress–Strain Relations for Anisotropic Materials 7
1.4 Typical Unidirectional Composite Properties 8
References 10

2 Analysis of Composite Materials 11
2.1 Constitutive Relations 11
2.1.1 Transformation of Stresses and Strains 14
2.1.2 Hygrothermal Strains 15
2.2 Micromechanics 17
2.2.1 Stiffness Properties of Unidirectional Composites 18
2.2.2 Expansion Coefficients 19
2.3 Laminated Plate Theory 20
2.4 St. Venant's Principle and End Effects in Composites 23
2.5 Lamina Strength Analysis 24
2.5.1 Maximum Stress Failure Criterion 25
2.5.2 Maximum Strain Failure Criterion 26
2.5.3 Tsai-Wu Failure Criterion 26
2.6 Laminate Strength Analysis 27
2.7 Fracture Mechanics Concepts 29
2.8 Strength of Composite Laminates Containing Holes 32
References 34

3 Processing of Composite Laminates 37
3.1 Processing of Thermoset Composites 38
3.1.1 Autoclave Molding 41
3.1.2 Resin Transfer Molding of Thermoset Composites 44
3.1.2.1 Vacuum-Assisted Resin Transfer Molding (VARTM) Processing 45

3.2 Autoclave Processing of Thermoplastic Composites 48
3.3 Determination of Volume Fractions of Fibers, Resin, and Voids 49
3.3.1 Chemical Matrix Digestion Method 50
3.3.1.1 Procedure 50
3.3.1.2 Calculation of Fiber Volume Fraction 51
3.3.1.3 Determination of Void Content 51
3.3.2 Photomicrographic Method 52
3.3.2.1 Procedure 52
3.3.2.2 Determination of Fiber Volume Fraction 53
References 55

4 Test Specimen Preparation, Strain, and Deformation Measurement Devices, and Testing Machines 57
4.1 Cutting the Composite Laminate 57
4.2 Tabbing Materials 60
4.3 Tab Bonding 61
4.4 Suggested Tab Bonding Procedure 63
4.5 Hinge Attachment for Double-Cantilever Beam (DCB) and Mixed-Mode Bending (MMB) Specimens 64
4.6 Specimen Conditioning 65
4.7 Strain and Displacement Measurements 66
4.8 Testing Machines 69
References 71

5 Lamina Tensile Response 75
5.1 The Need for Lamina Testing 75
5.2 Introduction to Tensile Testing 75
5.3 Load Introduction 76
5.4 Specimen Configurations and Test Procedures 79
5.5 Data Reduction 80
References 83

6 Lamina Compressive Response 85
6.1 Shear-Loading Test Methods 87
6.2 End-Loading Test Methods 88
6.3 CLC Test Methods 91
6.4 Compression Test Procedures 93
6.4.1 IITRI Test Procedure (ASTM D 3410) 95
6.4.2 Modified ASTM D 695 Test Procedure (SACMA SRM-1) 96
6.4.3 CLC Test Procedure (ASTM D 6641) 96
6.5 Failure Modes 97
6.6 General Data Reduction 98

6.7 Indirect Determination of Unidirectional Lamina Strength from a Test of a Cross-Ply Laminate 100
6.8 Summary of Compression Test Methods 102
References 103

7 Lamina Shear Response 105
7.1 Iosipescu Shear Test Method (ASTM D 5379) 106
7.2 Two-Rail Shear Test Method (ASTM D 4255) 111
7.3 Three-Rail Shear Test Method (ASTM D 4255) 114
7.4 $[\pm 45]_{ns}$ Tensile Shear Test Method (ASTM D 3518) 115
7.5 Short Beam Shear Test Method (ASTM D 2344) 117
7.6 Summary 119
References 119

8 Lamina Flexural Response 121
8.1 Testing Configurations 121
8.2 Three- Vs. Four-Point Flexure 124
8.3 Specimen Preparation and Flexure Test Procedure 126
8.4 Data Reduction 127
References 129

9 Lamina Off-Axis Tensile Response 131
9.1 Deformation and Stress in an Unconstrained Specimen 132
9.2 Influence of End Constraint 134
9.3 Off-Axis Tensile Strength 137
9.4 Test Procedure 138
9.5 Data Reduction 138
9.5.1 Elastic Properties 138
9.5.2 Tensile Strength of Off-Axis Specimen 141
References 142

10 Lamina Thermoelastic Response 143
10.1 Temperature Gage Sensing System 145
10.2 Temperature Compensation 145
10.3 Measurement of Thermal Expansion 147
10.4 Data Reduction 148
References 149

11 Laminate Mechanical Response 151
11.1 Data Reduction for Stiffness Properties 152
11.1.1 Axial Tension or Compression 152
11.1.2 Transverse Tension or Compression 153
11.1.3 In-Plane Shear 154
11.1.4 Flexure 154

11.2 Laminate Strength Analysis 156
11.3 Test Specimen Preparation 157
11.4 Test Procedures 157
11.4.1 Tension Test Procedures 157
11.4.2 Compression Test Procedures 158
11.4.3 Shear Test Procedures 158
11.4.4 Flexural Test Procedures 158
11.5 Data Reduction 159
11.6 Example of a Typical Analysis: Axial Tensile Response of a Laminate 159
References 161

12 Laminate Thermoelastic Response 163
12.1 Preparation of Test Specimens and Measurement of Thermal Expansion 164
12.2 Data Reduction 165
12.3 Analysis of Thermoelastic Response 166
References 167

13 Open-Hole Tensile and Compressive Strengths of Laminates 169
13.1 Point and Average Stress Criteria 170
13.1.1 Point Stress Criterion (PSC) 171
13.1.2 Average Stress Criterion (ASC) 172
13.1.3 Modification of PSC 173
13.2 Test Specimen Preparation 174
13.3 Tensile Test Procedure and Data Reduction 175
13.4 Standardized Open-Hole Tension Test Method 179
13.5 Standardized Open-Hole Compression Test Methods 180
13.5.1 Boeing Open-Hole Compression Test Method 180
13.5.2 Northrop Open-Hole Compression Test Method 181
13.5.3 Comparison of the Boeing and Northrop Open-Hole Compression Test Methods 182
13.5.4 Filled-Hole Tension and Compression Test Methods 183
References 183

14 Characterization of Delamination Failure 185
14.1 Double-Cantilever Beam (DCB) Test 186
14.1.1 DCB Specimen Preparation and Test Procedure 187
14.1.2 DCB Data Reduction 189
14.2 End-Notched Flexure (ENF) Test 191
14.2.1 ENF Specimen Preparation and Test Procedure 193
14.2.2 ENF Data Reduction 194

14.3 The Four-Point Bend ENF (4ENF) Test 196
14.3.1 4ENF Specimen Preparation 197
14.3.2 4ENF Test Fixture 197
14.3.3 4ENF Test Procedure 198
14.3.4 4ENF Data Reduction 199
14.4 Mixed-Mode Bending (MMB) Test 201
14.4.1 MMB Test Procedure 203
14.4.2 MMB Data Reduction 203
14.5 Edge-Cracked Torsion (ECT) Test 205
14.5.1 ECT Specimen Preparation 207
14.5.2 ECT Test Fixture 207
14.5.3 ECT Test Procedure 208
14.5.4 ECT Data Reduction 209
References 210

Appendix A Compliance and Stiffness Transformations and Matrix Operations 213

Appendix B Preparation of Test Specimens and Panels 215

Appendix C Sample Laboratory Report 227
Lamina Tensile Response 227
Procedure 227
Specimen Dimensions 228
Stress–Strain Data 228
Test Results 229
Reduced Data 229
Uncertainty Analysis 232
Micromechanics Predictions 233
References 234

Appendix D Unit Conversions 235

Index 237

1

Introduction

Most of the subject matter in this text has been taught for years to advanced undergraduate and first-year graduate students at the University of Delaware, Florida Atlantic University, and the University of Wyoming. During this time, the authors realized there was no textbook offering a concise treatment of the experimental characterization of composite materials. Most current textbooks deal only with the analysis of composite materials. If the present text appears to emphasize advanced composite materials, it is only because these materials often present the greatest challenges to experimental characterization. These also are the materials most often used in structural applications, where accurate characterization is most important. Interestingly, today, many high-performance designs demand the use of advanced composite materials.

The objective of this textbook is to present processing techniques, specimen preparation, analyses of test methods, test procedures, and data reduction schemes to determine mechanical properties, thermal expansion coefficients, and fracture and strength data for composite materials. Emphasis is placed on practical matters such as preparation and testing of specimens and data reduction methodology. Many of the test methods presented are American Society for Testing and Materials (ASTM) or other national or international standards. Others, although originating within an individual organization and sometimes continuing to be refined in terms of test specimen and fixture geometries, test procedures, and data reduction schemes, are being widely used within the composites testing community.

No attempt is made to present a detailed review of composite mechanics or fracture mechanics. Such a treatment has been presented in many other textbooks to which references are made. Only a brief elementary outline of the theoretical background is provided in Chapter 2. Moreover, no attempt is made to present an overview of all test methods; such reviews are available elsewhere, as will be referenced. The methods presented here are deemed the most appropriate and widely accepted at present. Additional developments can, however, be expected in this evolving field.

This text was prepared for students who have an interest in experimental aspects of composite materials. It will also be useful for engineers in industrial or government laboratories who desire to extend their expertise into experimental characterization of anisotropic materials.

1.1 Background

Composite materials, in the context of high-performance materials for structural applications, have been used increasingly since the early 1960s; although materials such as glass fiber-reinforced polymers were already being studied 20 years earlier. Initially, conventional test methods, originally developed for determining the physical and mechanical properties of metals and other homogeneous and isotropic construction materials, were used. It was soon recognized, however, that these new materials, which are nonhomogeneous and anisotropic (orthotropic), require special consideration for determining physical and mechanical properties.

During this initial period, composite materials technology was developed primarily within the aerospace community. Because composite material test methods were not standardized, each airframe manufacturer tended to develop its own procedures. Although these procedures were not usually proprietary, there was little incentive to adopt common test methods, particularly because few methods had emerged as being clearly superior to others of the same type. The problem was further complicated by the continuous emergence of new materials; e.g., boron and carbon fibers in the mid-1960s and Kevlar® fibers in the early 1970s, along with new epoxies, polyimides, and other matrix materials, including metals. A specific test method, which may have performed reasonably well for the types of composite materials being tested in the past, was not necessarily adequate for the material being evaluated at that time. That is, there was little possibility of standardization. As a result, many diverse test methods were developed for measuring the same properties. Some were easy to use but provided only limited results or data of questionable quality. Others were very complex, operator-dependent, and perhaps also of questionable quality.

In the U.S. the federal government sponsored much of the early development work in composite materials, primarily through agencies such as the National Aeronautics and Space Administration (NASA), the Air Force, and the Navy. The problems associated with the lack of standards were recognized, and attempts were made to identify general test methods, to generate a database for comparison purposes, and to establish standards. These attempts were largely unsuccessful, primarily because newer composite materials did not necessarily behave in the same manner as the prior generation of materials around which the test methods had been established.

Today, almost four decades after these initial attempts, general standards for testing composite materials still do not exist, and perhaps still for the same very practical reasons. That is, as new generations of composite materials are developed, existing test methods have to be modified to accommodate them. Rigid standardization would not permit this. On the other hand, consensus organizations such as ASTM have done much to maintain a degree of uniformity, and an awareness of the general problem of achieving standardization. As additional industries, e.g., automotive, sporting goods,

electronics, machine tool, and civil infrastructure, have moved toward the more extensive use of composite materials in their products, this general lack of standardization has become particularly disturbing to them. Most of the more traditional industries are accustomed to following specific design standards, purchasing materials to standards, and testing to standards. Thus, acceptance of the general lack of test method standards has become part of the indoctrination of newer industries into this relatively new technology.

This lack of standardization in composite materials testing is not necessarily a negative aspect, although it may often be inconvenient for the new user, and it should not be unexpected. That is, the term composite material does not define a specific class of fabrication materials, but rather a broad spectrum of materials of widely varying properties. Thus, it can be expected that different test methods will be required for different classes of composite materials. This philosophy is no different than that associated with using a different test method for testing low carbon steel than for testing a ceramic.

With this general background and philosophy in mind, current composite material characterization methods will be discussed and evaluated in the following chapters. Not every known method will be introduced, however. Some methods that were previously popular are now rapidly fading from use. Thus, although these names are familiar to many, and are frequently quoted in the literature, particularly in the older literature, they are becoming obsolete and need not be discussed here. Additional discussion can be found in References 1 and 2.

1.2 Laminate Orientation Code

Typically, the basic building block of a composite material structural component is a unidirectional lamina, i.e., a thin layer consisting of reinforcing fibers all oriented in the same direction and imbedded in a matrix such as a polymer. Alternatively, the reinforcement can be in the form of fibers woven to form a layer of fabric, a thin mat of randomly oriented fibers, or some similar form. All of these laminae are typically characterized experimentally using the test methods described in this text.

However, in the actual structural design process, these individual laminae are stacked and processed together to form a laminate of the desired properties. Such a laminate can be made as complex as required to satisfy the specified design criteria, by adding more and more plies of arbitrary orientations, reinforcement forms, and material types. Until the early 1970s there was no unified system for defining the lay-up patterns of composite laminates. As composite materials moved from the research laboratory to the production shop, the need for a common terminology became obvious.

The Air Force Structural Dynamics Laboratory included a Laminate Orientation Code in the third edition of its *Advanced Composites Design Guide* published

in January 1973 [3]. This code, established by general consensus of the aerospace industry at the time, has survived to the present with minimal modification and continues to be used almost universally by the composites community. Thus, it is important for the reader to know at least its general features.

The Laminate Orientation Code, as presented in the 1973 edition of the *Advanced Composites Design Guide*, is summarized in the following sections.

1.2.1 Standard Laminate Code

The Standard Laminate Code, used to describe a specific laminate uniquely, is most simply defined by the following detailed descriptions of its features:

1. The plies are listed in sequence from one laminate face to the other, starting with the first ply laid up, with square brackets used to indicate the beginning and end of the code.
2. A subscript capital T following the closing square bracket should be used to indicate that the total laminate is shown. Although it is not good practice, as will be seen subsequently, the T is sometimes omitted. For a symmetric laminate (see Chapter 2), only the plies on one side of the midplane are shown, and a subscript capital S follows the closing bracket. A subscript capital Q is also defined in the code, to designate an antisymmetric laminate (improperly termed a quasi-symmetric laminate in Reference [3]). However, antisymmetric laminates are not commonly used.
3. Each ply within the laminate is denoted by a number representing its orientation in degrees as measured from the geometric x-axis of the laminate to the lamina principal material coordinate direction (1-axis). Material and geometric coordinate axis systems are described in Chapter 2. Positive angles are defined as clockwise when looking toward the lay-up tool surface. Note that this convention is consistent with the definition of a positive angle in Figure 2.3, because there the view is toward the surface of the laminate, i.e., away from the lay-up tool surface.
4. When two or more plies of identical properties and orientation are adjacent to each other, a single number representing the angular orientation, with a numerical subscript indicating the number of identically oriented adjacent plies, is used.

   For example, a laminate consisting of just three –45° plies would be designated as $[-45_3]_T$. The notation $[-45]_{3T}$ is also acceptable, and in fact is more commonly used.
5. If the angles of otherwise identical adjacent plies are different, or if the angles are the same but the materials are different, the plies are separated in the code by a slash.

For example, a two-ply laminate consisting of a +45°–ply and a –30°–ply of the same material would be expressed as $[45/-30]_T$. Note that the first ply listed in the code is always the first ply to be laid up in the fabrication process. Note also that the plus sign is not used unless omitting it would create an ambiguity.

A six-ply symmetric laminate consisting of identical plies oriented at +45, 0, –30, –30, 0, and +45° would be expressed as $[45/0/-30]_S$.

When a symmetric laminate contains an odd number of plies of the same material, e.g., –30, 90, 45, 90, and –30°, the center ply is designated with an overbar, i.e., $[-30/90/\overline{45}]_S$.

6. When adjacent plies are at angles of the same magnitude but of opposite sign, the appropriate use of plus and minus signs is employed. Each plus or minus sign represents one ply and supercedes the use of the numerical subscript, which is used only when the directions are identical (as in item 4, above).

   For example, a four-ply laminate consisting of plies oriented at +20, +20, –30, and +30° would be designated as $[20_2/\mp 30]_T$. Note that $\mp$ and not $\pm$ is used here, to preserve the intended order.

7. Repeating sequences of plies are called sets and are enclosed in parentheses. A set is coded in accordance with the same rules that apply to a single ply.

   For example, a six-ply 45, 0, 90, 45, 0, and 90° laminate would be designated as $[(45/0/90)_2]_T$, or alternatively as $[(45/0/90)]_{2T}$. As in item 4, above, this latter form is no more correct, but is more commonly used.

8. If a laminate contains plies of more than one type of material and/or thickness, a distinguishing subscript (or superscript) is used with each ply angle, to define the characteristics of that ply. For example, $[0_g/90_k/45_c]_S$ for a glass, Kevlar®, and carbon/fiber laminate.

1.2.2 Basic Condensed Code

When the exact number of plies need not be specified (as in preliminary design when the laminate in-plane properties but not the final laminate thickness are needed), the Basic Condensed Code can be used. The plies are written in the order of ascending angle, with only the relative proportions being expressed by whole number subscripts.

For example an actual $[30_2/0_6/-45_2/90_4]_T$ laminate would be expressed using the Basic Condensed Code as $[0_3/30/-45/90_2]$. An actual 30-ply $[90/\pm(0/45)]_{3S}$ laminate would be expressed as $[0_2/\pm 45/90]$. In both examples, the lack of a subscript after the closing bracket indicates that it is a Basic Condensed Code.

1.2.3 Specific Condensed Code

When the total number of plies and their orientations need be preserved, but not their order (stacking sequence) within the laminate, the Specific Condensed Code is used. This code is useful at that point in preliminary design when the laminate is being sized (i.e., when the required total number of plies is being specified). It is also particularly useful to the materials purchasing group because the scrap losses during cutting of the plies, and thus the amount of material that must be ordered, depends on the orientation of each ply in the laminate.

Using the Specific Condensed Code, the actual 30-ply $[90/\pm(0/45)]_{3S}$ laminate used in the previous example would be expressed as $[0_2/\pm45/90]_{6C}$. Note that a full 30-ply laminate is still expressed, the subscript C indicating however that the stacking sequence of the plies has not been retained.

1.2.4 Summary

Although the Laminate Orientation Code may appear complicated at first, it is systematically constructed and is as concise as possible. For simple laminates the code reduces to a simple form, and is easily and quickly written. Yet the most complex laminate can be coded with equal conciseness.

1.3 Influences of Material Orthotropy on Experimental Characterization

The individual lamina (i.e., layer or ply) of a composite material is often the basic building block from which high-performance composite structures are designed, analyzed, and fabricated. Unless stated otherwise, the lamina material is usually assumed to exhibit linearly elastic material response as, for example, in the analyses presented in Chapter 2. In many cases this is a reasonable assumption. However, there are exceptions, particularly in terms of shear response, that sometimes must be accounted for.

1.3.1 Material and Geometric Coordinates

Each composite lamina typically possesses some degree of material symmetry, i.e., principal material coordinate axes can be defined. These lamina are then oriented within a multiple-lamina composite (the laminate) at arbitrary angles with respect to some general geometric coordinate system.

For example, in designing or analyzing the stresses in an automobile, it may be logical to define the x-axis as the forward direction of the vehicle, the y-axis as the lateral direction, and the z-axis as the vertical direction,

maintaining a right-handed coordinate system. This coordinate system is termed geometric (or global) because its directions correspond to the geometry of the body to which it is attached.

Because the stiffness and strength properties of a lamina (ply) of composite material are typically not isotropic, e.g., the material is typically orthotropic, it is convenient to define these material properties in terms of directions coinciding with any material symmetries that exist. The corresponding coordinate system is termed a material coordinate system.

For analysis purposes, it is necessary to express the properties of all lamina of the laminate in terms of a common (global) coordinate system, the logical choice being the geometric coordinate system. Thus, it is necessary to transform the material properties of each individual lamina from its own material coordinate system to the global (geometric) coordinate system. These transformation relations (familiar to many as the Mohr's circle transformations for stress and strain) must therefore be developed, and are presented in Chapter 2.

1.3.2 Stress–Strain Relations for Anisotropic Materials

The number of independent material constants relating stresses to strains, or strains to stresses, is dependent on the extent of material symmetry that exists. If the components of stress are expressed in terms of components of strain, these constants are called stiffnesses. If the components of strain are expressed in terms of components of stress, these constants are called compliances. Defying simple logic, the symbol C is customarily used to represent stiffnesses, and the symbol S is used to represent compliances. Literal translations from the non-English language of the original developers account for this confusion. These notations are now seemingly too ingrained to reverse, despite the novice's desire to do so.

In the most general case of a fully anisotropic material (i.e., no material symmetries exist), a total of 21 material constants must be experimentally determined. As material symmetry is introduced, it can be shown that certain of the stiffness terms (and the corresponding compliance terms) become zero, thus reducing the number of independent material constants. Some examples of practical interest are indicated in Table 1.1.

The last entry in Table 1.1, that of isotropic material behavior, is a familiar one. In this case, the material properties are the same in all directions, i.e., an infinite number of planes of symmetry exist, and only two stiffness constants are required to fully define the stress–strain response of the material. Engineers commonly utilize E, ν, and G, termed the Young's modulus, Poisson's ratio, and shear modulus, respectively. However, these three stiffness quantities must mutually satisfy the isotropic relation [5]

$$G = \frac{E}{2(1+\nu)} \tag{1.1}$$

Thus, only two of the three quantities can be independently prescribed.

TABLE 1.1

Number of Independent Material Constants as a Function of Material Symmetry [4]

Type of Symmetry	Number of Independent Material Constants
None (triclinic material)	21
One plane of symmetry (monoclinic)	13
Three planes of symmetry (orthotropic)	9
Transversely isotropic (one plane of isotropy)	5
Infinite planes of symmetry (isotropic)	2

In Chapter 2, an orthotropic material is chosen because it is the material symmetry of major interest. For example, it is representative of a unidirectional composite lamina, as well as many other composite material forms.

1.4 Typical Unidirectional Composite Properties

A very large number of different fiber–matrix combinations have been developed over the years. Nevertheless, the general classes of polymer–matrix composites can be characterized by a few representative materials. In the examples presented in Table 1.2, all properties are normalized to a common fiber volume of 60%.

The columns are ordered from left to right in terms of increasing composite axial stiffness, as primarily dictated by the fiber type. Spectra® is a polyethylene fiber developed by Allied Chemical Corporation, Petersburg, VA. Its relative inability to bond with polymer matrices accounts for the low transverse normal, longitudinal shear, and axial compressive strengths indicated for the unidirectional composite. Note that its highly oriented polymer structure also results in extreme values of coefficients of thermal expansion. Another polymeric fiber is Kevlar 49®, an aramid fiber produced by E.I. du Pont de Nemours and Company, Inc. While the compressive and transverse properties of this composite are generally better than those of the Spectra polyethylene fiber composite, they are still low relative to most of the other composites. AS4, IM6, and GY70 are all carbon fibers, representative of low, medium, and high modulus carbon fibers. The first two were produced by Hercules Corporation, and the third was produced by the Celanese Corporation. In all cases the epoxy matrix indicated is Hercules 3501-6 or a similar polymer. This is a high structural performance, but

TABLE 1.2

Typical Properties of Various Types of Polymer Matrix Unidirectional Composites (Nominal 60 Percent Fiber Volume)

Composite Property	Spectra/ Epoxy	E-Glass/ Epoxy	S2-Glass/ Epoxy	Kevlar 49/ Epoxy	AS4/ PEEK	AS4/ Epoxy	IM6/ Epoxy	BORON/ Epoxy	GY70/ Epoxy
E_1 (GPa)	31	43	52	76	134	138	172	240	325
E_2 (GPa)	3.4	9.7	11.7	5.5	10.1	10.3	10.0	18.6	6.2
G_{12} (GPa)	1.4	6.2	7.6	2.1	5.9	6.9	6.2	6.6	5.2
ν_{12}	0.32	0.26	0.28	0.34	0.28	0.30	0.29	0.23	0.26
X_1^T (MPa)	1100	1070	1590	1380	2140	2275	2760	1590	760
X_2^T (MPa)	8	38	41	30	80	52	50	60	26
X_1^C (MPa)	83	870	1050	275	1105	1590	1540	2930	705
X_2^C (MPa)	48	185	234	138	200	207	152	200	70
S_6 (MPa)	24	72	90	43	120	131	124	108	27
$\alpha_1(10^{-6}/°C)$	–11.0	6.4	6.2	–2.0	–0.1	–0.1	–0.4	4.5	–0.5
$\alpha_2(10^{-6}/°C)$	120	16	16	57	29	18	18	20	18
β_1 (10^{-4}/%M)	1.0	1.3	1.1	1.9	0.5	0.4	0.3	0.2	0.2
β_2 (10^{-3}/%M)	3.2	3.0	3.0	3.5	3.2	3.1	3.1	3.2	3.2
ρ (g/cm^3)	1.13	2.00	2.00	1.38	1.57	1.55	1.60	2.02	1.59

brittle, epoxy, resulting in strong but not highly impact resistant composites. The PEEK matrix is polyetheretherketone, a high-temperature thermoplastic. It is included here along with the brittle epoxy matrix to permit, in particular, a direct comparison with the AS4/epoxy composite system.

The rows in Table 1.2 indicate unidirectional composite in-plane material properties, i.e., stiffnesses, strengths, and hygrothermal properties. As will be discussed in greater detail in Chapter 2, the subscript 1 indicates the axial direction (the fiber direction), and subscript 2 indicates the in-plane transverse direction. Standard symbols are used and are defined as follows:

E_1	Axial stiffness
E_2	Transverse stiffness
G_{12}	In-plane shear stiffness
ν_{12}	Major Poisson's ratio
X_1^T	Axial tensile strength
X_2^T	Transverse tensile strength
X_1^C	Axial compressive strength
X_2^C	Transverse compressive strength
S_6	In-plane shear strength
α_1	Axial coefficient of thermal expansion
α_2	Transverse coefficient of thermal expansion
β_1	Axial coefficient of moisture expansion
β_2	Transverse coefficient of moisture expansion
ρ	Density

It is immediately obvious from Table 1.2 that the various unidirectional composite materials are highly orthotropic in terms of all of their mechanical and physical properties. The axial stiffness varies by an order of magnitude. Many have negative axial coefficients of thermal expansion, some much more negative than others. Yet, all of the materials have positive transverse coefficients of thermal expansion, although some are almost an order of magnitude higher than others. Many similar observations can be made by studying this table.

Overall, the use of composite materials offers the designer tremendous design flexibility and potential. However, because the strengths are also highly orthotropic, being very low in transverse tension and compression, and in shear, special care must be taken to design properly with them. The next chapter summarizes the analysis procedures required.

References

1. Y.M. Tarnopolskii and T.Y. Kincis, *Static Test Methods for Composites*, Van Nostrand Reinhold, New York, 1985.
2. J.M. Hodgkinson, ed., *Mechanical Testing of Advanced Fibre Composites*, CRC Press, Boca Raton, FL, 2000.
3. *Advanced Composites Design Guide*, 3rd ed., R.M. Neff, project engineer, Air Force Flight Dynamics Laboratory, Wright-Patterson Air Force Base, Dayton, OH January 1973.
4. R.M. Jones, *Mechanics of Composite Materials*, 2nd ed., Taylor & Francis, Philadelphia, 1999.
5. F.P. Beer and E.R. Johnston, Jr., *Mechanics of Materials*, 2nd ed., McGraw-Hill, New York, 1992.

2

Analysis of Composite Materials

2.1 Constitutive Relations

Laminated composites are typically constructed from orthotropic plies (laminae) containing unidirectional fibers or woven fabric. Generally, in a macroscopic sense, the lamina is assumed to behave as a homogeneous orthotropic material. The constitutive relation for a linear elastic orthotropic material in the material coordinate system (Figure 2.1) is [1–6]

$$\begin{bmatrix} \varepsilon_1 \\ \varepsilon_2 \\ \varepsilon_3 \\ \gamma_{23} \\ \gamma_{13} \\ \gamma_{12} \end{bmatrix} = \begin{bmatrix} S_{11} & S_{12} & S_{13} & 0 & 0 & 0 \\ S_{12} & S_{22} & S_{23} & 0 & 0 & 0 \\ S_{13} & S_{23} & S_{33} & 0 & 0 & 0 \\ 0 & 0 & 0 & S_{44} & 0 & 0 \\ 0 & 0 & 0 & 0 & S_{55} & 0 \\ 0 & 0 & 0 & 0 & 0 & S_{66} \end{bmatrix} \begin{bmatrix} \sigma_1 \\ \sigma_2 \\ \sigma_3 \\ \tau_{23} \\ \tau_{13} \\ \tau_{12} \end{bmatrix} \tag{2.1}$$

where the stress components (σ_i, τ_{ij}) are defined in Figure 2.1 and the S_{ij} are elements of the compliance matrix. The engineering strain components (ε_i, γ_{ij}) are defined as implied in Figure 2.2.

In a thin lamina, a state of plane stress is commonly assumed by setting

$$\sigma_3 = \tau_{23} = \tau_{13} = 0 \tag{2.2}$$

For Equation (2.1) this assumption leads to

$$\varepsilon_3 = S_{13}\sigma_1 + S_{23}\sigma_2 \tag{2.3a}$$

$$\gamma_{23} = \gamma_{13} = 0 \tag{2.3b}$$

Thus, for plane stress the through-the-thickness strain ε_3 is not an independent quantity and does not need to be included in the constitutive relationship. Equation (2.1) becomes

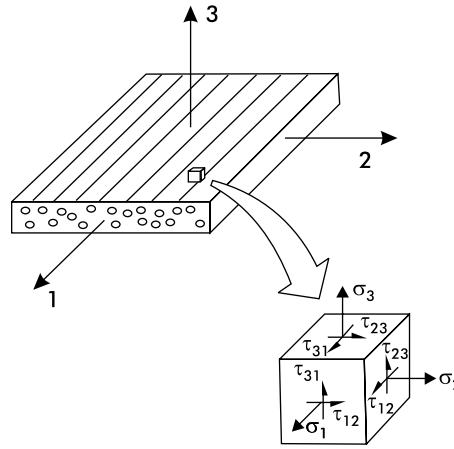

FIGURE 2.1
Definitions of principal material directions for an orthotropic lamina and stress components.

$$\begin{bmatrix} \varepsilon_1 \\ \varepsilon_2 \\ \gamma_{12} \end{bmatrix} = \begin{bmatrix} S_{11} & S_{12} & 0 \\ S_{12} & S_{22} & 0 \\ 0 & 0 & S_{66} \end{bmatrix} \begin{bmatrix} \sigma_1 \\ \sigma_2 \\ \tau_{12} \end{bmatrix} \tag{2.4}$$

The compliance elements S_{ij} may be related to the engineering constants (E_1, E_2, G_{12}, ν_{12}, ν_{21}),

$$S_{11} = 1/E_1, \quad S_{12} = -\nu_{12}/E_1 = -\nu_{21}/E_2 \tag{2.5a}$$

$$S_{22} = 1/E_2, \quad S_{66} = 1/G_{12} \tag{2.5b}$$

The engineering constants are average properties of the composite ply. The quantities E_1 and ν_{12} are the Young's modulus and Poisson's ratio, respectively, corresponding to stress σ_1 (Figure 2.2a)

$$E_1 = \sigma_1/\varepsilon_1 \tag{2.6a}$$

$$\nu_{12} = -\varepsilon_2/\varepsilon_1 \tag{2.6b}$$

E_2 and ν_{21} correspond to stress σ_2 (Figure 2.2b)

$$E_2 = \sigma_2/\varepsilon_2 \tag{2.7a}$$

$$\nu_{21} = -\varepsilon_1/\varepsilon_2 \tag{2.7b}$$

For a unidirectional composite E_2 is much less than E_1, and ν_{21} is much less than ν_{12}. For a balanced fabric composite $E_1 \approx E_2$ and $\nu_{12} \approx \nu_{21}$. The Poisson's ratios ν_{12} and ν_{21} are not independent

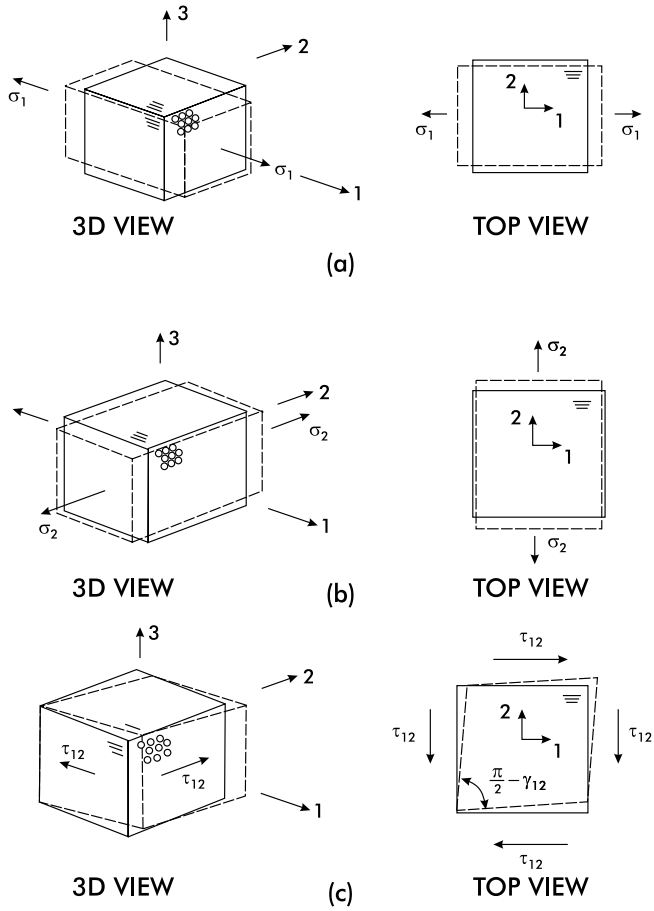

FIGURE 2.2
Illustration of deformations of an orthotropic material due to (a) stress σ_1, (b) stress σ_2, and (c) stress τ_{12}.

$$\nu_{21} = \nu_{12}E_2/E_1 \tag{2.8}$$

The in-plane shear modulus, G_{12}, is defined as (Figure 2.2c)

$$G_{12} = \tau_{12}/\gamma_{12} \tag{2.9}$$

It is often convenient to express stresses as functions of strains. This is accomplished by inversion of Equation (2.4)

$$\begin{bmatrix}\sigma_1\\ \sigma_2\\ \tau_{12}\end{bmatrix} = \begin{bmatrix} Q_{11} & Q_{12} & 0\\ Q_{12} & Q_{22} & 0\\ 0 & 0 & Q_{66}\end{bmatrix}\begin{bmatrix}\varepsilon_1\\ \varepsilon_2\\ \gamma_{12}\end{bmatrix} \tag{2.10}$$

where the reduced stiffnesses, Q_{ij}, can be expressed in terms of the engineering constants

$$Q_{11} = E_1/(1 - \nu_{12}\nu_{21}) \tag{2.11a}$$

$$Q_{12} = \nu_{12}E_2/(1 - \nu_{12}\nu_{21}) = \nu_{21}E_1/(1 - \nu_{12}\nu_{21}) \tag{2.11b}$$

$$Q_{22} = E_2/(1 - \nu_{12}\nu_{21}) \tag{2.11c}$$

$$Q_{66} = G_{12} \tag{2.11d}$$

2.1.1 Transformation of Stresses and Strains

For a lamina whose principal material axes (1,2) are oriented at an angle, θ, with respect to the x,y coordinate system (Figure 2.3), the stresses and strains can be transformed. It may be shown [1–6] that both the stresses and strains transform according to

$$\begin{bmatrix} \sigma_1 \\ \sigma_2 \\ \tau_{12} \end{bmatrix} = [T] \begin{bmatrix} \sigma_x \\ \sigma_y \\ \tau_{xy} \end{bmatrix} \tag{2.12}$$

and

$$\begin{bmatrix} \varepsilon_1 \\ \varepsilon_2 \\ \gamma_{12}/2 \end{bmatrix} = [T] \begin{bmatrix} \varepsilon_x \\ \varepsilon_y \\ \gamma_{xy}/2 \end{bmatrix} \tag{2.13}$$

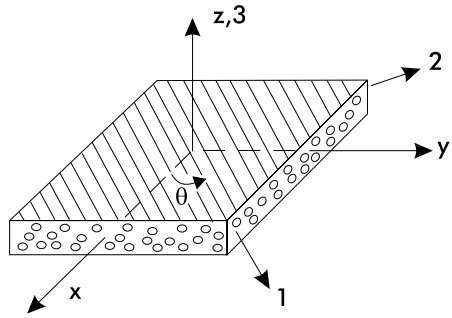

FIGURE 2.3
Positive (counterclockwise) rotation of principal material axes (1,2) from arbitrary x,y axes.

where the transformation matrix is [1–6]

$$[T] = \begin{bmatrix} m^2 & n^2 & 2mn \\ n^2 & m^2 & -2mn \\ -mn & mn & m^2 - n^2 \end{bmatrix} \tag{2.14}$$

and

$$m = \cos\theta \tag{2.15a}$$

$$n = \sin\theta \tag{2.15b}$$

From Equations (2.12) and (2.13) it is possible to establish the lamina strain–stress relations in the (x,y) coordinate system [1–6]

$$\begin{bmatrix} \varepsilon_x \\ \varepsilon_y \\ \gamma_{xy} \end{bmatrix} = \begin{bmatrix} \bar{S}_{11} & \bar{S}_{12} & \bar{S}_{16} \\ \bar{S}_{12} & \bar{S}_{22} & \bar{S}_{26} \\ \bar{S}_{16} & \bar{S}_{26} & \bar{S}_{66} \end{bmatrix} \begin{bmatrix} \sigma_x \\ \sigma_y \\ \tau_{xy} \end{bmatrix} \tag{2.16}$$

The $\bar{S}_{ij}$ terms are the transformed compliances defined in Appendix A. Similarly, the lamina stress–strain relations become

$$\begin{bmatrix} \sigma_x \\ \sigma_y \\ \tau_{xy} \end{bmatrix} = \begin{bmatrix} \bar{Q}_{11} & \bar{Q}_{12} & \bar{Q}_{16} \\ \bar{Q}_{12} & \bar{Q}_{22} & \bar{Q}_{26} \\ \bar{Q}_{16} & \bar{Q}_{26} & \bar{Q}_{66} \end{bmatrix} \begin{bmatrix} \varepsilon_x \\ \varepsilon_y \\ \gamma_{xy} \end{bmatrix} \tag{2.17}$$

where the overbars denote transformed reduced stiffness elements, defined in Appendix A.

2.1.2 Hygrothermal Strains

If fibrous composite materials are processed at elevated temperatures, thermal strains are introduced during cooling to room temperature, leading to residual stresses and dimensional changes. Figure 2.4 illustrates dimensional changes of a composite subjected to a temperature increase of ΔT from the reference temperature T. Furthermore, polymer matrices are commonly hygroscopic, and absorbing moisture leads to swelling of the material. The analysis of moisture expansion strains in composites is mathematically

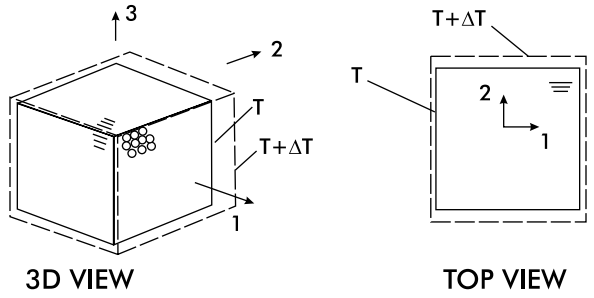

FIGURE 2.4
Deformation of a lamina subject to temperature increase.

equivalent to that for thermal strains [7,8] (neglecting possible pressure dependence of moisture absorption).

The constitutive relationship, when it includes mechanical-, thermal-, and moisture-induced strains, takes the following form [1,4]

$$\begin{bmatrix} \varepsilon_1 \\ \varepsilon_2 \\ \gamma_{12} \end{bmatrix} = \begin{bmatrix} S_{11} & S_{12} & 0 \\ S_{12} & S_{22} & 0 \\ 0 & 0 & S_{66} \end{bmatrix} \begin{bmatrix} \sigma_1 \\ \sigma_2 \\ \tau_{12} \end{bmatrix} + \begin{bmatrix} \varepsilon_1^T \\ \varepsilon_2^T \\ 0 \end{bmatrix} + \begin{bmatrix} \varepsilon_1^M \\ \varepsilon_2^M \\ 0 \end{bmatrix} \tag{2.18}$$

where superscripts T and M denote temperature- and moisture-induced strains, respectively. Note that shear strains are not induced in the principal material system by a temperature or moisture content change (Figure 2.4). Equation (2.18) is based on the superposition of mechanical-, thermal-, and moisture-induced strains. Inversion of Equation (2.18) gives

$$\begin{bmatrix} \sigma_1 \\ \sigma_2 \\ \tau_{12} \end{bmatrix} = \begin{bmatrix} Q_{11} & Q_{12} & 0 \\ Q_{11} & Q_{12} & 0 \\ 0 & 0 & Q_{66} \end{bmatrix} \begin{bmatrix} \varepsilon_1 & -\varepsilon_1^T & -\varepsilon_1^M \\ \varepsilon_2 & -\varepsilon_2^T & -\varepsilon_2^M \\ & \gamma_{12} & \end{bmatrix} \tag{2.19}$$

Consequently, the stress-generating strains are obtained by subtraction of the thermal- and moisture-induced strains from the total strains. The thermal- and moisture-induced strains are often approximated as linear functions of the changes in temperature and moisture concentration,

$$\begin{bmatrix} \varepsilon_1^T \\ \varepsilon_2^T \end{bmatrix} = \Delta T \begin{bmatrix} \alpha_1 \\ \alpha_2 \end{bmatrix} \tag{2.20}$$

$$\begin{bmatrix} \varepsilon_1^M \\ \varepsilon_2^M \end{bmatrix} = \Delta M \begin{bmatrix} \beta_1 \\ \beta_2 \end{bmatrix} \tag{2.21}$$

where ΔT and ΔM are the temperature change and moisture concentration change from the reference state.

The transformed thermal expansion coefficients ($\alpha_x, \alpha_y, \alpha_{xy}$) are obtained from those in the principal system using Equation (2.13). Note, however, that in the principal material coordinate system, there is no shear deformation induced [4], i.e., $\alpha_{16} = \beta_{16} = 0$,

$$\alpha_x = m^2\alpha_1 + n^2\alpha_2 \tag{2.22a}$$

$$\alpha_y = n^2\alpha_1 + m^2\alpha_2 \tag{2.22b}$$

$$\alpha_{xy} = 2mn(\alpha_1 - \alpha_2) \tag{2.22c}$$

The moisture expansion coefficients ($\beta_x, \beta_y, \beta_{xy}$) are obtained by replacing α with β in Equations (2.22).

The transformed constitutive relations for a lamina, when incorporating thermal- and moisture-induced strains, are

$$\begin{bmatrix} \varepsilon_x \\ \varepsilon_y \\ \gamma_{xy} \end{bmatrix} = \begin{bmatrix} \bar{S}_{11} & \bar{S}_{12} & \bar{S}_{16} \\ \bar{S}_{12} & \bar{S}_{22} & \bar{S}_{26} \\ \bar{S}_{16} & \bar{S}_{26} & \bar{S}_{66} \end{bmatrix} \begin{bmatrix} \sigma_x \\ \sigma_y \\ \tau_{xy} \end{bmatrix} + \begin{bmatrix} \varepsilon_x^T \\ \varepsilon_y^T \\ \gamma_{xy}^T \end{bmatrix} + \begin{bmatrix} \varepsilon_x^M \\ \varepsilon_y^M \\ \gamma_{xy}^M \end{bmatrix} \tag{2.23}$$

$$\begin{bmatrix} \sigma_x \\ \sigma_y \\ \tau_{xy} \end{bmatrix} = \begin{bmatrix} \bar{Q}_{11} & \bar{Q}_{12} & \bar{Q}_{16} \\ \bar{Q}_{12} & \bar{Q}_{22} & \bar{Q}_{26} \\ \bar{Q}_{16} & \bar{Q}_{26} & \bar{Q}_{66} \end{bmatrix} \begin{bmatrix} \varepsilon_x - \varepsilon_x^T - \varepsilon_x^M \\ \varepsilon_y - \varepsilon_y^T - \varepsilon_y^M \\ \gamma_{xy} - \gamma_{xy}^T - \gamma_{xy}^M \end{bmatrix} \tag{2.24}$$

2.2 Micromechanics

As schematically illustrated in Figure 2.5, micromechanics aims to describe the moduli and expansion coefficients of the lamina from properties of the fiber and matrix, the microstructure of the composite, and the volume fractions of the constituents. Sometimes, also the small transition region between bulk fiber and bulk matrix, i.e., interphase, is considered. Much fundamental work has been devoted to the study of the states of strain and stress in the constituents, and the formulation of appropriate averaging schemes to allow definition of macroscopic engineering constants. Most micromechanics analyses have focused on unidirectional continuous fiber composites, e.g. [9,10],

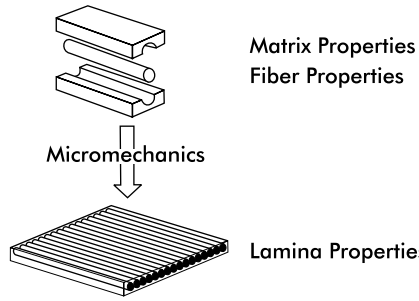

FIGURE 2.5
Role of micromechanics.

although properties of composites with woven fabric reinforcements can also be predicted with reasonable accuracy, see Reference [11].

The objective of this section is not to review the various micromechanics developments. The interested reader can find ample information in the above-referenced review articles. In this section, we will limit the presentation to some commonly used estimates of the stiffness constants, E_1, E_2, ν_{12}, ν_{21}, and G_{12}, and thermal expansion coefficients α_1 and α_2 required for describing the small strain response of a unidirectional lamina under mechanical and thermal loads (see Section 2.1). Such estimates may be useful for comparison to experimentally measured quantities.

2.2.1 Stiffness Properties of Unidirectional Composites

Although most matrices are isotropic, many fibers such as carbon and Kevlar (E.I. du Pont de Nemours and Company, Wilmington, DE,) have directional properties because of molecular or crystal plane orientation effects [4]. As a result, the axial stiffness of such fibers is much greater than the transverse stiffness. The thermal expansion coefficients along and transverse to the fiber axis also are quite different [4]. It is common to assume cylindrical orthotropy for fibers with axisymmetric microstructure. The stiffness constants required for plane stress analysis of a composite with such fibers are E_L, E_T, ν_{LT}, and G_{LT}, where L and T denote the longitudinal and transverse directions of a fiber. The corresponding thermal expansion coefficients are α_L and α_T.

The mechanics of materials approach reviewed in Reference [10] yields

$$E_1 = E_{Lf}V_f + E_mV_m \tag{2.25a}$$

$$E_2 = \frac{E_{Tf}E_m}{E_{Tf}V_m + E_mV_f} \tag{2.25b}$$

$$\nu_{12} = \nu_{LTf}V_f + \nu_mV_m \tag{2.25c}$$

$$G_{12} = \frac{G_{LTf} G_m}{G_{LTf} V_m + G_m V_f} \tag{2.25d}$$

where subscripts f and m represent fiber and matrix, respectively, and the symbol V represents volume fraction. Note that once E_1, E_2, and ν_{12} are calculated from Equations (2.25a), ν_{21} is obtained from Equation (2.8). Equations (2.25a) and (2.25c) provide good estimates of E_1 and ν_{12}. Equations (2.25b) and (2.25d), however, substantially underestimate E_2 and G_{12} [10]. More realistic estimates of E_2 and G_{12} are provided in References [10,12].

Simple, yet reasonable estimates of E_2 and G_{12} may also be obtained from the Halpin-Tsai equations [13],

$$P = \frac{P_m (1 + \xi \chi V_f)}{1 - \chi V_f} \tag{2.26a}$$

$$\chi = \frac{P_f - P_m}{P_f + \xi P_m} \tag{2.26b}$$

where P is the property of interest (E_2 or G_{12}) and P_f and P_m are the corresponding fiber and matrix properties, respectively. The parameter ξ is called the reinforcement efficiency; $\xi(E_2) = 2$ and $\xi(G_{12}) = 1$, for circular fibers.

2.2.2 Expansion Coefficients

Thermal expansion (and moisture swelling) coefficients can be defined by considering a composite subjected to a uniform increase in temperature (or moisture content) (Figure 2.4).

The thermal expansion coefficients, α_1 and α_2, of a unidirectional composite consisting of cylindrically or transversely orthotropic fibers in an isotropic matrix determined using the mechanics of materials approach [10] are

$$\alpha_1 = \frac{\alpha_{Lf} E_{Lf} V_f + \alpha_m E_m V_m}{E_{Lf} V_f + E_m V_m} \tag{2.27a}$$

$$\alpha_2 = \alpha_{Tf} V_f + \alpha_m V_m \tag{2.27b}$$

Predictions of α_1 using Equation (2.27a) are accurate [10], whereas Equation (2.27b) underestimates the actual value of α_2. An expression derived by Hyer and Waas [10] provides a more accurate prediction of α_2:

$$\alpha_2 = \alpha_{Tf} V_f + \alpha_m V_m + \frac{(E_{Lf} \nu_m + E_m \nu_{LTf})}{E_{Lf} V_f + E_m V_m} (\alpha_m - \alpha_{Lf}) V_f V_m \tag{2.28}$$

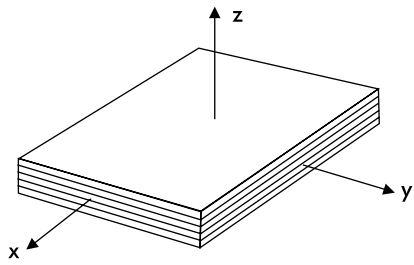

FIGURE 2.6
Laminate coordinate system.

2.3 Laminated Plate Theory

Structures fabricated from composite materials rarely utilize a single composite lamina because this unit is thin and anisotropic. To achieve a thicker cross section and more balanced properties, plies of prepreg or fiber mats are stacked in specified directions. Such a structure is called a laminate (Figure 2.6). Most analyses of laminated structures are limited to flat panels (see, e.g., References [1,2]). Extension to curved laminated shell structures may be found in References [5,14,15].

In this section, attention will be limited to a flat laminated plate under in-plane and bending loads. The classical theory of such plates is based on the assumption that a line originally straight and perpendicular to the middle surface remains straight and normal to the middle surface, and that the length of the line remains unchanged during deformation of the plate [1–6]. These assumptions lead to the vanishing of the out-of-plane shear and extensional strains:

$$\gamma_{xz} = \gamma_{yz} = \varepsilon_z = 0 \tag{2.29}$$

where the laminate coordinate system (x,y,z) is indicated in Figure 2.6. Consequently, the laminate strains are reduced to ε_x, ε_y, and γ_{xy}. The assumption that the cross sections undergo only stretching and rotation leads to the following strain distribution [1–6]:

$$\begin{bmatrix} \varepsilon_x \\ \varepsilon_y \\ \gamma_{xy} \end{bmatrix} = \begin{bmatrix} \varepsilon_x^0 \\ \varepsilon_y^0 \\ \gamma_{xy}^0 \end{bmatrix} + z \begin{bmatrix} \kappa_x \\ \kappa_y \\ \kappa_{xy} \end{bmatrix} \tag{2.30}$$

where $\left[\varepsilon_x^0, \varepsilon_y^0, \gamma_{xy}^0\right]$ and $\left[\kappa_x, \kappa_y, \kappa_{xy}\right]$ are the midplane strains and curvatures, respectively, and z is the distance from the midplane.

Force and moment resultants, $[N_x, N_y, N_{xy}]$ and $[M_x, M_y, M_{xy}]$, respectively, are obtained by integration of the stresses in each layer over the laminate thickness, h,

$$\begin{bmatrix} N_x \\ N_y \\ N_{xy} \end{bmatrix} = \int_{-h/2}^{h/2} \begin{bmatrix} \sigma_x \\ \sigma_y \\ \tau_{xy} \end{bmatrix}_k dz \tag{2.31}$$

$$\begin{bmatrix} M_x \\ M_y \\ M_{xy} \end{bmatrix} = \int_{-h/2}^{h/2} \begin{bmatrix} \sigma_x \\ \sigma_y \\ \tau_{xy} \end{bmatrix}_k zdz \tag{2.32}$$

where the subscript k represents the k^{th} lamina in the laminate. Combination of Equations (2.24) with (2.30–2.32) leads to the following constitutive relationships among forces and moments and midplane strains and curvatures:

$$\begin{bmatrix} N_x + N_x^T + N_x^M \\ N_y + N_y^T + N_y^M \\ N_{xy} + N_{xy}^T + N_{xy}^M \end{bmatrix} = \begin{bmatrix} A_{11} & A_{12} & A_{16} \\ A_{12} & A_{22} & A_{26} \\ A_{16} & A_{26} & A_{66} \end{bmatrix} \begin{bmatrix} \varepsilon_x^0 \\ \varepsilon_y^0 \\ \gamma_{xy}^0 \end{bmatrix} + \begin{bmatrix} B_{11} & B_{12} & B_{16} \\ B_{12} & B_{22} & B_{26} \\ B_{16} & B_{26} & B_{66} \end{bmatrix} \begin{bmatrix} \kappa_x \\ \kappa_y \\ \kappa_{xy} \end{bmatrix} \tag{2.33}$$

$$\begin{bmatrix} M_x + M_x^T + M_x^M \\ M_y + M_y^T + M_y^M \\ M_{xy} + M_{xy}^T + M_{xy}^M \end{bmatrix} = \begin{bmatrix} B_{11} & B_{12} & B_{16} \\ B_{12} & B_{22} & B_{26} \\ B_{16} & B_{26} & B_{66} \end{bmatrix} \begin{bmatrix} \varepsilon_x^0 \\ \varepsilon_y^0 \\ \gamma_{xy}^0 \end{bmatrix} + \begin{bmatrix} D_{11} & D_{12} & D_{16} \\ D_{12} & D_{22} & D_{26} \\ D_{16} & D_{26} & D_{66} \end{bmatrix} \begin{bmatrix} \kappa_x \\ \kappa_y \\ \kappa_{xy} \end{bmatrix} \tag{2.34}$$

where the A_{ij}, B_{ij}, and D_{ij} are called extensional stiffnesses, coupling stiffnesses, and bending stiffnesses, respectively [1–6], given by

$$A_{ij} = \sum_{k=1}^{N} \left(\overline{Q}_{ij}\right)_k \left(z_k - z_{k-1}\right) \tag{2.35a}$$

$$B_{ij} = \frac{1}{2} \sum_{k=1}^{N} \left(\overline{Q}_{ij}\right)_k \left(z_k^2 - z_{k-1}^2\right) \tag{2.35b}$$

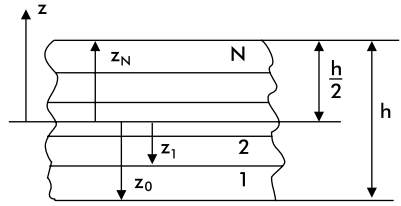

FIGURE 2.7
Definition of ply coordinates, z_k.

$$D_{ij} = \frac{1}{3}\sum_{k=1}^{N}\left(\overline{Q}_{ij}\right)_k\left(z_k^3 - z_{k-1}^3\right) \tag{2.35c}$$

The ply coordinates z_k, (k = 1, 2…N), where N is the number of plies in the laminate, are defined in Figure 2.7 and may be calculated from the following recursion formula:

$$z_0 = -h/2 \qquad k = 0 \tag{2.36a}$$

$$z_k = z_{k-1} + h_k \qquad k = 1, 2, \ldots, N \tag{2.36b}$$

in which h_k is the ply thickness of the kth ply.

For the steady-state condition considered, the temperature change is uniform throughout the laminate, and the thermal force resultants are determined from

$$\begin{bmatrix} N_x^T \\ N_y^T \\ N_{xy}^T \end{bmatrix} = \sum_{k=1}^{N}\begin{bmatrix} \overline{Q}_{11} & \overline{Q}_{12} & \overline{Q}_{16} \\ \overline{Q}_{12} & \overline{Q}_{22} & \overline{Q}_{26} \\ \overline{Q}_{16} & \overline{Q}_{26} & \overline{Q}_{66} \end{bmatrix}_k \begin{bmatrix} \alpha_x \\ \alpha_y \\ \alpha_{xy} \end{bmatrix}_k (z_k - z_{k-1})\Delta T \tag{2.37}$$

The moisture-induced force resultants $[N_x^M, N_y^M, N_{xy}^M]$ are obtained in the same manner as the thermal force resultants, but by replacing $[\alpha_x, \alpha_y, \alpha_{xy}]$ with $[\beta_x, \beta_y, \beta_{xy}]$, and ΔT with ΔM in Equation (2.37).

The thermal moment resultants $[M_x^T, M_y^T, M_{xy}^T]$ are determined from

$$\begin{bmatrix} M_x^T \\ M_y^T \\ M_{xy}^T \end{bmatrix} = \frac{1}{2}\sum_{k=1}^{N}\begin{bmatrix} \overline{Q}_{11} & \overline{Q}_{12} & \overline{Q}_{16} \\ \overline{Q}_{12} & \overline{Q}_{22} & \overline{Q}_{26} \\ \overline{Q}_{16} & \overline{Q}_{26} & \overline{Q}_{66} \end{bmatrix}_k \begin{bmatrix} \alpha_x \\ \alpha_y \\ \alpha_{xy} \end{bmatrix}_k (z_k^2 - z_{k-1}^2)\Delta T \tag{2.38}$$

The moisture-induced moment resultants $[M_x^M, M_y^M, M_{xy}^M]$ are obtained by replacing the α values with β values and ΔT with ΔM in Equations (2.38).

Most commonly, only the steady-state temperature and moisture concentration in the composite is of interest (ΔT and ΔC are constants). However, in a transient situation, the transfer of heat by conduction [16], or moisture diffusion [17,18] has to be considered. Pipes et al. [19] examined laminated plates subject to transient conditions. For laminates with the plies consisting of different materials, the moisture concentration may vary through the thickness in a stepwise manner. At steady-state this is incorporated into the analysis by letting $\Delta M = (\Delta M)_k$, [20].

Equations (2.33) and (2.34) may conveniently be written as

$$\begin{bmatrix} N \\ M \end{bmatrix} = \begin{bmatrix} A & B \\ B & D \end{bmatrix} \begin{bmatrix} \varepsilon^0 \\ \kappa \end{bmatrix} \tag{2.39}$$

where [N] and [M] represent the left-hand side of Equations (2.33) and (2.34), i.e., the sum of mechanical and hygrothermal forces and moments, respectively.

Equations (2.39) represent the stiffness form of the laminate constitutive equations. Sometimes it is more convenient to express the midplane strains and curvatures as a function of the forces and moments. This represents the compliance form of the laminate constitutive equations, which is obtained by inversion of Equations (2.39),

$$\begin{bmatrix} \varepsilon^0 \\ \kappa \end{bmatrix} = \begin{bmatrix} A' & B' \\ C' & D' \end{bmatrix} \begin{bmatrix} N \\ M \end{bmatrix} \tag{2.40}$$

Expressions for the matrices [A′], [B′], [C′], and [D′] are given in Appendix A.

2.4 St. Venant's Principle and End Effects in Composites

In the testing and evaluation of any material, it is generally assumed that load introduction effects are confined to a region close to the grips or loading points, and a uniform state of stress and strain exists within the test section. The justification for such a simplification is usually based on the St. Venant principle, which states that the difference between the stresses caused by statically equivalent load systems is insignificant at distances greater than the largest dimension of the area over which the loads are acting [21]. This estimate, however, is based on isotropic material properties. For anisotropic composite materials, Horgan et al. [22–25] showed that the application of St. Venant's principle for plane elasticity problems involving anisotropic materials is not justified in general. For the particular problem of a rectangular strip made of

highly anisotropic material and loaded at the ends, it was demonstrated that the stress approached the uniform St. Venant solution much more slowly than the corresponding solution for an isotropic material [23].

The size of the region where end effects influence the stresses in a rectangular strip loaded with tractions at the ends is given by [23]

$$\lambda \approx \frac{b}{2\pi}\left(E_1/G_{12}\right)^{1/2} \tag{2.41}$$

where b is the maximum dimension of the cross section, and E_1 and G_{12} are the longitudinal elastic and shear moduli, respectively.

In this equation λ is defined as the distance over which the self-equilibrated stress decays to 1/e of its value at the end. When the ratio E_1/G_{12} is large, the decay length is large and end effects are transferred a considerable distance along the gage section. Testing of highly anisotropic materials thus requires special consideration of load introduction effects. Arridge et al. [26], for example, found that a very long specimen with an aspect ratio ranging from 80 to 100 was needed to avoid the influence of clamping effects in tension testing of highly anisotropic, drawn polyethylene film. Several other cases are reviewed in Reference [25].

2.5 Lamina Strength Analysis

When any material is considered for a structure, an important task for the structural engineer is to assess the load-carrying ability of the particular material/structure combination. Prediction of the strength of composite materials has been an active area of research since the early work of Tsai [27]. Many failure theories have been suggested, although no universally accepted failure criterion exists [28]. As pointed out by Hyer [4], however, no single criterion could be expected to accurately predict failure of all composite materials under all loading conditions. Popular strength criteria are maximum stress, maximum strain, and Tsai-Wu criteria (see References [1–6,28]). These criteria are phenomenological in the sense that they do not rely on physical modeling of the failure process. The reason for their popularity is that they are based on failure tests on simple specimens in tension, compression, and shear (Chapters 5–7) and are able to predict load levels required to fail more complicated structures under combined stress loading.

In the following presentation, failure of the lamina will first be examined and then failure of the laminate will be briefly considered. It is assumed that the lamina, being unidirectional or a woven fabric ply, can be treated as a homogeneous orthotropic ply with known, measured strengths in the principal material directions. Furthermore, the shear strength in the plane of the

TABLE 2.1

Basic Strengths of Orthotropic Plies for Plane Stress

Direction/Plane	Active Stress	Strength	Ultimate Strain
1	σ_1	X_1^T, X_1^C	e_1^T, e_1^C
2	σ_2	X_2^T, X_2^C	e_2^T, e_2^C
1,2	τ_{12}	S_6	e_6

Note: All strengths and ultimate strains are defined by their magnitudes.

fibers is independent of the sign of the shear stress. The presentation is limited to plane stress in the plane of the fibers. Table 2.1 lists the five independent failure stresses and strains corresponding to plane stress.

Notice here that superscripts T and C denote tension and compression, respectively, and that strengths and ultimate strains are defined as positive, i.e., the symbols indicate their magnitudes. For example, a composite ply loaded in pure negative shear ($\tau_{12} < 0$) would fail at a shear stress $\tau_{12} = -S_6$ and shear strain $\gamma_{12} = -e_6$.

2.5.1 Maximum Stress Failure Criterion

The maximum stress failure criterion assumes that failure occurs when any one of the in-plane stresses σ_1, σ_2, or τ_{12} attains its limiting value independent of the other components of stress. If the magnitudes of the stress components are less than their values at failure, failure does not occur, and the element or structure is considered safe. For determining the failure load, any of the following equalities must be satisfied at the point when failure occurs:

$$\sigma_1 = X_1^T \tag{2.42a}$$

$$\sigma_1 = -X_1^C \tag{2.42b}$$

$$\sigma_2 = X_2^T \tag{2.42c}$$

$$\sigma_2 = -X_2^C \tag{2.42d}$$

$$\tau_{12} = S_6 \tag{2.42e}$$

$$\tau_{12} = -S_6 \tag{2.42f}$$

For unidirectional and fabric composites, Equations (2.42a and b) indicate failure of fibers at quite high magnitudes of stress, whereas Equations (2.4c–f) indicate matrix or fiber–matrix interface dominated failures at much lower

magnitudes of stress for unidirectional composites. For fabric composites, however, Equations (2.42c and d) indicate failure of the fibers oriented along the 2-direction.

2.5.2 Maximum Strain Failure Criterion

The maximum strain criterion assumes that failure of any principal plane of the lamina occurs when any in-plane strain reaches its ultimate value in uniaxial tension, compression, or pure shear. Failure should occur when any of the following equalities are satisfied (Table 2.1):

$$\varepsilon_1 = e_1^T \tag{2.43a}$$

$$\varepsilon_1 = -e_1^C \tag{2.43b}$$

$$\varepsilon_2 = e_2^T \tag{2.43c}$$

$$\varepsilon_2 = -e_2^C \tag{2.43d}$$

$$\gamma_{12} = e_6 \tag{2.43e}$$

$$\gamma_{12} = -e_6 \tag{2.43f}$$

In these expressions, the symbol e represents the magnitude of the ultimate strain. If any of the above conditions become satisfied, failure is assumed to occur by the same mechanism leading to failure in uniaxial loading or pure shear loading. Similar to the maximum stress criterion, the maximum strain criterion has the ability of predicting the failure mode.

2.5.3 Tsai-Wu Failure Criterion

Tsai and Wu [29] proposed a second-order tensor polynomial failure criterion for prediction of biaxial strength, which takes the following form for plane stress:

$$F_1\sigma_1 + F_2\sigma_2 + F_{11}\sigma_1^2 + F_{22}\sigma_2^2 + F_{66}\tau_{12}^2 + 2F_{12}\sigma_1\sigma_2 = 1 \tag{2.44}$$

Failure under combined stress is assumed to occur when the left-hand side of Equation (2.44) is equal to or greater than one. All of the parameters of the Tsai-Wu criterion, except F_{12}, can be expressed in terms of the basic strengths (Table 2.1).

$$F_1 = 1/X_1^T - 1/X_1^C \qquad F_{11} = 1/\left(X_1^T X_1^C\right)$$
$$F_2 = 1/X_2^T - 1/X_2^C \qquad F_{22} = 1/\left(X_2^T X_2^C\right) \tag{2.45}$$
$$F_{66} = 1/S_6^2$$

F_{12} is a strength interaction parameter that has to be determined from a biaxial experiment. Such experiments are, unfortunately, very expensive and difficult to properly conduct. As an alternative, Tsai and Hahn [30] suggested that F_{12} be estimated from the following relationship:

$$F_{12} = -\frac{1}{2}\sqrt{F_{11}F_{22}} \tag{2.46}$$

The Tsai-Wu criterion has found widespread applicability in the composite industry because of its versatility and that it provides quite accurate predictions of strength. It does not, however, predict the mode of failure.

2.6 Laminate Strength Analysis

Analysis of failure and strength of laminated composites is quite different from the analysis of strength of a single ply. Failure of laminates commonly involves delamination, i.e., separation of the plies, which will be discussed in Chapter 14. This failure mode is commonly influenced by the three-dimensional state of stress that develops near free edges in laminated specimens [31]. Furthermore, multidirectional composite laminates are commonly processed at elevated temperatures and the mismatch in thermal expansion between the plies leads to residual stresses in the plies upon cooling [32–34]. Exposure of the laminate to moisture will also influence the state of residual stress in the laminate [18,35].

A common failure mode in laminates containing unidirectional plies is matrix cracking, which is failure of the matrix and fiber–matrix interface in a plane perpendicular to the fiber direction (Figure 2.8). Such a failure is called first-ply failure and occurs because of the presence of a weak plane transverse to the fiber axis in such composites. In fabric composites, no such weak planes exist, and failure initiates locally in fiber tows and matrix pockets before ultimate failure occurs [36]. At any instant, local failures tend to arrest by constraint of adjacent layers or tows in the laminate before the occurrence of catastrophic failure of the laminate. Wang and Crossman et al. [37–39] and Flaggs and Kural [40] found a very large constraint effect in composite laminates with unidirectional plies. They examined matrix cracking in a set of

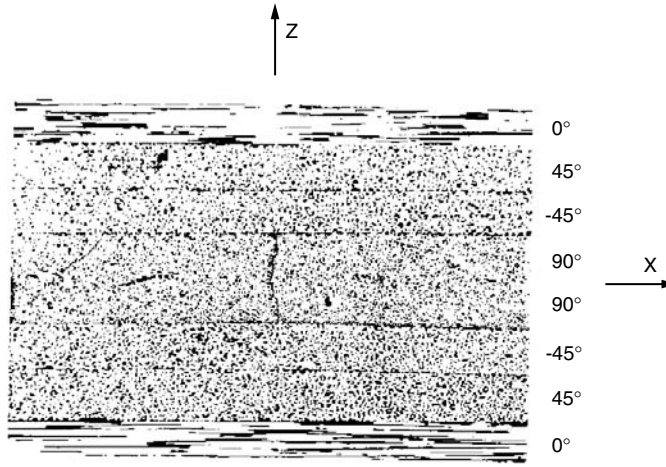

FIGURE 2.8
Matrix crack of a unidirectional ply in a laminate (first-ply failure).

laminates containing unidirectional 90° plies bonded together and found that the *in situ* strength depends strongly on the number of plies of the same orientation bonded together, and on the adjacent ply orientations. Consequently, there are a host of mechanisms influencing failure of laminates, and as a result, accurate failure prediction is associated with severe difficulties.

Various methods to predict ply failures and ultimate failure of composite laminates are reviewed by Sun [28]. A common method in laminate failure analysis is to determine the stresses and strains in the laminate using laminated plate theory (Section 2.3), and then examine the loads and strains corresponding to the occurrence of first-ply failure as predicted by the failure criterion selected. The ply failure mode is then identified. Swanson and Trask [41] and Swanson and Qian [42] performed biaxial tension–tension and tension–compression testing on several carbon/epoxy laminate cylinders made from unidirectional plies. Ply failures were identified using strength criteria mentioned in Section 2.5. Final failure of the cylinders was predicted by using a ply property reduction method (ply-by-ply discount method) where failed plies are identified and the transverse and shear moduli (E_2 and G_{12}) of the failed plies are assigned numbers very close to zero. The laminate with reduced stiffness is then again analyzed for stresses and strains [28]. Comparison of the predictions with measured ultimate failure data of the cylinders revealed good agreement for all criteria. It was concluded that the maximum stress and maximum strain criteria are quite insensitive to variations in the ply transverse failure strengths (X_2^T and S_6). This is an advantage because, as discussed, these strengths are very difficult to determine *in situ*. Hence, the failure criteria that do not demand accurate transverse ply failure strengths were concluded to be the most pertinent for failure prediction. For further reading, see References [1–6] and [28].

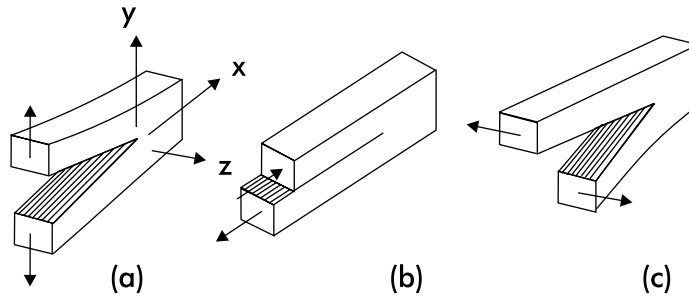

FIGURE 2.9
Modes of crack surface displacements. (a) Mode I (opening), (b) Mode II (sliding), and (c) Mode III (tearing).

2.7 Fracture Mechanics Concepts

The influence of defects and cracks on the strength of a material or structure is the subject of fracture mechanics. The object of fracture mechanics analysis is the prediction of the onset of crack growth for a body containing a flaw of a given size. To calculate the critical load for a cracked composite, it has generally been assumed that the size of the plastic zone at the crack tip is small compared to the crack length. Linear elastic fracture mechanics has been found useful for certain types of cracks in composites, i.e., interlaminar cracks [43] or matrix cracks in a unidirectional composite [37,44].

The equilibrium of an existing crack may be judged from the intensity of elastic stress around the crack tip. Solutions of the elastic stress field in isotropic [45] and orthotropic [46] materials show that stress singularities associated with in-plane cracks are of the $r^{-1/2}$ type, where r is the distance from the crack tip. Stress intensity factors may be determined for crack problems where the crack plane is in any of the planes of orthotropic material symmetry. It is possible to partition the crack tip loading into the three basic modes of crack surface displacement shown in Figure 2.9. Mode I refers to opening of the crack surfaces, Mode II refers to sliding, and Mode III refers to tearing.

It has, however, become common practice to investigate interlaminar cracks using the strain energy release rate, G. This quantity is based on energy considerations and is mathematically well defined and measurable in experiments. The energy approach, which stems from the original Griffith treatment [47], is based on a thermodynamic criterion for fracture by considering the energy available for crack growth of the system on one hand, and the surface energy required to extend an existing crack on the other hand. An elastic potential for a cracked body may be defined as

$$H = W - U \tag{2.47}$$

where W is the work supplied by the movement of the external forces, and U is the elastic strain energy stored in the body. If G_c is the work required to create a unit crack area, it is possible to formulate a criterion for crack growth,

$$\delta H \geq G_c \delta A \tag{2.48}$$

where δA is the increase in crack area.

A critical condition occurs when the net energy supplied just balances the energy required to grow the crack; i.e.,

$$\delta H = G_c \delta A \tag{2.49}$$

Equilibrium becomes unstable when the net energy supplied exceeds the required crack growth energy,

$$\delta H > G_c \delta A \tag{2.50}$$

The strain energy release rate, G, is defined as

$$G = \frac{\partial H}{\partial A} \tag{2.51}$$

In terms of G, the fracture criterion may thus be formulated as

$$G \geq G_c \tag{2.52}$$

This concept will be illustrated for a linear elastic body containing a crack of original length, a. Figure 2.10 shows the load, P, vs. displacement, u, for the cracked body where crack growth is assumed to occur either at constant load (fixed load) or at constant displacement (fixed grip).

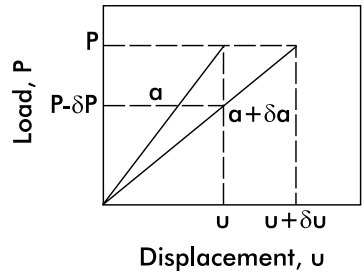

FIGURE 2.10
Load-displacement behavior for a cracked body at crack lengths a and a + δa.

For the *fixed-load* case,

$$\delta U = \frac{P\delta u}{2} \tag{2.53a}$$

$$\delta W = P\delta u \tag{2.53b}$$

Equation (2.47) gives

$$\delta H = P\delta u - P\delta u/2 = P\delta u/2 \tag{2.54}$$

and Equation (2.51) gives

$$G = \frac{P}{2}\frac{\partial u}{\partial A} \tag{2.55}$$

For the *fixed-grip* case, the work term in Equation (2.47) vanishes and

$$\delta U = \frac{u\delta P}{2} \tag{2.56}$$

Note that δP is negative because of the loss in stiffness followed by crack extension, and G is

$$G = -\frac{u}{2}\frac{\partial P}{\partial A} \tag{2.57}$$

For a linear elastic body, the relationship between load and displacement may be expressed as

$$u = CP \tag{2.58}$$

where C is the compliance of the specimen. Substitution into Equation (2.55) (fixed load) gives

$$G = \frac{P^2}{2}\frac{\partial C}{\partial A} \tag{2.59}$$

For the fixed-grip case, substitution of $P = u/C$ into Equation (2.57) gives

$$G = \frac{u^2}{2C^2}\frac{\partial C}{\partial A} = \frac{P^2}{2}\frac{\partial C}{\partial A} \tag{2.60}$$

Consequently, both fixed-load and fixed-grip conditions give the same expression. This expression is convenient for the experimental determination of G and will be employed in Chapter 14 for derivation of expressions for G for various delamination fracture specimens.

For a crack in a principal material plane, it is possible to decompose G into components associated with the three basic modes of crack extension illustrated in Figure 2.9:

$$G = G_I + G_{II} + G_{III} \tag{2.61}$$

Theoretically, the mode separation is based on Irwin's contention that if the crack extends by a small amount, Δa, the energy absorbed in the process is equal to the work required to close the crack to its original length [48]. For a polar coordinate system with the origin at the extended crack tip (Figure 2.9), the various contributions to the total energy release rate are

$$G_I = \lim_{\Delta a \to 0} \frac{1}{2\Delta a} \int_0^{\Delta a} \sigma_y(\Delta a - r)\overline{v}(r, \pi)dr \tag{2.62a}$$

$$G_{II} = \lim_{\Delta a \to 0} \frac{1}{2\Delta a} \int_0^{\Delta a} \tau_{xy}(\Delta a - r)\overline{u}(r, \pi)dr \tag{2.62b}$$

$$G_{III} = \lim_{\Delta a \to 0} \frac{1}{2\Delta a} \int_0^{\Delta a} \tau_{yz}(\Delta a - r)\overline{w}(r, \pi)dr \tag{2.62c}$$

where r is the radial distance from the crack tip, σ_y, τ_{xy} and τ_{yz} are the normal and shear stresses near the crack tip; and $\overline{v}, \overline{u}$, and $\overline{w}$ are the relative opening and sliding displacements between points on the crack faces, respectively. These expressions form the basis for the virtual crack closure (VCC) method for separation of the fracture modes using finite element solutions of crack problems [49].

2.8 Strength of Composite Laminates Containing Holes

Structures made from composite laminates containing cutouts or penetrations such as fastener holes (notches) offer a special challenge to the designer because of the stress concentration associated with the geometric discontinuity. In laminates containing notches, a complex fiber-bridging zone develops near the notch tip [50,51]. On the microscopic level, the damage appears in the

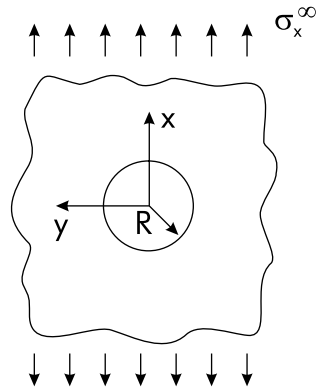

FIGURE 2.11
Infinite plate containing a circular hole under remote uniform tension.

form of fiber pullout, matrix microcracking, and fiber–matrix interfacial failure. The type of damage and its growth depends strongly on the laminate stacking sequence, type of resin, and the fiber. As a consequence of the damaged material, the assumptions of a small process zone and self-similar growth of a single crack, inherent in linear elastic fracture mechanics, break down. In experimental studies on notched laminates under tension or compression loads, the strength is substantially reduced compared to the strength of the unnotched specimen [51,52].

Because of the complexity of the fracture process for notched composite laminates, the methods developed for prediction of strength are semiempirical. Awerbuch and Madhukar [52] review strength models for laminates containing cracks or holes loaded in tension. In this text, only the technically important case of a laminate containing a circular hole will be considered.

A conservative estimate of the strength reduction is based on the stress concentration factor at the hole edge for a composite laminate containing a circular hole,

$$\frac{\sigma_N}{\sigma_0} = \frac{1}{K} \tag{2.63}$$

where σ_N and σ_0 are the notched and unnotched ultimate strengths of the laminate, and K is the stress concentration factor. The stress distribution can be obtained in closed form only for infinite, homogeneous, orthotropic plates containing an open hole [53]. The stress concentration factor, K_∞, for an infinite plate containing a circular hole (Figure 2.11) is given in terms of the effective orthotropic engineering constants of the plate [53],

$$K_\infty = 1 + \sqrt{2\left(\sqrt{E_x / E_y} - \nu_{xy} + E_x / (2G_{xy})\right)} \tag{2.64}$$

where x and y are coordinates along and transverse to the loading direction (Figure 2.11). The stress concentration factor for finite-width plates containing holes is larger than K_∞ [54,55]. Plates where the width and length exceed about six hole diameters, however, may be considered as infinite, and Equation (2.64) holds to a good approximation.

It can be easily verified from Equation (2.64) that the stress concentration factor for an isotropic material is 3. For highly anisotropic composites, the stress concentration factor is much greater (up to 9 for unidirectional carbon/epoxy).

References

1. I.M. Daniel and O. Ishai, *Engineering Mechanics of Composite Materials*, Oxford University Press, New York, 1994.
2. R.F. Gibson, *Principles of Composite Materials Mechanics*, McGraw-Hill, New York, 1994.
3. J.N. Reddy, *Mechanics of Laminated Composite Materials — Theory and Analysis*, CRC Press, Boca Raton, FL, 1997.
4. M.W. Hyer, *Stress Analysis of Fiber-Reinforced Composite Materials*, WCB/McGraw-Hill, Boston, 1998.
5. C.T. Herakovich, *Mechanics of Fibrous Composites*, John Wiley & Sons, New York, 1998.
6. R.M. Jones, *Mechanics of Composite Materials*, 2nd ed., Taylor & Francis, Philadelphia, 1999.
7. Z. Hashin, Analysis of composite materials — a survey, *J. Appl. Mech.*, 50, 481–505, 1983.
8. J.C. Halpin and N.J. Pagano, Consequences of environmentally induced dilatation in solids, *Recent Adv. Eng. Sci.*, 5, 33–46, 1970.
9. R.M. Christensen, *Mechanics of Composite Materials*, John Wiley & Sons, New York, 1979.
10. M.Y. Hyer and A.M. Waas, Micromechanics of linear elastic continuous fiber composite, in *Comprehensive Composite Materials*, A. Kelly and C. Zweben, eds., Vol. 1, Elsevier, Oxford, 2000, pp. 345–375.
11. J.-H. Byun and T. –W. Chou, Mechanics of textile composites, in *Comprehensive Composite Materials*, A. Kelly and C. Zweben, eds., Vol. 1, Elsevier, Oxford, 2000, pp. 719–761.
12. B.W. Rosen and Z. Hashin, Analysis of material properties, in *Engineered Materials Handbook*, Vol. 1, Composites, T.J. Reinhart, tech. chairman, ASM International, Metals Park, OH, 1987, pp. 185–205.
13. J.C. Halpin and J.L. Kardos, The Halpin-Tsai equations: a review, *Polym. Eng. Sci.*, 16, 344–352, 1976.
14. M.W. Hyer, Laminated plate and shell theory, in *Comprehensive Composite Materials*, A. Kelly and C. Zweben, eds., Vol. 1, Elsevier, Oxford, 2000, pp. 479–510.
15. J.R. Vinson and R.L. Sierakowsky, *The Behavior of Structures Composed of Composites Materials*, 2nd ed., Kluwer, Dordrecht, 2002.
16. M.N. Ozisik, *Heat Conduction*, John Wiley & Sons, New York, 1980.

17. W. Jost, *Diffusion*, 3rd ed., Academic Press, New York, 1960.
18. G.S. Springer, ed., *Environmental Effects on Composite Materials*, Technomic, Lancaster, PA, 1981.
19. R.B. Pipes, J.R. Vinson, and T.W. Chou, On the hygrothermal response of laminated composite systems, *J. Compos. Mater.*, 10, 129–148, 1976.
20. L.A. Carlsson, Out-of-plane hygroinstability of multi-ply paperboard, *Fibre Sci. Technol.*, 14, 201–212, 1981.
21. S.P. Timoshenko and J.N. Goodier, *Theory of Elasticity*, 3rd ed., McGraw-Hill, New York, 1970.
22. C.O. Horgan, Some remarks on Saint-Venant's principle for transversely isotropic composites, *J. Elasticity*, 2(4), 335–339, 1972.
23. I. Choi and C.O. Horgan, Saint-Venant's principle and end effects in anisotropic elasticity, *J. Appl. Mech.*, 44, 424–430, 1977.
24. C.O. Horgan, Saint-Venant end effects in composites, *J. Compos. Mater.*, 16, 411–422, 1982.
25. C.O. Horgan and L.A. Carlsson, Saint-Venant end effects for anisotropic materials, in *Comprehensive Composite Materials*, A. Kelly and C. Zweben, eds., Vol. 5, Elsevier, Oxford, 2000, pp. 5–21.
26. R.G.C. Arridge, P.I. Barham, C.J. Farell, and A. Keller, The importance of end effects in the measurement of moduli of highly anisotropic materials, *J. Mater. Sci.*, 11, 788–790, 1976.
27. S.W. Tsai, Strength theories of filamentary structures, in *Fundamental Aspects of Fiber Reinforced Plastic Composites*, R.T. Schwartz and H.S. Schwartz, eds., John Wiley & Sons, New York, 1968, pp. 3–11.
28. C.T. Sun, Strength analysis of unidirectional composites and laminates, in *Comprehensive Composite Materials*, A. Kelly and C. Zweben, eds., Vol. 1, Elsevier, Oxford, 2000, pp. 641–666.
29. S.W. Tsai and E.M. Wu, A general theory of strength for anisotropic materials, *J. Compos. Mater.*, 5, 58–80, 1971.
30. S.W. Tsai and H.T. Hahn, *Introduction to Composite Materials*, Technomic, Lancaster, PA, 1980.
31. R.B. Pipes, B.E. Kaminski, and N.J. Pagano, Influence of the free-edge upon the strength of angle-ply laminates, *ASTM Spec. Tech. Publ.*, 521, 218–228, 1973.
32. H.T. Hahn and N.J. Pagano, Curing stresses in composite laminates, *J. Compos. Mater.*, 9, 91–106, 1975.
33. Y. Weitsman, Residual thermal stresses due to cool-down of epoxy-resin composites, *J. Appl. Mech.*, 46, 563–567, 1979.
34. G. Jeronimidis and A.T. Parkyn, Residual stresses in carbon fibre-thermoplastic matrix laminates, *J. Compos. Mater.*, 22, 401–415, 1988.
35. L. Carlsson, C. Eidefeldt, and T. Mohlin, Influence of sublaminate cracks on the tension fatigue behavior of a graphite/epoxy laminate, *ASTM Spec. Tech. Publ.*, 907, 361–382, 1986.
36. N. Alif and L.A. Carlsson, Failure mechanisms of woven carbon and glass composites, *ASTM Spec. Tech. Publ.*, 1285, 471–493, 1997.
37. A.S.D. Wang and F.W. Crossman, Initiation and growth of transverse cracks and edge delamination in composite laminates. Part 1. An energy method, *J. Compos. Mater. Suppl.* 14, 71–87, 1980.
38. F.W. Crossman, W.J. Warren, A.S.D. Wang, and G.E. Law, Jr., Initiation and growth of transverse cracks and edge delamination in composite laminates. Part 2. Experimental correlation, *J. Compos. Mater. Suppl.* 14, 88–108, 1980.

39. F.W. Crossman and A.S.D. Wang, The dependence of transverse cracking and delamination on ply thickness in graphite/epoxy laminates, *ASTM Spec. Tech. Publ.*, 775, 118–139, 1982.
40. D.L. Flaggs and M.H. Kural, Experimental determination of the in-situ transverse lamina strength in graphite/epoxy laminates, *J. Compos. Mater.*, 16, 103–115, 1982.
41. S.R. Swanson and B.C. Trask, Strength of quasi-isotropic laminates under off axis loading, *Compos. Sci. Technol.*, 34, 19–34, 1989.
42. S.R. Swanson and Y. Qian, Multiaxial characterization of T300/3900-2 carbon/epoxy composites, *Compos. Sci. Technol.*, 43, 197–203, 1992.
43. D.J. Wilkins, J.R. Eisenmann, R.A. Camin, W.S. Margolis, and R.A. Benson, Characterizing delamination growth in graphite-epoxy, *ASTM Spec. Tech. Publ.*, 775, 168–183, 1982.
44. E.M. Wu, Application of fracture mechanics to anisotropic plates, *J. Appl. Mech.*, 34, 967–974, 1967.
45. H.M. Westergaard, Bearing pressure and cracks, *J. Appl. Mech.*, 6, A49–A53, 1939.
46. G.C. Sih, P.C. Paris, and G.R. Irwin, On cracks in rectilinearly anisotropic bodies, *Int. J. Fract. Mech.*, 1(3), 189–203, 1965.
47. A.A. Griffith, The phenomena of rupture and flow in solids, *Phil. Trans. R. Soc.*, A221, 163–198, 1920.
48. G.R. Irwin, Fracture, in *Handbuch der Physik*, Vol. 6, S. Flügge, ed., Springer, Berlin, 1958, pp. 551–590.
49. E.F. Rybicki and M.F. Kanninen, A finite element calculation of stress intensity factors by a modified crack closure integral, *Eng. Fract. Mech.*, 9, 931–938, 1977.
50. J.F. Mandell, S.S. Wang, and F.J. McGarry, The extension of crack tip damage zones in fiber reinforced plastic laminates, *J. Compos. Mater.*, 9, 266–287, 1975.
51. C.G. Aronsson, Tensile Fracture of Composite Laminates with Holes and Cracks, Ph.D. dissertation, The Royal Institute of Technology, Stockholm, Sweden, 1984.
52. J. Awerbuch and M.S. Madhukar, Notched strength of composite laminates, *J. Reinf. Plast. Compos.*, 4, 3–159, 1985.
53. S.G. Lekhnitskii, *Anisotropic Plates*, Gordon and Breach, New York, 1968.
54. H.J. Konish and J.M. Whitney, Approximate stresses in an orthotropic plate containing a circular hole, *J. Compos. Mater.*, 9, 157–166, 1975.
55. J.W. Gillespie, Jr., and L.A. Carlsson, Influence of finite width on notched laminate strength predictions, *Compos. Sci. Technol.*, 32, 15–30, 1988.

3

Processing of Composite Laminates

The processing of polymer matrix composite laminates has been the subject of considerable research during the last two decades [1–11]. Multiple physical and chemical phenomena must occur simultaneously and in the proper sequence to achieve desired laminate properties. There are several routes to achieve full consolidation and minimize void content of a polymeric matrix with a reinforcing fiber in volume fractions (50 to 60%) appropriate for structural applications. The most widely accepted approach is by impregnation of unidirectional fibers or textile fabrics to create a thin sheet or tape. If the polymer is a thermoset, it is often advanced in its curing state to the B stage (a state of cure of the matrix that is incomplete, but provides high room temperature viscosity of the prepreg). Known as *prepreg* in this form, it may be stored at low temperature (below freezing) to greatly reduce the rate of cure and thus increase the storage life. After being warmed to room temperature, these prepreg sheets or tapes may then be assembled into a laminate and subjected to a cure cycle.

It is also possible to assemble dry fibers into an appropriate geometric form, and then impregnate the entire laminate in a single step. This approach is known as resin transfer molding (RTM), and there are several variations. The weaving of a fabric from reinforcing fibers is a widely accepted approach to creating the fiber preform, although there are other techniques designed to avoid fiber crimp and develop microstructures typical of that achieved with prepreg tape.

For prepreg, heat and pressure are first applied to the laminate to reduce the viscosity of the polymer matrix, and achieve full densification of the laminate and coalescence of the laminae through matrix flow. The application of heat to the laminate is governed by the laws of heat transfer and is therefore a time-dependent phenomenon. Further, the pressure in the laminate is shared by the polymeric matrix and the fibers. For thermosetting polymers, the kinetic process to achieve gelation and vitrification is a themochemical process that is often exothermic. The decrease in polymer viscosity with temperature and its increase with degree of cure for theromsets requires that the necessary flow be achieved prior to gelation or vitrification. For thermoplastic polymers the process involves both viscosity changes and changes in the polymer morphology (degree of crystallinity). Thermoplastic

crystalline polymers will exhibit varying degrees of crystallinity depending upon their thermal history [5].

The instantaneous degree of cure of a thermoset polymer is measured by the fraction of total heat generated at a given time divided by the total heat of reaction. The degree of cure ranges from 0 to 1 and can be measured using differential scanning calorimetry (DSC), which determines the heat of reaction as a function of time. As the reaction progresses and the macromolecular network forms, the rate-controlling phenomenon changes from kinetic to diffusion because of the reduction in polymer free volume. An accompanying reduction in molecular mobility occurs because of molecular weight increase.

Uneven distribution of resin may result from nonuniform flow of the polymer through the fiber reinforcement. This is particularly pronounced for laminates with curvilinear geometry and tapered thickness in which local pressure gradients occur. The velocity of flow of a polymer through a porous medium such as fiber mats has been shown to be proportional to the pressure gradient and inversely proportional to the polymer viscosity [12]. The proportionality constant is known as the permeability [12].

3.1 Processing of Thermoset Composites

The development of an interlocking network during the cure of a thermoset polymer is illustrated in Figure 3.1. As temperature and time increase, the network interconnectivity grows according to the steps illustrated: (a) the prepolymer and curing agents are interspersed, (b) polymer molecular weight (size) increases, (c) gelation occurs and a continuous network is achieved, and (d) cure is complete (see the time–temperature transformation diagram, Figure 3.2). After the polymer approaches vitrification, i.e., the polymer changes from a rubbery to a glassy state, the rate of conversion decreases significantly. Should vitrification occur before completion of the cure reaction, polymer properties will not be fully achieved and voids may form in the laminate. These phenomena must be considered in the development of an appropriate cure cycle.

Figure 3.3 illustrates the flow and compaction phenomena during the curing and consolidation steps. Initially, the increase in temperature serves to decrease the viscosity of the polymer and the polymer carries the applied pressure. As the laminate is vented and flow begins, the fibers deform and act as an elastic spring in assuming a portion of the applied pressure (Figure 3.3). Volatiles produced in the chemical reaction or trapped gases will then escape from the laminate. Finally, the total pressure is carried by the fully consolidated composite panel.

Given that composite laminates are often processed in an autoclave, wherein heat transfer is achieved with a pressurizing medium (normally

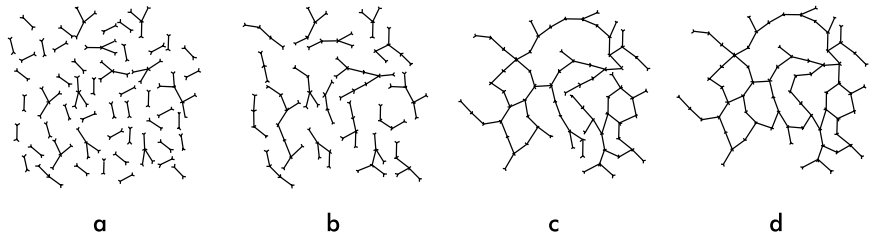

FIGURE 3.1
Dynamics of thermoset gelation and vitrification. (From L.A. Berglund and J.M. Kenny, *SAMPE J.*, 27(2), 1991. With permission.)

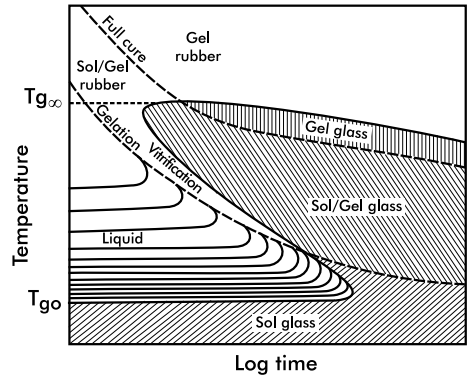

FIGURE 3.2
Time–temperature transformation diagram. (From L.A. Berglund and J.M. Kenny, *SAMPE J.*, 27(2), 1991. With permission.)

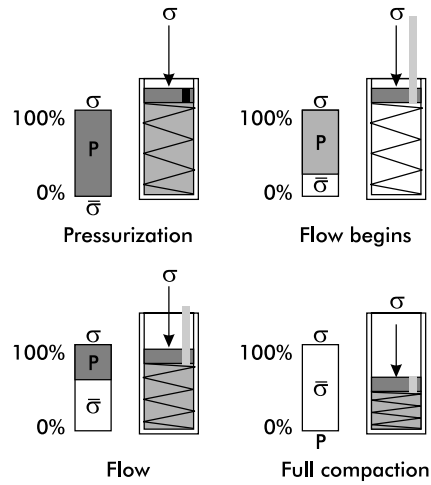

FIGURE 3.3
Polymer and perform pressurization and flow. (From P. Hubert, Ph.D. Thesis, University of British Columbia, 1996. With permission.)

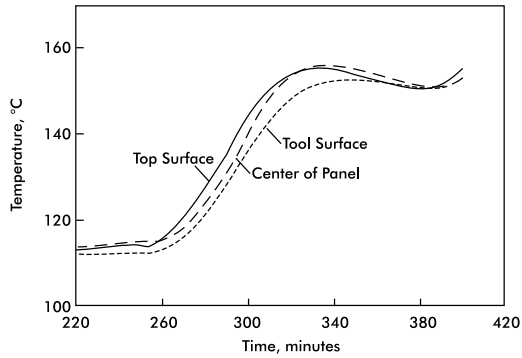

FIGURE 3.4
Heat transfer through laminate thickness. (From P. Hubert, University of British Columbia Composites Group Report, 1994. With permission.)

nitrogen, an inert gas), it is important to recognize that the instantaneous temperature within the laminate may not be equal to that of the autoclave. Figure 3.4 illustrates a typical thermal cycle and shows that the temperature of the laminate can differ from top surface to interior (center) to tool surface. Thus, the dynamics of heat transfer must be considered when an appropriate cure cycle is developed.

Consider the typical cure cycle shown in Figure 3.5, where internal composite temperature lags autoclave temperature. Initially, the autoclave temperature is increased at a constant rate of 2 to 3°C/min until it reaches 110°C, and then it is held constant for approximately 1 h. During this stage the polymer is in the liquid state. Next the autoclave temperature is increased to and held at approximately 180°C for 2 h. During this stage the polymer passes through gelation at a degree of cure of 0.46 and then approaches vitrification. Vitrification occurs when the instantaneous glass transition temperature (defined as the temperature at which the polymer passes from the rubbery or gel state to the glassy state) of the polymer reaches the temperature of the laminate. In Figure 3.5, the vitrification point occurs prematurely at

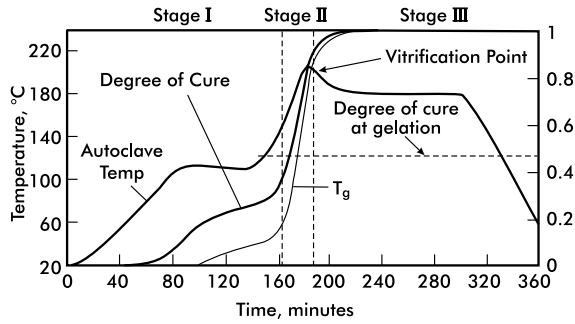

FIGURE 3.5
Cure cycle with premature vitrification. (From P. Hubert, University of British Columbia Composites Group Report, 1994. With permission.)

approximately 190 min into the cycle. Because the rubbery-to-glass transition occurs at vitrification, stresses developed as a result of the shrinkage of the polymer with cure progression may not relax during the remainder of the curing cycle. For the case in which vitrification is delayed until a point much later in the process close to cooling, much of this stress will be eliminated by completion of the cycle. Hence, the cure cycle can be tailored to the specific polymer to minimize residual stresses. Of course, thermal residual stresses develop in the laminate upon cooling because of anisotropic thermal expansion, as discussed in Chapters 10 and 12.

3.1.1 Autoclave Molding

Figure 3.6 shows the vacuum bag lay-up sequence for a typical epoxy matrix prepreg composite. Different lay-up sequences can be used for other types of prepregs.

1. Thoroughly clean the aluminum plate (10) using acetone or a detergent. Then apply mold-release agent to the top surface of the aluminum plate twice.
2. Lay one sheet of Teflon film (1) and the peel-ply (2) (nonstick nylon cloth) on the aluminum plate. The Teflon film is used to release the lay-up from the aluminum plate, and the peel-ply is used to achieve the required surface finish on the laminate. Note: There should be no wrinkles or raised regions in the peel-ply, and its dimensions should be identical to those of the laminate.
3. Place the prepreg stack (3) on the plate, being sure to keep it at least 50 mm from each edge. Note: Do not cover up the vacuum connection in the plate.

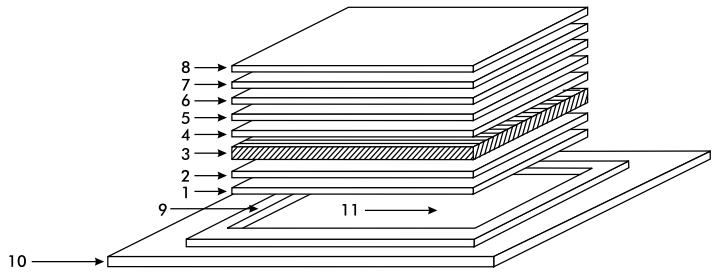

1. Teflon Film
2. Peel Ply
3. Laminate (prepreg stack)
4. Peel Ply
5. Teflon Coated Glass Fabric
6. Glass Bleeders (1 per 3.5 plies)
7. Teflon Film (holes every 50 mm)
8. Vent Cloth
9. Cork or Rubber Dam
10. Aluminum Plate
11. Release Agent

FIGURE 3.6
Vacuum bag preparation for autoclave cure of thermoset matrix composite.

4. Place a strip of the cork–rubber material (9) along each edge of the panel, making sure that no gaps exist and a complete dam is formed around the laminate. The dam around the lay-up prevents lateral motion of the panel, and minimizes resin flow parallel to the aluminum plate and through the edges of the laminate (9).
5. Completely encircle the prepreg stack and dam with bagging adhesive making sure that the adhesive material is adjacent to the dam. The purpose of the adhesive material is to form a vacuum seal.
6. Place a peel-ply (4) and a ply of Teflon-coated glass fabric (5) (with the same dimensions as the panel) on top of the prepreg stack. The purpose of the Teflon-coated glass fabric is to prevent the bleeder sheets (6) from sticking to the laminate.
7. Place the proper number of glass bleeder sheets (6) (e.g., style 181 glass cloth with the same dimensions as the prepreg stack) over the Teflon-coated fabric (5). The bleeder sheets absorb the excess resin from the laminate.
8. Place a sheet of perforated Teflon film (7) (0.025 mm) over the bleeder material. The Teflon film, perforated on 50 mm centers, prevents excess resin from saturating the vent cloth (8).
9. Place a porous continuous-vent cloth (8) (e.g., style 181 glass cloth) on top of the lay-up. Extend the cloth over the vacuum line attachment. Make sure that the vacuum line is completely covered by the vent cloth. The vent cloth provides a path for volatiles to escape when the vacuum is applied and achieves a uniform distribution of vacuum.
10. Place nylon bagging film over the entire plate, and seal it against the bagging adhesive. Allow enough material so that the film conforms to all contours without being punctured.
11. Place the plate in the autoclave and attach the vacuum line (Figure 3.7). An autoclave is generally a large pressure vessel equipped with a temperature- and pressure-control system. The elevated pressures and temperatures, required for processing of the laminate, are commonly achieved by electrically heating a pressurized inert gas (nitrogen). The use of an inert gas will reduce oxidizing reactions that otherwise may occur in the resin at elevated temperatures, and will prevent explosion of evolving volatiles.
12. Turn on the vacuum pump and check for leaks. Maintain a vacuum of 650 to 750 mm of mercury for 20 min and check again for leaks.
13. After closing the autoclave door, apply the pressure and initiate the appropriate cure cycle (see example shown in Figure 3.8). As the temperature is increased, the resin viscosity decreases rapidly and the chemical reaction of the resin begins. At the end of the temperature hold, at 127°C in Figure 3.8, the resin viscosity is at a minimum and pressure is applied to squeeze out excess resin. The

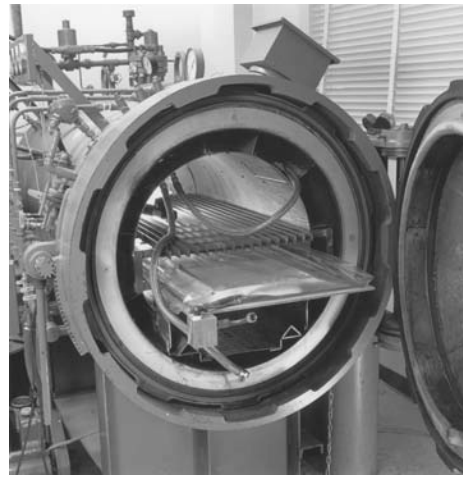

FIGURE 3.7
Vacuum bag sequence and tool plate placed in an autoclave.

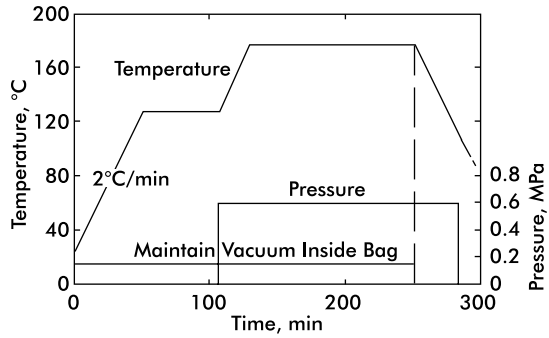

FIGURE 3.8
Typical cure cycle for a carbon/epoxy prepreg.

temperature hold controls the rate of the chemical reaction and prevents degradation of the material by the exotherm. The pressure is held constant throughout the cure cycle to consolidate the plies until the resin in the laminate is in its glassy state at the end of the cooling phase. The vacuum should be checked throughout the cure cycle. The vacuum is applied to achieve a uniform pressure on the laminate and draw out volatiles created during the cure. Loss of vacuum will result in a poorly consolidated laminate.

14. After the power is turned off to the autoclave, maintain pressure until the inside temperature has dropped to about 100°C.
15. Carefully remove the laminate from the aluminum plate. Gently lift it in a direction parallel to the main principal direction of the laminate.
16. Clean the aluminum plate, and store it for future use.

3.1.2 Resin Transfer Molding of Thermoset Composites

Resin transfer molding (RTM) of composite laminates is a process wherein the dry-fiber preform is infiltrated with a liquid polymeric resin and the polymer is advanced to its final cure after the impregnation process is complete. An extensive review of the resin transfer molding process can be found in Reference [12]. The process consists of four steps: fiber preform manufacture, mold filling, cure, and part removal. In the first step, textile technology is typically utilized to assemble the preform. For example, woven textile fabrics are often assembled into multilayer laminates that conform to the geometry of the tool. Braiding and stitching provide mechanisms for the creation of three-dimensional preform architectures.

Typically, a thermosetting polymer of relatively low viscosity is used in the RTM process. There have been applications for thermoplastic polymers, but they are rare. Pressure is applied to the fluid polymer to inject it into a mold containing the fiber preform, and the mold may have been preheated. The flow of the fluid through the fiber preform is governed by Darcy's Law [12], wherein the velocity of the flow is equal to the product of the pressure gradient, the preform permeability, and the inverse of the polymer viscosity. Clearly, the lower the polymer viscosity, the greater the flow rate, and the greater the permeability, the greater the flow rate. Note also that because the fiber preforms typically exhibit different geometries in the three principal directions, permeability is a tensor and exhibits anisotropic characteristics. That is, for a given pressure gradient, the flow rates in three mutually orthogonal directions will differ. Flow through the thickness of a fiber preform that contains many layers of unidirectional fibers will be quite different than flow in the planar directions. In addition, the permeability of the preform depends on the fiber volume fraction of the preform. The greater the volume fraction, the lower the permeability. It is important to vent the mold to the atmosphere to remove displaced gases from the fiber preform during the mold filling process. Otherwise trapped gases will lead to voids within the laminate.

After the polymer has fully impregnated the fiber preform, the third step occurs: cure. This step will begin immediately upon injection of the polymer into the mold and will occur more rapidly if the mold is at an elevated temperature. As the cure of the polymer advances to the creation of a cross-link network, it passes through a gelation phase wherein the polymer viscosity increases and transforms the polymer into a viscoelastic substance, where it possesses both viscous and elastic properties. As this process proceeds and the cross-link network continues to grow, the instantaneous glass transition temperature of the polymer increases. Finally, vitrification of the polymer occurs when its glass transition temperature exceeds the laminate temperature. Should gelation or vitrification (or both) occur prior to completion of mold filling and preform impregnation, the resulting laminate will not be fully impregnated.

The viscosity of most polymers is highly dependent on temperature and polymer cure kinetics are controlled by temperature as well. Therefore, heat

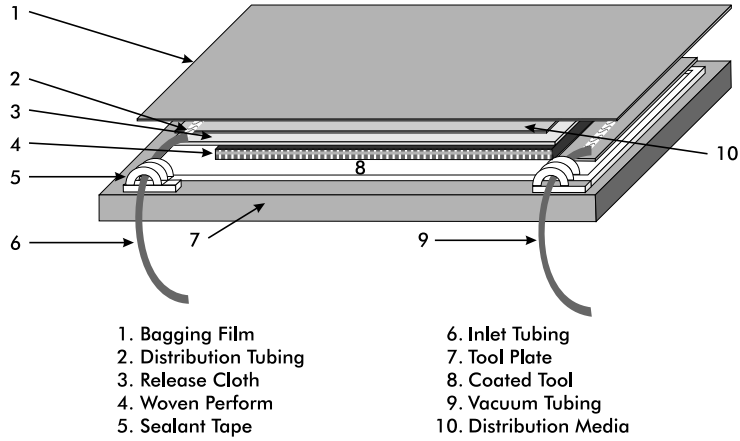

FIGURE 3.9
VARTM process. (Courtesy of B. Grimsley, NASA Langley Research Center, 2001.)

transfer phenomena must be managed for successful RTM processes. Heat transfer between the polymer and the fiber preform, and between tool, preform, and polymer, as well as exothermic heat generation during the cure of the polymer, are three such phenomena that influence the process [12].

3.1.2.1 Vacuum-Assisted Resin Transfer Molding (VARTM) Processing

Both open-mold approaches, where one surface is bagged with a flexible film, and closed-mold approaches to resin transfer molding are practiced. An example of open-mold RTM, vacuum-assisted resin transfer molding (VARTM) is a common method employed as an alternative to autoclave use. In VARTM, atmospheric pressure is utilized to achieve consolidation and impregnation by vacuum bagging the laminate in the same way as discussed in Section 3.1.1. An inlet for the polymer is located at one or more points in the tool or bag, and vacuum outlets are located some distance away. The vacuum pump creates a pressure gradient of approximately 1 atm within the bag, which is sufficient for the impregnation of laminates large in size and complex in geometry. For processes in which final cure occurs after the mold is filled, completion of the cure can be carried out in an oven while atmospheric pressure is maintained on the impregnated laminate.

The VARTM procedure for a representative flat $61.0 \times 30.5 \times 0.64$ cm panel (Figure 3.9) is described in the following steps:

1. *Tool surface.* The tool is a flat aluminum plate with planar dimensions sufficient to accommodate the proposed composite panel. First, clean the metal tool surface using sandpaper and acetone. On the cleaned surface, create a 71×30.5 cm picture frame using masking tape. Apply several coats of release agent to the metal surface inside of the masked frame. Remove the masking tape.

2. B*agging tape.* In place of the masking tape, apply a 1.3-cm-wide silicone bagging tape to the bare metal surface. The silicone tape should again form a 71 × 30.5 cm frame. Add a strip of the tape, 5 cm in length, to the outer edge of the length of the frame at either end. These two strips will provide an added adhesive surface for attachment of the inlet and outlet tubing. Leave the paper backing on the silicone tape to protect it during the remainder of the lay-up procedure.
3. *Preform.* Place the fiber preform stack on the coated tool, inside the tape frame. A 5.1-cm gap should exist between the silicone tape and both edges of the preform to allow room for tubing. No gap should exist between the silicon tape and fiber preform along the panel width to avoid providing a flow pathway outside the preform to the vacuum port.
4. *Release cloth.* Cut one layer of porous release film to 66 × 30.5 cm, and place it on top of the preform. Place the cloth so that it completely covers the preform and allow 5.1 cm in length to overhang and contact the coated metal surface at the injection side of the lay-up. The release film will allow the composite laminate to release from the distribution media. Cut a second piece of release cloth to 5.1 × 30.5 cm, and place it on the tool surface at the vacuum side of the preform. This patch of cloth provides a clear path for the vacuum.
5. *Distribution media.* Cut one to six layers of highly permeable distribution media, e.g., biplanar nylon 6 mesh to dimensions of 63.5 × 28.0 cm and stack them above the Armalon™ release cloth. Place the layers of media so that a 2.5-cm gap exists on the top of the preform at the vacuum end. This gap will force the resin to fill through the thickness rather than be drawn directly into the vacuum port. The length of this gap will vary with the desired thickness of the composite panel. A 1.3-cm gap should exist between the media and the sides of the preform. This will help prevent resin flow outside the preform. A 5-cm length of the media will overhang the preform at the resin inlet end of the lay-up.
6. *Distribution tubing.* Place a 28.0-cm length of distribution tubing across the width of the laminate at points 2.5 cm in front of the preform (inlet) and 2.5 cm away from the preform (vacuum). On the inlet side, place the tubing on top of the distribution media that overhangs the preform. At the vacuum side, place the tubing on the 5 × 30.5 cm piece of release cloth. Spiral-wrap, 18-mm-diameter conduit is an ideal choice for the distribution tubing because it allows the resin to flow quickly into the distribution media and preform in a continuous line across the width. A plastic tube with holes at 2.5-cm intervals also works well. Attach a 13-mm portion of the spiral tubing to both the inlet–supply tubing and the vacuum

tubing using Kapton™ tape (E.I. duPont de Nemours and Co.). Embed the free end of the spiral tubing in a 2.5-cm-diameter roll of the silicone bagging tape, and then afix it to the strip of bagging tape forming the frame of the laminate.

7. *Resin supply and vacuum tubing.* Use flexible plastic tubing (vinyl or Teflon, depending on temperature requirements) approximately 1.5 m in length to supply resin and draw vacuum on the laminate. Tape one end of the tube to the distribution tubing inside of the bag. At a point just past this taped interface, wind one layer of silicone vacuum tape twice about the outer surface of the tubing. This 2.5-cm-long sleeve of vacuum tape on the tube should match the tape frame and added strips that exist on the tool surface. Attach the taped tubes to the tool at these locations and place two more 7-cm-long strips of tape on top of the tool and tape sealant to form a smooth, airtight joint when the bagging film is in place. Clamp the free end of the resin supply tubing to ensure a temporary airtight seal. Connect the free end of the vacuum tubing to a resin trap, which catches any resin that might be pulled into the tube on its way to the vacuum pump.
8. *Vacuum bag.* With the laminate complete and the tubing in place, the part can be bagged using an appropriate film. Take care to eliminate creases in the bag and ensure an airtight seal with the tool surface and silicone bagging tape. Once bagging is complete, the laminate should be fully evacuated to 762 mmHg using the vacuum pump. Leaks can be detected by using either a listening device or by clamping the vacuum line and using a vacuum gauge. Even a small leak in the system may result in voids and poor consolidation of the final composite part.
9. *Resin degassing.* Before infiltration can occur, the resin must be degassed to remove any air bubbles that were introduced during mixing. Perform degassing separately in a vacuum chamber; degassing can typically require 1 to 4 h, depending on the resin viscosity. All air bubbles must be removed prior to infiltration. Contain the resin in a bucket.
10. *Resin infiltration.* With the bagged laminate under full vacuum, submerge the clamped end of the resin supply tubing in the degassed resin bucket. Remove the clamp while the tube end is submerged to prevent any air entering the tube and the part ahead of the resin. With the tube clamp removed, the resin flows through the supply tubing and into the distribution tubing. The spiral distribution tubing allows the resin to spread quickly across the width of the lay-up as it enters the distribution media. The distribution media provides the path for the resin to flow quickly down the length of the preform and then through the laminate thickness.

11. *Completion of infiltration.* The flow-front of resin through the part can be viewed through the bagging film. Halt the flow of resin when the preform is fully infiltrated, as evidenced by resin beginning to enter the vacuum distribution tubing. Stop the resin flow by first clamping and severing the resin supply tubing and then clamping and severing the vacuum tubing. Again, these clamps must provide an airtight seal, because any leaks during cure will result in poor consolidation of the part. It is recommended that a second envelope bag be used to pull vacuum on the part during cure. Finally, place the vacuum-sealed part in an oven, and heat it according to a cure cycle prescribed by the resin supplier.

3.2 Autoclave Processing of Thermoplastic Composites

Thermoplastic composites may be processed in a high-temperature autoclave. Figure 3.10 shows the autoclave lay-up sequence for a carbon/polyetheretherketone (PEEK) composite. Place Kapton film of slightly larger size than the panel, each side being coated with a release agent, on the tool plate. Place Kapton bagging film over the lay-up and seal the bag against the tool plate using A800 G3 (or equivalent) tacky tape. Place the tool plate and laminate in the autoclave and attach the vacuum line. The following processing cycle is recommended for a carbon/PEEK composite.

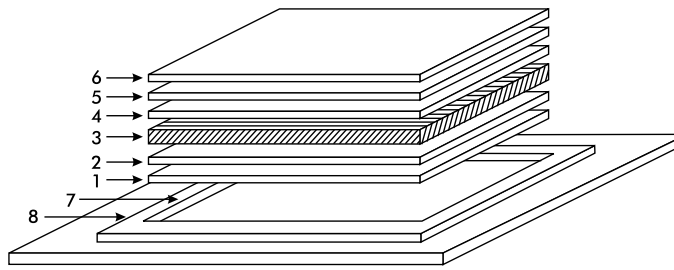

1. Kapton film coated with release agent on both sides
2. High temperature capability peel ply
3. Thermoplastic composite prelam stack
4. High temperature capability peel ply
5. Airweave breather plies (4) (high temperature capability)
6. High temperature bagging film (Kapton-no release)
7. Tacky sealant tape (A800 G3 or equivalent)
8. Tool plate

FIGURE 3.10
Vacuum bag preparation for autoclave processing of thermoplastic matrix composite.

1. Maintain a vacuum of 650 to 750 mmHg.
2. Apply a contact pressure of 0.5 MPa.
3. Simultaneously ramp the temperature as rapidly as possible to 390°C.
4. Apply a consolidation pressure of 1.4 MPa.
5. Hold the pressure at a temperature of 390°C for 5 min per 8 plies, but not for more than 30 min.
6. Cool the laminate rapidly to room temperature. The degree of crystallinity for crystalline polymers is influenced by cooling rate. Pressure can be released as the laminate temperature falls below the glass transition temperature of the matrix (≈140°C).

3.3 Determination of Volume Fractions of Fibers, Resin, and Voids

As discussed in Chapter 2, the stiffness and strength properties of composites are strongly dependent on the fiber volume fraction, and this parameter thus constitutes an important quality measure of such materials. This section details measurement of fiber volume fraction for polymer matrix composites reinforced with glass, carbon, or aramid fibers.

The fiber volume fraction of a composite may be determined by chemical matrix digestion, the burn-off technique, or by photomicrographic techniques. The matrix digestion method is standardized (ASTM D 3171 [13]) and consists of dissolving the (polymer) matrix in a hot digestion medium — concentrated nitric acid for epoxy matrix composites or sulfuric acid followed by hydrogen peroxide for polyimides and PEEK or other digestion media (see ASTM D 3171 [13]). Care must be taken to select a medium that attacks the matrix, but does not attack the fibers. After the matrix is dissolved, the fibers are weighed. The volume fractions are calculated from the weights and densities of the constituents. The resin burn-off method (ASTM D 2584 [14]) is sometimes used for glass fiber composites because glass fibers (as opposed to carbon and Kevlar [E.I. du Pont de Nemours and Company] fibers) are resistant to oxidation at the temperatures required to burn off the matrix (500 to 600°C). Similar to the chemical matrix digestion method, the fibers are weighed after the matrix has been removed to enable calculations of fiber volume fractions.

The photomicrographic method is not an ASTM standard, but it provides an independent estimate of the fiber volume fraction. The method requires a photograph of a polished cross section of a composite and many samples to produce reliable results, because the area viewed is only about a hundredth of a square millimeter. On the other hand, it is possible to obtain an image of the distribution of fibers and to detect voids.

FIGURE 3.11
Acid digestion procedure.

3.3.1 Chemical Matrix Digestion Method

Equipment needed for this procedure (Figure 3.11) includes:

1. Fume hood with a vacuum system
2. Large flask which can be attached to the vacuum system
3. Buchner funnel with filter
4. A 400-ml beaker
5. Nitric acid
6. Glass stirring rod
7. Bunsen burner or electric heater
8. Desiccator
9. Precision balance
10. Rubber gloves and goggles

3.3.1.1 Procedure

1. Take a 50×50 mm composite sample and weigh it. Also weigh the dry Buchner funnel with the filter.
2. Put on rubber gloves and goggles and activate a hood vent fan. Place the sample in the 400-ml beaker and pour in 200 ml of the nitric acid (use the glass stirring rod for controlled, slow pouring of the acid). Heat the beaker with the Bunsen burner until the acid fumes, but avoid boiling; stir occasionally. Continue heating until the matrix is dissolved and the sample disintegrates, leaving bare fibers.

3. Insert the funnel into the large flask attached to the vacuum system, and transfer the acid and the fibers into the funnel. Turn on the vacuum pump and wash the fibers three times with 20 ml of nitric acid, and then follow with a water wash.
4. Remove the funnel and the fibers and dry them in an oven at 100°C for at least 90 min. Break up the fiber flocks occasionally with a glass rod to facilitate drying. Remove the funnel and the fibers and let them cool in a desiccator. Weigh the funnel containing the fibers.

3.3.1.2 Calculation of Fiber Volume Fraction

From the weights of the fibers and matrix (W_f and W_m), and their known densities (ρ_f and ρ_m), the volume fraction of fibers, V_f, is determined from

$$V_f = \frac{\rho_m W_f}{\rho_f W_m + \rho_m W_f} \tag{3.1}$$

where it is assumed that the void content of the composite is negligible.

As an example, consider the following data for a carbon/epoxy composite:

W_f = 3.0671 g; W_m = 1.2071 g (weight of composite minus W_f).

Table 3.1 gives densities for some current fibers and matrix resins. Using the following densities in Table 3.1: ρ_f = 1.65 g/cm^3 and ρ_m = 1.265 g/cm^3, Equation (3.1) gives V_f = 0.66.

TABLE 3.1

Fiber and Resin Properties

Fiber Type	Carbon AS4	Carbon IM6	E-Glass	Kevlar 49
Density	1.80	1.73	2.60	1.44
Matrix Type	**Epoxy N5208**	**Epoxy 3501-6**	**K-Polymer**	**PEEK**
Density	1.20	1.265	1.37	1.30[a]

[a] 30% crystallinity.

3.3.1.3 Determination of Void Content

Voids may form in the composite as a result of gases and volatiles evolved during processing becoming trapped in the matrix. Voids are generally undesired. For autoclave-produced composite parts, a void content of less than 1% is commonly desired. The procedure for measurement of void content is given in ASTM D 2734 [15]. Void content requires an accurate measurement of the density of the composite

$$\rho_c = \frac{W}{V} \tag{3.2}$$

where W and V are the weight and volume of the composite, respectively. Methods for density measurements are presented in ASTM D 1505 [16] and D 3800 [17]. To obtain the void content, consider the following condition for the various volume fractions:

$$V_f + V_m + V_v = 1 \tag{3.3}$$

where subscripts f, m, and v represent fiber, matrix, and voids, respectively. From Equation (3.3) an expression for the void content can be obtained

$$V_v = 1 - \frac{\left(W_f/\rho_f + W_m/\rho_m\right)\rho_c}{W} \tag{3.4}$$

in which W_f, W_m, and W represent the weights of fiber, matrix, and composite, respectively ($W_f + W_m = W$). This method enables verification that an acceptable void content (e.g., <1%) has been achieved.

3.3.2 Photomicrographic Method

Equipment needed for this procedure includes:

1. Polishing table
2. Specimen mounted (embedded) in a specimen holder [18]
3. Metallographic optical microscope (400×) with a camera

3.3.2.1 Procedure

1. Cut the specimen perpendicular to the fiber direction to expose the desired cross section.
2. Place the specimen inside a mounting cup and pour a potting material (epoxy) into the cup [18]. After the mounting material is cured, the specimen is ready for grinding and subsequent polishing.
3. Grind the specimen by working through four sandpaper grades (180, 240, 320, and 400). Then proceed to polish the specimen on a polishing table (Figure 3.12) using the 5-, 1-, and, if necessary, use 0.3-μm particles. Polishing is the final step to obtain a flat surface with a mirror-like finish. Choose any direction to start the polishing and maintain that direction for that step. When changing to finer paper grades, alter the polishing angle by 90° each time to remove scratches from the previous step. Rinse the specimen after each step to remove grit.

FIGURE 3.12
Polishing of the specimen embedded in mounting material.

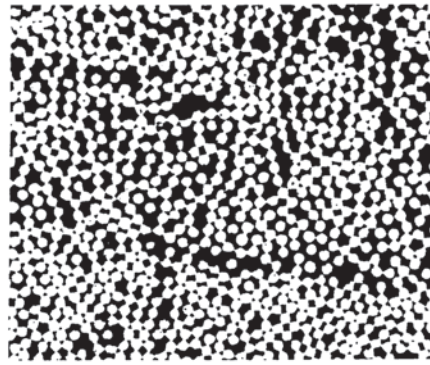

FIGURE 3.13
Photomicrograph of a polished cross section. (Courtesy of S. Nilsson, FOI, Stockholm, Sweden.)

4. When the specimen is polished, it is ready to be examined in the optical microscope. Take a photograph of a polished cross section like the one shown in Figure 3.13.

3.3.2.2 Determination of Fiber Volume Fraction

The fiber volume fraction can be determined from the photomicrograph in two ways, as illustrated in Figure 3.14. One way is to determine the total area of the fibers in a given area of the micrograph. This can be done directly with a quantitative image analyzer or by counting the number of fibers in the area and calculating the total fiber area from their average diameter. The fiber volume fraction is determined as

$$V_f = A_f/A \tag{3.5}$$

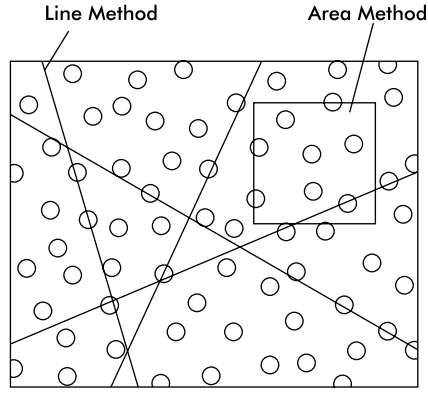

FIGURE 3.14
Illustration of area and line methods.

where A_f and A are the total fiber area and the area of the selected region of the micrograph, respectively.

An alternative way, the line method (Figure 3.14), can also be used to determine the fiber volume fraction from the micrograph. In this method, a number of lines are randomly drawn on the micrograph. The fiber volume fraction is evaluated as the ratio of the cumulative length of fiber cross sections along the line to the length of the line. For a representative result, an average value should be determined from measurements along several lines.

For a cross section of the carbon/epoxy composite discussed in the previous section, the results shown in Table 3.2 were obtained. From these data an average fiber volume fraction was determined, $V_f = 0.62$, which can be compared with $V_f = 0.65$, determined with the acid digestion method. Differences between the two methods are likely due to the smaller region of the composite which is studied in the micrograph and to uncertainty in determining the length of the fiber cross sections.

TABLE 3.2

Determination of Fiber Volume Fraction with the Line Method

Line	$L_{f\,(mm)}$[a]	V_f
1	44.5	0.58
2	40.8	0.54
3	54.9	0.72
4	45.3	0.60
5	48.3	0.63
6	48.1	0.63

[a] L_f = cumulative length of fiber cross sections. Total length of each line was 76.2 mm.

References

1. W.I. Lee, A.C. Loos, and G.S. Springer, Heat of reaction, degree of cure, and viscosity of Hercules 3501-6 resin, *J. Compos. Mater.*, 16, 510–520, 1982.
2. A.C. Loos and G.S. Springer, Curing of epoxy matrix composites, *J. Compos. Mater.*, 17, 135–169, 1983.
3. J.L. Kardos, M.P. Dudukovic, E.L. McKague, and M.W. Lehman, Void formation and transport during composite laminate processing, *ASTM Spec. Tech. Publ.*, 797, 96–109, 1983.
4. S. Nilsson, L. Carlsson, and P. Bergmark, Influence of thickness on three-dimensional elastic properties of graphite/epoxy composites, *J. Reinf. Plast. Compos.*, 4, 383–395, 1985.
5. C.N. Velisaris and J.C. Seferis, Crystallization kinetics of polyetheretherkeytone (PEEK) matrices, *Polym. Sci. Eng.*, 26, 1574–1581, 1986.
6. R. Dave, J.L. Kardos, and M.P. Dudukovic, A model for resin flow during composite processing, *Polym. Compos.*, 8(1), 29–38, 1987.
7. M.R. Dusi, W.I. Lee, P.R. Ciriscioli, and G.S. Springer, Cure kinetics and viscosity of Fiberite 976 resin, *J. Compos. Mater.*, 21(3), 243–261, 1987.
8. M.V. Bruschke and S.G. Advani, A finite-element/control volume approach to mold filling in anisotropic porous media, *Polym. Compos.*, 11(6), 398–405, 1990.
9. L.A. Berglund and J.M. Kenny, Processing science for high performance thermoset composites, *SAMPE J.*, 27(2), 27–37, 1991.
10. T.A. Bogetti and J.W. Gillespie, Two-dimensional cure simulation of thick thermosetting composites, *J. Compos. Mater.*, 25(3), 239–273, 1991.
11. S.N. Lee, M.T. Chiu, and H.S. Lin, Kinetic model for the curing reaction of a tetraglycidyl diamino diphenyl methane/diamino diphenyl sulfone (TGDDM/DDS) epoxy resin system, *Polym. Eng. Sci.*, 32(15), 1037–1046, 1992.
12. S.G. Advani, *Flow and Rheology in Polymer Composites Manufacturing*, in the series, *Composite Materials*, R.B. Pipes, Ed., Elsevier, Amsterdam, 1994, pp. 465–511.
13. ASTM Standard D 3171-99, *Test Method for Constituent Content of Composite Materials*, American Society for Testing and Materials, West Conshohocken, PA, 2001.
14. ASTM Standard D 2584-94, *Test Method for Ignition Loss of Cured Reinforced Resins*, American Society for Testing and Materials, West Conshohocken, PA, 2001.
15. ASTM Standard D 2734-94, *Test Method for Void Content of Reinforced Plastics*, American Society for Testing and Materials, West Conshohocken, PA, 2001.
16. ASTM Standard D 1505-98, *Test Method for Density of Plastics by the Density-Gradient Technique*, American Society for Testing and Materials, West Conshohocken, PA, 2001.
17. ASTM Standard D 3800-99, *Test Method Standard Test Method for Density of High-Modulus Fibers*, American Society for Testing and Materials, West Conshohocken, PA, 2001.
18. *Buehler Sampl-Kup*, Buehler, Ltd., Evanston, IL.

4

Test Specimen Preparation, Strain, and Deformation Measurement Devices, and Testing Machines

The quality of the experimental data ultimately obtained is a function of many factors. Composite processing was discussed in the previous chapter. Another critical step is specimen preparation. Care must be taken to avoid damaging the material when cutting individual specimens from a composite panel. Likewise, it is important that the testing equipment being used is in good working order and that measurements of forces, strains, and displacements are accurately conducted.

Many test methods require the use of tabs bonded to the test specimens. As will be described in relation to specific tests, tabs are used to reduce stress concentrations and protect the specimen from the aggressive action of the loading device, e.g., wedge grips. However, the tab bonding procedure can introduce its own sources of error. The type of tabbing material can be inappropriate for the application or be of poor quality. The adhesive used can be inadequate or improperly applied.

4.1 Cutting the Composite Laminate

Care must be taken when cutting composite materials for use as test specimens [1–3]. The material can be damaged in the process, resulting in reduced strength properties. One way this damage can be induced is by excessive heat buildup in the cutting zone. It may be necessary to alter the cutting tool speed, reduce the feed rate, use a different type of cutter, and use a cooling fluid. A suitable combination of these factors is often arrived at by experimentation for the particular composite being machined.

There might be concern when using a cooling fluid, which may be water based, that the composite properties would be altered by moisture absorption. All polymer–matrix composites absorb moisture, although to varying degrees and with varying consequences [4]. However, moisture diffusion is a relatively slow process [5]. Thus, brief exposure to water during the cutting

process (typically measured in minutes) will usually not result in large amounts of moisture absorption. However, it should be realized that once moisture enters the surface of the composite, it will in part continue to diffuse inward independent of the subsequent change in surface conditions. Even if the surface is immediately dried after cutting and the material is placed in a desiccator, some of the absorbed moisture will continue to diffuse inward (toward a lower moisture concentration), while the remaining moisture diffuses back out. This is not usually a problem because the total absorbed amounts are small. Conversely, it is incorrect to assume that placing the composite in a desiccator or drying oven for even several times the water exposure time will totally dry the material again. Long-term storage in a desiccator will ultimately eliminate the moisture in the test sample.

Glass-fiber composites are very abrasive to cutting tools, because of the inherent hardness of these fibers [1–3,6–8]. In addition, the small glass particles produced in the cutting process can damage the wear surfaces (ways, bearings, lead screws) of the cutting device being used. Boron, silicon carbide, and other ceramic fibers present similar problems. Using cutting fluids will help wash away these harmful abrasive particles. Carbon-fiber composites are much less of a problem because the particles produced act as a lubricant. However, carbon fibers are electrically conductive. Thus, the dust particles produced can cause shorts in electrical contacts such as switches and relays, and create other electrical problems. The use of a cutting fluid to minimize airborne carbon particles can be advantageous.

Aramid (e.g., Kevlar, E.I. du Pont de Nemours and Company), polyethylene (e.g., Spectra, Allied Chemical Corporation), and other organic fibers are particularly difficult to cut [1–3]. Because these fibers are highly oriented (orthotropic), they tend to break up into subfibers (i.e., fray) under the cutting forces and thus do not cut cleanly. Special cutter designs have been developed to cut these fibers and their composites more effectively.

For general-purpose use, carbide milling cutters and drills and aluminum oxide abrasive cutoff blades and grinding wheels are an appropriate starting point [2]. They are relatively low cost and often do a good job. In general, medium-grit abrasive cutters perform better than fine-grit cutters because particles of the material being cut do not tend to become imbedded in the cutter surface, i.e., the cutter does not load up as readily. Diamond particle impregnated cutting tools [1] are extensively used and are very durable, but they can also become clogged (loaded up) more readily with cutting debris. A clogged cutter is inefficient and can generate excessive amounts of frictional heat.

A surface grinder is a very useful specimen preparation device. Its cutting depth, table translation speed, and traversing motion can all be controlled directly. It is desirable to employ a used (reconditioned) machine for this purpose because of the potential abrasive wear problems cited above. Either a grinding wheel or a cutoff blade can be mounted in the grinder, depending on the operation to be performed. Although such devices frequently have

magnetic tables, the composite being cut will probably not be magnetic. Thus, double-sided tape (e.g., carpet tape) is commonly used to hold the composite to a sacrificial plate. This sacrificial plate is preferably an easily cut material (for example, an inexpensive polymer such as polymethyl methacrylate [PMMA], commonly known as Plexiglas®, Röhm, GmbH & Co. KG, Darmstadt, Germany), because it will be scored as the cutter blade completes the cut through the composite panel thickness. This assembly can in turn be taped to the surface grinder table, or to a steel plate held by the magnetic table.

A table saw with an abrasive blade, or a band saw with a suitable blade, can be useful for making rough initial cuts. A wire saw (which utilizes a thin wire impregnated with diamond particles) can be used for making cuts of very narrow kerf width, e.g., from 0.1 to 0.4 mm wide, to conserve material. It is also well suited for making cuts of complex shape because the wire can cut in any direction. However, the cutting rates tend to be slow. If curved cuts need to be made, it may be more practical to use a table router and routing jig. Commercial units are available [9]. A computer numerically controlled (CNC) milling machine is also an option, although the abrasive cutting particles generated can be detrimental to the machine, as previously discussed.

Water-jet and abrasive water-jet cutting of composites is being used more often in composite structural component fabrication [3]. If properly controlled, these techniques can provide clean cuts with relatively little surface damage. They hold promise for laboratory specimen preparation as well, and have been used as such, but not yet very extensively. Such cutting devices tend to be expensive because of the high-pressure water pump required, and thus they are not readily available. Current-generation laser beam industrial cutters are used even less often. The heat developed at the surface of the cut can be detrimental to the properties of the test coupon material [2,10]. The same is true of electrical discharge machining (EDM) [11].

In Chapter 13 tension and compression testing of laminates containing circular holes will be discussed. It is important to machine the hole, usually by drilling, without causing delamination of the hole edge, and to position the hole at the center of the specimen. One method of drilling holes without causing delamination is to back up the specimen with a strip of plastic such as PMMA. Position the drill at the center of the specimen within ±0.2 mm. A high-speed (about 2000 rpm), water-cooled diamond core bit works well to drill the holes, and a number of other suitable techniques exist [1–3]. Inspect the quality of the hole, and in addition to measuring the hole diameter, measure the net section dimensions on both sides of each hole to check that the hole is centered.

Whatever method of cutting or drilling is used, the finished specimens should be carefully examined for indications of surface damage that could degrade the strength properties. Along with visual inspection, optical microscope, x-ray, ultrasonic scan, dye penetrant, and other techniques are usually suitable for inspection purposes.

4.2 Tabbing Materials

Some test methods, tensile and compressive tests in particular, require the use of tabs on the test specimen. As will be discussed in detail in relation to the individual test methods, tabs are used to transfer the applied loading into the test specimen from the loading device. Often these loading devices are wedge grips, with roughened gripping surfaces. The tabs then also protect the surface of the composite test material from damage by the grips.

Currently, glass fabric/epoxy tabs are most commonly used. However, at one time aluminum tabs were also used extensively. Special surface preparation of the aluminum is usually required to achieve a strong adhesive bond. Low carbon steel tabs are also sometimes used. However, steel is harder to cut during the slicing of individual specimens than glass fabric/epoxy or aluminum, and the cutter may catch an edge of a tab of this stiff material and pop it off, ruining the specimen. Most important, however, is that glass fabric/epoxy tabs are superior performers [12–14]. A more compliant material reduces the stress concentration induced because of the discontinuity at the tab end, and glass fabric/epoxy is approximately one third as stiff as aluminum, and only about one tenth as stiff as steel. Glass fabric/epoxy is also a very tough and relatively strong material, able to absorb the surface damage induced when aggressive wedge grips are used in testing. For convenience in cutting, the glass fabric/epoxy is usually used in a [0/90] orientation, although a [±45] orientation would produce an even more compliant tab [12]. Although not as durable, $[0/90]_{ns}$ cross-ply laminates are sometimes used instead of fabric laminates.

The common source of high quality glass fabric/epoxy sheet for use as tabbing material is commercially available printed circuit board. This material is fabricated to tight thickness tolerances, which also is an important characteristic of a tabbing material. Printed circuit board is used in large quantities by the electronics industry and thus is readily available. It is also relatively low in cost. A commonly available sheet thickness of 1.6 mm is usually adequate. For use on relatively thick specimens of high-strength composites, it may be advantageous to increase the thickness, for example to 3.2 mm (another readily available thickness), because the roughened grip faces tend to cut deeper into the tabs as the force required to fail the specimen increases.

An even more compliant material than glass fabric/epoxy could be used as the tabbing material, but highly compliant materials tend to have insufficient strength to withstand the high stresses induced during testing of the composite specimen. If the tabbing material fails before the composite, the test is ruined.

At one time the concept prevailed that the stiffness of the tabbing material should match that of the composite being tested. This was frequently stated in standards and other publications. Thus, tabs were often fabricated of the same material as the test specimen. This concept has now been disproved,

however [13,14]. In fact, a tabbing material such as unidirectional carbon/epoxy used on an identical unidirectional carbon/epoxy composite may not even function. Typically, such tabs will have insufficient longitudinal shear strength to resist the shear loads induced by the grips during a test, and will shear off before the specimen fails.

4.3 Tab Bonding

Tabs are normally not bonded to each individual specimen, but rather to the full composite plate from which a group of specimens is to be cut. This plate is then sliced into individual specimens, as indicated in Figure 4.1, perhaps using a thin abrasive disk in a surface grinder, as described in Section 4.1. If the tabs are to be tapered, as shown in the example of Figure 4.1, they are tapered before being bonded to the composite plate, typically by grinding.

Tabs can be applied to individual specimens, and years ago before a better method was developed they were, but this is a labor-intensive process, more prone to tab alignment errors. (A piece of tabbing material with uncured adhesive between it and the specimen can be very slippery. Holding four such pieces in place simultaneously during positioning and cure can be very difficult.) Even with a full composite plate, misalignment can be a problem if a suitable procedure is not used. Tabbing jigs have been developed, such as shown in Figure 4.2 [15,16]. These consist of a base plate with projecting

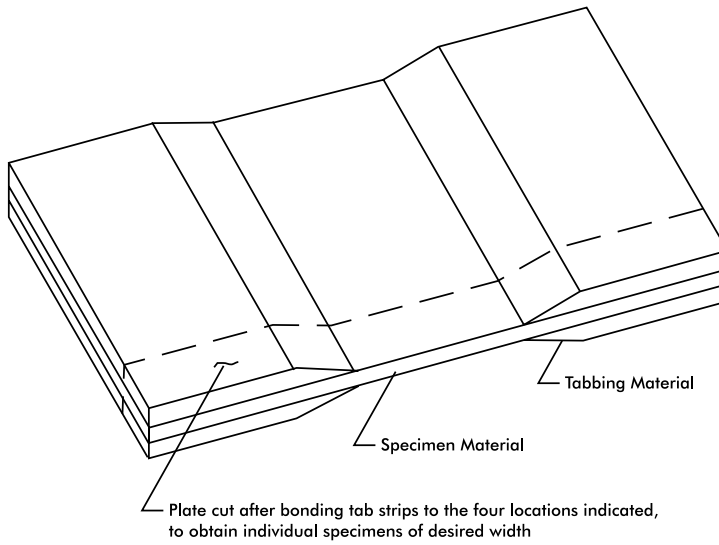

FIGURE 4.1
Fabrication of tabbed specimens.

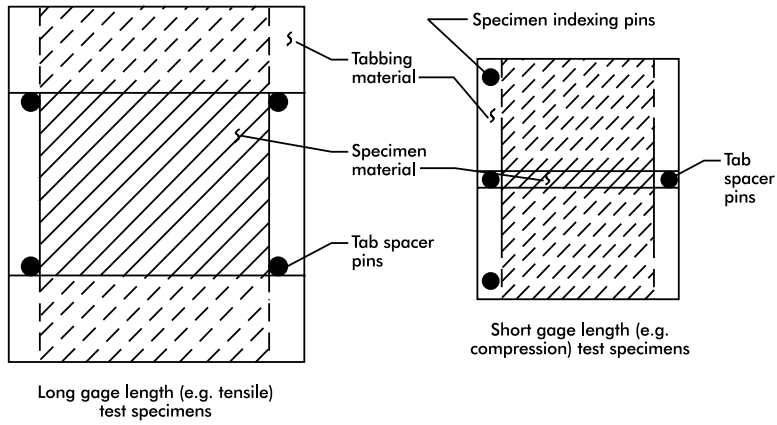

a

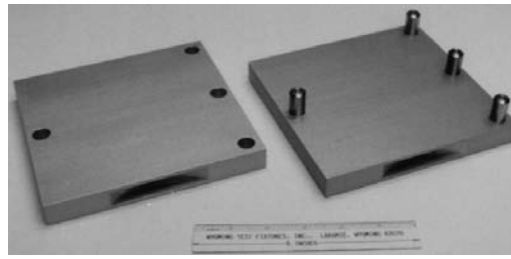

b

FIGURE 4.2

Specimen tabbing jigs. (a) Typical tabbing jigs (cover plate not shown). Note that left edge of composite material panel is indexed against pins. (b) Typical compression tabbing jig. (Courtesy of Wyoming Test Fixtures, Inc. [16].)

pins to index the composite panel and the tabbing strips against, and a cover plate containing holes to receive the pins. After the five components (the composite plate and four strips of tabbing material) are positioned in the jig, the adhesive must be cured. Particularly for a room-temperature cure adhesive, a weight can be placed on the top plate to provide some compaction during cure. However, it is usually more convenient to use a press. Even if only a relatively moderate compaction pressure of, for example, 70 kPa is desired, a force of 2.6 kN would be required to cure a 150×250 mm tab area. If up to 1 atm of pressure is adequate, a vacuum bag can be used as an alternative to a press.

Often the particular adhesive being used must be cured at an elevated temperature. Also, the cure time for a room-temperature cured adhesive can be reduced by subjecting it to a slightly elevated temperature. In these cases it is convenient to cure the assembly of composite plate and tabs in a heated platen press. Because of this potential application, tabbing jigs are typically fabricated of an aluminum alloy, because of its good heat conduction properties [16].

As an alternative to a tabbing jig, simple masking tape can be used to hold the composite plate and tabbing strips in place during cure of the adhesive, and a vacuum bag rather than a press can be used to apply suitable compaction pressure. Cure at elevated temperature can be achieved by placing the assembly in an oven. This method works well, although it is more time consuming than using a tabbing jig, and extra time is then also required to remove the tape, particularly after an elevated temperature cure.

4.4 Suggested Tab Bonding Procedure

Prior to bonding, it is necessary to carefully prepare the bonding surfaces of the specimen panel and the tabbing strips. A suggested procedure is as follows:

1. Lightly sand or grit blast the regions of the panel where the tabs are to be bonded, and the bonding surfaces of the tab strips. Do not abrade the gage section surfaces of the specimen panel as this may weaken the material. Use a medium-fine sandpaper or emery cloth (about 180 grit). This step both cleans and slightly roughens the surfaces, enhancing adhesive bonding.
2. Use a wire brush to remove loose particles.
3. Clean the surfaces with a solvent such as acetone to remove any remaining loose particles. Do not touch the cleaned surfaces.
4. Prepare the adhesive. Cut film adhesives to the size required. Mix the components of a two-part adhesive. Desirable characteristics of the adhesive are low stiffness, high shear strength, and thick bond line. Low cure temperature is desirable, but must be compatible with the subsequent testing temperature. Thus, a compromise must always be made since these characteristics are not mutually attainable. In the test environment the shear strength of the adhesive must be adequate.
5. Apply the adhesive to the bonding surfaces of both the specimen panel and the tabbing strips and assemble as previously described. **Take care to keep the gage section regions of the specimen panel free of adhesive. Excessive adhesive is both difficult to remove after cure and the removal process may damage the specimen surface.**
6. Cure the assembly as required for the adhesive being used.
7. Inspect the cured panel for proper positioning and alignment of the tabs, absence of excess adhesive, and bond lines of uniform thickness.

4.5 Hinge Attachment for Double-Cantilever Beam (DCB) and Mixed-Mode Bending (MMB) Specimens

Double cantilever beam (DCB) and mixed mode bending (MMB) specimens for delamination fracture characterization (Chapter 14) require the attachment of loading tabs. These are typically in the form of hinges (so that no moment is introduced into the specimen). Commercially available metal hinges can be used, if desired. They can be adhesively bonded or bolted onto the surface, or both. The former is less time consuming and is thus preferred, unless a sufficiently strong adhesive is not available. If the hinges are bonded onto the surface, the bonding length is typically on the order of 25 mm, but can be shorter if sufficient strength can be attained. The bonding procedure can be the same as that suggested in Section 4.4. A typical specimen with hinges attached by bolting is shown in Figure 4.3. Note that each hinge is bolted to only half the specimen thickness, by counterboring the fastener holes from opposite sides, as required.

The hinges must be aligned with the specimen axis and with each other. For this purpose, some type of hinge mounting jig is recommended, such as that shown in Figure 4.4. The hinges can be debonded and reused after completion of the specimen test, if the hinges are undamaged.

Bolted hinges are used when the maximum test loading is greater than can be supported by adhesively bonded tabs. As indicated in Figure 4.3 and discussed in detail in Chapter 14, the end of the specimen to which the hinges

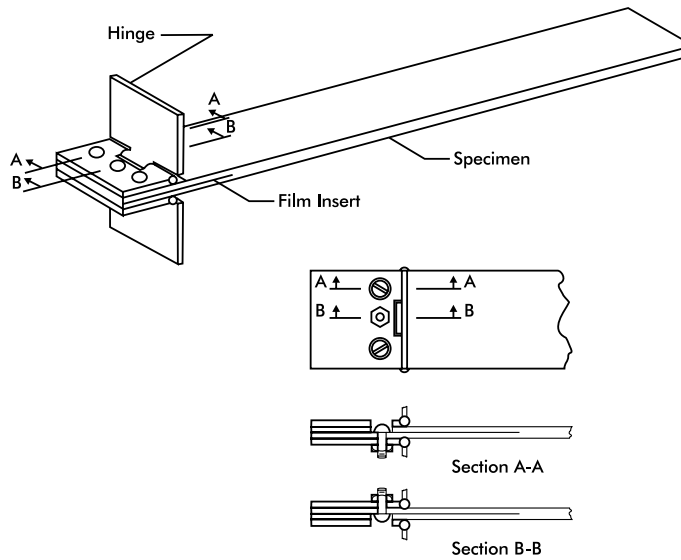

FIGURE 4.3
DCB specimen with hinges attached by bolting.

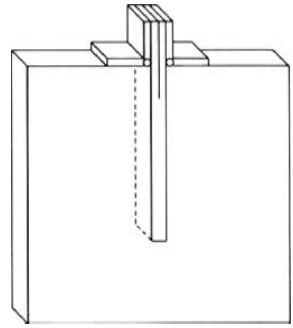

FIGURE 4.4
Jig for alignment and mounting of hinges for DCB and MMB specimens.

are to be attached is fabricated with a delamination at the thickness midplane. A hinge must be bolted to each half. This is typically achieved by drilling a hole through the total thickness of the laminate, and then counterboring through the half-thickness to provide clearance for the bolt head, as illustrated in Figure 4.3. These attachment holes are placed in a staggered pattern on opposite sides of the specimen, as required, and the hole patterns in the hinges are drilled accordingly. Proper alignment of the hinges must be achieved. The hinges can be adhesively bonded as well as bolted, for additional strength if required. As suggested above, the use of bolted hinges is much more labor intensive and thus not normally used if avoidable. The hinges can be unbolted and reused, if undamaged.

4.6 Specimen Conditioning

It is common practice to store and test specimens in the ambient laboratory environment. Often this environment is relatively uncontrolled, although 23°C and 50% relative humidity (50% RH) is a commonly stated standard condition. It is important to note that the total amount of moisture a polymer absorbs from the surrounding air is directly proportional to the relative humidity [5]. Thus, given sufficient exposure time, a polymer–matrix composite at 50% RH will attain one half of its maximum moisture absorption capability (one half of its saturation level). If the influence of moisture on composite properties is a concern, and normally it should be, it is obviously important to control the conditioning environment.

Unlike thermal equilibrium, moisture equilibrium at any given percent RH requires long exposure times, typically measured in months and even years, depending on the thickness of the composite and the exposure temperature [5]. The moisture diffusion coefficient increases with increasing temperature [5,6]. Thus, it is common practice to moisture condition and dry polymer–matrix composites at elevated temperatures. It is important that

the temperature not be too high, however, because the moisture gradient at the surface can produce damage. For example, consider a moisture-saturated polymer–matrix composite placed in a desiccator at a high temperature. Because of the high coefficient of moisture diffusion at that temperature, the surface will lose moisture rapidly, whereas the inner layers are still relatively unaffected. The surface material tends to contract (shrink) as it dries out, but is restrained by the material below it. This induces tensile stresses in the surface material, which can become high enough to cause local cracking (termed microcracking) at the surface [17,18] and irreversible (permanent) damage of the material.

4.7 Strain and Displacement Measurements

In Chapter 2 the engineering constants were defined in terms of the stress–strain response of the composite, and the specimen compliance was defined in terms of the displacement at the point of load application. To measure strains and displacements of test specimens, the three most common transducers used are electrical resistance strain gages, extensometers, and linear variable differential transformers (LVDT). Optical methods are also used, but to a lesser extent.

For strain measurement, electrical resistance strain gages are very versatile, reliable, and accurate [19–26]. Because they consist of thin metal foils bonded to the surface of the specimen, they cannot be reused. Fortunately, their cost is moderate [27]. A schematic of a typical strain gage is shown in Figure 4.5. If the composite is very inhomogeneous, such as a coarse-weave fabric composite, the gage must be large enough to cover a representative area of the microstructure, such as the weave structure [28].

The resistance of the gage used is important because of gage heating effects. The strain gage is normally wired into a Wheatstone bridge circuit and is activated by application of a constant voltage to the gage [20–26]. When the specimen, and hence the gage, is deformed, the strain gage resistance changes in proportion to the strain. This produces a calibrated voltage offset.

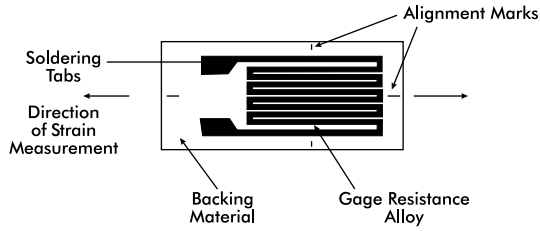

FIGURE 4.5
Schematic of an electrical resistance strain gage.

Because the power dissipated by the strain gage is proportional to the square of the voltage divided by the resistance of the gage, higher-resistance gages cause less heating for a given voltage [20]. Gage heating can be a problem with polymer–matrix composites because the polymer–matrix is a poor heat conductor. This allows heat to build up in the gage. The resulting temperature change causes a resistance change, which is falsely recorded as an apparent strain. Therefore, the use of 350-Ω strain gages is commonly recommended for composite testing, although 120-Ω gages are sometimes used. The gage excitation voltage should be less than 5 V. Sometimes temperature compensation is necessary, as discussed in References [25–27].

The accuracy of strain measurement using bonded foil strain gages relies on a high-quality bond between the gage and the test specimen. The specimen surface should be carefully prepared as instructed in the gage application literature [26,27]. The adhesive must be usable at the test temperature of interest.

Accuracy is also influenced by the transverse sensitivity of the strain gage. As indicated in Figure 4.5, the thin metal foil elements oriented in the direction of the desired strain measurement are connected by transverse foil elements to maintain continuity of the current flow. Because of Poisson effects for uniaxial loading, or deliberate biaxial loading, these transverse elements become strained and thus also change in resistance, adding to the total resistance change of the gage. If these transverse strains are not negligible, results can be modified to account for transverse sensitivity. Guidelines for determining when corrections are necessary and a discussion of correction procedures are given in References [19,20,29].

Extensometers can also be used to measure strains. A typical single-axis extensometer is shown in Figure 4.6. Biaxial units, to measure both axial and transverse strain and to permit the determination of Poisson's ratio (see Chapter 2), are also available, as are other special configurations [30–32]. Extensometers often contain strain gages bonded to the arms of the device. As the arms deflect, the strain gages are activated just as discussed above. Thus, these units are sometimes also called strain gage extensometers, to

FIGURE 4.6
Typical single-axis extensometer, mounted on a tensile specimen. (Courtesy of Epsilon Technology Corporation.)

distinguish them from the now much less commonly used dial gage and optical (rotating mirror) extensometers.

The accuracy of strain gage extensometers can be equal to that of bonded strain gages, as might be expected because the basic technology is the same. For a strain gage, the gage length is the length of the foil grid (Figure 4.5). Commonly used gage lengths are in the 1.5 to 6 mm range. The gage length of an extensometer is the distance between contact points on the specimen. Typical extensometers have gage lengths in the range of 12 to 50 mm. A commonly used gage length is 25 mm. Thus, the gage length of an extensometer tends to be much longer than that for a strain gage, which can be an advantage or a disadvantage depending upon the application. For example, if there are steep strain gradients in the specimen, a long gage length is a disadvantage if a local (point) strain is desired. On the other hand, if it is desirable to average out local surface strain variations (such as for the coarse-weave fabric composite noted above), a longer gage length is advantageous. Extensometers are also less sensitive to local roughness of the specimen surface.

Strain gage extensometers are less commonly used in composites testing than they were some years ago. Extensometers have increased in price proportionally much more than strain gages during the past 20 years. An extensometer is relatively expensive [30–32] and thus must be used many times to amortize the purchase price. However, it is often desirable to leave the extensometer attached to the specimen until the specimen fails; this produces a complete stress–strain curve. Failures of composites can sometimes be rather violent because the large amount of stored elastic strain energy is suddenly released. This can damage or destroy the expensive extensometer. Extensometers can also be damaged or destroyed when they are accidentally dropped on the floor during installation (and perhaps then stepped on in the attempt to catch them). Thus, often the extensometer does not survive to reach its amortization life. As previously noted, strain gages are intended to be used only once, and the cost per gage is relatively low.

LVDTs, such as those shown schematically in Figure 4.7, can also be used to measure strains. (All measurement devices actually measure displacements, which are then divided by the gage length to obtain strains.) Usually, however, LVDTs are designed to measure larger displacements than strain gages and extensometers, being intended for direct use in monitoring displacements [32]. Examples include the center span displacement of a beam (as will be discussed in Chapter 8), or the load-point displacement of a fracture specimen (Chapter 14).

The LVDT produces an electrical output as its core moves. This output voltage, however, is directly proportional to the core displacement only over a specified range — the working range of that particular LVDT. The resolution of an LVDT depends on the electronic system used to convert the input signal. A displacement resolution on the order of 25 μm can be achieved [24,33].

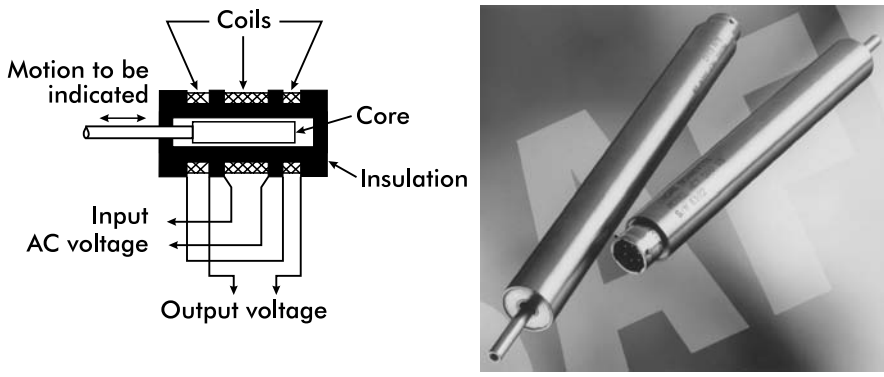

FIGURE 4.7
(a) Principle of a linear variable differential transformer LVDT.
(b) Photograph of typical LVDTs. (Courtesy of Lucas Shaevitz, Inc.)

Whatever type of device is used, it is important that it does not reinforce the surface of the composite and thus indicate erroneously low strains. This can be of particular concern when metal foil strain gages are used [19]. Membrane stiffness of the gage should not be greater than 10% of the substrate material. Optical (noncontacting) strain measurement devices have a distinct advantage in this regard because reinforcement of the surface is nonexistent. Although specialized, full-field techniques such as moire, holography, and speckle interferometry exist [20], designed to measure strains throughout an area rather than at a point, their use requires considerable training. In contrast, the use of a laser beam to track the relative movement of two points on the surface of the specimen being strained is much more straightforward, and commercial equipment is available [30,31,34]. However, the initial acquisition cost of a laser extensometer is typically considerably higher than that for a strain gage, extensometer, or LVDT measurement system, and the resolution of the currently available laser systems is generally not as high [34]. The acquisition cost factor, in particular, has limited their use to date. An excellent recent survey of optical strain measurement technology is presented in Reference [34].

4.8 Testing Machines

Specialized test fixtures will be described in relation to specific tests as they are discussed in the following chapters. In most cases, these specialized fixtures are designed to be mounted in a universal testing machine. As the name implies, these are general-purpose machines. They vary greatly in physical size, load capacity, versatility, and sophistication. The most basic machine should be

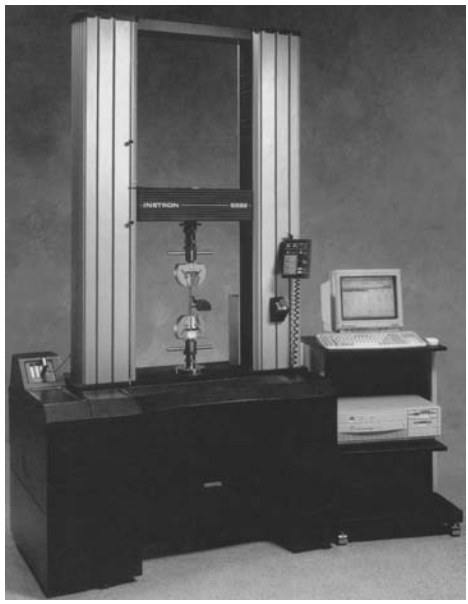

FIGURE 4.8
Typical electromechanical universal testing machine. (Courtesy of Instron Corporation.)

FIGURE 4.9
Typical servohydraulic universal testing machine. (Courtesy of MTS Corporation.)

capable of applying a uniaxial tensile loading (by controlling the motion of a moving crosshead) and indicating the corresponding force on the specimen. Most modern machines can apply both axial tensile and compressive loading. They can be operated in force or strain control as well as (crosshead) displacement control. An electronic load cell and multiple-channel strain–displacement signal conditioning electronics feed into a computerized controller, which processes these data and presents and stores the results in the forms desired. These can include stress–strain, stress–displacement, and strain–strain (for Poisson's ratio) plots, tabulations of axial stiffness, Poisson's ratio, ultimate strength, or whatever quantity is desired.

Each universal testing machine is designed to have a maximum load capacity. Small units may have a load capacity of only a few hundred newtons, and sometimes even less. There is no limit on maximum load capacity. Machines of 10 MN capacity and larger exist, and are used routinely. However, a very common capacity for most composites testing is on the order of 100 kN; some test methods will require a larger machine.

The size of the load cell may also limit how much force any machine can exert; these load cells are designed to be readily interchangeable. For example, a 100-kN machine can be used to test single fibers with breaking forces of less than 1 N if a sufficiently small load cell is used.

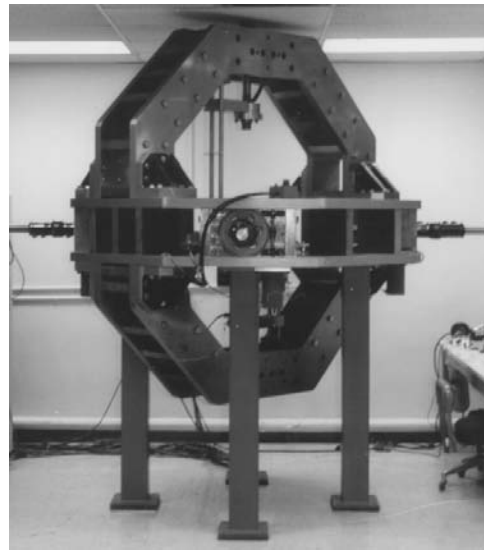

FIGURE 4.10
Example of a triaxial test apparatus. (Courtesy of the University of Wyoming.)

Most universal testing machines are of two basic types, electromechanical or servohydraulic. Electromechanical machines are typically screw-driven, with electronic feedback. Servohydraulic machines, as the name implies, are hydraulically powered with electronically controlled servovalves. Typical examples of commercially available machines of each type are shown in Figures 4.8 and 4.9.

In addition to universal testing machines, special devices are often developed for specific purposes. Examples include creep frames (for determining time-dependent deformations under constant applied force), resonant frequency fatigue machines, impact devices (e.g., drop weight and swinging pendulum), and biaxial and even triaxial loading machines. An example of a triaxial test apparatus designed specifically for composite materials is shown in Figure 4.10.

References

1. S. Abrate and D.A. Walton, Machining of composite materials. Part I: traditional methods, *Compos. Manuf.*, 3(2), 75–83, 1992.
2. T.S. Srivatsan, C.T. Lane, and D.M. Bowden, Eds., *Machining of Composite Materials II,* ASM International, Materials Park, OH, 1994.
3. M. Ramulu and D. Arola, Traditional and non-traditional machining of fiber reinforced plastic composites, *Proceedings of the 39th International SAMPE Symposium*, Anaheim, CA, Society for the Advancement of Material and Process Engineering, Covina, CA, April 1994, pp. 1073–1087.

4. Browning, G.E. Husman, and J.M. Whitney, Moisture effects in epoxy matrix composites, in *Composite Materials: Testing and Design (Fourth Conference)*, ASTM Spec. Tech. Publ. 617, 1977, American Society for Testing and Materials, West Conshohocken, PA, pp. 481–496.
5. C.W. Shen and G.S. Springer, Moisture absorption and desorption of composite materials, *J. Compos. Mater.*, 10(1), 2–20, 1976.
6. K. Sakuma and M. Seto, Tool wear in cutting glass-fiber-reinforced plastics, *Bull. JSME*, 26(218), 1420–1427, 1983.
7. K. Sakuma, M. Seto, M. Taniguchi, and Y. Yokoo, Tool wear in cutting carbon fiber reinforced plastics, *Bull. JSME*, 28(245), 2781–2788, 1985.
8. R. Komanduri, Machining fiber-reinforced composites, *Mech. Eng.*, April, 58–63, 1993.
9. *Precision Equipment for the Preparation of Physical Test Specimens*, Product Catalog, Tensilkut Engineering, Maryville, TN, 1997.
10. S.G. Howarth and A.B. Strong, Edge Effects with Waterjet and Laser Beam Cutting of Advanced Composite Materials, *Proceedings of the 35th International SAMPE Symposium*, Anaheim, CA, Society for the Advancement of Material and Process Engineering, Covina, CA, April 1990, pp. 1684–1697.
11. W.S. Lau and W.B. Lee, A comparison between EDM wire-cut and laser cutting of carbon fibre composite materials, *Mater. Manuf. Process.*, 6(2), 331–342, 1991.
12. L.J. Hart-Smith, Generation of Higher Composite Materials Allowables Using Improved Test Coupons, *Proceedings of the 36th International SAMPE Symposium*, Anaheim, CA, Society for the Advancement of Material and Process Engineering, Covina, CA, April 1991, pp. 1029–1044.
13. M.E. Cunningham, S.V. Schoultz, and J.M. Toth, Jr., Effect of End-Tab Design on Tension Specimen Stress Concentrations, *Recent Advances in Composites in the United States and Japan*, ASTM Spec. Tech. Publ. 864, J.R. Vinson and M. Taya, Eds., American Society for Testing and Materials, Materials Park, OH, 1985, pp. 253–262.
14. M. Xie and D.F. Adams, Effect of specimen tab configuration on compression testing of composite materials, *J. Compos. Technol. Res.*, 17(2), 77–83, 1995.
15. *Tensile and Compression Specimen Fabrication and Testing*, Technical Service Bulletin TS-002, Hercules Composite Products Group, Magna, UT, January 1990.
16. *High Performance Test Fixtures*, Product Catalog No. 106, Wyoming Test Fixtures, Inc., Laramie, WY, 2000 (*also*, www.wyomingtestfixtures.com).
17. J.M. Mahishi and D.F. Adams, Analysis of neat resin cracking induced by rapid moisture loss, *Compos. Technol. Rev.*, 6(4), 159–163, 1984.
18. A.W. Obst, M.R. Van Landingham, R.F. Eduljee, and J.W. Gillespie, Jr., The Effect of Hygrothermal Cycling on the Microcracking Behavior of Fabric Laminates, *Proceedings of the 28th International SAMPE Technical Conference*, Seattle, WA, Society for the Advancement of Material and Process Engineering, Covina, CA, November 1996, pp. 994–1002.
19. C.H. Jenkins, Ed., *Manual on Experimental Methods of Mechanical Testing of Composites*, 2nd ed., Society for Experimental Mechanics, Inc., Bethel, CT, 1998, chap. 4–8.
20. J.M. Whitney, I.M. Daniel, and R. B. Pipes, *Experimental Mechanics of Fiber Reinforced Composite Materials*, revised ed., Society for Experimental Mechanics, Prentice Hall, Englewood Cliffs, NJ, 1984.
21. A.S. Kobayashi, Ed., *Handbook on Experimental Mechanics*, 2nd ed., Society for Experimental Mechanics, Inc., Bethel, CT, 1993.

22. J.W. Dally and W.F. Riley, *Experimental Stress Analysis*, 3rd ed., John Wiley & Sons, New York, 1991.
23. R. S. Figliola and D. E. Beasley, *Theory and Design for Mechanical Measurements*, John Wiley & Sons, New York, 1991.
24. M.E. Tuttle and H.F. Brinson, Resistance-foil strain gage technology as applied to composite materials, *Exp. Mech.*, 23(1), 54, 1984.
25. *Student Manual for Strain Gage Technology*, Bulletin 309A, Measurements Group, Education Division, Raleigh, NC, 1996.
26. *Strain Gage Measurements on Plastics and Composites*, Measurements Group, Inc., Raleigh, NC, November 1995.
27. *Precision Strain Gages*, Micro-Measurements Catalog 500, Measurements Group, Inc., Raleigh, NC, June 2000.
28. J.E. Masters and P.G. Ifju, Strain gage selection criteria for textile composite materials, *J. Compos. Technol. Res.*, 19(3), 152–167, 1997.
29. *Errors Due to Transverse Sensitivity in Strain Gages*, Technical Note TN-509, Measurements Group, Inc., Raleigh, NC, 1982.
30. *Guide to Advanced Materials Testing*, Product Catalog, Instron Corporation, Canton, MA, 1997.
31. *Material Testing Products*, 7th ed., MTS Systems Corporation, Eden Prairie, MN, 1999.
32. *Version 104 Extensometer Catalog*, Epsilon Technology Corporation, Jackson, WY, 1997.
33. *Linear & Angular Displacement Transducers*, Catalog No. 101, Lucas Schaevitz, Inc., Pennsauken, NJ, 1990.
34. D.V. Moon, Design and Fabrication of a High Resolution Laser Extensometer, M.S. thesis, Department of Mechanical Engineering, University of Wyoming, Laramie, WY, December 1999.

5

Lamina Tensile Response

5.1 The Need for Lamina Testing

For most composites in use today, the individual lamina (i.e., the individual layer or ply) is the basic unit or building block, whether it is in the design, the analysis, or the fabrication process stage. This lamina may be a unidirectional prepreg, a fabric, a chopped-strand mat, or another fiber form, with or without the matrix present prior to laminate fabrication. However, some composites are not fabricated of individual layers. As discussed in Chapter 3, such alternate processes include resin transfer molding (RTM), and vacuum-assisted resin transfer molding (VARTM). However, the resulting composites are typically still nonhomogeneous and anisotropic in terms of strength, stiffness, and physical properties. Thus, even in these cases the designed composite component still consists of individual layers (or regions) of differing material properties.

In summary, whatever the material form or fabrication process, the properties of the individual laminae (regions, layers, or whatever form the composite takes) must be known for design and analysis purposes. Determination of the tensile strength and stiffness properties of these individual laminae will be the topic of the present chapter, whereas compressive, shear, and flexural properties will be addressed in Chapters 6, 7, and 8, respectively. Lamina thermoelastic properties are discussed in Chapter 10.

5.2 Introduction to Tensile Testing

Tensile properties are often the first to be thought of when a composite material is considered for a design application. Although tensile properties do not always ultimately determine the design, as will be shown in subsequent chapters, they are nevertheless among those of primary importance.

The difficulty of performing an acceptable tensile test typically increases as the orthotropy of the material increases, i.e., as the ratio of the axial

stiffness (or strength) to the transverse stiffness (or strength) and the longitudinal shear stiffness (or strength) increases. Thus, a unidirectional composite lamina is often the most difficult material form to test. For this reason, particular emphasis here and in the following three chapters will be on suitable methods for testing unidirectional composites. Often if a unidirectional composite can be successfully tested using a particular procedure, almost any other laminate form can be tested as well. Conversely, it may be possible to successfully test a material of less orthotropy using alternative procedures that are more efficient in terms of time and cost.

For example, it is possible to test a $[90/0]_{ns}$ cross-ply laminate and then use classical lamination theory (Chapter 2) to back out the unidirectional ply properties. This technique has been examined extensively and shown to be very viable for compression testing (as discussed in Chapter 6), but has not yet been shown to be acceptable for tensile testing. Other examples will be discussed in the remainder of this chapter.

5.3 Load Introduction

Proper introduction of the applied force into the test specimen is one primary concern. For materials of low orthotropy, this may be as simple as pin-loading through a hole in each end of a dog-bone-shaped specimen (or dumbbell-shaped, as termed in ASTM Standard D 638 [1]). However, for most composites the high bearing stresses induced by the pins would cause local failures around the holes. Thus, it is more common to use some type of clamping grip at each end of the dog-bone-shaped specimen. A sketch of a dog-bone-shaped specimen (without holes in the ends) is shown in Figure 5.1(a). Several specific dog-bone specimen shapes are suggested in ASTM D 638.

When clamping grips are used, the tensile loading in the specimen is induced via shear at the clamp–specimen interface. This shear force is equal to the clamping force times the effective coefficient of friction at the interface. Usually, little can be done to increase the coefficient of friction of the specimen surface without potentially degrading the properties of the material being tested. However, the faces of the clamp can be altered. The most common technique is to roughen them, by machining or by coating [1,2]. Machined patterns of increasing aggressiveness (e.g., from swirls to crosshatches to straight grooves) can be used, with deeper and sharper profiles more effectively penetrating the surface of the specimen and thus producing a higher effective coefficient of friction. An alternative is to coat the clamps with a friction-enhancing material. Rubber coatings can be used when testing low-strength materials. Emery cloth placed between the clamps and the specimen surfaces has long been used to increase the gripping force. This has led to the use of tungsten carbide particles thermal-sprayed on the grip

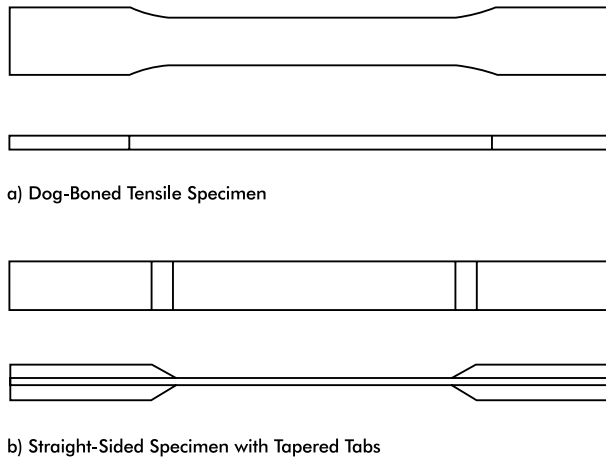

FIGURE 5.1
Typical tensile test specimen geometries.

surfaces [2]. The roughness of the clamp faces is dictated by the size of particles used. Typically, roughnesses on the order of 80 to 150 grit are used [1–3].

The more severely the surface is penetrated, the greater the danger of premature specimen failure, whatever type of clamp face is used. The alternative is to increase the clamping force. However, the through-thickness compressive strength of most composites is low relative to the axial tensile strength. Thus there is a limit to how much clamping force can be applied without crushing or otherwise degrading the specimen material.

For low-strength composites, simple mechanical clamps or pneumatically actuated grips and relatively smooth grip faces may be adequate. However, wedge grips are more commonly used. Two types of wedge grips are in common use: mechanical and hydraulic [4,5]. Examples of each are shown in Figures 5.2 and 5.3, respectively. The wedging action of mechanical wedge grips is in direct proportion to the magnitude of the tensile force being applied, and inversely proportional to the angle to which the wedges are machined, which is typically on the order of 10°. If the wedge angle is too low, the clamping force may crush the specimen being gripped. The wedges of hydraulic grips are loaded by hydraulic pressure prior to the start of the tensile test. The magnitude of the hydraulic pressure to be used must be predetermined. Suppliers of commercially available hydraulic wedge grips provide guidelines for the pressure required as a function of the anticipated total axial force to be applied by the grips [4,5].

Although hydraulic wedge grips perform well, they are much heavier and bulkier than mechanical wedge grips, and also much more expensive [4,5]. However, for repeated loading (e.g., fatigue), they perform better than mechanical wedge grips. Mechanical wedge grips tend to progressively tighten with successive cycles and may eventually crush the specimen ends [6].

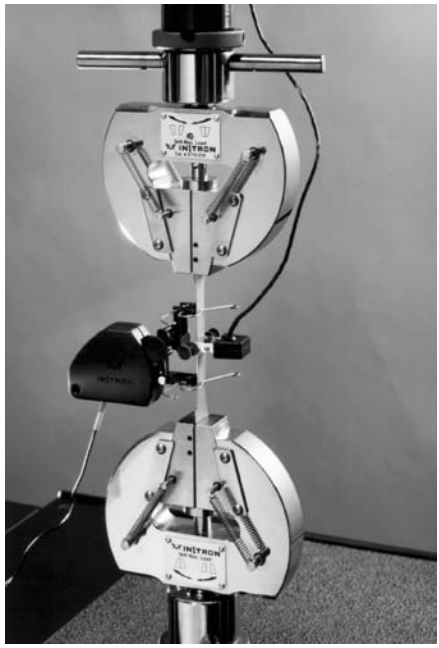

FIGURE 5.2
Typical mechanical wedge grips, with axial and transverse extensometers attached to a tensile test specimen. (Photograph courtesy of Instron Corporation.)

FIGURE 5.3
Typical hydraulic wedge grips. (Photograph courtesy of MTS Corporation.)

The above discussion was particularly directed toward composite materials of low orthotropy; the emphasis was on the use of untabbed, dog-bone-shaped specimens. As the composite material becomes more highly orthotropic, dog-bone-shaped specimens become less suitable. As indicated in Section 5.2, the longitudinal shear strength of such highly orthotropic composites becomes progressively less relative to the axial tensile strength. Thus, at some point the wide ends of the dog-bone-shaped specimen begin to fail in longitudinal shear in the width-transition regions, effectively converting the dog-bone-shaped specimen into a straight-sided specimen (a specimen of constant width), which pulls out of the grips.

Thus, if this type of shear failure is likely to occur during the test, it is logical to simply start with a straight-sided specimen. This configuration is the basis for ASTM Standard D 3039 [7]. If one assumes that the material has a relatively high axial tensile strength, it has to be gripped firmly to prevent slipping, or more aggressive grip faces must be used. In either case, stress concentrations are induced in the unprotected specimen ends, promoting premature (grip) failures. Thus, it becomes necessary to use tabs, as discussed in Chapter 4, in an attempt to reduce these stress concentrations and to protect the specimen ends from grip damage. A sketch of a typical tabbed,

straight-sided tensile specimen is shown in Figure 5.1(b). Unfortunately, the presence of the tabs induces new stress concentrations because of the relatively abrupt change in specimen thickness at the tab ends. Thus, the tabs are typically tapered, as shown in Figure 5.1(b), in an attempt to reduce the abruptness of the thickness change. Stress analyses of tabbed specimens [8–10] indicate that significant out-of-plane (through thickness) peel (i.e., transverse tensile) and interlaminar shear stresses are induced in the test material at the tab ends, as well as axial tensile stress concentrations, particularly for tapered tabs. ASTM D 3039 does not suggest a specific taper angle, and indicates only that the angle should be between 5 and 90° (a rather broad guideline). (Note that an untapered tab is defined as having a taper angle of 90°.) Results of a recent round robin experimental study reported by Hojo et al. [11] suggest that there is no significant difference between 10 and 90° tab taper angle specimen tensile strengths for two different unidirectional carbon/epoxy composites. On the basis of these results, the International Organization for Standardization (ISO) has adopted the untapered tab specimen as their tensile specimen configuration. It appears that the geometric discontinuity reduction benefits of tab tapering are offset by the through-thickness (peel) stresses induced in the specimen. Obviously, additional study is required in this area.

Consistent with the above discussion, ASTM D 3039 recognizes the possibility of successfully testing untabbed, straight-sided specimens of lower strength materials such as fabric-reinforced composites and $[\pm 45]_{ns}$ laminates (such as those tested to determine composite shear properties, as will be discussed in Chapter 7).

5.4 Specimen Configurations and Test Procedures

Recommended dog-bone-shaped and straight-sided specimen configurations and dimensions are presented in ASTM Standards D 638 and D 3039, respectively. Although considerable detail is presented, these standards recognize and accept that certain composite materials and test conditions may require modifications. Prior experience must then be relied upon whenever possible.

For unidirectional composites of 0° fiber orientation, a specimen width of 12.7 mm and a specimen thickness of 6 to 8 plies are common, assuming a typical ply thickness on the order of 0.127 mm. Unidirectional 90° specimens are typically 25 mm wide and 16 to 24 plies thick; the number of plies depends on the actual ply thickness. Loading eccentricity may arise because of variations in tab and specimen thicknesses. Tolerances for tab and specimen thicknesses are ±1 and ±4%, respectively [8]. The tab length (see Figure 5.1(b) or 5.4), should be at least 38 mm, and the tab material should

FIGURE 5.4
Photograph of tensile specimen with axial and transverse strain gages attached.

be 1.6 to 3.2 mm thick. The gage length (distance between tabs) is commonly 125 to 155 mm. Variations of the specimen width should not exceed 1%. If Poisson's ratio is desired, a 0/90 strain gage rosette should be bonded in the center gage section region of the specimen (see Figure 5.4) or a biaxial extensometer should be used. If only axial stiffness and strength are desired, a longitudinal strain gage or a uniaxial extensometer is sufficient.

Accurate measurement of the specimen cross-sectional area in the gage section is particularly important, along with careful alignment of the specimen in the grips of the testing machine. Observers should wear adequate eye protection during the test procedure. Composite materials, and particularly axially loaded high-strength unidirectional composites, can splinter and fragment violently upon failure.

Measure the cross-sectional dimensions at several points on the specimen. Insert the specimen in the grips of a properly aligned and calibrated test frame. Set the crosshead rate at 2 mm/min. Avoid unprotected eyes in the test area, especially for the 0° tensile test. The strain readings may be recorded continuously or at discrete load intervals. If discrete data are taken, a sufficient number of data points must be recorded to reproduce the stress–strain behavior. At least 25 data points are needed in the linear response region. A total of 40 to 50 points is desirable to establish the total stress–strain response. Monitor all specimens to failure.

5.5 Data Reduction

The elastic stiffnesses E_1 and E_2 and the Poisson's ratios ν_{12} and ν_{21} are defined as

- E_1: The initial slope of the stress–strain curve ($\Delta\sigma_1/\Delta\varepsilon_1$) for the 0° tensile test
- ν_{12}: The negative ratio of the transverse to longitudinal strains ($-\varepsilon_2/\varepsilon_1$) for the 0° tensile test
- E_2: The initial slope of the stress–strain curve ($\Delta\sigma_2/\Delta\varepsilon_2$) for the 90° tensile test
- ν_{21}: The negative ratio of the transverse to longitudinal strains ($-\varepsilon_1/\varepsilon_2$) for the 90° tensile test.

The longitudinal and transverse tensile strengths, X_1^T and X_2^T, are defined as the ultimate values of σ_1 and σ_2 for the 0 and 90° tensile tests, respectively. The ultimate strains, e_1^T and e_2^T are the strains corresponding to X_1^T and X_2^T, respectively.

A representative example of stress σ_1 vs. strains ε_1 and $-\varepsilon_2$ curves for a $[0]_6$ unidirectional carbon/epoxy composite is shown in Figure 5.5, where ε_1 and ε_2 are the longitudinal and transverse strains, respectively, and the stress σ_1 is defined as the maximum force applied to the specimen divided by test section cross-sectional area. The modulus, E_1, was obtained using a least-squares linear fit [12] to the linear initial portion of the curve σ_1 vs. ε_1; Poisson's ratio, ν_{12}, was determined from the ratio of initial slopes of σ_1 vs. ε_1 and σ_1 vs. $-\varepsilon_2$. Values of E_1, ν_{12}, and X_1^T so reduced are listed in Figure 5.5. Figures 5.6–5.9 show examples of stress–strain curves for other unidirectional ([0] and [90]) composites. In addition, a sample laboratory report for the tests discussed above is given in Appendix C.

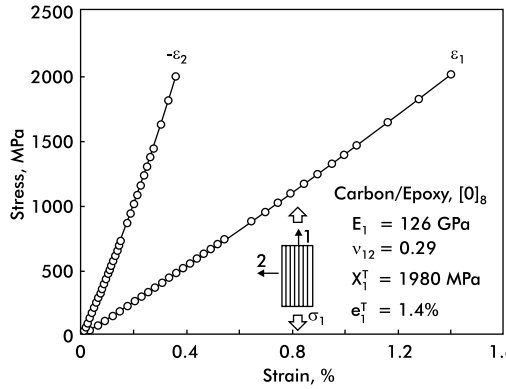

FIGURE 5.5
Tensile stress–strain response of a $[0]_8$ carbon/epoxy specimen.

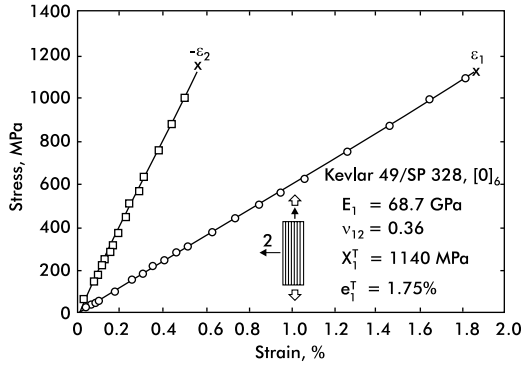

FIGURE 5.6
Tensile stress–strain response of a $[0]_6$ Kevlar/epoxy specimen.

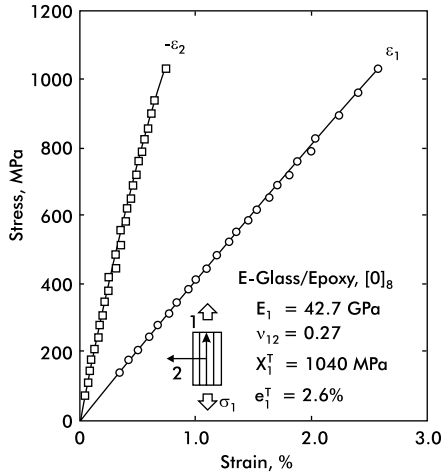

FIGURE 5.7
Tensile stress–strain response of a $[0]_8$ E-glass/epoxy specimen.

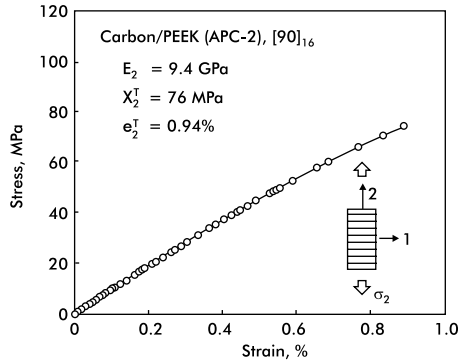

FIGURE 5.8
Tensile stress–strain response of a $[90]_{16}$ carbon/polyetheretherketone (PEEK) specimen.

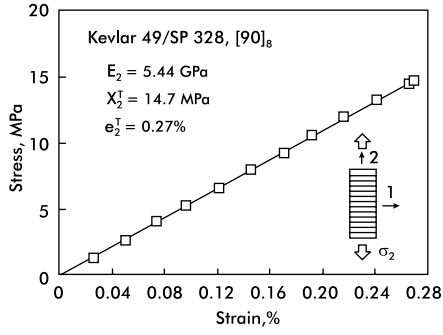

FIGURE 5.9
Tensile stress–strain response of a $[90]_8$ Kevlar/epoxy specimen.

References

1. ASTM Standard D 638-00, *Standard Test Method for Tensile Properties of Plastics*, American Society for Testing and Materials, West Conshohocken, PA, 2001.
2. R.J. Coguill and D.F. Adams, Selection of the Proper Wedge Grip Surface for Tensile Testing Composite Materials, *Proceedings of the 44th International SAMPE Symposium*, Long Beach, CA, May 1999, pp. 2332–2345.
3. *High Performance Test Fixtures*, Product Catalog No. 106, Wyoming Test Fixtures, Inc., Laramie, WY, 2000. (*also*, www.wyomingtestfixtures.com).
4. *Guide to Advance Materials Testing*, Product Catalog, Instron Corporation, Canton, MA, 1997.
5. *Material Testing Products*, Product Catalog, 7th ed., MTS Systems Corporation, Eden Prairie, MN, 1999.
6. E.M. Odom and D.F. Adams, *A Study of Polymer Matrix Fatigue Properties*, Report No. NADC-83053-60, Naval Air Development Center, Warminster, PA, June 1983.
7. ASTM Standard D 3039-00, *Standard Test Method for Tensile Properties of Polymer Matrix Composite Materials*, American Society for Testing and Materials, West Conshohocken, PA, 2001.
8. S. Chatterjee, D. F. Adams, and D.W. Oplinger, Test Methods for Composites — a Status Report, Vol. I, *Tension Test Methods*, DOT/FAA/CT-93/17-I, FAA Technical Center, Atlantic City International Airport, NJ, June 1993.
9. D.W. Oplinger, K.R. Gandhi, and B.S. Parker, *Studies of Tension Test Specimens for Composite Material Testing*, AMMRC TR 82-27, Army Materials and Mechanics Research Center, Watertown, MA, April 1982.
10. M.H. Kural and D.L. Flaggs, A finite element analysis of composite tension specimens, *Compos. Technol. Rev.*, Spring, 11–17, 1983.
11. M. Hojo, Y. Sawada, and H. Miyairi, Influence of clamping method on tensile properties of unidirectional CFRP in 0° and 90° directions — round robin activity for international standardization in Japan, *Composites*, 25(8), 786–796, 1994.
12. I. Miller, J.E. Freund, and R.A. Johnson, *Probability and Statistics for Engineers*, 4th ed., Prentice-Hall, Englewood Cliffs, NJ, 1990.

6

Lamina Compressive Response

When fiber-reinforced composites containing unidirectional plies oriented in, or at small angles to, the loading direction are loaded in compression, the fibers may buckle in small regions of the test section [1]. This is followed by the formation of kink zones [2] and failure of the fibers at the boundaries of the kink zones because of locally large bending stresses (Figure 6.1).

Compression loading of a composite perpendicular to the fibers involves failure of the matrix and fiber–matrix interface, often exhibited as a shearing type (inclined failure planes), such as illustrated in Figure 6.2. A detailed discussion of the various compressive failure modes observed in fiber-reinforced composites can be found in References [3,4].

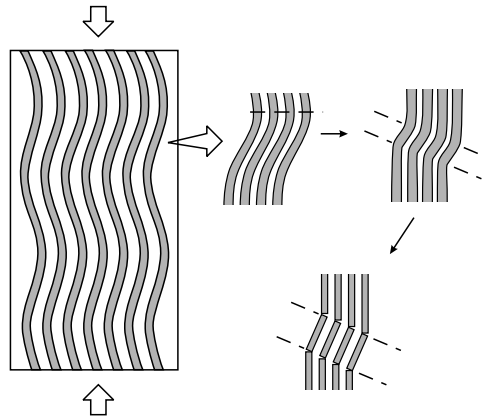

FIGURE 6.1
Mechanism of compressive failure through kink band formation of a composite loaded in the fiber direction.

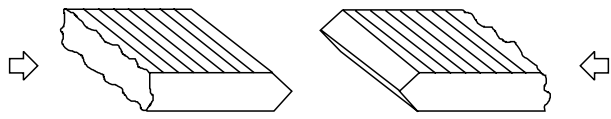

FIGURE 6.2
Shear type of compression failure in a composite loaded in the transverse direction.

When the many existing compression tests available [5,6] are examined, each method should be judged by its ability to produce compression failure without introducing loading eccentricity and severe stress concentrations at the loaded ends, while avoiding global buckling instability (Euler buckling) of the specimen. The fulfillment of those criteria makes the determination of the true compressive strength difficult. In fact, measurement of the true compressive strength of the composite has only rarely been achieved, and perhaps is of minimal practical interest because it is seldom achieved in practical applications [7].

The evaluation of test methods for determining lamina compressive response has received exceptional attention in recent years. Prior to 1975, when ASTM Standard D 3410 was first issued [8], there was no standard for compression testing of composite laminae, although a number of methods had been proposed during the prior 20 years and some were being used within the composites testing community [6]. The first ASTM standard focused on the Celanese compression test fixture, so-called because it had been developed by the Celanese Corporation [9]. Its several deficiencies were soon established, leading to the development of the Illinois Institute of Technology Research Institute (IITRI) test fixture [10], which was not added to ASTM D 3410 until 1987. Both of these are shear-loaded specimen test methods; that is, the load is introduced into the specimen via the shearing action of wedge grips loaded in compression.

Another form of shear loading that has received minor attention over the years is that achieved by the flexural testing of a sandwich beam consisting of thin laminate face sheets bonded to a core material. The core of the sandwich is typically a honeycomb material. The face sheet on the compressive side of the beam is the test material, whereas the face sheet on the tensile side, designed to have an axial stiffness equivalent to that of the test laminate can be of any material sufficiently strong that it will not fail before the compressive face sheet. This test method was incorporated into ASTM D 3410 at the same time as the IITRI compression test method, and then later given its own designation, as ASTM D 5467 [11]. However, this test method has never been commonly used for several reasons. The specimen is relatively large (560 mm long, 25 mm wide, and 40 mm thick) and thus consumes considerable test material. The specimen is also relatively expensive to fabricate, and proper sandwich beam fabrication requires special skills not always available to the test laboratory. Improper design or fabrication may lead to core shear failure, core crushing, tensile face sheet failure, or failure of an adhesive bond line prior to compressive face sheet failure, thus invalidating the test.

A more obvious method of applying compression is direct end loading of the specimen. However, if relatively thin laminae are to be tested, lateral supports must be provided to prevent gross buckling. Such a procedure had already been standardized for the compression testing of plastics in ASTM D 695, first published in 1942 [12]. In the early 1980s, a major modification of this general testing concept was developed for high-performance composites [13]. Although it is commonly termed the Modified ASTM D

695 compression test method, ASTM has not adopted it. It is, however, a Suppliers of Advanced Composite Materials Association (SACMA) recommended method [14].

There are advantages and disadvantages of both shear loading and end loading. Thus, recently a new combined loading compression test method was standardized by ASTM, as ASTM D 6641 [15], which attempts to combine the favorable features of both loading types.

The various compression test methods in common use are discussed in greater detail in the following three subsections.

6.1 Shear-Loading Test Methods

The IITRI compression test method and its several modifications [16,17] persists as the shear-loading test method of choice. In fact, the Celanese test method was recently removed from ASTM D 3410, leaving only the IITRI method in that standard.

A schematic of a typical IITRI fixture is shown in Figure 6.3, and a photograph of an actual fixture is shown in Figure 6.4. Its principal features are the use of flat wedge grips, and a pair of alignment rods and bearings. Either untabbed or tabbed specimens are permitted. However, tabbed specimens are most commonly used, to protect the test material from the high clamping

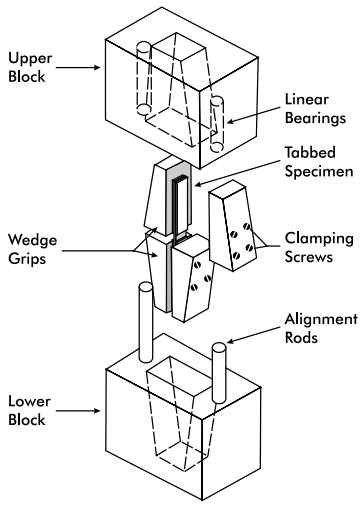

FIGURE 6.3
Sketch of the basic IITRI compression test fixture.

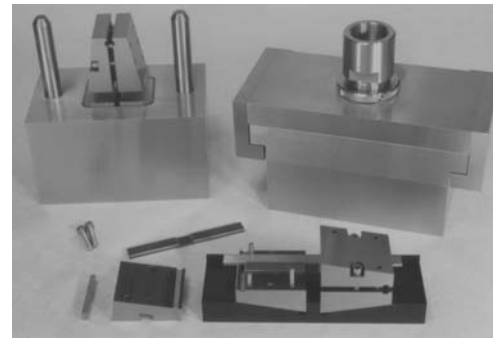

FIGURE 6.4
Photograph of a typical IITRI compression test fixture, with an extra set of wedge grips mounted in a specimen installation jig. (Photo courtesy of Wyoming Test Fixtures, Inc.)

forces of the wedge grips, and surface damage if aggressive grip faces are used. The flat wedge grips permit variation of specimen thickness within the available range of movement of the wedges. Typically, the range is between 4 and 5 mm [16], providing considerable flexibility in terms of specimen preparation. With the use of interchangeable inserts of different thicknesses in the upper and lower blocks of the fixture, a broad range of specimen thicknesses can be accommodated. For example, some commercially available fixtures can accommodate specimens ranging in thickness from 4 to 15 mm [16], and obviously a fixture to test a specimen in any practical thickness range could be designed. The standard specimen length is 140 mm, with a 12.7-mm gage length (unsupported length). A specimen width of 12.7 mm is common, although some fixtures can accommodate a width up to 38 mm [16].

The alignment rods and linear ball bearings of the IITRI fixture will not bind, and provide minimal frictional resistance. One disadvantage of the IITRI fixture is its relatively large size. The result is a heavy (>40 kg) and relatively expensive fixture. Thus, some excellent scaled-down versions and alternate configurations have been developed [16,17]. However, if cost or weight is not a barrier, the IITRI fixture remains a good choice of a shear-loaded compression fixture because it is very versatile in the range of specimen sizes it can accommodate.

6.2 End-Loading Test Methods

Although a large number of end-loading test methods have been developed over the years [6], the so-called Modified ASTM D 695 method is the most common at present. Its only feature in common with the actual ASTM D 695 test method [12] is the shape of the lateral supports used to prevent specimen buckling. The standard ASTM D 695 specimen is dog-bone-shaped and untabbed (see Figure 6.5(a)), whereas the modified specimen is straight-sided and tabbed (Figure 6.5(b)). The straight sides acknowledge the fact that highly orthotropic (e.g., unidirectional composites) will simply split longitudinally under load, thereby converting the dog-bone-shaped specimen into a straight-sided specimen. Because the purpose of the dog bone shape of the specimen is to increase the load bearing area at the ends and thereby eliminate end crushing, tabs were added to the straight-sided specimen to achieve the same result.

In both cases the specimen is nominally about 80 mm long, specifically 79.5 mm for the standard dog-bone-shaped specimen and 80.8 mm for the tabbed, straight-sided specimen. There is no technical reason for the modified specimen to be slightly longer, and the same test fixture can be used for both specimens. A photograph of the Modified ASTM D 695 fixture as commonly configured is shown in Figure 6.6. This version of the fixture was

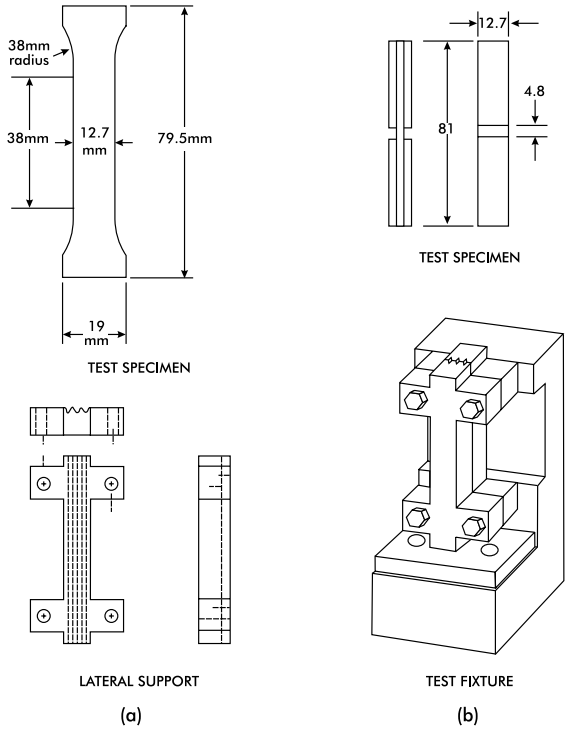

FIGURE 6.5
Sketches of ASTM D 695 and Modified D 695 compression test fixtures. (a) ASTM D 695 dog-bone-shaped compression test specimen and lateral supports [12]; (b) Modified D 695 straight-sided tabbed compression strength test specimen and loading fixture with integral lateral supports [13,14].

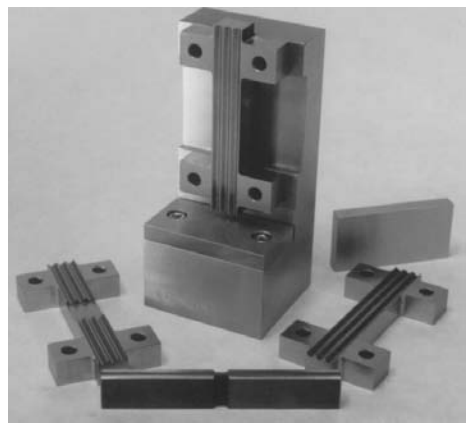

FIGURE 6.6
Photograph of a Modified D 695 compression test fixture with tabbed strength specimen and both strength and stiffness (cutout) lateral supports. (Photo courtesy of Wyoming Test Fixtures, Inc.)

adopted by the Boeing Company in 1982 [13], and subsequently published as a Recommended Method by SACMA in 1989 [14]. ASTM has given no indication of adding this configuration to their existing standard, or making it a new standard. It was, in fact, evaluated during the same round-robin testing at the time the IITRI and sandwich beam flexure test methods were being considered for ASTM standardization, and was not recommended [18].

Because the modified specimen was developed to test relatively thin laminae (typically an eight-ply unidirectional composite about 1 mm thick), it was necessary to keep the gage length (the unsupported central section between the tabs) short, to prevent gross (Euler) buckling. A gage length of 4.8 mm was adopted. There was concern among many potential users that the strength results obtained would be influenced by the close proximity of the tabs [19]. Because this gage length is also too short to permit the practical attachment of strain instrumentation (strain gages or extensometers), it is necessary to test a second, untabbed, specimen if compressive modulus is to be determined. An untabbed specimen can be used because only a fraction of the ultimate force need be applied to obtain sufficient data to establish a modulus (the slope of the initial portion of the stress–strain curve). A complete stress–strain curve to failure is thus not available when using this test method because the untabbed specimen will end crush if the loading becomes too high. In addition, because two tests rather than one must be performed, the total cost of testing is increased significantly.

Lateral supports without cutouts are used for the strength test, as shown in Figure 6.6. If a strain gage is used for the modulus test, a lateral support with a shallow cutout (such as that shown at the bottom of the photograph of Figure 6.6) is substituted. The cutout provides clearance for the strain gage. If back-to-back gages are used, two lateral supports with cutouts are needed. If an extensometer is used, it can be clipped onto either edge of the specimen, because the standard 12.7-mm-wide specimen is slightly wider than the central portion of the lateral support. In this case, a lateral support with a cutout is not needed. The recess in the back of the base provides additional clearance for the body of the extensometer.

Another problem with the Modified ASTM D 695 fixture (Figure 6.4) is the potential introduction of a redundant load path. This occurs when the fixture screws are tightened to press the lateral supports against the specimen. Friction between the specimen and lateral supports provides the redundant load path, which results in both apparent strength and modulus determinations that are higher than the actual values. The error introduced is proportional to the degree of tightening of the screws. The Boeing [13] and SACMA [14] procedures call for the screws to be torqued to from 0.68 to 1.13 N·m and 0.57 to 1.13 N·m, respectively, which is not much more than finger tight. However, it is not uncommon for considerably higher torques to be used, with corresponding increases in the induced error [7]. Many users of the fixture apparently do not realize the negative consequence of increasing the torque. It perhaps is intuitive that because the purpose of the lateral

supports is to prevent buckling, the tighter they are clamped against the specimen the better.

Despite these various disadvantages and limitations, the Modified ASTM D 695 test method was very popular during the 1990s. The fixture is compact, lightweight, relatively inexpensive, and comparatively easy to use. However, its use is now waning, both because of the limitations discussed above and the introduction of improved fixtures, such as the Wyoming Combined Loading Compression (CLC) test method [20,21], which is now an ASTM standard [15].

6.3 Combined Loading Compression (CLC) Test Methods

The early concept of combined loading apparently evolved from the desire to eliminate end crushing of end-loaded compression specimens. The Royal Aircraft Establishment (RAE) test method developed in the early 1970s utilized a straight-sided specimen, adhesively bonded into a slot in an aluminum block at each end [22]. The adhesive transmitted a portion (perhaps on the order of 20%) of the applied loading via shear through the adhesive into the specimen faces. (To further minimize end crushing, the specimen was also thickness-tapered in the gage section to reduce the cross-sectional area.) Although acceptable results were provided, the concept did not become very popular, and was never standardized. The requirement to clean up the aluminum blocks for reuse, and the specification of thickness tapering, were definite drawbacks of the test method.

More recently, a new CLC test method was standardized as ASTM D 6641 [15]. It was developed at the University of Wyoming [20,21] to combine the best features of shear loading and end loading, and minimize the deficiencies of each. In addition, acknowledging the difficulties of successfully testing highly orthotropic, strong composite materials, it promotes the testing of cross-ply laminates and then backing out the unidirectional lamina strength using classical lamination theory, as will be discussed in Section 6.7.

A sketch of the test fixture is presented in Figure 6.7, and a photograph is shown in Figure 6.8. The shear-loading component is achieved by clamping pairs of lateral support blocks, which have high-friction contact surfaces, to each end of the specimen. The end-loading component is induced directly because each end of the specimen is flush with the outer surfaces of the support blocks. The ratio of shear loading to end loading can be controlled by varying the torque in the clamping screws. The goal is to achieve just enough shear loading to avoid end crushing of the specimen. Because the fixture grip surfaces contain relatively small tungsten carbide particles, they do not significantly penetrate and damage the specimen surfaces. Combined with the fact that the through-the-thickness clamping forces on the specimen do not have to be very high, it is typically possible to test an untabbed, straight-sided specimen. This simplifies specimen preparation considerably.

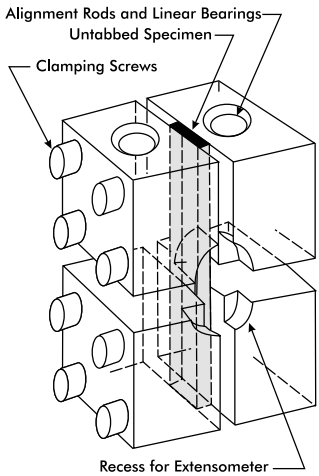

FIGURE 6.7
Sketch of Wyoming CLC test fixture.

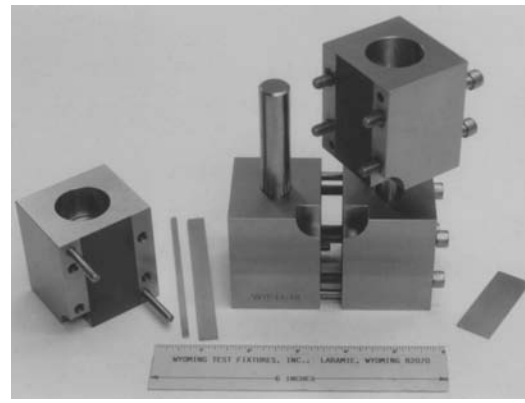

FIGURE 6.8
Photograph of a partially assembled Wyoming CLC test fixture, with specimen centering strips. (Photo courtesy of Wyoming Test Fixtures, Inc.)

Compared to the IITRI (shear-loaded) test method, the clamping forces on the ASTM D 6641 specimen are much less, thus inducing lower stress concentrations. Because no specimen tabs are used, the stress concentrations associated with geometric discontinuities are minimized. Compared to the Modified ASTM D 695 (end-loaded) test method, tabs are not needed for ASTM D 6641 because only a (controlled) portion of the total applied load is end loading. In addition, there is no redundant load path in the fixture because there is a gap between the upper and lower pairs of support blocks, which are maintained in alignment by posts and linear bearings (similar to the IITRI fixture). The Wyoming CLC fixture is a relatively simple fixture, comparable in weight and cost to the Modified ASTM D 695 fixture [16].

Cross-ply, angle-ply, quasi-isotropic lay-up, and similar laminate forms can all be readily tested using an untabbed specimen. However, data obtained by testing such laminates, and then indirectly determining unidirectional lamina properties, is sometimes not accepted by the potential user. However, testing untabbed, straight-sided specimens of highly orthotropic, high compressive strength, unidirectional composites using the CLC fixture does present some problems. Relatively high clamping forces may be required to prevent end crushing [21,23]. This induces stress concentrations, which are undesirable. Tabs can be used to increase the end-loading area (as for the Modified ASTM D 695 test method) and thus reduce the clamping force (shear-loading component) required, but tabs induce stress concentrations because of the geometric discontinuity created [24,25].

A viable solution to the above problems is the use of an untabbed, straight-sided, thickness-tapered specimen, such as that shown in Figure 6.9. This thickness tapering is conceptually similar to that used with the RAE specimen

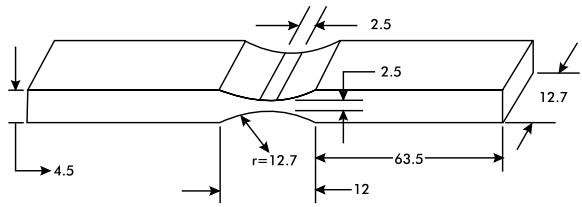

FIGURE 6.9
Sketch of a typical thickness-tapered compression test specimen (dimensions in mm).

years ago [22]. However, greatly improved machining techniques and an enlightened composites community (which is now more willing to permit machining of the as-cured surfaces of composites) makes thickness tapering much more acceptable today. Although thickness tapering of a CLC specimen is not yet part of ASTM D 6641, results published in the literature [23,26,27] are very encouraging. These studies have also suggested that thickness tapering a specimen is no more difficult or time consuming than tabbing a specimen, thus minimizing this potential concern.

6.4 Compression Test Procedures

The three compression test methods emphasized in this chapter require certain test procedures that are common to all three, as will be outlined in this section. The general aspects of test specimen preparation are discussed in Chapter 4.

Proper alignment of the testing machine, and of the associated test fixture relative to the machine, is particularly important for compression loading, considering the stability (buckling) issues involved. Any misalignment can induce bending of the specimen and promote buckling. The use of a spherical seat platen or other alignment device in the load train is sometimes encouraged to accommodate misalignments. However, a more positive approach is to achieve proper alignment by careful checking and adjusting of the test setup prior to beginning testing [21]. Specimen bending and buckling cannot usually be detected visually during the test, or by microscopic examination of the failed specimen [14]. As discussed in the various standards, the use of two strain gages, mounted on the faces perpendicular to the minimum thickness of the specimen in the gage section, is the only reliable method of detecting bending and buckling. Although some bending can be tolerated, buckling cannot. The governing standards [8,15] specify an acceptable bending limit of 10%, although Reference [21] suggests that greater amounts of bending, as much as even 20 or 30%, may not be detrimental.

A significant source of potential problems is in the specimen. It is obvious that the specimen should be checked for proper fiber alignment, particularly

for an axial test of a unidirectional composite lamina, because composite strength and modulus decrease rapidly with off-axis loading. Fiber alignment within ±1° is attainable if sufficient attention is given to mutual alignment of the individual plies of prepreg and the establishment of a visible reference axis during laminate fabrication [28]. A few fiber threads of a contrasting color, e.g., glass fibers in a carbon–fiber composite, can be inserted during prepreg manufacture to assist in attaining alignment. As a final check after the unidirectional composite is cured, the sample is fractured along the fiber direction. A clean break indicates that the individual plies are well aligned. This edge can also serve as a reference axis when individual specimens are cut from the composite. If a clean break is not obtained, the panel should be remade.

The ends of end-loaded and combined-loading specimens must be flat, mutually parallel, and perpendicular to the specimen axis. Specified parallel and perpendicular tolerances are typically on the order of 0.03 mm. Specimen end flatness is particularly important, so that the loading is introduced along the central axis of the specimen and local end crushing, which is likely to occur if uniform contact is not achieved, is avoided. Particularly for composites containing high-stiffness, relatively brittle fibers, such local crushing may then propagate throughout the specimen, negating the test results. Lower-stiffness, ductile fibers (e.g., Kevlar [E.I. du Pont de Nemours and Company, Wilmington, DE], Spectra [Allied Chemical Company, Petersburg, VA], and other organic fibers) are much more tolerant of specimen end-flatness irregularities.

Uniform specimen thickness from end to end is also important. It is not uncommon for composite panels to have a taper from side to side or end to end, induced by poor alignment of the curing platens or caul plates during panel fabrication. This nonuniformity can result in loading misalignments when specimens are subsequently prepared and tested. Uniformity of specimen thickness from end to end within 0.06 mm is commonly specified [15].

Whenever specimen tabs are used, many additional sources of error exist. Just as for specimen thickness, variations in thickness of any of the tabbing strips can occur, along with variations in thickness of the adhesive bond lines. Not just end-to-end variations, but also differences in thickness of the tab and adhesive components on one side of the specimen relative to those on the other, are important. Symmetry must be maintained to achieve uniform axial loading.

In all cases the specimen should fail in the gage section. Unfortunately, failure often occurs at the very end of the gage section. This is due to the unavoidable stress concentrations induced in these regions by the tabs (if used), grips, or lateral supports. Thus, although undesirable, such failures are commonly accepted [8,14,15,21].

The general test procedure is summarized as follows:

1. Examine each individual specimen for fabrication and material defects, and either note the nature and severity of the defect, or discard the specimen if deemed necessary.

2. Carefully measure and record the critical dimensions of each specimen (overall length, gage length, width, thickness) and verify that the specified parallelism, perpendicularity, and flatness requirements are met. Reject all out-of-tolerance specimens.
3. Attach electrical resistance strain gages, if they are required, and verify that the quality of the gage installation is acceptable.
4. Align the specimen in the test fixture, verifying that the fixture itself is clean, properly lubricated, and undamaged.
5. Mount the fixture in the testing machine.
6. Set and record the required load range and specified loading rate of the testing machine.
7. Initiate the test and manually record data or confirm that the automated data acquisition system is functioning properly.
8. During the test, using suitable eye protection, and a transparent shield surrounding the specimen if deemed necessary, carefully observe the specimen for indications of end crushing, tab debonding, and other anomalies. Note any anomalies and also the observed failure mode.
9. Verify that the test results and failure mode are reasonable before proceeding to test the next specimen. Suspend testing and identify and correct any suspected problems.

6.4.1 IITRI Test Procedure (ASTM D 3410)

Many of the existing IITRI fixtures have serrated or knurled grip faces that are relatively aggressive. In such cases, the use of tabs is essential to protect the specimen surfaces. ASTM D 3410 does not require a specific type of grip surface. Some newer fixtures have thermal-sprayed surfaces (tungsten carbide particles imbedded in the grip surfaces), typically producing a roughness equivalent to only about 100-grit emery cloth or less. In these cases it may be possible to use untabbed specimens. However, because of the high clamping forces, some type of cushion, such as bonded (or unbonded) tabs or softer pads, is commonly used.

Because of the massiveness of the IITRI test fixture, its main components normally remain in the testing machine. During specimen installation, just the grips are removed. The specimen is mounted in these grips, the assembly is placed back in the cavity in the lower block of the fixture (Figures 6.3 and 6.4), and then the upper block (which is attached to the crosshead) is lowered to engage the upper grips (and the alignment rods).

Because the sloping surfaces of the wedge grips make their handling awkward during specimen installation, it is convenient to use some type of installation jig when mounting the specimen in the grips. This aids in properly aligning the specimen in the grips. Two different methods of maintaining alignment are discussed in ASTM D 3410 [8].

6.4.2 Modified ASTM D 695 Test Procedure (SACMA SRM-1)

The Modified ASTM D 695 test fixture is compact, weighing only about 2 kg, and thus is easily handled (Figure 6.6). During use, its base rests on a flat platen in the base of the testing machine. A second flat platen mounted in the crosshead is used to apply load to the upper end of the specimen, which extends approximately 3 mm above the lateral supports. Because the fixture is not directly attached to the testing machine, it can be readily moved to a bench for specimen installation.

It is important that the specimen be axially aligned in the fixture. This is typically achieved visually, using the edges of the lateral supports as a guide. Special alignment jigs have also been developed [13,16], but are not commonly used.

As previously discussed in Section 6.2, it is important that the clamping screws be torqued only to the level specified in the governing standard (0.57 to 1.13 N·m), to avoid the development of a significant friction effect through the redundant load path.

During the strength test (for which tabs are used) it is important to watch for specimen end crushing, possibly induced by debonding of one or more of the tabs, which would invalidate the test. This can occur if the wrong combination of tab material, tab thickness, and adhesive in conjunction with the specific composite material being tested is used. If the tabs are too stiff or too thick relative to the test specimen, they will carry too high a percentage of the applied force and will either end crush or debond. If the tabs are too compliant or too thin, the specimen will end crush. The proper ratios are typically determined experimentally.

6.4.3 CLC Test Procedure (ASTM D 6641)

The CLC test fixture, like the Modified ASTM D 695 compression test fixture, is compact, relatively lightweight (5.5 kg), and is not attached to the testing machine. It rests on a flat platen and is loaded by a second flat platen mounted in the crosshead of the testing machine. The entire fixture can be moved to a bench for specimen installation.

To install a specimen, the two halves of the fixture are separated and the eight socket-head cap screws (Figures 6.7 and 6.8) are loosened sufficiently to permit insertion of the (typically untabbed, straight-sided) specimen from one end of the lower half. Two uniform-width metal strips are provided with the standard fixture [16,21]: the wider strip is used with 12.7-mm-wide specimens, and the narrower strip is used with 25.4-mm-wide specimens. Additional strips can be fabricated as required for specimens of other nominal widths. Indexing pins are provided in the lower half of the fixture, and the appropriate strip is inserted between these pins and the specimen to center the specimen while the four fixture screws are being tightened sufficiently to hold it in position. The outer end of the specimen should be flush with the end of the fixture. This can be achieved easily by performing the

installation on a flat surface. The centering strip is then removed and the upper half of the fixture is mated with the lower half, which is aligned automatically by the fixture posts and bearings. With the upper end of the specimen flush with the end of the upper fixture half, the four screws are tightened sufficiently to hold the assembly in position.

The assembly can then be placed on its side, with the screws facing up, and all eight screws tightened to the desired final torque level, in several increments using a controlled tightening pattern, so that the clamping forces on the specimen are distributed as uniformly as possible on each end. The desired torque level is that just sufficient to prevent end crushing of the specimen. Excessive torquing increases the detrimental clamping stress concentrations and provides no positive benefit. It has been found that, for most composite materials, torques on the 1/4-in. diameter, 28 threads/inch screws of the standard fixture on the order of 2.3 to 2.8 N·m are adequate [15,21]. This is a low torque, resulting in low clamping stress concentrations relative to, for example, the IITRI fixture, in which the clamping forces cannot be controlled.

6.5 Failure Modes

Some typical failure modes are sketched in Figure 6.10. As already noted, gross buckling (Figure 6.10(d)) is unacceptable. However, the other failure modes are typically accepted. Extensive descriptions of such failure modes are presented in Reference [14]. ASTM D 3410 [8] also characterizes acceptable and unacceptable modes.

As previously discussed, the only reliable way of detecting gross buckling is by the use of back-to-back strain gages. This is illustrated in Figure 6.11.

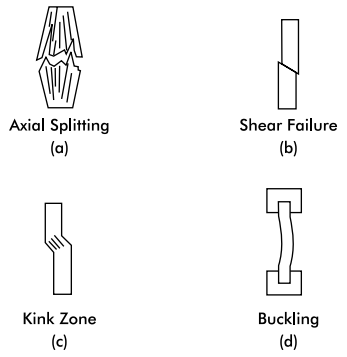

FIGURE 6.10
Typical failure modes for compression specimens.

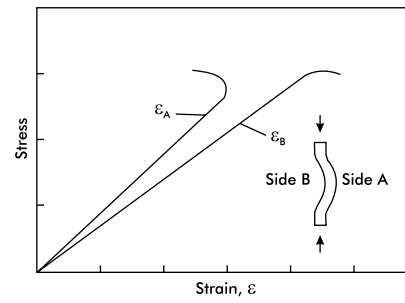

FIGURE 6.11
Schematic of compressive stress–strain responses for back-to-back strain-gaged specimen that failed by Euler buckling.

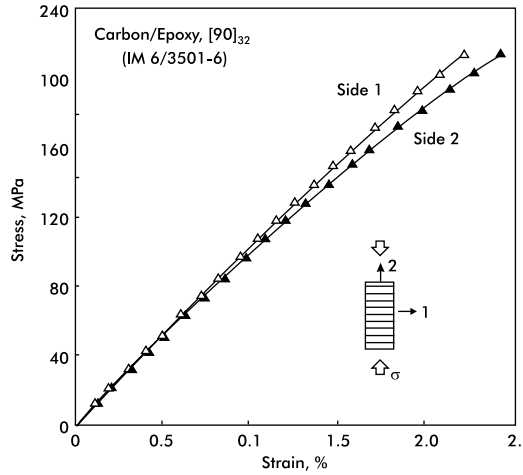

FIGURE 6.12
Compressive stress–strain response for a back-to-back strain-gaged $[90]_{32}$ carbon/epoxy specimen loaded uniformly.

At the applied stress level at which the specimen buckles, the strains suddenly diverge. Divergence of the strain readings prior to this level (also shown in Figure 6.11) is an indication of specimen bending.

The kink band formation indicated in Figure 6.10(c) is due to a local instability at the fiber level when the lamina is axially loaded. It progresses from elastic deflections of the fibers to actual fiber fractures, as indicated in Figure 6.1.

In contrast, when a unidirectional lamina is loaded transversely, a shear failure is typical, such as indicated in Figure 6.10(b). Figure 6.2 indicates an alternate form of this shear failure mode. The corresponding stress–strain curves for a transversely loaded specimen are shown in Figure 6.12.

6.6 General Data Reduction

One can plot the load vs. strain data, for each gage if back-to-back gages are used, and examine the plots for global buckling or excessive bending (Figure 6.11). To determine the compressive moduli, recall the definitions of Chapter 2:

- E_1: The initial slope of the stress–strain curve ($\Delta\sigma_1/\Delta\varepsilon_1$) for the 0° compressive test
- E_2: The initial slope of the stress–strain curve ($\Delta\sigma_2/\Delta\varepsilon_2$) for the 90° compressive test

Each modulus is thus evaluated from the initial slope of the average response curve, which can be obtained, for example, by using a linear least-squares regression fit of the data. If plots from two gages are available, the reported modulus is the average of the two values obtained. The various standards outline specific procedures in detail. The ultimate stresses, X_1^c and X_2^c, are obtained directly from the plots, whereas the ultimate strains, e_1^c and e_2^c, are taken as the average of the two values obtained, if two plots are available. Figures 6.13–6.16 show examples of compressive responses for various composites.

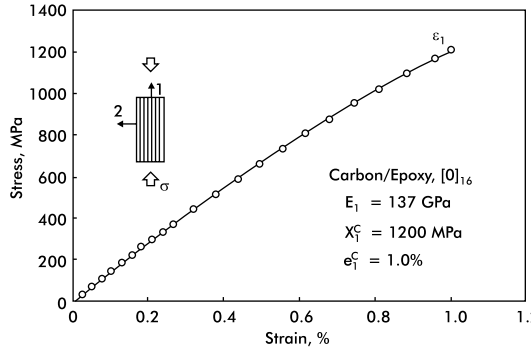

FIGURE 6.13
Compressive stress–strain response for a $[0]_{16}$ carbon/epoxy specimen.

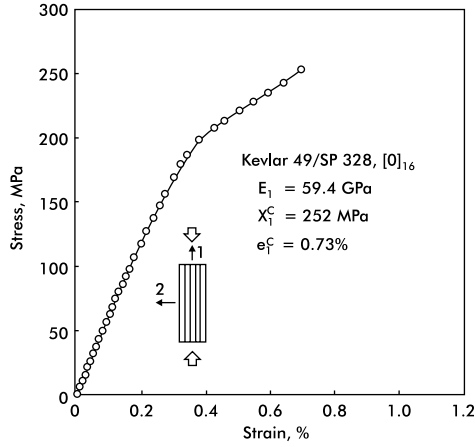

FIGURE 6.14
Compressive stress–strain response for a $[0]_{16}$ Kevlar/epoxy specimen.

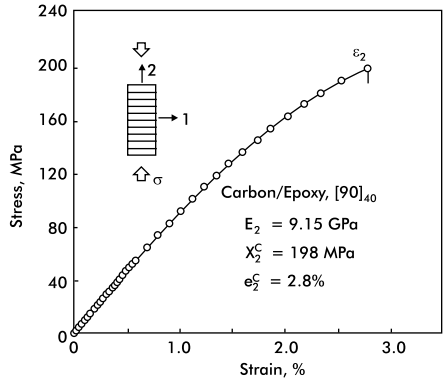

FIGURE 6.15
Compressive stress–strain response of a $[90]_{40}$ carbon/epoxy specimen.

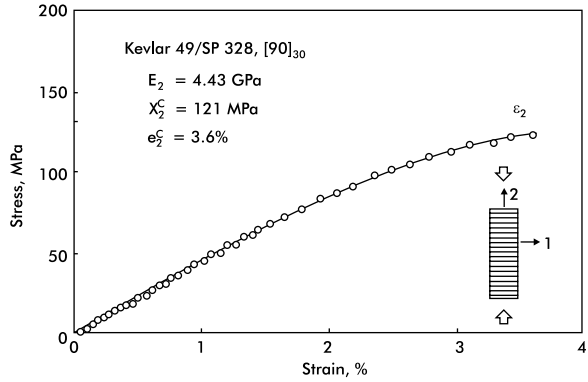

FIGURE 6.16
Compressive stress–strain response for a $[90]_{30}$ Kevlar/epoxy specimen.

6.7 Indirect Determination of Unidirectional Lamina Strength from a Test of a Cross-Ply Laminate

In the early 1990s, considerable interest developed in the possibility of compression testing a general laminate of arbitrary lay-up orientation, but containing some 0° plies, and then indirectly determining the strength of these 0° plies using a suitable analysis [29]. That is, the compressive strength of a unidirectional composite is estimated by multiplying the measured compressive strength of the chosen laminate by a factor (the back-out factor [BF]) calculated using the stiffness properties of the unidirectional material and classical lamination theory as applied to the chosen laminate.

Although initial attempts were made to indirectly determine strengths from both tensile and compressive tests, emphasis soon focused on compressive strength. This was in part because the determination of compressive strength directly from unidirectional composite specimen tests was considered to be much more difficult, and the accuracy of the results much more uncertain. In addition, these initial studies indicated that backing-out tensile strength might not work as well. Although backing-out tensile strength may eventually prove to be viable, insufficient additional study has been conducted to date to make this determination.

In the meantime, major progress has been made in determining compressive strengths. In fact, the Wyoming CLC test method and fixture presented in Sections 6.3 and 6.4.3 were developed specifically for this purpose.

Although a wide range of both cross-ply and angle-ply laminates were initially considered, it was soon realized that using a simple $[90/0]_{ns}$ cross-ply laminate has significant advantages. In particular there is no shear coupling between plies (see Chapter 2), eliminating the need to predetermine the lamina shear stiffness in calculating the BF. The lack of shear coupling also reduces the degree of nonlinearity of the laminate response [30], permitting the use of a much simpler linear analysis such as classical lamination theory (Chapter 2). The use of a $[90/0]_{ns}$ rather than a $[0/90]_{ns}$ laminate is deliberate, the 90° plies on the surfaces tending to protect the immediately adjacent 0° plies from fixture- and tabbing-induced stress concentrations. Of course, as n becomes larger, the importance of protecting these 0° plies next to the surface becomes less important because they become a smaller percentage of the total number of primary load-bearing plies (i.e., 0° plies) present.

The BF for a $[90/0]_{ns}$ cross-ply laminate (or a $[0/90]_{ns}$ laminate) is [21,30]

$$BF = \frac{\frac{1}{2}E_1\left(E_1 + E_2\right) - \left(\nu_{12}E_2\right)^2}{\frac{1}{4}\left(E_1 + E_2\right)^2 - \left(\nu_{12}E_2\right)^2} \tag{6.1}$$

where E_1 and E_2 are the axial and transverse stiffnesses of the unidirectional lamina, respectively, and ν_{12} is the major Poisson's ratio of the unidirectional lamina. These three stiffness properties must be determined from axial (E_1,ν_{12}) and transverse (E_2) compression tests of a unidirectional composite. This is not a difficulty, however, because the composite does not have to be loaded to high stress levels to determine these stiffness properties.

Note that the BF in Equation (6.1) will typically not be very sensitive to ν_{12} because its value (on the order of 0.25) is small and $E_2 < E_1$. That is, the second terms in the numerator and denominator will be small relative to the first terms. In addition, because $E_2 < E_1$, BF is less sensitive to E_2 than to E_1. This latter point is significant because a transverse compression stress–strain plot is typically slightly nonlinear and thus, in principal, E_2 should be measured at failure [30]. But achieving a full transverse compression stress–strain curve to failure can be difficult, particularly for brittle-matrix composites. There is a tendency for premature failure of the unidirectional composite caused by

stress concentrations at specimen edges and in the grip regions, nonuniform loading caused by induced bending, either in plane or out of plane, and other testing anomalies. Because the BF is not extremely sensitive to the transverse stiffness, the initial (linearly elastic) transverse stiffness can usually be used with little introduced error [30].

Equation (6.1) is thus relatively easy to implement in backing out the 0° lamina compressive strength from the results of a test of a $[90/0]_{ns}$ cross-ply laminate. Again using classical lamination theory, corresponding equations can be derived for other types of laminates as well [21,30].

6.8 Summary of Compression Test Methods

Of the many compression test methods for use with composite materials in existence, only three have been detailed here. These represent the most viable of each of the three common loading modes, and the three most commonly used.

The IITRI fixture is the oldest of the three, and perhaps the best known. However, it is commonly used in conjunction with tabbed specimens, which are known to induce stress concentrations [24,25] and thus reduce measured strengths. The need for tabs also increases the specimen preparation cost significantly. The typical IITRI fixture is massive and expensive. For these reasons it is likely that the use of the IITRI fixture will decrease in coming years.

The Modified ASTM D 695 fixture was popular during the last decade because of its small size and relatively low fabrication cost. However, because of the need to perform two separate tests if both modulus and strength are to be determined (the other two methods achieve both measurements in a single test), most if not all of this fixture cost advantage is lost. In addition, a complete stress–strain curve to failure is never achieved. Because it requires a tabbed specimen for measuring strength, it suffers the same disadvantage as the IITRI fixture, i.e., induced stress concentrations and increased specimen preparation cost. Unlike the other two fixtures, the Modified ASTM D 695 fixture also introduces a redundant load path, which can lead to erroneously high measured strength and modulus values if the clamping screw torques utilized are too high.

The CLC test fixture is relatively compact and inexpensive to fabricate. Although the CLC fixture can be used with tabbed specimens, it is designed specifically for untabbed, straight-sided specimens, which offers major testing time, cost, and performance advantages relative to the other two test methods. Like the IITRI fixture, there is no redundant load path to consider. Of course, a major advantage of the CLC fixture is the ability to control the ratio of end-to shear-loading, thus employing the favorable attributes of both of these alternate test methods. For these reasons, it is likely that use of the CLC test method will eventually dominate that of the other two compression test methods.

References

1. B.W. Rosen, Mechanics of composite strengthening, in *Fiber Composite Materials*, ASTM International, Metals Park, OH, 1965.
2. A.G. Evans and W.F. Adler, Kinking as a mode of structural degradation in carbon fiber composites, *Acta Metall.*, 26(5), 725–738, 1978.
3. N.A. Fleck, Compressive failure of fiber composites, *Adv. Appl. Mech.*, 33, 43–117, 1977.
4. E.M. Odom and D.F. Adams, Failure modes of unidirectional carbon/epoxy composite compression specimens, *Composites*, 21(4), 289–296, 1990.
5. D.W. Wilson and L.A. Carlsson, Mechanical characterization of composite materials, in *Physical Methods of Chemistry*, 2nd ed., John Wiley & Sons, New York, 1991, pp. 139–221.
6. S.N. Chatterjee, D.F. Adams, and D.W. Oplinger, *Test Methods for Composites – A Status Report, Vol. II: Compression Test Methods*, Report DOT/FAA/CT-93/17-II, FAA Technical Center, Atlantic City International Airport, NJ, June 1993.
7. J.S. Welsh and D.F. Adams, Current status of compression test methods for composite materials, *SAMPE J.*, 33(1), 35–43, 1997.
8. ASTM Standard D 3410-95, *Compressive Properties of Polymer Matrix Composite Materials with Unsupported Gage Section by Shear Loading*, American Society for Testing and Materials, West Conshohocken, PA, 2001.
9. I.K. Park, Tensile and Compressive Test Methods for High-Modulus Graphite Fibre-Reinforced Composites, *Proceedings of the International Conference on Carbon Fibres, Their Composites, and Applications*, Paper No. 23, The Plastics Institute, London, April 1971.
10. K.E, Hofer, Jr., and P.N. Rao, A new static compression fixture for advanced composite materials, *J. Test. Eval.*, 5(4), 278–283, 1977.
11. ASTM Standard D 5467-97, *Compressive Properties of Unidirectional Polymer Matrix Composites Using a Sandwich Beam*, American Society for Testing and Materials, West Conshohocken, PA, 2001.
12. ASTM Standard D 695-96, *Compressive Properties of Rigid Plastics*, American Society for Testing and Materials, West Conshohocken, PA, 2001.
13. Boeing Specification Support Standard BSS 7260, *Advanced Composite Compression Tests*, The Boeing Company, Seattle, WA (originally issued February 1982, revised December 1988).
14. SACMA Recommended Method SRM 1-94, *Compressive Properties of Oriented Fiber-Resin Composites*, Suppliers of Advanced Composite Materials Association, Arlington, VA (originally issued April 1989, revised 1994).
15. ASTM Standard D 6641-01, *Determining the Compressive Properties of Polymer Matrix Composite Laminates Using a Combined Loading Compression (CLC) Test Fixture*, American Society for Testing and Materials, West Conshohocken, PA, 2001.
16. *High Performance Test Fixtures*, Product Catalog No. 106, Wyoming Test Fixtures, Inc., Laramie, WY, 2000 (*also,* www.wyomingtestfixtures.com).
17. D.F. Adams and E.W. Odom, Influence of test fixture configuration on the measured compressive strength of a composite material, *J. Compos. Technol. Res.*, 13(1), 36–40, 1991.

18. N.R. Adsit, Compression testing of graphite/epoxy, in *Compression Testing of Homogeneous Materials and Composites*, ASTM Spec. Tech. Publ. 808, R. Chait and R. Papirno, Eds., American Society for Testing and Materials, West Conshohocken, PA, 1983, pp. 175–196.
19. M.A. Smoot, *Compressive Response of Hercules AS1/3501-6 Graphite/Epoxy Composites*, Report CCM-82-16, Center for Composite Materials, University of Delaware, Newark, DE, June 1982.
20. D.F. Adams and J.S. Welsh, The Wyoming combined loading compression (CLC) test method, *J. Compos. Technol. Res.*, 19(3), 123–133, 1997.
21. P.M. Wegner and D.F. Adams, *Verification of the Combined Load Compression (CLC) Test Method*, Report No. DOT/FAA/AR-00/26, Federal Aviation Administration Technical Center, Atlantic City, NJ, August 2000.
22. P.D. Ewins, *Tensile and Compressive Test Specimens for Unidirectional Carbon Fiber Reinforced Plastics*, Technical Report 71217, Royal Aircraft Establishment, Farnborough, U.K., November 1971.
23. S.L. Coguill and D.F. Adams, Use of the Wyoming Combined Loading Compression (CLC) Fixture to Test Unidirectional Composites, *Proceedings of the 44th International SAMPE Symposium*, Long Beach, CA, Society for the Advancement of Material and Process Engineering, Covina, CA, May 1999, pp. 2322–2331.
24. S.C. Tan and M. Knight, An extrapolation method for the evaluation of compression strength of laminated composites, in *Compression Response of Composite Structures*, ASTM Spec. Tech. Publ. 1185, S.E. Groves and A.L. Highsmith, Eds., American Society for Testing and Materials, West Conshohocken, PA, 1994, pp. 323–337.
25. D.F. Adams, Tabbed vs. untabbed fiber-reinforced composite compression specimens, in *Composite Materials: Testing, Design, and Acceptance Criteria*, ASTM Spec. Tech. Publ. 1416, A.T. Nettles and A. Zureick, Eds., American Society for Testing and Materials, West Conshohocken, PA, 2002.
26. D.F. Adams and G.A. Finley, Experimental study of thickness-tapered unidirectional composite compression specimens, *Exp. Mech.*, 36(4), 348–355, 1996.
27. G.A. Finley and D.F. Adams, *An Analytical and Experimental Study of Unidirectional Composite Thickness-Tapered Compression Specimens*, Interim Report, Grant 94-G-009, Federal Aviation Administration Technical Center, Atlantic City, NJ; Report UW-CMRG-R-95-101, Composite Materials Research Group, University of Wyoming, Laramie, WY, January 1995.
28. D.F. Adams and E.M. Odom, Influence of specimen tabs on the compressive strength of a unidirectional composite material, *J. Compos. Mater.*, 25(6), 774–786, 1991.
29. L.J. Hart-Smith, Backing-out composite lamina strengths from cross-ply testing, Chapter 5.07 of Volume 5 (L.A. Carlsson, Ed.) in the series, *Comprehensive Composite Materials*, A. Kelly and C. Zweben, Eds., Elsevier Science, Oxford, U.K., 2000, pp. 149–161.
30. J.S. Welsh and D.F. Adams, Unidirectional composite compression strengths obtained by testing cross-ply laminates, *J. Compos. Technol. Res.*, 18(4), 241–248, 1996.

7

Lamina Shear Response

A shear test of a composite material is performed to determine the shear modulus or shear strength, or both. Ideally, both properties can be determined from the same test, but this is not always the case. In addition, the shear response of a composite material is commonly nonlinear, and full characterization thus requires generating the entire shear stress–strain curve to failure. However, many shear test methods are not capable of generating the entire curve, and sometimes not even a portion of it. Figure 7.1 defines the in-plane shear stress, τ_{12} (and τ_{21}) and shear strain, γ_{12} (and γ_{21}). The other shear stress and strain components are defined accordingly. The in-plane shear modulus is denoted by G_{12}, and the shear strength by S_6. Additional definitions and notation are presented in Chapter 2.

The major deficiency of all existing shear test methods for composite materials is the lack of a pure and uniform state of shear stress in the test section. Thus, compromises have to be made. Although many shear test methods are described in the literature [1,2], only a relatively few are in common use.

In particular, the torsional loading of a thin-walled, hoop-wound tube will not be detailed here. Most discussions of shear testing start with the statement, "The torsional loading of a thin-walled tube produces a uniform state of shear stress, but…" Then some or all of the following negative aspects of tube testing are enumerated. Fabrication of the tube, which is typically hoop-wound using the filament winding process, requires special equipment and expertise. Fabrication of a tube with fibers oriented along the axis of the tube is even more difficult. In both cases the resulting tube is relatively fragile.

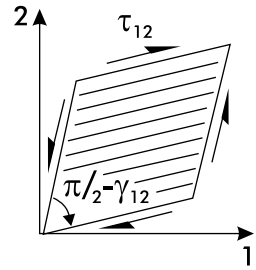

FIGURE 7.1
Definition of in-plane shear stress (τ_{12}) and shear strain (γ_{12}).

Equally important, a tube is usually not representative of the material form used in the eventual structural design. For example, because of the radical differences in the processes used to fabricate tubes vs. flat (or curved) panels or structural shapes in general, the material may not have the same strength properties. A torsional loading machine of sufficiently low torque capacity is required, and often not available. The tube specimen must be reinforced at each end in some manner so that it can be gripped within the torsion machine without damaging it. A hoop-wound tube in particular is very susceptible to inadvertent bending loads induced during testing because of nonaxial torsional loads. Any induced bending stresses combine with the shear stress to induce premature failure and thus low shear strength.

The five most popular current shear tests all happen to be ASTM standards. They include the Iosipescu shear test, ASTM D 5379 [3]; the two- and three-rail shear tests, ASTM D 4255 [4]; the $[\pm 45]_{ns}$ tension shear test, ASTM D 3518 [5]; and the short beam shear test, ASTM D 2344 [6]. These test methods are listed above in the order of their relative validity and versatility, and will be discussed in that order as well.

7.1 Iosipescu Shear Test Method (ASTM D 5379)

The Iosipescu shear test method and specimen configuration shown in Figure 7.2 are based on the original work with metals by Nicolai Iosipescu of Romania [7], from which the test method derives its name. The Composite Materials Research Group (CMRG) at the University of Wyoming led its application to composite materials [8,9]. The test method became an ASTM standard for composite materials in 1993 [3]. Analysis of the specimen under load reveals that a state of uniform shear stress exists in the center of the notched specimen on the cross section through the notches, although not in the immediate vicinity of the notch roots [9–11]. In addition, the normal stresses (the nonshear stresses) are low everywhere on this cross section. By orienting the specimen's longitudinal axis along any one of the three axes of material orthotropy, any one of the six shear stress components, representing the three independent shear stress components (see Chapter 2), can be developed.

For example, Figure 7.3 shows the required specimen orientations for measuring the two (nonindependent) in-plane shear stress components, τ_{12} and τ_{21}, for a unidirectional composite. However, note that a 0° orientation (fibers parallel to the long axis of the specimen) forms a much more robust specimen and is strongly preferred over a 90° orientation. A $[0/90]_{ns}$ (cross-ply) specimen is even more robust. Because there is no shear coupling between the plies of a $[0/90]_{ns}$ laminate (see Chapter 2), this orientation will theoretically produce the same shear properties as those of a unidirectional composite. In practice, it is likely to produce shear strengths closer to the

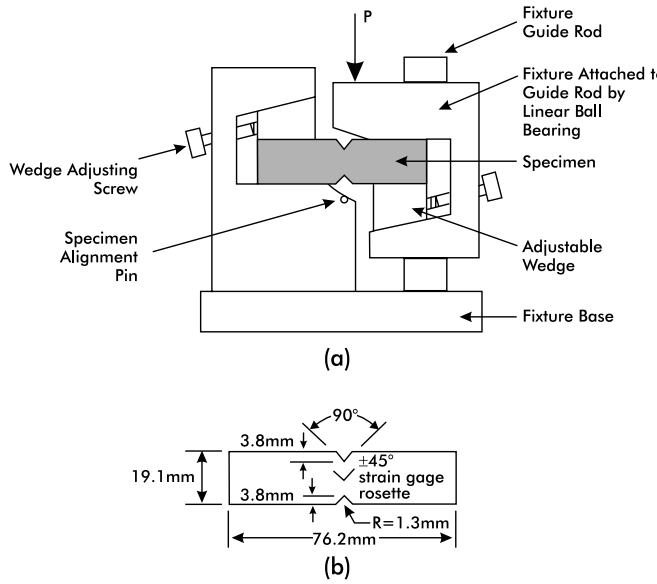

FIGURE 7.2
Sketches of (a) Iosipescu shear test fixture, and (b) test specimen.

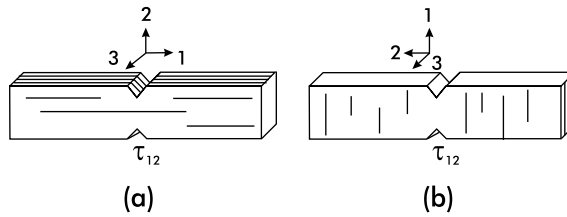

FIGURE 7.3
Iosipescu shear test specimens for in-plane shear testing: (a) 0° specimen, and (b) 90° specimen.

true shear strength of the composite material because premature failures are less likely to occur. That is, the cross-ply laminate is likely to produce more accurate (and in this case higher) shear strengths. However, note that presently, the 0° orientation unidirectional specimen is still much more commonly used, in part because a unidirectional laminate is more likely to be available for testing. This may change if the use of cross-ply laminates and back-out factors to determine unidirectional lamina compressive strength, as discussed in Section 6.7 of Chapter 6, increases in popularity.

When a strain gage is attached to one (or both) faces of the specimen in the central region between the notches, a complete shear stress–shear strain curve can be obtained. These attractive features, along with the relatively small specimen size and the general ease of performing the test, have made the Iosipescu shear test method very popular.

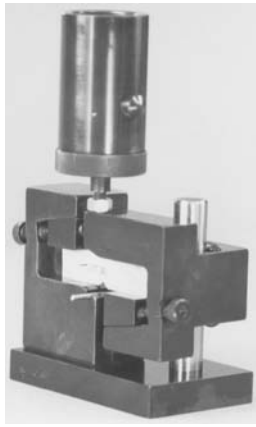

FIGURE 7.4
Photograph of an Iosipescu shear test fixture with specimen installed. (Photograph courtesy of Wyoming Test Fixtures, Inc.)

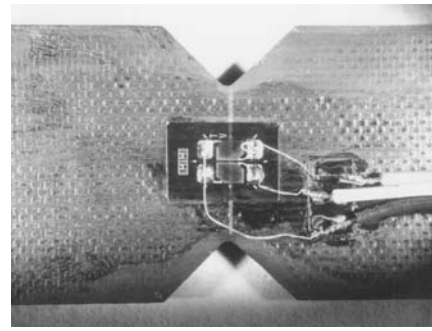

FIGURE 7.5
A ±45° biaxial strain gage rosette bonded to an Iosipescu shear test specimen.

The standard Iosipescu specimen is shown in Figure 7.2(b). The top and bottom edges must be carefully machined to be flat, parallel to each other, and perpendicular to the faces of the specimen, to avoid out-of-plane bending and twisting when the load is applied (see Figure 7.2(a)). The geometry of the notches is less critical [9]. The standard fixture, shown in Figure 7.4, can accommodate a specimen thickness up to 12.7 mm, although a thickness on the order of 2.5 mm is commonly used. For most composite materials it is convenient and economical to form the V-shaped notches using a shaped grinding wheel. The notch on one edge of a stack of specimens can be formed, the stack turned over, and the other notch formed.

If shear strain is to be measured, a two-element strain gage rosette with the elements oriented ±45° relative to the specimen longitudinal axis can be attached to the central test section region, such as shown in Figure 7.5, and the rosette wired in a half-bridge circuit. A single-element gage oriented at either plus or minus 45° can be used and wired in a quarter-bridge circuit, but this is not common practice. If out-of-plane bending and twisting of the specimen are a concern, back-to-back strain gages can be used to monitor these undesired effects [3,12]. However, this is normally not necessary.

The specimen should be centered horizontally in the test fixture using the specimen-centering pin (Figures 7.2(a) and 7.4). Vertical alignment is achieved by keeping the back face of the specimen in contact with the fixture while the wedge adjusting screws are finger-tightened to close any gap between the specimen and the fixture. Note that these wedges are not clamps and need not be tightened. They are provided to accommodate any tolerance in the width dimension of the specimen.

The upper half of the test fixture is loaded in compression through a suitable adapter, attaching it to the crosshead of the testing machine. The applied load and strain signals are monitored until the specimen fails.

The (average) shear stress across the notched section of the specimen is calculated using the simple formula

$$\tau = P/A \tag{7.1}$$

where P is the applied force, and A is the cross-sectional area of the specimen between the notches. For a unidirectional composite specimen tested in the 0° orientation, detailed stress analyses [9–12] indicate that an initially non-uniform elastic stress state exists. However, if any inelastic material response occurs, and particularly if there is initiation and arrested propagation of a crack parallel to the reinforcing fibers at each notch tip (which will occur well before the ultimate loading is attained), the local stress concentrations are significantly relieved. The stress distribution then becomes even more uniform across the entire cross section of the specimen, and increases further the accuracy of Equation (7.1).

Shear strain, γ, is simply calculated as the sum of the absolute values of the ±45° strain gage readings,

$$\gamma = |\varepsilon(45°)| + |\varepsilon(-45°)| \tag{7.2}$$

or, if only a single-element gage mounted at plus or minus 45° is used,

$$\gamma = 2|\varepsilon(45°)| \tag{7.3}$$

The shear modulus, G, is obtained as the initial slope of the shear stress–shear strain curve.

Premature damage in the form of longitudinal matrix cracks initiating from the notch roots is a common occurrence in 0° unidirectional specimens. Load decreases are observed at about two thirds of the eventual ultimate load when these cracks initiate and propagate, but they quickly arrest and the specimen then carries additional load until the true shear failure occurs, which involves multiple matrix cracks parallel to the fibers and concentrated in the region of the specimen between the two notches. Because 90° specimens often fail prematurely, particularly for brittle-matrix composites, as a result of stress concentrations and induced bending, they may not produce a representative failure stress. Figure 7.6 shows schematic stress–strain curves for unidirectional composites tested in the 90° and 0° directions. The 90° specimen usually fails suddenly, parallel to the fibers (Figure 7.7(a)). The 0°specimen fails in a more gradual manner. As noted, a small load decrease is often observed at approximately two thirds of the ultimate shear strength (Figure 7.6), because of cracking at the notch root, as indicated in Figure 7.7(b). Two decreases, relatively close to each other, will occur if the notch root cracks do not happen to occur simultaneously. These are stress-relieving mechanisms, as discussed above, and do not represent the shear strength. The stress that results in total failure across the test section, as shown in Figure 7.7(c), is the failure stress S_6. Figures 7.8 and 7.9 show typical

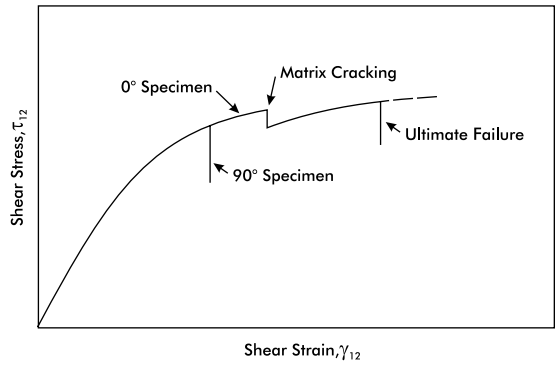

FIGURE 7.6
Schematic stress–strain curves for 0° and 90° Iosipescu shear test specimens.

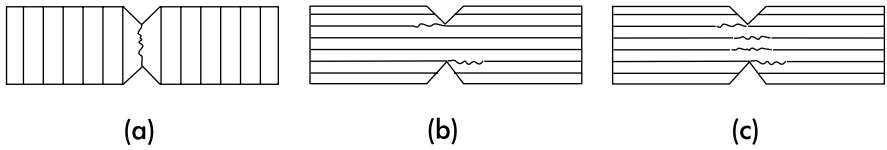

FIGURE 7.7
Failure modes of Iosipescu shear test specimens: (a) matrix cracking in a 90° specimen, and (b) and (c) matrix cracking in a 0° specimen.

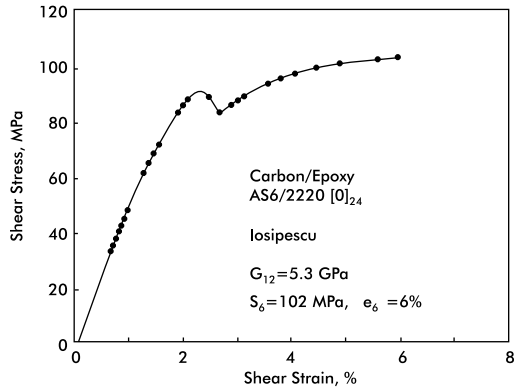

FIGURE 7.8
Shear stress–strain curve for a $[0]_{24}$ carbon/epoxy Iosipescu shear specimen.

stress–strain curves for 0° specimens of two different types of composite materials. Note that no load drop is evident in the shear stress–strain curve of Figure 7.9 because the polyphenylene sulfide (PPS) thermoplastic matrix is relatively ductile, relieving the local shear stress concentrations at the notch roots sufficiently to avert local failures. Additional examples of acceptable and unacceptable failure modes are presented in ASTM D 5379.

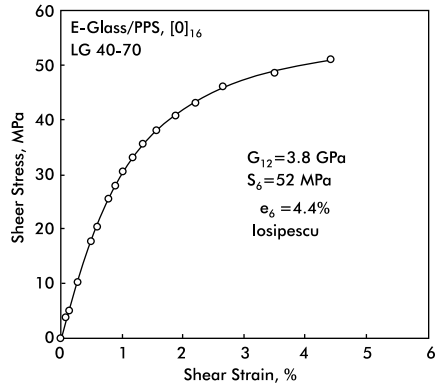

FIGURE 7.9
Shear stress–strain curve for a $[0]_{16}$ glass/PPS Iosipescu shear specimen.

7.2 Two-Rail Shear Test Method (ASTM D 4255)

This is an in-plane shear test method. Both the two- and three-rail shear tests are included in the same ASTM Standard D 4255 [4]. They will be discussed in separate sections here because they utilize different test fixtures and offer different advantages and disadvantages. Presently, these two test methods are used somewhat less frequently than the other three test methods. This is particularly true for the three-rail shear test method, for reasons to be discussed later. However, the two-rail shear test method is given a more prominent position in the present discussion because it has some very favorable technical attributes that the two test methods to be discussed next (the $[\pm 45]_{ns}$ tension shear and the short beam shear test methods) do not exhibit. That is, although presently it is not used as extensively as are the others, it has significant potential for future improvements and hence increased use.

The commonly used tensile-loading version of the two-rail shear test fixture is shown schematically in Figure 7.10(a). A compression-loading fixture also exists, but is not commonly used. The tensile-loading fixture has had a long history, and presumably is based on fixture designs originally developed even earlier (circa 1960) for the shear testing of plywood panels [13]. As a consequence, it contains some features that are not fully logical for use with composite materials. For example, note that in Figure 7.10(a), the specimen is loaded at a slight angle relative to its axis (indicated as 7° in ASTM D 4255). There does not appear to be a technical reason for this; rather, it is probably an artifact of a test fixture for plywood (ASTM 2719) developed in the early 1960s [14]. In that case, because of the type of loading apparatus used, it was convenient to apply the load to the large (610 × 430 mm) plywood test panel slightly off-axis.

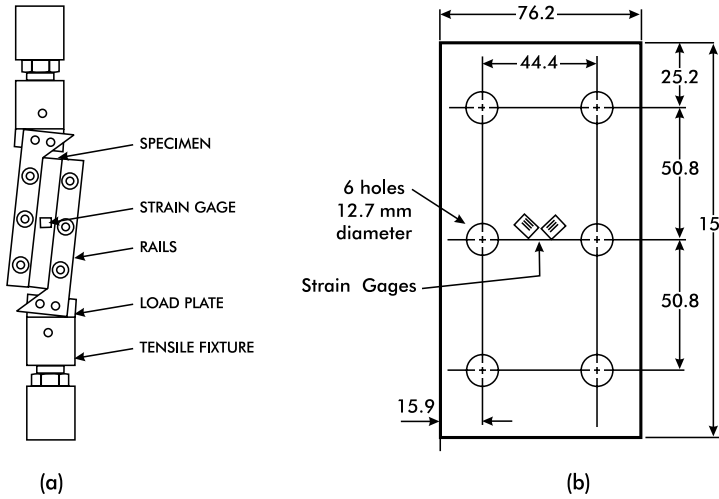

FIGURE 7.10
Two-rail shear test method: (a) fixture configuration, and (b) specimen geometry (all in mm).

The two-rail shear test specimen is shown in Figure 7.10(b). As indicated, the specimen is 76.2 × 152.4 mm, thus consuming eight times more test material than the Iosipescu shear specimen. Note also that there are six holes in the otherwise simple rectangular specimen. These are clearance holes for the six bolts that clamp the specimen to the rails. Not only do these holes potentially introduce stress concentrations in the test specimen, there is always some inherent concern about making holes in a composite material without introducing auxiliary damage. In addition, for very high shear strength composites the clamping forces have to be very high to avoid slipping of the rails during the test. A bolt torque of 100 N·m, which is a very high torque for the 9.5-mm-diameter bolts, is specified [4].

Despite these current deficiencies of the two-rail shear test method, there are distinct positive attributes of the method as well. The loading mode is actually much like that for the Iosipescu shear test method. That is, an essentially pure shear loading is applied to the gage section of the specimen (the 12.7-mm-wide portion of the specimen exposed between the rails). The shear stress along the length of the specimen (parallel to the rails) is relatively constant, except near the ends (which must be at a zero shear stress because they are free surfaces). Some extraneous normal (tensile and compressive) stresses are introduced by the presence of the rails, particularly near the boundaries of the gage section. Finite element analyses have been conducted to characterize these stresses [10,15], and undoubtedly specimen and fixture modifications can be made to significantly reduce, if not eliminate, them. Studies are currently in progress.

One previously stated advantage of the Iosipescu shear test method is the relatively small specimen size. Seemingly contradictory is the potential

advantage of the two-rail shear test fixture, which can test larger specimens. When coupons taken directly from large structural components are tested, it is sometimes desirable to test a specimen of a more representative size.

For all of the reasons discussed here, the two-rail shear test method holds promise for increased usage as some of the present deficiencies are eliminated. More details are presented in Reference [15].

When a two-rail shear test is conducted, the specimen must first be properly prepared, heeding in particular the cautions already noted regarding formation of the required six clearance holes in the specimen without introduction of auxiliary damage. When a unidirectional lamina is tested, the fibers can be oriented either parallel (90° orientation) or perpendicular (0° orientation) to the rails. However, a fiber orientation perpendicular to the rails is much preferred, because extraneous bending and edge effects have much less influence on the measured properties and the specimen is much more robust [15]. In fact, testing a $[0/90]_{ns}$ (cross-ply) laminate may be even better; the specimen is even more robust than a unidirectional lamina with fibers oriented perpendicular to the rails. Because there is no shear coupling between the plies of a $[0/90]_{ns}$ laminate (see Chapter 2), this orientation will theoretically produce the same shear properties as a unidirectional composite. In practice, it is likely to produce shear strengths closer to the true shear strength of the composite material because premature failures are less likely to occur. That is, the cross-ply laminate is likely to produce more accurate (and in this case higher) shear strengths. Note that this same general logic was stated in Section 7.1 with reference to the Iosipescu shear test specimen.

The specimen to be tested is clamped between the pairs of rails, as indicated in Figure 7.10(a). It is important that the rails do not slip during the test. If they do slip, the clamping bolts can bear against the clearance holes in the specimen, inducing local stress concentrations leading to premature failure. This, of course, results in an unacceptable test. Most currently available fixtures have thermal-sprayed tungsten carbide particle gripping surfaces [16], although ASTM D 4255 does not specifically require them. The thermal-sprayed surfaces generally have much better holding power than the other types of grip surfaces listed in the standard, as discussed in Reference [15].

If shear strain is to be measured, a single-element or a dual-element strain gage is bonded to the specimen at the center of the gage section. If bending or buckling is suspected, back-to-back strain gages can be used, just as discussed for the Iosipescu shear test method in the previous section. Likewise, the calculations of shear stress, shear strain, and shear modulus are also the same; the cross-sectional area in the present case is the length of the specimen parallel to the rails times the specimen thickness.

In summary, the two-rail shear test method clearly has many attributes in common with the Iosipescu shear test method. In fact, it is conceivable that at some future time the two test methods will converge into one.

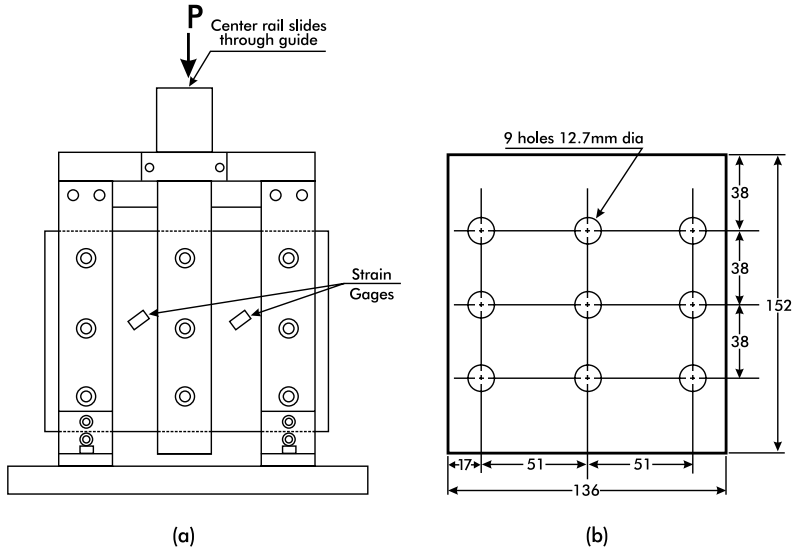

FIGURE 7.11
Three-rail shear test method: (a) fixture configuration, and (b) specimen geometry (all in mm).

7.3 Three-Rail Shear Test Method (ASTM D 4255)

Although the in-plane shear stress state induced in the three-rail shear test specimen is generally similar to that induced in the two-rail shear test specimen, there also are significant differences between the two test methods. In particular, the test fixtures are quite different. A sketch of the three-rail shear fixture is shown in Figure 7.11. The standard fixture shown is designed to be loaded in compression between the flat platens of a testing machine. Tensile loading is also permissible if the fixture is modified to permit attachment to the base and crosshead of the testing machine. However, in practice this is not commonly done. In fact, the fixture drawings available from ASTM only include the compression-loaded configuration.

Unlike the two-rail shear fixture, the three-rail shear fixture does shear load the specimen along its geometric axes. However, nine rather than six clearance holes must be cut into the specimen, and the size of the standard specimen is 136 × 152 mm rather than 76 × 152 mm, i.e., 1.8 times larger. These are both distinct disadvantages, i.e., causing increased specimen preparation time (and hence cost) and increased test material consumption, respectively. The (two) gage sections are each 25.4 mm wide, twice as wide as for the (single) gage section of the two-rail shear specimen, which could be an advantage in some cases, as discussed relative to the two-rail shear fixture. However, the gage width of the two-rail shear specimen could also simply be increased to 25.4 mm, if desired. In any case, the potential for

buckling in the gage section is always a concern as the gage section width is increased.

The methods of specimen gripping, specimen strain gaging, and reducing the test data are essentially the same as for the two-rail shear test method, as detailed in Section 7.2.

In summary, the disadvantages of the three-rail shear test method relative to the two-rail shear test method generally outweigh the advantages. Thus it is presently used much less frequently [16].

7.4 $[\pm 45]_{ns}$ Tensile Shear Test Method (ASTM D 3518)

The $[\pm 45]_{ns}$ tensile coupon can be employed to determine the shear properties of the unidirectional lamina. These include the in-plane shear modulus, G_{12}, and the ultimate shear stress and strain, S_6 and e_6, respectively. The test specimen is relatively simple to prepare and requires no special test fixture other than standard tensile grips. The test method has been standardized as ASTM D 3518 [5].

The state of stress in each lamina of the $[\pm 45]_{ns}$ laminate is not pure shear. Each lamina contains tensile normal stresses, σ_1 and σ_2, in addition to the desired shear stress, τ_{12}. In addition, an interlaminar shear stress, τ_{xz}, is present near the laminate free edge [5], as discussed in Chapter 2. Normally, these considerations would lead to the rejection of this test geometry. However, there are mitigating circumstances that reduce these concerns. First, the shear stress–strain responses of many types of composite laminae are nonlinear, and may exhibit strain softening characteristics. Thus, although the biaxial state of stress present in the specimen likely causes the measured value of shear strength to be lower than the true value, the reduction may be small because of the nonlinear softening response. Second, the magnitudes of the interlaminar stresses for laminates containing laminae with high orthotropy ratios are a maximum at ply angles of 15 to 25°, and the interlaminar stresses are considerably smaller for 45° ply angles. Therefore, the $[\pm 45]_{ns}$ tensile shear test method may often be reliable in determining lamina shear strength and modulus.

The test specimen geometry for the $[\pm 45]_{ns}$ tensile shear coupon is shown in Figure 7.12. The width of the specimen typically is on the order of 25 mm. End tabs may not be required because the tensile strength of a $[\pm 45]_{ns}$ laminate is low relative to that of an axially loaded unidirectional composite. The $[\pm 45]_{ns}$ laminate tension test provides an indirect measure of the in-plane shear stress-strain response in the material coordinate system. The tensile specimen is instrumented with a 0°/90° biaxial strain gage rosette as shown in Figure 7.12. The specimen is prepared, and tested in tension to ultimate failure following the procedures outlined for the tension test in Chapter 5.

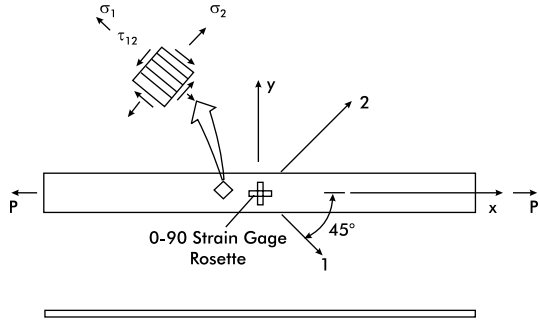

FIGURE 7.12
The $[\pm 45]_{ns}$ tensile specimen for evaluation of the shear stress–strain response of unidirectional composites, and the stress state in a ply.

Determination of the intrinsic (lamina) shear properties from the tension test results uses a stress analysis of the $[\pm 45]_{ns}$ specimen. The shear stress, τ_{12} (Figure 7.12), is simply [5]

$$\tau_{12} = \sigma_x/2 \tag{7.4}$$

where σ_x is the axial stress (P/A). The shear strain is

$$\gamma_{12} = \varepsilon_x - \varepsilon_y \tag{7.5}$$

where ε_x and ε_y are the axial and transverse strains, respectively ($\varepsilon_y < 0$). Hence, the in-plane shear modulus, G_{12}, is readily determined by plotting $\sigma_x/2$ vs. $(\varepsilon_x - \varepsilon_y)$ and establishing the slope of the initial portion of the curve. The ultimate shear stress, S_6, is defined as the maximum value of $\sigma_x/2$. Figures 7.13 and 7.14 show typical shear stress–shear strain curves for the lamina as determined from the laminate tensile test.

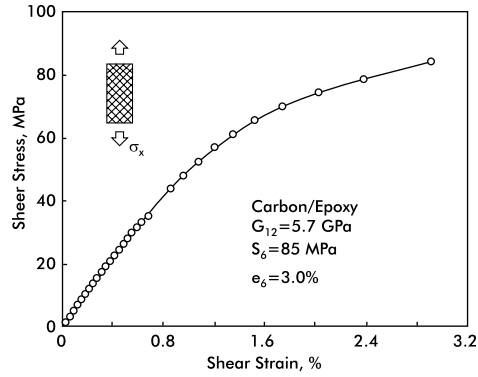

FIGURE 7.13
Shear stress–strain curve obtained from a tensile test of a $[\pm 45]_{2s}$ carbon/epoxy test specimen.

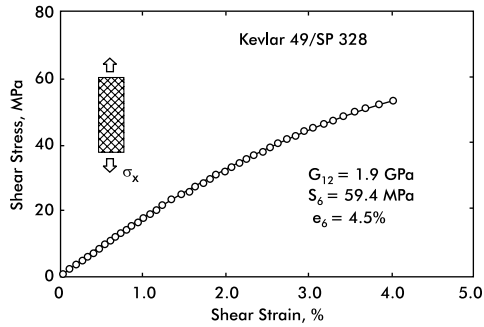

FIGURE 7.14
Shear stress–strain curve obtained from a tensile test of a $[\pm 45]_{2s}$ Kevlar/epoxy test specimen.

As an alternative to determining the shearing modulus using the method presented above, it is also possible to measure the axial stiffness and Poisson's ratio of the [±45] laminate, i.e., E_x and υ_{xy}, and then determine the shear modulus according to the following relationship:

$$G_{12} = \frac{E_x}{2\,(1+\nu_{xy})} \tag{7.6}$$

7.5 Short Beam Shear Test Method (ASTM D 2344)

This is an interlaminar shear test method. For a unidirectional composite the τ_{13} component is the shear stress applied, assuming the fibers to be oriented parallel to the beam axis. However, if the shear strengths in the 13 and 12 directions are equal, as is often assumed for a unidirectional composite, this test method can be, and often is, used to determine the in-plane shear strength of a unidirectional lamina. As for the $[\pm 45]_{ns}$ tension shear test method, it is in common use despite some serious limitations. This ASTM standard was titled "Apparent Interlaminar Shear Strength…" for many years, the word "apparent" acknowledging these limitations [6].

A specimen with a low support span length-to-specimen thickness ratio (typically a ratio of 4) is subjected to three-point loading. Both bending (flexural) and interlaminar shear stresses are induced in any beam loaded in this manner, as discussed in more detail in Chapter 8. The axial bending stresses are compressive on the surface of the beam where the load is applied, and tensile on the opposite surface, varying linearly through the beam thickness if the material response is elastic. By definition, the neutral axis (neutral plane) is where the bending stress passes through zero. It is on this neutral plane that the interlaminar shear stress is theoretically at maximum, varying

parabolically from zero on each surface of the beam. Thus, although a combined stress state exists in general, the stress state should be pure shear on the neutral plane. For a shear test, by keeping the span length-to-specimen thickness ratio low, the bending stresses can be kept low, promoting shear failures on the neutral plane. Unfortunately, the concentrated loadings on the beam at the loading and support points create stress concentrations throughout much of the short beam [17,18], complicating the stress state. As the result, the assumption of a parabolic stress distribution with a maximum at the neutral plane becomes only an approximation. Nevertheless, the ASTM standard assumes a parabolic stress distribution, which for a beam of rectangular cross section results in a maximum shear stress of

$$\tau_{13} = 0.75\ P/A \tag{7.7}$$

where P is the applied load on the beam, and A is the cross-sectional area of the beam. This assumption is the reason for the use of "apparent" in the previous title of ASTM D 2344. Despite these limitations, the short beam shear test method usually produces reasonable values of shear strength [19].

The specimen can be very small, consuming a minimal amount of material. For example, when a span length-to-specimen thickness ratio of 4 and a 2.5-mm-thick composite are used, the span length is only 10 mm. If one specimen thickness of overhang is allowed on each end, the total specimen length is still only 15 mm. In addition, minimum specimen preparation time is required because the length and width dimensions, and the quality of the cut edges of the specimen, are not critical. The test fixturing can be relatively simple and a test can be performed quickly. A typical short beam shear test fixture is shown in Figure 7.15.

For the above-described reasons, the short beam shear test is used extensively as a materials screening and quality control test. It has definite advantages for these purposes. However, another reason the test is both quick and economical is that no strain or displacement measurements are made because the span length-to-specimen thickness ratio is too small. Unfortunately, this means that shear modulus cannot be determined, and a shear stress–strain curve is not obtained.

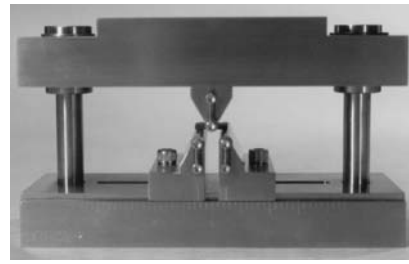

FIGURE 7.15
Short beam shear test fixture with adjustable support span. (Photograph courtesy of Wyoming Test Fixtures, Inc.)

7.6 Summary

Of the many shear test methods in existence, the Iosipescu shear test method is judged superior in meeting the various requirements of an ideal test. The two-rail shear test method is a viable alternative, and may become more prominent as it is further developed. The $[\pm 45]_{ns}$ tensile shear test utilizes a relatively simple specimen geometry and test configuration, but the influences of the biaxial stress state present can diminish shear strength measurements. Many of the other shear test methods have serious deficiencies, which limit their validity.

References

1. S.N. Chatterjee, D.F. Adams, and D.W. Oplinger, *Test Methods for Composites — A Status Report, Vol. III: Shear Test Methods*, Report DOT/FAA/CT-93/17-III, Federal Aviation Administration Technical Center, Atlantic City International Airport, NJ, June 1993.
2. D.F. Adams, Test methods for mechanical properties, Chapter 5.1.6 of Volume 5 (L.A. Carlsson, Ed.) in the series, *Comprehensive Composite Materials*, A. Kelly and C. Zweben, Eds., Elsevier Science, Oxford, U.K., 2000, pp. 113–148.
3. ASTM D 5379-98, *Test Method for Shear Properties of Composite Materials by the V-Notched Beam Method*, American Society for Testing and Materials, West Conshohocken, PA, 2001.
4. ASTM D 4255-01, *Test Method for In-Plane Shear Properties of Polymer Matrix Composite Materials by the Rail Shear Method*, American Society for Testing and Materials, West Conshohocken, PA, 2002.
5. ASTM D 3518-94 (2001), *Practice for In-Plane Shear Stress-Strain Response of Unidirectional Polymer Matrix Composite Materials by Tensile Test of ±45° Laminate*, American Society for Testing and Materials, West Conshohocken, PA, 2001.
6. ASTM D 2344-00, *Test Method for Short Beam Strength of Polymer Matrix Composite Materials and their Laminates by Short-Beam Method*, American Society for Testing and Materials, West Conshohocken, PA, 2001.
7. N. Iosepescu, New accurate procedure for single shear testing of metals, *J. Mater.*, 2, 537–566, 1967.
8. D.F. Adams and D.E. Walrath, Iosipescu shear properties of SMC composite materials, in *Composite Materials: Testing and Design (Sixth Conference)*, ASTM Spec. Tech. Publ. 787, American Society for Testing and Materials, West Conshohocken, PA, 1982, pp. 19–33.
9. D.E. Walrath and D.F. Adams, *Verification and Application of the Iosipescu Shear Test Method*, Report No. UWME-DR-401-103-1, Department of Mechanical Engineering, University of Wyoming, Laramie, WY, June 1984.
10. H.W. Bergner, Jr., J.G. Davis, Jr., and C.T. Herakovich, *Analysis of Shear Test Methods for Composite Laminates*, Department of Engineering Science and Mechanics, Report VPI-E-77-14, Virginia Polytechnic Institute & State University, Blacksburg, VA, 1977.

11. H. Ho, J. Morton, and G.L. Farley, Non-linear numerical analysis of the Iosipescu specimen for composite materials, *Compos. Sci. Technol.*, 50, 355–365, 1994.
12. J. Morton, H. Ho, M.Y. Tsai, and G.L. Farley, An evaluation of the Iosipescu specimen for composite materials shear property measurement, *J. Compos. Mater.*, 26(6), 708–750, 1992.
13. K.H. Boller, *A Method to Measure Intralaminar Shear Properties of Composite Laminates*, Technical Report AFML-TR-69-311, Air Force Materials Laboratory, Wright-Patterson Air Force Base, OH, December 1969.
14. ASTM D 2719-89 (1994), *Test Methods for Structural Panels in Shear Through-the-Thickness*, American Society for Testing and Materials, West Conshohocken, PA, 1994.
15. A.K. Hussain and D.F. Adams, *An Analytical and Experimental Evaluation of the Two-Rail Shear Test for Composite Materials*, Report UW-CMRG-R-98-105, Composite Materials Research Group, University of Wyoming, Laramie, WY, February 1998.
16. *High Performance Test Fixtures*, Product Catalog No. 106, Wyoming Test Fixtures, Inc., Laramie, WY, 2000 (*also,* wyomingtestfixtures.com).
17. C.A. Berg, J. Tirosh, and M. Israeli, Analysis of short beam bending of fiber reinforced composites, in *Composite Materials: Testing and Design (Second Conference),* ASTM Spec. Tech. Publ. 497, American Society for Testing and Materials, West Conshohocken, PA, 1972, pp. 206–218.
18. S. Kotha and D.F. Adams, *Analytical Investigation of Crack Initiation and Propagation in Composite Materials*, Report UW-CMRG-R-98-119, Composite Materials Research Group, University of Wyoming, Laramie, WY, August 1998.
19. D.F. Adams and E.Q. Lewis, Experimental assessment of four composite material shear test methods, *J. Test. Eval.*, 25(2), 174–181, 1997.

8

Lamina Flexural Response

As defined in the three previous chapters, pure, uniform tension, compression, and shear loadings must be individually applied to establish the fundamental strength and stiffness properties of a composite material. A flexure test, i.e., the bending of a beam, typically induces tensile, compressive, and shear stresses simultaneously. Thus it is not usually a practical means of determining the fundamental properties of a composite material [1,2].

Nevertheless, flexure tests are popular, because of the simplicity of both specimen preparation and testing, as will be discussed subsequently. Gripping of the specimen, the need for end tabs, obtaining a pure stress state, avoiding buckling, and most of the other concerns discussed in the previous three chapters are usually nonissues when conducting a flexure test.

Flexural testing can, for example, be a simple method of monitoring quality during a structural fabrication process. The usual objective of a flexure test is to determine the flexural strength and flexural modulus of the beam material. This might be particularly relevant if the component being fabricated is to be subjected to flexural loading in service. However, because of the complex stress state present in the beam, it is typically not possible to directly relate the flexural properties obtained to the fundamental tensile, compressive, and shear properties of the material.

8.1 Testing Configurations

Figure 8.1 indicates the configuration of the ASTM D 790 three-point flexure test [3]. This standard was created in 1970 by the plastics committee within ASTM for use with unreinforced and reinforced plastics and electrical insulating materials, as its title suggests. For more than 25 years, until 1996 when it was removed, this standard also included four-point flexure. In response to demands by the composite materials community, in 1998 a new standard, ASTM D 6272, was introduced by the plastics committee for the same classes of plastics, but specifying four-point flexure [4]. That is, two standards now exist. Thus, the composites committee of ASTM is presently writing its own flexural test standard specifically for composite materials, ASTM D XXXX-02,

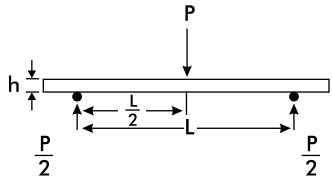

FIGURE 8.1
Three-point flexure loading configuration.

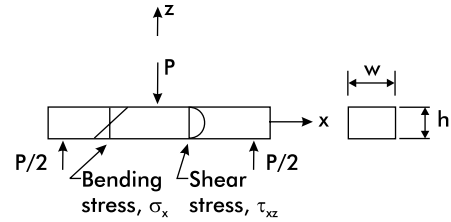

FIGURE 8.2
Stresses in a beam subjected to three-point flexure.

which includes both three-point and four-point flexure [5]. The three standards differ sufficiently in detail that it is advisable to refer to all three for guidance. It is unfortunate, but understandable because of its long existence, that many experimentalists still (incorrectly) only quote ASTM D 790 as the governing standard for all flexural testing.

Analysis of a macroscopically homogeneous beam of linearly elastic material [6] indicates that an applied bending moment is balanced by a linear distribution of normal stress, σ_x, as shown in Figure 8.2. For the three-point flexural loading shown, the top surface of the beam is in compression while the bottom surface is in tension. Assuming a beam of rectangular cross section, the midplane contains the neutral axis and is under zero bending stress. The interlaminar shear stress, τ_{xz}, is maximum on this midplane, varying parabolically from zero on the free surfaces as shown [6]. For three-point flexure, the shear stress is constant along the length of the beam, and directly proportional to the applied force P. However, the flexural stresses, in addition to being directly proportional to P, vary linearly with position along the length of the beam, and are zero at each end support and maximum at the center. Thus, the stress state is highly dependent on the support span length-to-specimen thickness ratio (L/h). Beams with small L/h ratios are dominated by shear. As discussed in Chapter 7, a short-span (L/h = 4) three-point flexure test is commonly used for interlaminar shear strength determination. Beams with long spans usually fail in tension or compression. Typically, composite materials are stronger in tension than compression. Also, the concentrated loading is applied at the point of maximum compressive stress in the beam, often inducing local stress concentrations. Thus, the composite beam usually fails in compression at the midspan loading point.

Although testing of a unidirectional lamina is the primary subject of the present chapter, laminates of various other orientations can also be tested in flexure, as will be discussed in more detail in Chapter 11.

Flexural testing of a unidirectional lamina is generally limited to beams with the fibers aligned parallel to the beam axis. That is, 0° flexural properties are determined. Beams with fibers oriented perpendicular to the beam axis almost always fail in transverse tension on the lower surface because the transverse tensile strength of most composite materials is lower than the transverse compressive strength, usually by a factor of three or more, and

is lower than the interlaminar shear strength [7]. In fact, the transverse tensile flexure test has been suggested as a simple means of obtaining the transverse tensile strength of a unidirectional composite [7], although there has been no movement to standardize it as such.

As do the other two flexural test standards, ASTM D XXXX requires that a sufficiently large support span-to-specimen thickness ratio be chosen, "such that failures occur in the outer fibers of the specimens, due only to the bending moment." The standard recommends support span-to-thickness ratios of 16:1, 20:1, 32:1, 40:1, and 60:1, indicating that, "as a general rule support span-to-thickness ratios of 16:1 are satisfactory when the ratio of the tensile strength to shear strength is less than 8 to 1." High-strength unidirectional composites can have much higher strength ratios, requiring correspondingly higher support span-to-thickness ratios. For example, ASTM D XXXX suggests a ratio of 32:1 for such materials. These ratios are specified to be the same for three-point and four-point flexure.

Per ASTM D XXXX, the diameter of the loading noses and supports should be 6 mm. The other two ASTM standards have slightly different requirements. This perhaps confirms experimental observations that the test results obtained are not strongly influenced by the specific diameters used, as long as the diameters are not so small that local bearing damage of the composite material occurs [8].

It has become customary when testing in four-point flexure to use either "third-point" or "quarter-point" loading, as shown in Figure 8.3. For third-point loading, the loading points are each positioned one third of the support span length from the respective support, and hence are also one third of the support span length from each other. For quarter-point loading, the loading points are each positioned one quarter of the support span length from the respective support, and hence are one half of the support span length from each other. ASTM D XXXX includes only quarter-point loading.

Although the specimen thickness can be arbitrary (as long as the recommended span-to-thickness ratio is maintained), ASTM D XXXX suggests a 100-mm-long, 2.4-mm-thick, 13-mm-wide specimen for high-strength laminae, supported on an 76.8-mm span. This results in a specimen overhang of 11.6 mm at each end. Suggestions are given for other types of composites as well. The other two ASTM standards recommend slightly different specimen sizes and amounts of overhang. Again, this suggests that the exact specimen size is not critical.

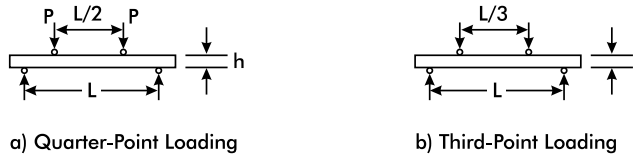

FIGURE 8.3
Four-point flexure test configurations: (a) quarter-point loading, and (b) third-point loading.

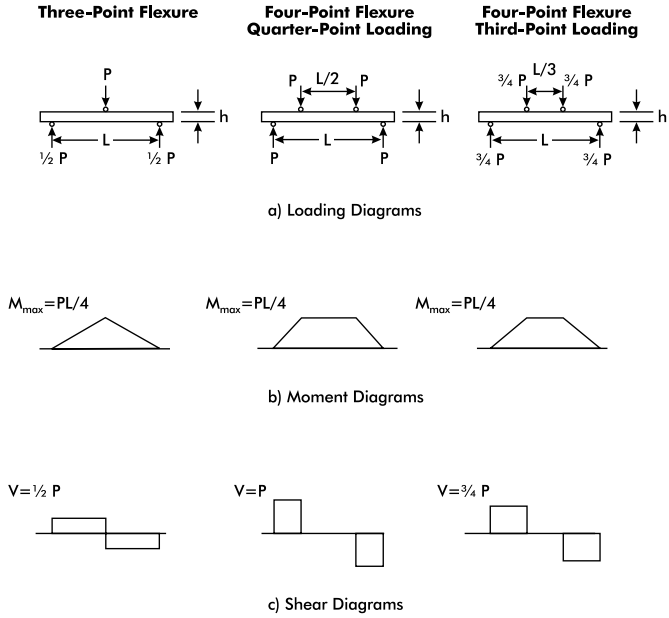

FIGURE 8.4
Required loadings for equal maximum bending moment in various beam configurations, with corresponding vertical shear force distributions: (a) loading diagrams, (b) moment diagrams, and (c) shear diagrams.

8.2 Three- Vs. Four-Point Flexure

As noted in the previous section, either three- or four-point flexure can be, and is, used. The various ASTM standards make no specific recommendations concerning when to use each test. In fact, there is no clear advantage of one test over the other, although there are significant differences. Figure 8.4 indicates the required loadings and the corresponding bending moment (M) and transverse shear force (V) distributions in the beam for each of the loadings.

For three-point flexure the maximum bending moment in the beam, and hence the location of the maximum tensile and compressive flexural stresses, is at midspan and is equal to $M_{max} = PL/4$. For four-point flexure with loading at the quarter points, attaining the same maximum bending moment, i.e., $M_{max} = PL/4$, requires twice the testing machine force, i.e., 2P; this maximum bending moment is constant over the entire span L/2 between the applied loads (Figure 8.4(b)). For four-point flexure with loading at the one-third points, attaining the same maximum bending moment, i.e., $M_{max} = \frac{3}{4} P\ (L/3) = PL/4$, requires 50% more testing machine force, i.e., 1.5P, than for three-point flexure. This maximum bending moment is constant over the entire span L/3 between the applied loads.

Thus, for quarter-point loading the force exerted by the testing machine must be twice as high, and for third-point loading the force must be one and one-half times as high, as for three-point flexure. Normally this is not in itself a significant factor because the loads required to fail a beam in flexure are not extremely high. What may be more significant is the magnitude of the required concentrated force at the loading point(s), and the magnitude of the corresponding induced stress concentrations, because the flexural stresses are a maximum at these locations. As noted in Figure 8.4, for both three-point flexure and four-point flexure with quarter-point loading, the maximum concentrated force on the beam is P. However, for four-point flexure with third-point loading, it is only $\frac{3}{4}$ P. This indicates an advantage for third-point loading.

There are other considerations, however. The maximum transverse shear force, V, and hence the maximum interlaminar shear stress in the beam, also varies with the type of loading, as indicated in Figure 8.4. For three-point loading the shear force is equal to $\frac{1}{2}$ P and is constant over the entire support span. For four-point flexure, quarter-point loading, it is equal to P and exists only over the end quarters of the beam. For four-point flexure, third-point loading, it is equal to $\frac{3}{4}$ P and exists only over the end thirds of the beam. As discussed in the previous section, it is desirable to keep the ratio of interlaminar shear stress to flexural stress sufficiently low to avoid shear failures at the midplane rather than tensile or compressive failures at the beam surfaces. As explained, this is normally achieved by controlling the span length-to-specimen thickness ratio. Assuming the same specimen thickness for all loadings, three-point flexure ($V = \frac{1}{2}$ P) would be preferred, because it minimizes the required support span length, followed by four-point flexure, third-point loading ($V = \frac{3}{4}$ P).

One additional consideration should be noted, although it is usually of lesser importance. As will be discussed in Section 8.4, it may also be desired to calculate flexural modulus, which is often based on the measured deflection of the beam. The shear stresses in the beam contribute to the total deformation, in proportion to the product of the shear force and the length over which it acts. Because the entire length of the beam in three-point flexure is subjected to the shear force $\frac{1}{2}$ P, but only one half of the four-point flexure, quarter-point loading beam is subjected to the shear force P, and only two thirds of the four-point flexure, third-point loading beam is subjected to the shear force $\frac{3}{4}$ P, the net shear deformation effect is the same in all three cases. This consideration is important when beam deflection is used to determine modulus.

In summary, quarter-point flexure with third-point loading appears to be a good overall choice. However, each of the three loading modes (Figure 8.4) has some individual advantages. Thus, all three are used, with three-point flexure being the most common, perhaps only because it requires the simplest test fixture. A typical test fixture, with adjustable loading and support spans such that it can be used for both three- and four-point flexure, is shown in Figure 8.5.

As an aside, note that three-point flexure is commonly (although perhaps erroneously) referred to as three-point loading, and likewise four-point flexure

FIGURE 8.5
Photograph of a flexure test fixture with interchangeable three- and four-point loading heads and adjustable spans. (Photograph courtesy of Wyoming Test Fixtures, Inc.)

is referred to as four-point loading. As a result, this has become accepted terminology, included in all three ASTM standards.

8.3 Specimen Preparation and Flexure Test Procedure

The flexure specimen is simply a strip of test material of constant width and thickness. As noted in Section 8.1, for a unidirectional lamina subjected to longitudinal flexure, the suggested dimensions in ASTM D XXXX are support span length, 76.8 mm; specimen total length, 100 mm; specimen width, 13 mm; and specimen thickness, 2.4 mm. Suggested tolerances on these dimensions are also given in the standard.

Although all three ASTM standards specify the use of a deflection-measuring device mounted under the midspan of the specimen, occasionally a strain gage is used instead. One longitudinal strain gage can be mounted at the midspan on the tension side (bottom surface) of the specimen. The test fixture support span is to be set according to the beam thickness, specimen material properties, and fiber orientation, as discussed previously. ASTM D XXXX specifies that the specimen is to be loaded at a testing machine crosshead rate of 1 mm/min. ASTM D 790 specifies that the testing machine crosshead rate, $\dot{x}$, be selected such that the maximum strain rate (of the surface fibers) is, $\dot{\varepsilon} = 0.01$/min. This leads to [1],

$$\dot{x} = \frac{\dot{\varepsilon} L^2}{6h} \tag{8.1}$$

Commonly, a crosshead rate in the range of 1 to 5 mm/min is selected.

The beam deflection, δ, is measured using a calibrated linear variable differential transformer (LVDT) at the beam midspan. Alternatively, the beam displacement may be approximated as the travel of the testing machine crosshead if the components of this travel that are due to the machine compliance and to the indentations of the specimen at the loading and support points are subtracted out. If a strain gage is used, the specimen is to be placed in the fixture with the strain gage on the tension side of the beam and centered at midspan. The strain or displacement readings may be recorded continuously or at discrete load intervals. If discrete data are recorded, the load and strain–displacement readings should be taken at small load intervals, with at least 25 points in the linear response region (so that an accurate flexural modulus can be determined). The total number of data points should be enough to accurately describe the complete beam response to failure.

8.4 Data Reduction

From simple beam theory [6], the tensile and compressive stresses at the surfaces of the beam at any location where the bending moment is a maximum is

$$\sigma_{max} = \frac{M_{max}(h/2)}{I} \tag{8.2}$$

where M_{max} is the maximum bending moment, h is the thickness of the beam, and $I = wh^3/12$ is the moment of inertia of a beam of rectangular cross section, with w being the beam width.

For three-point flexure, for example, the bending moment is maximum, i.e., $M_{max} = PL/4$, at the midlength of the beam. Substitution into Equation (8.2) gives

$$\sigma_{max} = \frac{3PL}{2wh^2} \tag{8.3}$$

This equation enables construction of a stress–strain plot from the recorded load vs. displacement or load vs. strain data.

A reasonable approximation for most materials is that the modulus in tension is the same as in compression. If a strain gage is used, the initial slope of the flexural stress–strain plot can be obtained using a linear least-squares fit. Figures 8.6 and 8.7 show typical stress–strain curves obtained from three-point flexure tests.

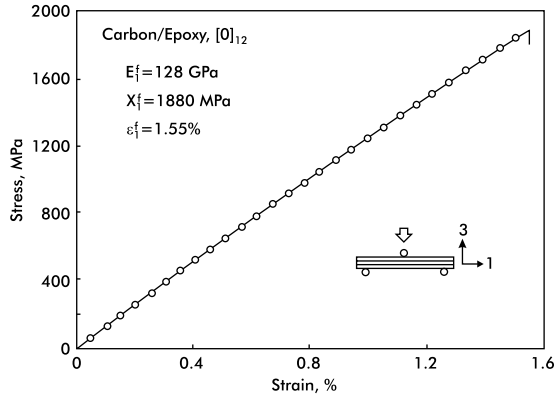

FIGURE 8.6
Flexural stress–strain response of a $[0]_{12}$ carbon/epoxy test specimen.

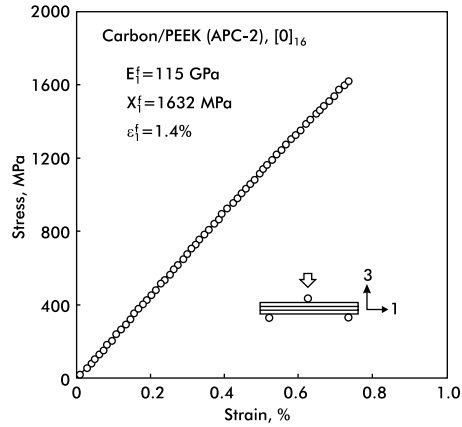

FIGURE 8.7
Flexural stress–strain response of a $[0]_{16}$ carbon/PEEK test specimen.

For the case where the three-point flexure specimen is not strain-gaged, the flexural modulus may be determined from a plot of load, P, vs. center deflection, δ, as

$$E_f = \frac{L^3}{4wh^3}\frac{\Delta P}{\Delta \delta} \tag{8.4}$$

This relation, however, assumes that shear deformation is negligible. For $[90]_n$ beams (fibers perpendicular to the beam axis), shear deformation is generally insignificant and Equation (8.4) should be accurate. On the other hand, the results of Zweben [9] for $[0]_n$ beams (fibers parallel to the beam axis) shown in Figure 8.8 illustrate that for certain unidirectional composites, large support span-to-thickness ratios, L/h, are required to minimize the influence of shear deformation and thus produce an accurate flexural modulus.

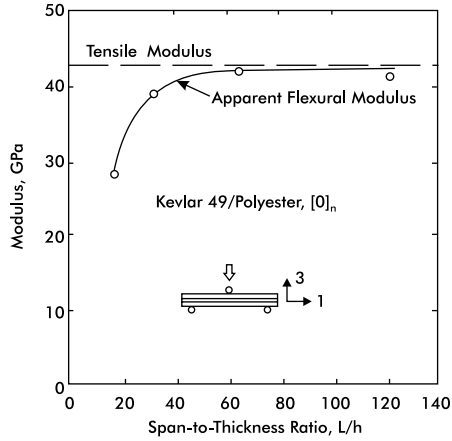

FIGURE 8.8
Apparent flexural modulus of a $[0]_n$ Kevlar 49–polyester specimen as a function of span-to-thickness ratio [9].

If a flexural test is conducted for which the shear deformation component is significant, the following equation may be used to evaluate the flexural modulus:

$$E_f = \frac{L^3}{4wh^3}\left(1+\frac{6h^2E_f}{5L^2G_{13}}\right)\frac{\Delta P}{\Delta \delta} \tag{8.5}$$

where G_{13} is the interlaminar shear modulus. The second term in the parentheses of Equation (8.5) is a shear correction factor that may be significant for composites with a high axial modulus and a low interlaminar shear modulus. The flexural and shear moduli (E_f and G_{13}), however, may not be known prior to the test. For Equation (8.5), the modulus E_f may be replaced by the tensile modulus, E_1, and the shear modulus can be approximated as the in-plane shear modulus, G_{12}, assuming the fibers are oriented along the beam axis. If the shear correction factor is not determined, the flexural modulus can be evaluated using Equation (8.4) for tests conducted at increasing span lengths until a constant value is achieved, as suggested in Figure 8.8.

Additional details of data reduction, including for four-point flexure, can be found in the three ASTM flexural testing standards cited in this chapter.

References

1. J.M. Whitney, I.M. Daniel, and R.B. Pipes, *Experimental Mechanics of Fiber Reinforced Composite Materials*, rev. ed., Society for Experimental Mechanics, Prentice-Hall, Englewood Cliffs, NJ, 1984.

2. D.F. Adams, Test methods for mechanical properties, Chapter 5.1.6 of Volume 5 (L.A. Carlsson, ed.) in the series, *Comprehensive Composite Materials*, A. Kelly and C. Zweben, Eds., Elsevier Science, Oxford, U.K., 2000, pp. 113–148.
3. ASTM Standard D 790-00, *Test Methods for Flexural Properties of Unreinforced and Reinforced Plastics and Electrical Insulating Materials*, American Society for Testing and Materials, West Conshohocken, PA, 2001.
4. ASTM Standard D 6272-00, *Test Method for Flexural Properties of Unreinforced and Reinforced Plastics and Electrical Insulating Materials by Four-Point Bending*, American Society for Testing and Materials, West Conshohocken, PA, 2001.
5. Draft ASTM Standard D XXXX-02, *Test Methods for Flexural Properties of Fiber-Reinforced Polymer Matrix Composites*, American Society for Testing and Materials, West Conshohocken, PA, 2002.
6. S. P. Timoshenko, *Strength of Materials*, Part 1, 3rd. ed., Krieger, Malabar, FL, 1984.
7. D.F. Adams, T.R. King, and D.L. Blacketter, Evaluation of the transverse flexure test method for composite materials, *Compos. Sci. Technol.*, 39, 341–353, 1990.
8. D.F. Adams and E.Q. Lewis, Experimental study of three- and four-point shear test specimens, *J. Compos. Technol. Res.*, 17(4), 341–349, 1995.
9. C. Zweben, Static strength and elastic properties, in *Delaware Composites Design Encyclopedia*, Vol. 1, L.A. Carlsson and J.W. Gillespie, Jr., Eds., Technomic, Lancaster, PA, 1990, pp. 49–70.

9

Lamina Off-Axis Tensile Response

The off-axis tension test of unidirectional composites has received considerable attention by the composites community. "Off-axis" here refers to the material axes (1-2) being rotated through an angle θ with respect to the specimen axis and direction of loading (Figure 9.1). The off-axis specimen is typically 230 mm long and between 12.7 and 25.4 mm wide. A thickness of eight plies is common (0.127 mm ply thickness).

The off-axis tension test is rarely used to determine basic ply properties. Most commonly, the purpose of this test is to verify material properties determined in tension, compression, and shear, as discussed in Chapters 5–7, using the transformed constitutive relations discussed in Chapter 2. Testing of specimens at off-axis angles between 10 and 20° produces significant shear in the principal material system. Consequently, the 10° off-axis test has been proposed as a simple way to conduct a shear test [1]. The test has been used

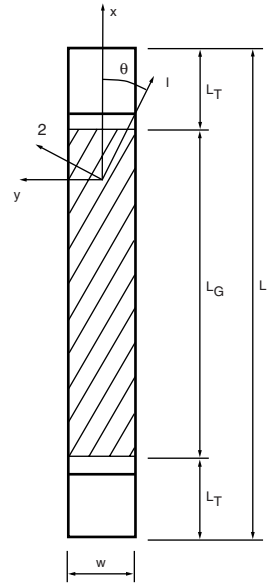

FIGURE 9.1
Geometry of the off-axis tensile coupon.

also to verify biaxial strength criteria because, as will be discussed, uniaxial loading will lead to a combined state of stress in the principal material system.

9.1 Deformation and Stress in an Unconstrained Specimen

Because of the off-axis configuration of the specimen, the in-plane response is characterized by a fully populated compliance matrix, as shown in Equation (2.16)

$$\begin{bmatrix} \varepsilon_x \\ \varepsilon_y \\ \gamma_{xy} \end{bmatrix} = \begin{bmatrix} \bar{S}_{11} & \bar{S}_{12} & \bar{S}_{16} \\ \bar{S}_{12} & \bar{S}_{22} & \bar{S}_{26} \\ \bar{S}_{16} & \bar{S}_{26} & \bar{S}_{66} \end{bmatrix} \begin{bmatrix} \sigma_x \\ \sigma_y \\ \tau_{xy} \end{bmatrix} \tag{9.1}$$

where the x-y system is defined in Figure 9.1, and expressions for the transformed compliance elements $\bar{S}_{ij}$ are given in Appendix A.

For an ideal, uniformly stressed off-axis tensile coupon, the only stress acting is σ_x, ($\sigma_y = \tau_{xy} = 0$), and Equations (9.1) give the state of strain in the specimen,

$$\begin{bmatrix} \varepsilon_x \\ \varepsilon_y \\ \gamma_{xy} \end{bmatrix} = \sigma_x \begin{bmatrix} \bar{S}_{11} \\ \bar{S}_{12} \\ \bar{S}_{16} \end{bmatrix} \tag{9.2}$$

Consequently, the off-axis coupon subjected to a uniform uniaxial state of stress thus exhibits shear strain (γ_{xy}) in addition to the axial and transverse strains (ε_x and ε_y) (Figure 9.2).

A set of material properties may be evaluated based on measurement of axial stress (σ_x) and axial, transverse, and shear strains (ε_x, ε_y, γ_{xy}). It is customary to determine the axial Young's modulus (E_x) and Poisson's ratio (ν_{xy}) of the off-axis specimen

$$E_x = \frac{\sigma_x}{\varepsilon_x} \tag{9.3}$$

$$\nu_{xy} = -\frac{\varepsilon_y}{\varepsilon_x} \tag{9.4}$$

In addition, a ratio (η_{xy}), which quantifies coupling between shear and axial strains, is defined according to

$$\eta_{xy} = \frac{\gamma_{xy}}{\varepsilon_x} \tag{9.5}$$

The off-axis tension test may also be used to determine the in-plane shear modulus, G_{12}, in the principal material coordinate system. This property is, according to Equation (2.9), defined by

$$G_{12} = \frac{\tau_{12}}{\gamma_{12}} \tag{9.6}$$

Consequently, determination of G_{12} requires determination of shear stress and strain in the principal material coordinate system. Equations (2.12) and (2.14) yield

$$\tau_{12} = -mn\sigma_x \tag{9.7}$$

where $m = \cos\theta$ and $n = \sin\theta$. The shear strain is obtained from Equations (2.14)

$$\gamma_{12} = 2mn(\varepsilon_y - \varepsilon_x) + (m^2 - n^2)\gamma_{xy} \tag{9.8}$$

where the strain (ε_x) is directly measured, and the transverse strain (ε_y) and shear strain (γ_{xy}) are determined as subsequently explained.

The properties E_x, ν_{xy}, η_{xy}, and G_{12} can be evaluated from test data using procedures detailed later in this chapter. The mechanical properties so determined can be compared to theoretical values calculated from the compliance relations, Equations (9.2), and the definitions in Equations (9.3–9.5),

$$E_x = \frac{1}{\bar{S}_{11}} \tag{9.9a}$$

$$\nu_{xy} = \frac{-\bar{S}_{12}}{\bar{S}_{11}} \tag{9.9b}$$

$$\eta_{xy} = \frac{\bar{S}_{16}}{\bar{S}_{11}} \tag{9.9c}$$

If the principal (basic) material properties (E_1, E_2, ν_{12}, and G_{12}) are known from previous tests (Chapters 5–7), it is possible to calculate the off-axis properties E_x, ν_{xy}, and η_{xy} using Equations (A.1) (Appendix A), and compare those to the experimentally determined values. G_{12} may be compared to the modulus measured in the off-axis test (Equation (9.6)).

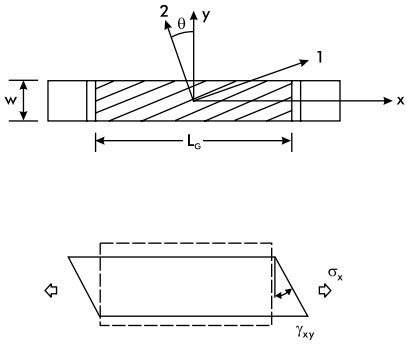

FIGURE 9.2
Off-axis coupon under uniform axial stress.

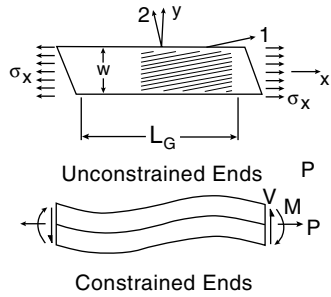

FIGURE 9.3
Influence of gripped end regions on deformation of off-axis specimen [2].

9.2 Influence of End Constraint

As first pointed out by Halpin and Pagano [2], most test machines used in testing laboratories employ rigid grips that constrain the shear deformation illustrated in Figure 9.2. As a result, the specimen assumes a shape schematically illustrated in Figure 9.3 [2]. To quantify the influence of gripping on the response of an off-axis tension specimen, Halpin and Pagano [2] performed a stress analysis of a constrained coupon and obtained the following expressions for the shear strain and longitudinal strain at the specimen centerline.

$$\gamma_{xy} = \bar{S}_{16} C_2 - \bar{S}_{66} C_0 w^2 / 4 \tag{9.10a}$$

$$\varepsilon_x = \bar{S}_{11} C_2 - \bar{S}_{16} C_0 w^2 / 4 \tag{9.10b}$$

with

$$C_0 = \frac{12\bar{S}_{16}\varepsilon_0}{3w^2\left(\bar{S}_{11}\bar{S}_{66} - \bar{S}_{16}^2\right) + 2\bar{S}_{11}L_G^2} \tag{9.11a}$$

$$C_2 = \frac{C_0}{12\bar{S}_{16}}\left(3\bar{S}_{66}w^2 + \bar{S}_{11}L_G^2\right) \tag{9.11b}$$

where $\varepsilon_0 = \Delta L / L_G$ (elongation/gage length) and w and L_G are specimen width and gage length, respectively (Figure 9.1).

On the basis of this analysis, it is possible to derive an expression for the apparent axial Young's modulus including end constraint

$$(E_x)_a = \sigma_x/\varepsilon_x \tag{9.12}$$

where σ_x and ε_x are the stress and strain at the centerline of the constrained off-axis coupon. $(E_x)_a$ may be expressed as

$$\left(E_x\right)_a = \frac{E_x}{1-\xi} \tag{9.13}$$

in which E_x is the modulus for an unconstrained off-axis specimen. The parameter ξ is given by

$$\xi = \frac{1}{\bar{S}_{11}}\left[\frac{3\bar{S}_{16}^2}{3\bar{S}_{66}+2\bar{S}_{11}\left(L_G/w\right)^2}\right] \tag{9.14}$$

Examination of the above equations reveals that $\xi \to 0$ and $(E_x)_a \to E_x = 1/\bar{S}_{11}$ when $L_G/w \to \infty$.

Similarly, Pindera and Herakovich [3] derived an expression for the apparent Poisson's ratio, $(\nu_{xy})_a$

$$\left(\nu_{xy}\right)_a = \nu_{xy}\,\frac{1-\frac{3}{2}\left(\frac{\bar{S}_{26}}{\bar{S}_{11}}\right)\beta}{1-\frac{3}{2}\left(\frac{\bar{S}_{16}}{\bar{S}_{12}}\right)\beta} \tag{9.15}$$

where β is given by [3],

$$\beta = \frac{\left(\frac{w}{L_G}\right)^2\left(\frac{\bar{S}_{16}}{\bar{S}_{11}}\right)}{1+\frac{3}{2}\left(\frac{w}{L_G}\right)^2\left(\frac{\bar{S}_{66}}{\bar{S}_{11}}\right)} \tag{9.16}$$

The apparent shear coupling ratio of the specimen subjected to end constraint is

$$(\eta_{xy})_a = \gamma_{xy}/\varepsilon_x \tag{9.17}$$

Substitution of Equations (9.10) and (9.11) into (9.17) yields

$$\left(\eta_{xy}\right)_a = \frac{\bar{S}_{16}}{\bar{S}_{11}}\left[1+\frac{3}{2}\left(\frac{w}{L_G}\right)^2\left(\frac{\bar{S}_{66}}{\bar{S}_{11}}-\left(\frac{\bar{S}_{16}}{\bar{S}_{11}}\right)^2\right)\right]^{-1} \tag{9.18}$$

Note that when the length-to-width ratio, $L_G/w \to \infty$, $(\eta_{xy})_a \to \bar{S}_{16}/\bar{S}_{11}$, as given by Equation (9.9c).

Pindera and Herakovich [3] examined the influence of end constraint on the evaluation of shear modulus, G_{12}, from the off-axis tension specimen using the elasticity solution of Halpin and Pagano [2] and found that the procedure outlined in Section 9.1 leads to error in G_{12}. The main source of error is the neglect of the shear stress τ_{xy} in Equation (9.7). The proper transformation is [3]

$$\tau_{12} = -mn\sigma_x + (m^2 - n^2)\tau_{xy} \tag{9.19}$$

This equation, combined with the definition of G_{12} (Equation (9.6)), yields an expression for the correct value of the shear modulus in terms of the apparent modulus $(G_{12})_a$, evaluated using the procedure in Section 9.1 [3],

$$G_{12} = \left(G_{12}\right)_a \frac{1+\dfrac{3\left(m^2-n^2\right)}{2mn}\beta}{1-\beta\left(\bar{S}_{16}/\bar{S}_{11}\right)} \tag{9.20}$$

where $m = \cos\theta$, $n = \sin\theta$, and β is defined in Equation (9.16). As $(w/L_G) \to \infty$, $\beta \to 0$, and the apparent shear modulus approaches G_{12}.

The above expressions for apparent off-axis properties $(E_x)_a$, $(\nu_{xy})_a$, and $(\eta_{xy})_a$ may be used to correct measured values, or to design the off-axis specimen for minimum error resulting from end constraint. An obvious way to reduce the error is to use specimens with large aspect ratios, L_G/w. As mentioned early in this chapter, specimens are typically 230 mm long and between 12.7 and 25.4 mm wide. For 38-mm-long tabs at the ends, this corresponds to aspect ratios between 6 and 12. For a carbon/polyimide composite specimen with an aspect ratio of 10 and 10° off-axis angle, Pindera and Herakovich [3] found an error in E_x of about 2 to 4%. The error in shear coupling ratio is larger, as will be discussed later.

The error in shear modulus G_{12} for a 10° off-axis carbon/polyimide specimen at $L_G/w = 10$ is approximately 12 to 15% [3]. For proper determination of G_{12}, Pindera and Herakovich [3] recommend use of coupons with an aspect ratio of 10 or more and an off-axis angle of 45°.

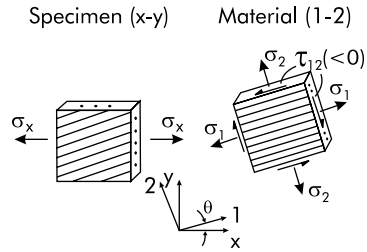

FIGURE 9.4
State of stress in the specimen for an off-axis tension test.

9.3 Off-Axis Tensile Strength

As mentioned earlier in this chapter, the off-axis tension test has been used to examine theories proposed for prediction failure of composites under combined stress. In such studies, slender specimens are used for strength measurements to avoid the complications of end constraint effects discussed above. This leads to a stress state in the on-axis system, as given by Equations (2.12) and (2.14):

$$\begin{bmatrix} \sigma_1 \\ \sigma_2 \\ \tau_{12} \end{bmatrix} = \sigma_x \begin{bmatrix} m^2 \\ n^2 \\ -mn \end{bmatrix} \tag{9.21}$$

Therefore, as illustrated in Figure 9.4, the state of stress in the principal material coordinate system is biaxial.

Experimental studies conducted on on-axis and off-axis specimens, e.g., in References [4,5], show that the off-axis specimen under tension fails along planes parallel to the fibers except for zero and very small angles, where failure involves fiber fractures. To predict the failure stress of the off-axis tension specimen, the on-axis stresses given by Equations (9.21) are substituted into the failure criterion of choice (see Section 2.5). The maximum stress and strain criteria (see Section 2.5), yield three equations for the ultimate stress, σ_x^{ult}, and the appropriate strength is identified by the least of the three values. Substitution of the stresses given by Equations (9.21) into the Tsai-Wu criterion, Equation (2.44), yields a quadratic equation in σ_x^{ult}, of the type

$$A\left(\sigma_x^{ult}\right)^2 + B\sigma_x^{ult} - 1 = 0 \tag{9.22}$$

The solution of Equation (9.22) yields two roots, the positive associated with the tensile strength and the negative associated with the compressive strength of the off-axis specimen.

As mentioned early in this chapter, the 10° off-axis tension test has been proposed for measuring the in-plane shear strength (S_6) of unidirectional composites [1]. However, because failure occurs under the influence of normal stresses σ_1 and σ_2 (Figure 9.4), which separate the specimen in two pieces, this test is not recommended for the generation of shear strength [6].

9.4 Test Procedure

1. Prepare off-axis tension coupons from a unidirectional, six- to eight-ply-thick panel. The specimens should be about 230 mm long and between 12.5 and 25 mm wide. Select at least three different off-axis angles, e.g., 15, 30, and 60°. Use the same tolerances as for the tension specimen discussed in Chapter 5, and bond end tabs as described in Chapter 4.
2. The off-axis test specimen is instrumented with a three-element strain gage rosette with one of the elements aligned with the coupon axis (x-direction in Figure 9.1), one element at 45°, and one element at –45°.
3. Measure the specimen cross-sectional dimensions (average six measurements).
4. Mount the specimen in a properly aligned and calibrated test frame. Set the crosshead rate at about 0.5 to 1 mm/min.
5. Monitor the load-strain response of the specimen (all three elements). Take strain readings at small load intervals to collect at least 25 data points in the linear region. Load the specimen to failure.

9.5 Data Reduction

9.5.1 Elastic Properties

Axial modulus, Poisson's ratio and shear coupling ratio may be determined from measured stress-strain data according to Equations (9.3)-(9.5). The axial strain, ε_x, is obtained directly from the axially oriented strain gage. Transverse strain and shear strain, ε_y and γ_{xy}, are obtained from the ±45° gages using Equations (2.13).

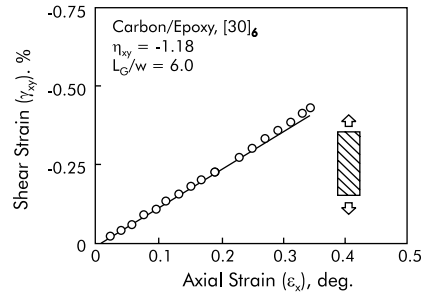

FIGURE 9.5
Shear strain vs. axial strain for a $[30]_6$ carbon/epoxy composite.

$$\varepsilon(45°) = (\varepsilon_x + \varepsilon_y + \gamma_{xy})/2 \tag{9.23a}$$

$$\varepsilon(-45°) = (\varepsilon_x + \varepsilon_y - \gamma_{xy})/2 \tag{9.23b}$$

Combining Equations (9.23) yields

$$\varepsilon_y = \varepsilon(45°) + \varepsilon(-45°) - \varepsilon_x \tag{9.24}$$

$$\gamma_{xy} = \varepsilon(45°) + \varepsilon(-45°) \tag{9.25}$$

Young's modulus, E_x, is determined from the initial slope of the curve σ_x vs. ε_x. Poisson's ratio, ν_{xy}, is obtained by plotting the negative of the strain ε_y vs. ε_x and determining the slope of the line. The shear coupling ratio, η_{xy}, is determined by plotting shear strain vs. axial strain, as shown in Figure 9.5 for a 30° off-axis carbon/epoxy specimen. Note that the experimentally determined properties are apparent because they may be influenced by the constraints imposed by the grips.

Figures 9.6–9.8 show experimentally obtained off-axis modulus, Poisson's ratio, and shear coupling ratio vs. off-axis angle for carbon/fiber composites. Shown in these graphs are reduced data (apparent), theoretical curves calculated assuming the ends of the specimen are free to rotate (Equations (9.9)), and theoretical curves calculated using a correction for end constraint according to Section 9.2. It is observed that the apparent modulus and Poisson's ratio are larger than the unconstrained value, whereas the magnitude of the apparent shear coupling ratio is reduced because of end constraints. The expressions in Section 9.2 incorporating end constraints due to finite aspect ratio bring the analytical results in close agreement with measured data.

The apparent shear modulus, G_{12}, determined for a carbon/polyimide composite using Equations (9.6) – (9.8) and corrected for shear stress and end constraint using Equation (9.20), is shown vs. off-axis angle in Figure 9.9. At off-axis angles up to 30° the end constraint will increase the apparent

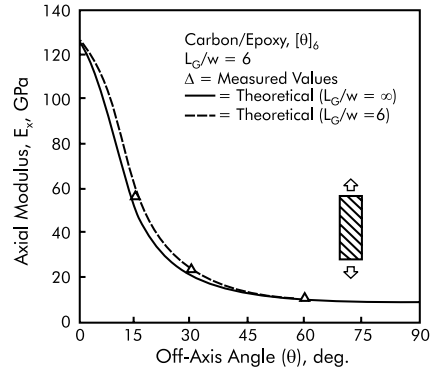

FIGURE 9.6
Axial modulus vs. off-axis angle for a carbon/epoxy composite.

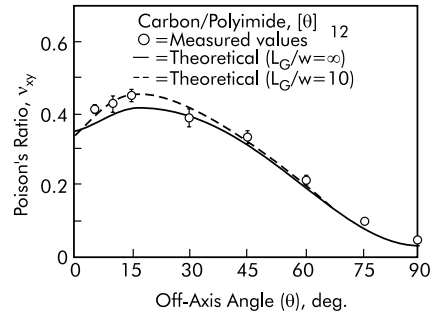

FIGURE 9.7
Poisson's ratio vs. off-axis angle for a carbon/polyimide composite.

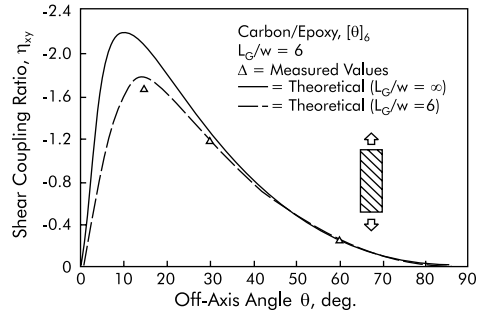

FIGURE 9.8
Shear coupling ratio vs. off-axis angle for a carbon/epoxy composite.

modulus. Correction of the apparent shear modulus for end constraint brings the value closer to the asymptotic value. This graph emphasizes the need to use off-axis specimens of angles 45° or greater when evaluating the shear modulus.

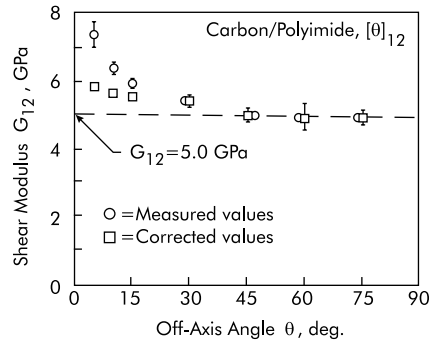

FIGURE 9.9
Shear modulus vs. off-axis angle for a carbon/polyimide composite [3].

TABLE 9.1

Basic Ply Mechanical Properties for Carbon/Epoxy and Carbon/Polyimide Composites Considered in Figures 9.5–9.10

Material	E_1 (GPa)	E_2 (GPa)	ν_{12}	G_{12} (GPa)
Carbon/epoxy	126	10.0	0.30	5.2
Carbon/polyimide [3]	137	9.79	0.35	5.0

As a reference, basic ply properties for the carbon/epoxy and carbon/polyimide composites considered are listed in Table 9.1.

9.5.2 Tensile Strength of Off-Axis Specimen

Table 9.2 presents off-axis tensile strength data for the carbon–epoxy composite. Figure 9.10 shows experimentally determined failure stress vs. off-axis angle for a carbon/epoxy composite (Table 9.2). Excellent agreement is noted.

TABLE 9.2

Off-Axis Strength Data for a Carbon/Epoxy Composite

Angle, θ (degrees)	Tensile Strength (MPa)
5	780
15	305
30	112
60	65

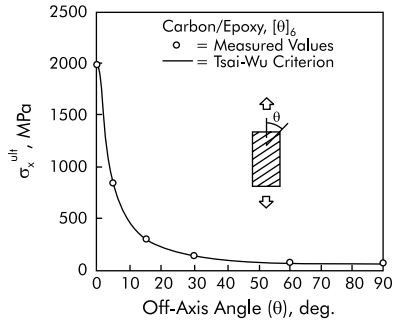

FIGURE 9.10
Tensile failure stress vs. off-axis angle for a carbon/epoxy composite.

References

1. C.C. Chamis and J.H. Sinclair, Ten-degree off-axis test for shear properties in fiber composites, *Exp. Mech.*, 17, 339–346, 1977.
2. J.C. Halpin and N.J. Pagano, Influence of end constraint in the testing of anisotropic bodies, *J. Compos. Mater.*, 2, 18–31, 1968.
3. M.J. Pindera and C.T. Herakovich, Shear characterization of unidirectional composites with the off-axis tension test, *Exp. Mech.*, 26, 103–112, 1986.
4. R.B. Pipes and B.W. Cole, On the off-axis strength test of anisotropic materials, *J. Compos. Mater.*, 7, 246–256, 1973.
5. M.J. Pindera and C.T. Herakovich, *An Endochronic Theory for Transversely Isotropic Fibrous Composites*, Report VPI-E-81-27, Virginia Polytechnic Institute and State University, Blacksburg, VA, 1981.
6. S. Chatterjee, D.F. Adams, and D.W. Oplinger, *Test Methods for Composites — A Status Report*, Vol. III., Shear Test Methods, DOT/FAA/CT-93/17 III, FAA Technical Center, Atlantic City International Airport, NJ, June 1993.

10

Lamina Thermoelastic Response

Most materials change their dimensions as the temperature is changed. Thermal expansion is defined as the change of dimensions of a body or material as a result of a temperature change. Such a property is very important in the application of composite materials in structures that undergo temperature changes, such as engine parts and space structures. The material property constant describing this phenomenon is the coefficient of thermal expansion (CTE), indicated by the symbol α, and defined as

$$\alpha = \frac{\Delta\varepsilon}{\Delta T} \tag{10.1}$$

where $\Delta\varepsilon$ is the increment of strain measured for an unconstrained material subject to a temperature change, ΔT. For an orthotropic composite lamina under plane deformation, Equation (10.1) becomes

$$\alpha_1 = \frac{\Delta\varepsilon_1}{\Delta T} \tag{10.2a}$$

$$\alpha_2 = \frac{\Delta\varepsilon_2}{\Delta T} \tag{10.2b}$$

where $\Delta\varepsilon_1$ and $\Delta\varepsilon_2$ are the thermally induced strains in the principal material directions.

Several methods have been devised for measuring thermal expansion coefficients of composite materials [1]. Basically, this determination requires a controlled temperature chamber and a deformation measuring device. ASTM Standards E228 [2], D696 [3], and E831 [4] propose using a vitreous silica dilatometer or thermomechanical analysis (TMA) apparatus for materials with CTE values as small as 5×10^{-6}/°C. ASTM Standard E289 [5] describes a method based on interferometry, which permits determination of CTE of materials with extremely small thermal expansion coefficients, as low as 10^{-8}/°C, over a large temperature range. For composites, strain gages have been successfully used for measuring thermal expansion coefficients as low as about 10^{-5}/°C [6–8]. Strain gages are readily available and require

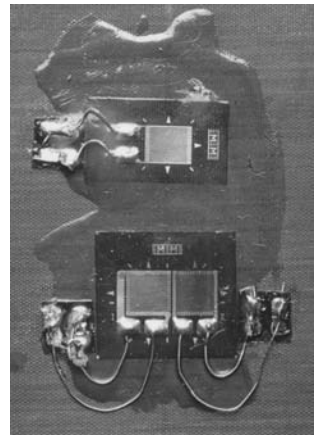

FIGURE 10.1
Typical carbon/epoxy specimen fitted with strain gages (bottom) and temperature sensor (top).

no special apparatus except for the strain-reading instrument. Strain gages may be bonded to the surface of a specimen or embedded between the plies in a laminate. Here, we will restrict attention to surface-bonded strain gages.

The test specimen used for determining the CTEs of a unidirectional lamina or woven fabric ply using strain gages should be a flat panel. Although the in-plane dimensions are not critical, a commonly used specimen size is 50 × 50 (mm) (Figure 10.1). The thickness of the panel is commonly about 1 mm. Panels that are too thin are easily cracked if they are unidirectional, and panels that are too thick require a long soaking time to achieve thermal equilibrium (uniform temperature). The temperature can be monitored with a temperature sensor or a thermocouple. The temperature range should be selected with regard to the type of strain gages and sensors used and the temperature capability of the resin in the composite. For a typical 175°C-cure epoxy–matrix composite, a suitable temperature range is 20 to 150°C. Because moisture induces dimensional changes in many resin systems, it is important to dry the specimens in an oven at 70°C until the weight stabilizes before measuring the thermal strains. As discussed in Reference [1], an important limitation of strain gages is their upper use temperature. Maximum-accuracy gages can only be used up to 65°C [9]. Other types of strain gages may be used to extend this range. Another important limitation of the use of strain gages is undesirable local reinforcement of the test material by the metal foil strain gage [1]. At elevated temperatures the transverse stiffness of unidirectional polymer– matrix composites will decrease as a result of softening of the matrix resin. Local reinforcement of the tested material by the gage would lead to apparent CTE values that are too small.

The adhesive bond between the strain gage and specimen is also an important factor when measuring CTE with strain gages. Because it is typically a polymer resin, the adhesive may soften at elevated temperatures and exhibit viscoelastic creep or stress relaxation effects that would

influence the strain readings. Selection of strain gage adhesive to match the anticipated temperature range is thus important.

10.1 Temperature Gage Sensing System

To monitor temperature, it is convenient to use a resistance gage circuit, which allows the experimenter to monitor the temperature of a test specimen while simultaneously taking strain readings. The temperature gage (such as a Micro Measurements Type ETG-50B or equivalent [9]) consists of a sensing grid of high-purity nickel foil that is bonded to the specimen by standard strain gage techniques using a high-temperature adhesive (M-Bond 600 or equivalent [9]) (Figure 10.1). This temperature sensor exhibits a linear change in resistance with temperature.

After the gage has been properly mounted and wired, it is connected to the gage scanning equipment along with the other strain gages being used. A special resistance network (Micro Measurements Type LST-10F-350D, or equivalent [9]) may be incorporated in the circuit, which modifies the gage signal, producing a direct readout of the temperature in degrees celsius or fahrenheit. The temperature readout is set to room temperature before testing, and then the proper gage factor is set. Lead wires exposed to temperatures greater than about 75°C should be protected with a high-temperature plastic wrap. Many laboratories use thermocouples as an alternative to temperature gages. One or several thermocouples may be attached to the specimen.

10.2 Temperature Compensation

In nonisothermal applications of strain gages, techniques must be employed to compensate for changes in the performance characteristics of the gages resulting from a change in temperature [10]. The change in performance of the gage relates to the following:

- The gage dimensions change with temperature.
- The resistance of the gage changes with temperature.
- Transverse strain sensitivity of the gage (Chapter 4) will induce an error in the measurements.
- The gage factor may change with temperature.

To account for the influence of some of these factors, consider a strain gage bonded to a composite specimen. For a given temperature change $\Delta T = T - T_0$,

where T_0 is the initial temperature, the relative change in gage resistance, $\Delta R/R$, may be expressed as

$$(\Delta R/R) = (\alpha_c - \alpha_g)S_g\Delta T + \gamma\Delta T \tag{10.3}$$

where α_c and α_g are the CTEs of the composite and the gage, respectively; γ is the temperature coefficient of resistivity of the gage material; and S_g is the gage factor, here assumed to be constant. For a large temperature change, it is also necessary to take into account the temperature dependence of the gage factor. Thus, the gage will be subjected to a strain mismatch of $(\alpha_c - \alpha_g)\Delta T$. If the coefficient γ is not zero, the strain measuring system will record an apparent strain that physically does not exist. To correct the apparent strain reading, a common temperature compensation method includes a reference gage, identical to the one bonded to the composite, mounted on a substrate with known CTE. For the gage bonded to the composite, Equation (10.3) gives

$$(\Delta R_1/R) = (\alpha_c - \alpha_g)S_g\Delta T + \gamma\Delta T \tag{10.4a}$$

and for the gage bonded to the reference substrate,

$$(\Delta R_2/R) = (\alpha_r - \alpha_g)S_g\Delta T + \gamma\Delta T \tag{10.4b}$$

where α_r is the CTE of the reference substrate. Combining of Equations (10.4) yields

$$\alpha_c = \alpha_r + \frac{\Delta R_1 - \Delta R_2}{RS_g\Delta T} \tag{10.5}$$

or equivalently,

$$\alpha_c = \alpha_r + (\varepsilon_c - \varepsilon_r)/\Delta T \tag{10.6}$$

where ε_c and ε_r are the strain readings for the composite and the reference substrate, respectively.

If the gages are connected in a Wheatstone half-bridge, the changes in resistance of the two gages, ΔR_1 and ΔR_2, are subtracted (Figure 10.2). Thus, the output voltage of the bridge is directly proportional to the difference $(\varepsilon_c - \varepsilon_r)$.

The choice of reference material should be determined by the anticipated magnitude of α_c. If the values of α_c and α_r are very close, the apparent strain measured, $\varepsilon_c - \varepsilon_r$, will be very small and the sensitivity of the measurement will suffer. A common reference material is quartz (with $\alpha_r \approx 0.56 \times 10^{-6}/°C$). Consequently, measurements of CTEs less than $0.56 \times 10^{-6}/°C$ may exhibit poor resolution. In addition, the accuracy of the gage and strain measuring

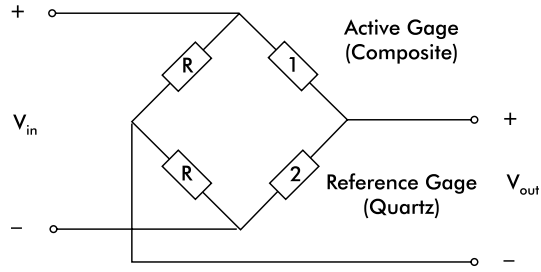

FIGURE 10.2
Wheatstone half bridge circuit.

system, typically $\pm 2 \times 10^{-6}$, may limit the accuracy of the measurement of small CTEs.

To measure the generally very small CTEs in the fiber direction of unidirectional composites (see Table 1.2) with sufficient accuracy, it may be necessary to use the dilatometric or interferometry techniques mentioned early in this chapter.

10.3 Measurement of Thermal Expansion

1. Bond two strain gages (Micro Measurements Type WK-06-125AC or equivalent [9]) and one temperature sensor (or thermocouple) to the composite specimen. Align the strain gages (Figure 10.1) parallel to the principal material directions. Use a high temperature strain gage adhesive cured according to adhesive specifications. Locate the strain gages and temperature sensor near the specimen center and on the same side to minimize the possible influence of thermal gradients.
2. Place the composite specimen and the reference material inside a laboratory oven (near the center). The gage lead wires inside the oven should be protected by a temperature-resistant coating such as Teflon.
3. Connect the strain gages and the temperature sensor (or thermocouple, or both) to the recording system.
4. Raise the oven temperature slowly to 150°C. Monitor the oven thermometer, making strain and temperature measurements at regular temperature intervals. After a temperature of 150°C is reached, reduce the oven temperature slowly to room temperature. Take strain and temperature measurements also during this cool down period. Occasionally some composites display hysteresis during the first cycle, but stabilize during subsequent cycles. Multiple temperature cycles are therefore desirable.

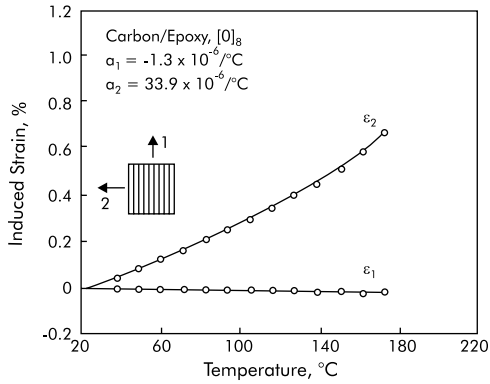

FIGURE 10.3
Thermal expansion strains for a carbon/epoxy composite. (From Whitney, J.M., Daniel, I.M., and Pipes, R.B., *Experimental Mechanics of Fiber Reinforced Composite Materials*, rev. ed., Prentice-Hall, Englewood Cliffs, NJ, 1984. With permission.)

10.4 Data Reduction

From the apparent strain measured via the half bridge, $\varepsilon_A = \varepsilon_c - \varepsilon_r$, the actual strain, ε_c, is determined from Equation (10.6),

$$\varepsilon_c = \alpha_r \Delta T + \varepsilon_A \tag{10.7}$$

Plot ε_c vs. the temperature, T, or the change in temperature, $\Delta T = T - T_0$, where T_0 is the initial temperature of the specimen. Figure 10.3 shows typical thermal strain data for a carbon/epoxy specimen upon heating [6]. To determine the CTE in the actual temperature range, evaluate the slope of the strain vs. temperature plot. Figure 10.4 shows examples of plots of thermal strains vs. temperature for Kevlar (E.I. du Pont de Nemours and Company)/epoxy and S-glass/epoxy composites. The determination of CTE discussed here inherently assumes linear expansion over the temperature range considered. For polymers at temperatures above their glass transition temperature, T_g, the CTE is larger than at temperatures below T_g. Such phenomena and other factors make the expansion vs. temperature curve more complex, and sometimes nonlinear. For such cases it is common to specify a temperature range of interest and calculate CTE for this range using a linear least-squares fit.

Hysteresis is often observed upon cooling (Figure 10.5). Hysteresis is generally thought to be a result of viscoelastic creep and stress relaxation effects in the adhesive that bonds the gage to the specimen that are magnified by the increased temperature. It is also possible that residual thermal stresses in the composite will relax at elevated temperatures, which may change the dimensions. Higher rates of temperature change appear to

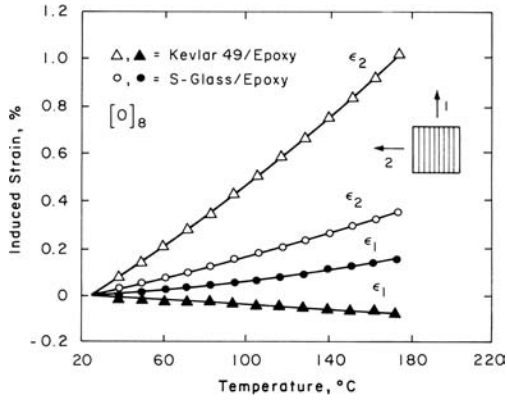

FIGURE 10.4

Thermal expansion strains for Kevlar/epoxy and S-glass/epoxy composites. Kevlar/epoxy: $\alpha_1 = -4.0 \times 10^{-6}/°C$, $\alpha_2 = 57.6 \times 10^{-6}/°C$. S-glass/epoxy: $\alpha_1 = 6.6 \times 10^{-6}/°C$, $\alpha_2 = 19.7 \times 10^{-6}/°C$. (From Whitney, J.M., Daniel, I.M., and Pipes, R.B., *Experimental Mechanics of Fiber Reinforced Composite Materials*, rev. ed., Prentice-Hall, Englewood Cliffs, NJ, 1984. With permission.)

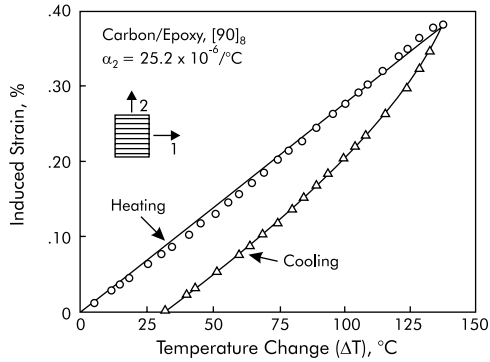

FIGURE 10.5

Thermal expansion response in the transverse direction for a carbon/epoxy composite showing hysteresis upon cooling.

produce more hysteresis, indicating that the material is not in thermal equilibrium. However, at lower temperatures the slopes of the heating and the cooling curves are consistent.

References

1. D.F. Adams, *Dimensional Stability (Thermal)*, Section 6.4.9.1 in MIL-HDBK-17, Technomic, Lancaster, PA, 2000.
2. ASTM Standard E 228-95, *Test Method for Linear Thermal Expansion of Solid Materials with a Vitreous Silica Dilatometer*, American Society for Testing and Materials, West Conshohocken, PA, 2001.

3. ASTM Standard D 696-98, *Test Method for Coefficient of Linear Thermal Expansion of Plastics between –300C and 30C*, American Society for Testing and Materials, West Conshohocken, PA, 2001.
4. ASTM Standard E 831-00, *Test Method for Linear Thermal Expansion of Solid Materials by Thermomechanical Analysis*, American Society for Testing and Materials, West Conshohocken, PA, 2001.
5. ASTM Standard E 289-99, *Test Method for Linear Thermal Expansion of Rigid Solids with Interferometry*, American Society for Testing and Materials, West Conshohocken, PA, 2001.
6. J.M. Whitney, I.M. Daniel, and R.B. Pipes, *Experimental Mechanics of Fiber Reinforced Composite Materials*, rev. ed., Society for Experimental Mechanics, Prentice-Hall, Englewood Cliffs, NJ, 1984.
7. W. Freeman and M.D. Campbell, Thermal expansion characteristics of graphite reinforced composite materials, *ASTM Spec. Tech. Publ.*, 497, 121–142, 1972.
8. G. Yaniv, G. Peimanidis, and I.M. Daniel, Method for hygromechanical characterization of graphite/epoxy composite, *J. Compos. Technol. Res.*, 9, 21–25, 1987.
9. *Measurement of Thermal Expansion Coefficient Using Strain Gages*, Report TN-513, Measurements Group, Raleigh, NC, Feb. 1987.
10. J.W. Dally and W.F. Riley, *Experimental Stress Analysis*, 3rd ed., McGraw-Hill, New York, 1991.

11

Laminate Mechanical Response

The same mechanical tests used to characterize a lamina, i.e., tension, compression, shear (except for the $[\pm 45]_{ns}$ tensile shear test), and possibly flexure, must be performed to experimentally characterize a laminate as well. However, the complexity of the mechanical behavior of a laminated plate (Figure 11.1) is considerably greater than that of the lamina discussed in previous chapters. Because the laminate generally includes off-axis plies (a unidirectional composite consisting of multiple unidirectional laminae is sometimes also referred to as a laminate), the stress state in a given ply is biaxial in the interior. Moreover, at free edges a fully three-dimensional stress state develops [1–3], and edge delamination may occur [2]. The free-edge effect, however, has been shown to be limited to a boundary-layer region, which extends only about one laminate thickness in from the free edge [1–3]. Classical laminated plate theory [4], reviewed in Chapter 2, is an accurate predictor of the stress state in the remainder of the laminate, and of the overall behavior of the laminate. In this chapter, all analysis will therefore be based on classical laminated plate theory.

The mechanical response of the composite laminate is typically monitored using the same strain instrumentation as previously discussed for lamina response, to establish similar stiffness, strength, and strain to failure properties. The specimen configurations and sizes are usually similar, if not identical. Correspondingly, when appropriate, the specimens must be end tabbed, strain-gaged, and then loaded to ultimate failure.

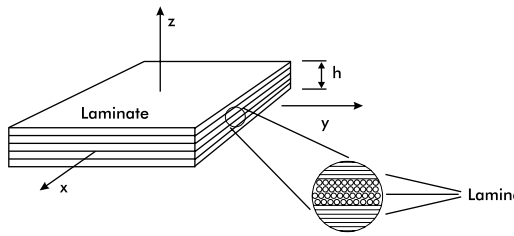

FIGURE 11.1
Forming a laminate by stacking unidirectional plies.

Specimens investigated in this chapter will be limited to symmetric and balanced laminates. Symmetric means that for each ply above the midsurface of the laminate, there is an identical ply of the same orientation at the same distance below the midsurface. Balanced means that for each angle-ply with an orientation angle θ with respect to the x-axis (Figure 11.1), there is an identical ply oriented at –θ with respect to the x-axis. Note that this identical ply can be anywhere within the laminate. Typical examples of such laminates are $[0/\pm45/90]_s$, $[0_2/\pm45]_s$, and $[0/90]_s$.

11.1 Data Reduction for Stiffness Properties

11.1.1 Axial Tension or Compression

The laminate axial tensile or compressive properties to be measured usually include:

- Axial tensile stiffness, E_x
- Major Poisson's ratio, ν_{xy}
- Ultimate axial tensile stress and strain, σ_x^{ult} and ε_x^{ult}

For axial tensile or compressive loading of a symmetric and balanced laminate, the constitutive relation, Equation (2.33), becomes [4]

$$\begin{bmatrix} N_x \\ 0 \\ 0 \end{bmatrix} = \begin{bmatrix} A_{11} & A_{12} & 0 \\ A_{12} & A_{22} & 0 \\ 0 & 0 & A_{66} \end{bmatrix} \begin{bmatrix} \varepsilon_x \\ \varepsilon_y \\ \gamma_{xy} \end{bmatrix} \tag{11.1}$$

where thermal- and moisture-induced stresses have been neglected. Inversion of Equation (11.1) yields

$$\varepsilon_x = \frac{A_{22}N_x}{A_{11}A_{22} - A_{12}^2} \tag{11.2a}$$

$$\varepsilon_y = \frac{-A_{12}\varepsilon_x}{A_{11}} \tag{11.2b}$$

$$\gamma_{xy} = 0 \tag{11.2c}$$

The axial stiffness, E_x, is obtained from Equation (11.2a) as

$$E_x = \frac{N_x}{\varepsilon_x h} = \frac{A_{11}A_{22} - A_{12}^2}{A_{22}h} \tag{11.3}$$

where h is the laminate thickness. The major Poisson's ratio, ν_{xy}, is obtained from Equation (11.2b) as

$$\nu_{xy} = -\frac{\varepsilon_y}{\varepsilon_x} = A_{12}/A_{22} \tag{11.4}$$

11.1.2 Transverse Tension or Compression

The laminate transverse tensile or compressive properties to be measured usually include:

- Transverse tensile stiffness, E_y
- Minor Poisson's ratio, ν_{yx}
- Ultimate transverse tensile stress and strain, σ_y^{ult} and ε_y^{ult}

For transverse tensile or compressive loading of a symmetric and balanced laminate, the constitutive relation, Equation (2.33), becomes [4]

$$\begin{bmatrix} 0 \\ N_y \\ 0 \end{bmatrix} = \begin{bmatrix} A_{11} & A_{12} & 0 \\ A_{12} & A_{22} & 0 \\ 0 & 0 & A_{66} \end{bmatrix} \begin{bmatrix} \varepsilon_x \\ \varepsilon_y \\ \gamma_{xy} \end{bmatrix} \tag{11.5}$$

where thermal- and moisture-induced stresses have been neglected. Inversion of Equation (11.5) yields

$$\varepsilon_x = \frac{-A_{12}\varepsilon_y}{A_{11}} \tag{11.6a}$$

$$\varepsilon_y = \frac{A_{11}N_y}{A_{11}A_{22} - A_{12}^2} \tag{11.6b}$$

$$\gamma_{xy} = 0 \tag{11.6c}$$

The transverse stiffness, E_y, is obtained from Equation (11.6b) as

$$E_y = \frac{N_y}{\varepsilon_y h} = \frac{A_{11}A_{22} - A_{12}^2}{A_{11}h} \tag{11.7}$$

where h is the laminate thickness. The minor Poisson's ratio, ν_{yx}, is obtained from Equation (11.6a) as

$$\nu_{yx} = -\frac{\varepsilon_x}{\varepsilon_y} = A_{12}/A_{11} \tag{11.8}$$

11.1.3 In-Plane Shear

The laminate in-plane shear properties to be measured usually include in-plane shear stiffness (G_{xy}) and ultimate in-plane shear stress and strain, τ_{xy}^{ult} and γ_{xy}^{ult}.

For in-plane shear loading of a symmetric and balanced laminate, the constitutive relation, Equation (2.33) becomes [4]

$$\begin{bmatrix} 0 \\ 0 \\ N_{xy} \end{bmatrix} = \begin{bmatrix} A_{11} & A_{12} & 0 \\ A_{12} & A_{22} & 0 \\ 0 & 0 & A_{66} \end{bmatrix} \begin{bmatrix} \varepsilon_x \\ \varepsilon_y \\ \gamma_{xy} \end{bmatrix} \tag{11.9}$$

where thermal- and moisture-induced stresses have been neglected. Inversion of Equation (11.9) yields

$$\gamma_{xy} = N_{xy}/A_{66} \tag{11.10}$$

The in-plane shear stiffness, G_{xy}, is obtained from Equation (11.10) as

$$G_{xy} = \frac{N_{xy}}{\gamma_{xy} h} = \frac{A_{66}}{h} \tag{11.11}$$

11.1.4 Flexure

Unlike for the in-plane loadings discussed in Sections 11.1.1–11.1.3, the flexural response of a laminate, including a balanced, symmetric laminate, is a function of the stacking sequence of the plies. Nevertheless, because classical lamination theory is applicable, the same general approach can be used. For any symmetric laminate the B matrix is zero. Thus, again neglecting thermal- and moisture-induced effects, Equation (2.34) becomes:

$$\begin{bmatrix} M_x \\ 0 \\ 0 \end{bmatrix} = \begin{bmatrix} D_{11} & D_{12} & D_{16} \\ D_{12} & D_{22} & D_{26} \\ D_{16} & D_{26} & D_{66} \end{bmatrix} \begin{bmatrix} \kappa_x \\ \kappa_y \\ \kappa_{xy} \end{bmatrix} \tag{11.12}$$

Here, M_x is the bending moment in the beam at a particular location along its length. Note that, even if the laminate is balanced, the D_{16} and D_{26} terms are not automatically zero as was previously the case with the A_{16} and A_{26} terms. They are zero for the special case of a cross-ply laminate.

For analysis of bending of a laminated beam it is useful to consider Equation (11.12) in the inverted (compliance) form,

$$\begin{bmatrix} \kappa_x \\ \kappa_y \\ \kappa_{xy} \end{bmatrix} = \begin{bmatrix} D'_{11} & D'_{12} & D'_{16} \\ D'_{12} & D'_{22} & D'_{26} \\ D'_{16} & D'_{26} & D'_{66} \end{bmatrix} \begin{bmatrix} M_x \\ 0 \\ 0 \end{bmatrix} \tag{11.13}$$

To develop a beam formulation it is customary to assume that the deflection, w, is a function of x only, which is reasonable for long and narrow beams [5]

$$w = w(x) \tag{11.14}$$

Combining the definition of κ_x with Equations (11.13) and (11.14) yields

$$\frac{d^2w}{dx^2} = -D'_{11}M_x \tag{11.15}$$

This equation is identical to the classical differential equation governing bending of isotropic and homogeneous beams [6] (if κ_{xy} is unconstrained), and may be integrated to yield the deflection for various loading and support conditions. Caution has to be exercised, however, for laminated beams with D_{16} terms, which indicate a tendency for the beam to twist under bending loads, as indicated by Equation (11.13) (see also Reference [5]).

For the analysis of stresses in each ply (k) of the beam, Equation (2.30) may be combined with Equations (2.24) and (11.13) to yield

$$\begin{bmatrix} \sigma_x \\ \sigma_y \\ \tau_{xy} \end{bmatrix}_k = z \begin{bmatrix} \overline{Q}_{11} & \overline{Q}_{12} & \overline{Q}_{16} \\ \overline{Q}_{12} & \overline{Q}_{22} & \overline{Q}_{26} \\ \overline{Q}_{16} & \overline{Q}_{26} & \overline{Q}_{66} \end{bmatrix}_k \begin{bmatrix} \kappa_x \\ \kappa_y \\ \kappa_{xy} \end{bmatrix} \tag{11.16}$$

The $\overline{Q}$ terms in Equation (11.16) are defined in Appendix A.

At this point, a specific laminate configuration must be selected to evaluate the $\overline{Q}$ terms. For example, Reference [7] details a solution for a specific condition where there is no bending–twisting coupling, i.e., all the plies are oriented at either 0° or 90°.

Having carried through the analysis for a specific laminate of interest, comparisons with experimental data can be made using the same equations presented in Chapter 8 to reduce the experimental data.

11.2 Laminate Strength Analysis

Strength analysis of the laminate is performed as outlined in Section 2.5. The ply stresses are calculated for a unit load, e.g., $N_x = 1$, and for the actual temperature and moisture conditions experienced, and substituted into the selected failure criterion. N_x is then increased until that failure criterion is satisfied and first-ply failure occurs. Many current designs do not allow first-ply failure.

Failure of a ply may or may not lead to laminate failure. If the remaining plies of the laminate are able to carry the load redistributed at first-ply failure, further loading may be applied to the laminate. A conservative estimate of the laminate behavior after first-ply failure is based on the assumption that certain of the elastic stiffness properties are removed from the laminate constitutive relation. For example, matrix cracking in a unidirectional composite ply, illustrated schematically in Figure 11.2, leaves the fibers intact, and the ply still can carry load in the fiber direction. Jones [4] presents a laminate failure analysis where the modulus E_1 remains intact while the following transverse properties of the cracked ply are assumed to be close to zero:

$$E_2 = \nu_{12} = G_{12} \approx 0 \tag{11.17}$$

From this assumption, new stiffness matrices, Equation (11.1), for the lamina and laminate containing ply cracks are determined, and further load is applied until the next ply failure occurs. This procedure is repeated until last-ply failure occurs, indicating total failure. More elaborate analyses of damaged composites are presented in References [8,9].

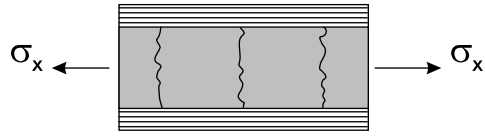

FIGURE 11.2
Matrix cracking of a ply in a laminate.

11.3 Test Specimen Preparation

Symmetric and balanced laminate panels should be prepared. Typical examples are $[0/\pm45/90]_s$, $[0_2/\pm45]_s$, and $[0_2/90_2]_s$. A typical specimen preparation procedure is to bond end tabs if required (Chapter 4) and machine the specimens to the required dimensions. It is critical that the specimens be taken from the fabricated panel in the orientations desired. For example, the $[0_2/\pm45]_s$ laminate becomes a $[90_2/\mp45]_s$ laminate if cut from the panel perpendicular to the direction intended.

Measure the cross-sectional dimensions (average six measurements) and check for parallelism of the edges and of the end-tab surfaces. If required, apply strain gages as appropriate for the specific test to be performed.

11.4 Test Procedures

Many test procedure details are common to all types of testing to be performed. These details include, for example, correctly installing the specimen in the grips or test fixture and ensuring that proper alignment is attained and proper gripping–clamping forces are used when appropriate. Testing machine settings, particularly load range, strain instrumentation calibrations, and data acquisition systems, should be checked.

11.4.1 Tension Test Procedures

A laminate tensile specimen is typically about 225 mm long and 25 mm wide. For an axial tensile test, two strain gages are mounted at the center of each specimen, one in the longitudinal direction and one in the transverse direction, so that both the axial stiffness, E_x, and major Poisson's ratio, ν_{xy}, can be determined.

Mount the specimen in mechanical wedge grips or hydraulic grips, as discussed in Chapter 4. Set the crosshead rate at about 0.5 to 1 mm/min. Avoid unprotected eyes in the test area. The strain readings may be recorded continuously, or at discrete load intervals. If discrete data are recorded, a sufficient number of data points are required to adequately reproduce the stress–strain behavior. A total of 40 to 50 points, with at least 25 data points in the linear response region, are desirable to establish the total stress–strain response. Monitor all specimens to failure. Plot the data for subsequent reduction.

11.4.2 Compression Test Procedures

Because only relatively thin laminates are usually available for testing, gross buckling of the specimen must be prevented. Thus, some type of lateral restraint fixturing is required. It is important to ensure that this fixturing does not create a redundant load path. As discussed in Chapter 6, each compression test method has its own unique fixture. However, in all cases proper specimen installation in the fixture is critical. Specimen dimensions are typically the same as for lamina testing.

Whether the specimen is end-loaded or shear-loaded, specimen tabs may be required, either to prevent end crushing or gripping surface damage. However, because laminates typically have lower compressive strengths than unidirectional composites, a particular test may not require tabs. It is important to recognize when tabs are not needed because their use increases specimen preparation cost and potentially introduces additional stress concentrations and loading abnormalities, as discussed in Chapter 6.

11.4.3 Shear Test Procedures

As noted in Chapter 7, for a unidirectional composite the short beam shear test method can be used to indirectly obtain the lamina in-plane shear strength, by assuming $\tau_{12} = \tau_{13}$. For a laminate, however, only interlaminar shear strength is obtained using this test method.

The ±45° tensile shear test is not applicable for laminates. The Iosipescu and rail shear test methods are applicable. However, the in-plane shear failure modes for laminates are quite different than those for unidirectional composites. Unidirectional composites subjected to shear loadings fail in a clean manner parallel to the fibers. Laminates do not have these weak through-the-specimen-thickness planes of failure because the individual plies are at different orientations. The resulting failure path can be very tortuous and the damage zone very extensive. It is important that the test fixture geometry not inhibit the failure mode. The dimensions of the Iosipescu and short beam shear specimens are the same as for lamina testing.

11.4.4 Flexural Test Procedures

As previously noted in Section 11.1.4, the ply stacking sequence of the laminate influences the composite stiffness properties measured in a flexural test. It also influences the flexural strength. Thus, it is important to verify that the orientation of the laminate being tested is that intended.

Because both the flexural stiffness and the shear stiffness vary with the laminate orientation being tested, a different span length-to-specimen thickness ratio may be required than would be used to test a unidirectional composite of the same material. The same guidelines as indicated in Section 8.1 apply, however.

11.5 Data Reduction

To determine the laminate properties, recall the following definitions:

E_x	Initial slope of the axial normal stress-strain curve ($\Delta\sigma_x/\Delta\varepsilon_x$) for the laminate tension or compression test
ν_{xy}	Negative ratio of the transverse to longitudinal strains ($-\varepsilon_y/\varepsilon_x$) for the laminate axial tension or compression test
σ_x^{ult}	Ultimate load/initial cross-sectional area for the axial tension or compression test
G_{xy}	Initial slope of the shear stress-strain curve ($\Delta\tau_{xy}/\Delta\gamma_{xy}$) for the laminate shear test
τ_x^{ult}	Shear strength as calculated for the particular shear test method used
E_x^{flex}	Initial slope of the flexural stress–strain curve for the laminate axial flexural test
σ_x^{flex}	Axial flexural stresses at failure in each ply as calculated using Equation (11.16) for the particular laminate configuration being subjected to a flexural loading

Determine the axial tensile and compressive stiffnesses and major Poisson's ratios by least-squares fits of the initial slopes of σ_x vs. ε_x and σ_x vs. ε_y. The transverse tensile and compressive stiffnesses, and if they are to be determined, the minor Poisson's ratios, are determined accordingly, for loadings in the y direction. The shear stiffness and flexural stiffness are likewise determined by least-squares fits of the initial slopes of the corresponding stress–strain curves.

Figure 11.3 shows typical axial tensile stress–strain responses for a $[0/\pm45/90]_s$ carbon/epoxy laminate. Data reduction gave the following mechanical properties of the laminate: $E_x = 56.5$ GPa, $\nu_{xy} = 0.34$, and $\sigma_x^{ult} = 626$ MPa.

11.6 Example of a Typical Analysis: Axial Tensile Response of a Laminate

To analyze the tensile response of the laminate, the lamina properties are required. Consider the following set of carbon/epoxy ply properties:

$E_1 = 140$ GPa	$X_1^T = 1950$ MPa	$S_6 = 85$ MPa
$E_2 = 10.3$ GPa	$X_1^C = 1500$ MPa	$\alpha_1 = -0.7 \times 10^{-6}/°C$

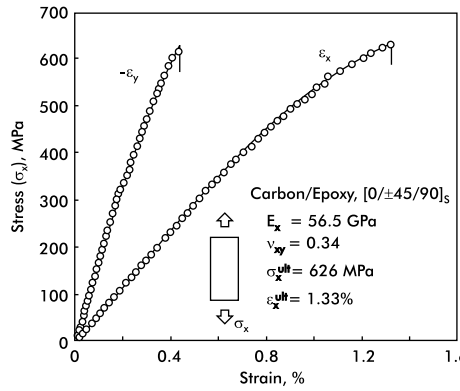

FIGURE 11.3
Tensile stress–strain response for a $[0/\pm45/90]_s$ carbon/epoxy test specimen.

$\nu_{12} = 0.29$ $\quad X_2^T = 48$ MPa $\quad \alpha_2 = 31.2 \times 10^{-6}/°C$

$G_{12} = 5.15$ GPa $\quad X_2^C = 130$ MPa $\quad h_{ply} = 0.127$ mm

Lamination theory gives, with the above lamina properties, $E_x = 54.2$ GPa and $\nu_{xy} = 0.31$, in good agreement with measured values listed in Figure 11.3. Nonlinear behavior is noted beyond approximately 400 MPa in Figure 11.3. This may be due to ply cracking, which renders the laminate more compliant.

Failure of the laminate was analyzed using both the maximum stress and Tsai-Wu strength criteria (see Section 2.5). Stress–strain levels for ply failures were calculated on the basis of the ply properties listed above and a temperature change $\Delta T = -150°C$. The results are listed in Table 11.1. It is observed that the 90° ply is predicted to fail first. The ±45° plies then fail, followed by last-ply failure of the 0° plies (fiber failure). Note that the 90° ply is predicted to fail at stresses significantly lower than the experimentally measured ultimate stress, $\sigma_x^{ult} = 626$ MPa. Last-ply failure, on the other hand, is predicted to occur at stresses somewhat greater than the experimentally determined value. The ply failures preceding ultimate laminate failure were neglected in the calculations. Incorporation of ply failures by degradation

TABLE 11.1

Calculated Ply Failure Stresses and Strains in the Laminate Coordinate System for a $[0/\pm45/90]_s$ carbon/epoxy laminate ($\Delta T = -150°C$)

Ply Angle (deg)	σ_x (MPa)	
	Max. Stress Criterion	Tsai-Wu Criterion
90	113	102
±45	231	220
0	768	738

of transverse properties should result in more realistic ultimate strength predictions. The differences between the ply failure predictions as a result of the choice of failure criterion will also be noted.

Note that the analyses of laminate ultimate strength reviewed here are highly approximate because the damage introduced after the occurrence of first-ply failure is not considered or is considered in an ad-hoc manner. The prediction of first-ply-failure stress is more reliable because the laminate is undamaged up to this point. The first-ply-failure criterion is appropriate for many current designs that do not allow ply cracks in any part of a structure.

References

1. N.J. Pagano and R.B. Pipes, The influence of stacking sequence on laminate strength, *J. Compos. Mater.*, 5, 50–57, 1971.
2. N.J. Pagano and R.B. Pipes, Some observations on the interlaminar strength of composite laminates, *Int. J. Mech. Sci.*, 15, 679–688, 1973.
3. R.B. Pipes, B.E. Kaminski, and N.J. Pagano, Influence of the free-edge upon the strength of angle-ply laminates, *ASTM Spec. Tech. Publ.*, 521, 218–228, 1973.
4. R.M. Jones, *Mechanics of Composite Materials*, 2nd ed., Taylor & Francis, Philadelphia, 1999.
5. J.M. Whitney, *Structural Analysis of Laminated Anisotropic Plates*, Technomic, Lancaster, PA, 1987.
6. J.M. Gere and S.P. Timoshenko, *Mechanics of Materials*, 4th ed., PWS Publishing, Boston, 1997.
7. R.F. Gibson, *Principles of Composite Material Mechanics*, McGraw-Hill, New York, 1994.
8. A.L. Highsmith and K.L. Reifsnider, Stiffness-reduction mechanisms in composite laminates, *ASTM Spec. Tech. Publ.*, 115, 103–117, 1982.
9. Z. Hashin, Analysis of cracked laminates — a variational approach, *Mech. Mater.*, 4, 121–136, 1985.

12

Laminate Thermoelastic Response

The thermoelastic response of a general laminate may be very complex [1]. For the particular case of unsymmetric laminates, bending–extension coupling, Equations (2.44) and (2.45) indicate the existence of out-of-plane deflections for a laminate subject to a temperature change. Hyer [2] and Dang and Hyer [3] have performed very detailed experiments and analysis of warping deformations of unsymmetric composite laminates during cooling from elevated (cure) temperatures. For symmetric laminates, however, it can be shown that the bending–extension coupling disappears, [B] = [0]. For a balanced laminate, $A_{16} = A_{26} = 0$. Hence, a symmetric and balanced laminate behaves as a homogeneous orthotropic material in a macroscopic sense. Typical balanced symmetric laminates are $[0/\pm45/90]_s$, $[0_2/\pm45]_s$, and $[0_2/90_2]_s$.

For a symmetric and balanced laminate, Equation (2.51) yields

$$\begin{bmatrix} \varepsilon^\circ \\ \kappa \end{bmatrix} = \begin{bmatrix} A' & 0 \\ 0 & D' \end{bmatrix} = \begin{bmatrix} N^T \\ M^T \end{bmatrix} \tag{12.1}$$

where $[N^T]$ and $[M^T]$ are given by Equations (2.37) and (2.38). It may also be shown that the thermal moment resultants vanish, $[M^T] = [0]$, and the thermal in-plane shear force resultant $N_{xy}^T = 0$. Equations (12.1) then yield

$$\left[\varepsilon^0\right] = \left[A'\right]\left[N^T\right] \tag{12.2a}$$

$$[\kappa] = [0] \tag{12.2b}$$

Hence, a symmetric laminate does not bend due to a temperature change (Equation (12.2b)). The expanded form of Equation (12.2a) is

$$\begin{bmatrix} \varepsilon_x \\ \varepsilon_y \\ \gamma_{xy} \end{bmatrix} = \begin{bmatrix} A'_{11} & A'_{12} & 0 \\ A'_{12} & A'_{22} & 0 \\ 0 & 0 & A'_{66} \end{bmatrix} \begin{bmatrix} N_x^T \\ N_y^T \\ 0 \end{bmatrix} \tag{12.3}$$

Consequently, $\gamma_{xy} = 0$, which shows that a balanced laminate will not deform in shear due to the temperature change.

The thermal expansion coefficients of the laminate, α_x and α_y, are obtained from

$$\alpha_x = \frac{\varepsilon_x}{\Delta T} \tag{12.4a}$$

$$\alpha_y = \frac{\varepsilon_y}{\Delta T} \tag{12.4b}$$

where ΔT is the temperature change from the reference state. Combining Equations (12.3) and (12.4) yields

$$\alpha_x = \left(A'_{11}N_x^T + A'_{12}N_y^T\right)\Big/\Delta T \tag{12.5a}$$

$$\alpha_y = \left(A'_{12}N_x^T + A'_{22}N_y^T\right)\Big/\Delta T \tag{12.5b}$$

where the compliance elements, A'_{ij}, are

$$A'_{11} = \frac{A_{22}}{A_{11}A_{22} - A_{12}^2} \tag{12.6a}$$

$$A'_{12} = \frac{-A_{12}}{A_{11}A_{22} - A_{12}^2} \tag{12.6b}$$

$$A'_{22} = \frac{A_{11}}{A_{11}A_{22} - A_{12}^2} \tag{12.6c}$$

To determine the laminate thermal expansion coefficients, the effective thermal forces $[N_x^T, N_y^T]$ and the stiffnesses A_{11}, A_{12}, and A_{22} are calculated using Equations (2.37) and (2.35a), respectively. Such calculation requires knowledge of the basic ply (lamina) mechanical properties and thermal expansion coefficients. The calculation of the laminate thermal expansions is quite involved. It is recommended that a computer code be used.

12.1 Preparation of Test Specimens and Measurement of Thermal Expansion

The test specimen used for determining thermal expansion coefficients should be a representative 50×50 mm flat panel of the laminate. Apply two

strain gages and one temperature sensor (or thermocouple) according to the procedure outlined in Chapter 10. Align the gages with the principal directions of the laminate. Follow the procedures outlined in Chapter 10 when measuring the laminate thermoelastic response.

12.2 Data Reduction

Plot the laminate expansional strains ε_x and ε_y vs. temperature or temperature change, $\Delta T = T - T_0$, where T_0 is the initial (reference) temperature of the laminate. Figure 12.1 shows typical results for a quasi-isotropic $[0/\pm45/90]_s$ carbon/epoxy laminate. To determine the thermal expansion coefficient in the actual temperature range, evaluate the slope of the strain vs. temperature plot. Hysteresis will be noted at higher temperatures in Figure 12.1b. However, at lower temperatures, the heating and cooling slopes are consistent within experimental error.

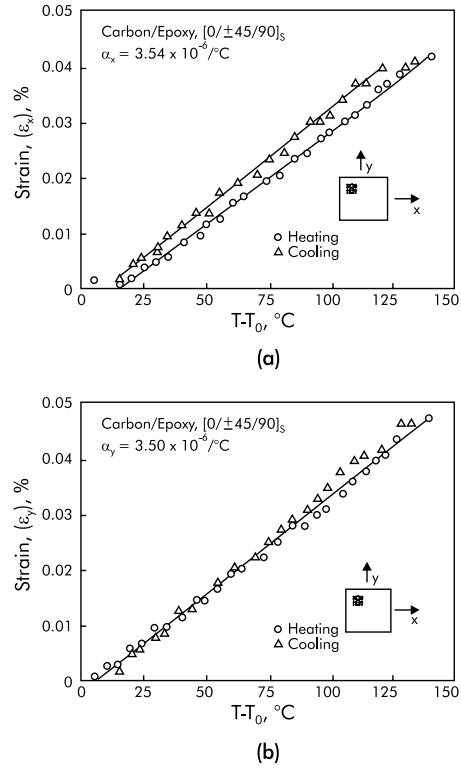

FIGURE 12.1
Thermal expansion strains for a quasi-isotropic $[0/\pm45/90]_s$ carbon/epoxy laminate: (a) ε_x, and (b) ε_y.

12.3 Analysis of Thermoelastic Response

The following thermal expansion coefficients were evaluated from the thermal expansion strain data shown in Figure 12.1 for the quasi-isotropic $[0/\pm45/90]_s$ laminate: $\alpha_x = 3.54 \times 10^{-6}/°C$, and $\alpha_y = 3.50 \times 10^{-6}/°C$. The following set of ply properties were independently measured:

$$E_1 = 140 \text{ GPa} \qquad \alpha_1 = -0.7 \times 10^{-6}/°C$$

$$E_2 = 10.3 \text{ GPa} \qquad \alpha_2 = 31.2 \times 10^{-6}/°C$$

$$\nu_{12} = 0.29 \qquad G_{12} = 5.15 \text{ GPa}$$

Calculation of the thermal expansion coefficients for the quasi-isotropic $[0/\pm45/90]_s$ laminate from Equations (12.5) gives

$$\alpha_x = \alpha_y = 3.30 \times 10^{-6}/°C$$

This value is in reasonable good agreement with those experimentally observed.

Table 12.1 displays thermal expansion data for a carbon/epoxy $[0/\pm60/0]_s$ laminate with the following ply properties:

$$E_1 = 160 \text{ GPa} \qquad \alpha_1 = 0.64 \times 10^{-6}/°C$$

$$E_2 = 9.2 \text{ GPa} \qquad \alpha_2 = 28.1 \times 10^{-6}/°C$$

$$\nu_{12} = 0.33 \qquad G_{12} = 5.24 \text{ GPa}$$

The experimental and predicted coefficients of thermal expansion listed in Table 12.1 can be compared. It is observed that the data are reasonably consistent upon heating and cooling. The analysis somewhat underpredicts α_x and overpredicts α_y. Note also the significant anisotropy in thermal expansion for this lay-up.

TABLE 12.1

Measured and Predicted Thermal Expansion Coefficients (in units of $10^{-6}/°C$ for a $[0/\pm60/0]_s$ carbon/epoxy [IM6/3501-6] laminate)

CTE	Measured	Predicted
α_x	1.97 (H)[a]	1.68
	2.04 (C)[a]	
α_y	3.15 (H)	3.94
	3.41 (C)	

[a] H and C represent heating and cooling, respectively.

References

1. M.F. Hyer, *Stress Analysis of Fiber-Reinforced Composite Materials*, WCB/McGraw-Hill, Boston, 1998.
2. M.W. Hyer, Calculations of the room temperature shape of unsymmetric laminates, *J. Compos. Mater.*, 15, 296–310, 1981.
3. M.-L. Dang and M.W. Hyer, Thermally-induced deformation behavior of unsymmetric laminates, *Int. J. Solids Struct.*, 35, 2101–2120, 1998.

13

Open-Hole Tensile and Compressive Strengths of Laminates

Experiments have shown that the tensile and compressive strengths of a composite laminate containing a hole or notch depend on hole or notch size. Because of the complexity of the fracture process in notched laminates, most strength models are semiempirical. In this chapter some of the more commonly accepted and computationally simple strength models, i.e., the point and average stress criteria developed by Whitney and Nuismer [1] will be discussed. In addition, a modification of the point stress criterion, proposed by Pipes et al. [2], will be introduced.

Reasons for the substantial tensile and compressive strength reductions of composites because of holes and notches are the brittleness of the material and the large stress concentration factors brought about by the anisotropy of the material. These strength reductions are not necessarily the same for tensile and compressive loading because the failure modes are typically different.

As discussed in Chapter 2, the stress concentration factor for a plate containing a circular hole of radius, R (Figure 13.1) is

$$K = \frac{\sigma_x(R,0)}{\overline{\sigma}_x} \tag{13.1}$$

where R is the hole radius, and $\overline{\sigma}_x$ is the average normal stress applied on the horizontal boundaries of the plate (Figure 13.1). For an infinite plate, i.e., where L,w $\rightarrow \infty$, Lekhnitski [3] derived the following expression

$$K_\infty = 1 + \sqrt{2\left(\sqrt{E_x/E_y} - \nu_{xy} + E_x/\left(2G_{xy}\right)\right)} \tag{13.2}$$

where E_x, E_y, ν_{yx}, and G_{xy} are the effective engineering constants of the plate. Note that the x-axis is oriented along the loading direction, and the y-axis is oriented transverse to the loading direction.

It is observed from Equation (13.2) that the stress concentration factor for an infinite plate is independent of hole radius. For an ideally brittle infinite plate, the notched strength would thus be

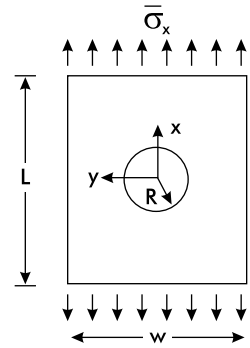

FIGURE 13.1
Finite-size plate containing a hole of diameter D = 2R subject to uniaxial tension.

$$\sigma_N = \sigma_0 / K_\infty \tag{13.3}$$

where σ_0 is the strength of the plate without a hole, i.e., the unnotched strength. Experiments, however, show that the strength of composite plates containing large holes is much less than that observed for small holes [1,2]. Such a difference for large plates cannot be explained by a net area reduction. Consequently, there must be factors other than the stress concentration factor controlling the notched strength. Consideration of the normal stress distribution across the ligaments of the plate adjacent to the hole reveals some interesting features. The approximate stress distribution in an infinite plate containing a circular hole is [4]

$$\sigma_x(y,0) = \frac{\sigma_x(\infty)}{2}\left[2 + \xi^2 + 3\xi^4 - (K_\infty - 3)(5\xi^6 - 7\xi^8)\right] \tag{13.4}$$

where $\xi = y/R$, and $\sigma_x(\infty)$ is the far-field normal stress. Figure 13.2 shows the stress, $\sigma_x(y,0)/\sigma_x(\infty)$, across a ligament for isotropic plates containing holes of two sizes ($R/R_0 = 0.1$ and 1.0), where R_0 is a reference radius. It is observed that the volume of material subject to a high stress is much more localized for the plate with a smaller hole, thus leading to a greater opportunity for stress redistribution to occur, explaining the increased notched strength with decreased hole size.

13.1 Point and Average Stress Criteria

The point and average stress criteria [1] incorporate the hole size effect in computationally simple fracture criteria where failure of the notched laminate is assumed to occur when the stress, σ_x, at a certain distance d_0 ahead

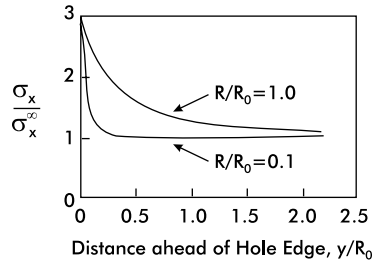

FIGURE 13.2
Normal stress distributions ahead of the hole edge for isotropic plates containing holes of two sizes.

of the notch reaches the unnotched strength, σ_0 (point stress criterion [PSC]), or the stress, σ_x, averaged over a certain distance across the ligament reaches the unnotched strength (average stress criterion [ASC]). Mathematically, these criteria can be expressed as

$$\text{PSC: } \sigma_x(R + d_0, 0) = \sigma_0 \tag{13.5a}$$

$$\text{ASC: } \frac{1}{a_0}\int_{R}^{R+a_0} \sigma_x(y, 0)dy = \sigma_0 \tag{13.5b}$$

13.1.1 Point Stress Criterion (PSC)

Combination of the PSC (Equation (13.5a)) and the expression for the stress distribution (Equation (13.4)) yields

$$\frac{\sigma_N}{\sigma_0} = \frac{2}{2 + \lambda^2 + 3\lambda^4 - (K_\infty - 3)(5\lambda^6 - 7\lambda^8)} \tag{13.6}$$

where

$$\lambda = \frac{R}{R + d_0} \tag{13.7}$$

Note that for very large holes, d_0 is small compared with R, and Equation (13.6) gives

$$\frac{\sigma_N}{\sigma_0} = 1/K_\infty \tag{13.8}$$

Consequently, the notched strength ratio for a large hole is given by the inverse of the stress concentration factor. Furthermore, a notch-insensitive

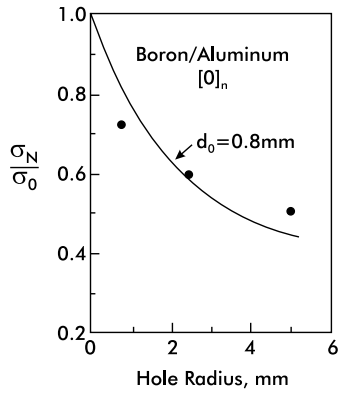

FIGURE 13.3
Experimental data on notched strength of a boron–aluminum composite and predictions based on the point stress criterion. (From R.F. Karlak, *Proceedings of a Conference on Failure Models in Composites (III)*, American Society for Metals, Chicago, 1977. With permission.)

laminate is characterized by a large d_0 in comparison to R. For that case, $\lambda \approx 0$ in Equation (13.6) and $\sigma_N/\sigma_0 \approx 1.0$.

The PSC thus contains two parameters (d_0, σ_0) that have to be determined by experiment. Having established d_0 and σ_0, the PSC allows for strength predictions of laminates containing holes of arbitrary size. Figure 13.3 shows σ_N/σ_0 plotted vs. hole size for a unidirectional $[0]_n$ boron/aluminum composite [3]. Reasonable agreement with experimental data is observed.

13.1.2 Average Stress Criterion (ASC)

Substitution of the stress distribution (Equation (13.4)) into the ASC (Equation (13.5b)) yields, after integration, the following expression for the notched laminate strength

$$\frac{\sigma_N}{\sigma_0} = \frac{2}{(1+\delta)\left(2+\delta^2+\left(K_\infty-3\right)\delta^6\right)} \tag{13.9}$$

with

$$\delta = \frac{R}{R+a_0} \tag{13.10}$$

Figure 13.4 shows experimental strength data for a $[0_2/\pm45]_s$ carbon/epoxy laminate [5]. Experimental results are in good agreement with the ASC with a_0 = 5 mm.

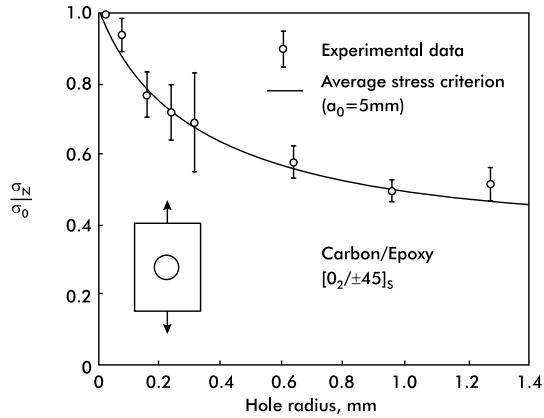

FIGURE 13.4
Notched strength data and predictions based on the average stress criterion for a notched $[0_2/\pm45]_s$ carbon/epoxy laminate [4].

13.1.3 Modification of PSC

To improve the accuracy of notched strength predictions using the PSC, Pipes et al. [2], following Karlak's modification [3], let the characteristic distance, d_0 (Equation (13.6)) become a power function of hole radius

$$d_0 = (R/R_0)^m/C \tag{13.11}$$

where m is an exponential parameter, R_0 is a reference radius, and C is the notch sensitivity factor. In essence, this model adds one more parameter (the exponential parameter) to the PSC. The reference radius may arbitrarily be chosen as $R_0 = 1$ mm. The parameter λ (Equation (13.7)) then becomes

$$\lambda = 1/(1 + R^{m-1}C^{-1}) \tag{13.12}$$

Figures 13.5 and 13.6 display the influences on notched strength, σ_N/σ_0, of the parameters m and C. Figure 13.5 shows that the exponential parameter affects the slope of the notch sensitivity curve, while Figure 13.6 shows that the notch sensitivity factor shifts the curves along the log R axis without affecting the shape of the curves. The admissible ranges for the parameters are $0 \le m < 1$ and $C \ge 0$. A notch-insensitive laminate is characterized by a large d_0 in comparison to R. This corresponds to $m \to 1$ and $C \to 0$.

Figure 13.7 shows notched strength vs. hole radius for two quasi-isotropic carbon/epoxy laminates with $[\pm45/0/90]_s$ and $[90/0/\pm45]_s$ lay-ups and the magnitudes of the corresponding fitting parameters m and C determined as outlined in Section 13.3.

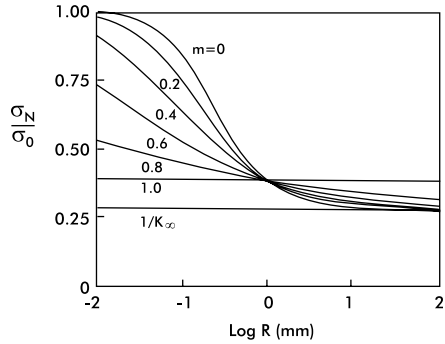

FIGURE 13.5
Influence of exponential parameter on notched strength, C = 10.0 mm^{-1} [2].

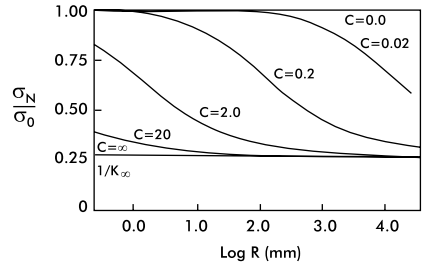

FIGURE 13.6
Influence of notch sensitivity factor on notched strength, m = 0.5, unit of C is mm^{-1} [2].

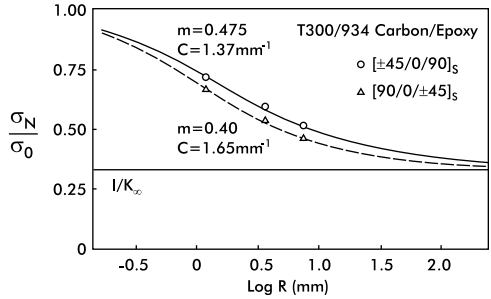

FIGURE 13.7
Notched strength data for $[\pm 45/0/90]_s$ and $[90/0/\pm 45]_s$ carbon/epoxy laminates [2].

13.2 Test Specimen Preparation

Although any laminate configuration can be used, most commonly a $[0/\pm 45/90]_{ns}$ (quasi-isotropic) laminate is selected. Laminates with higher

percentages of 0° plies are tested when of specific interest to the intended design application.

Often the same specimen configuration is used for both tensile and compressive open-hole tests. One commonly used specimen size is 305 mm long and 38 mm wide. Another standard open-hole compression test method utilizes a specimen only 75 mm long and 25 mm wide, as will be discussed later. If the test facilities permit, it is strongly recommended that wide specimens be used to accommodate a large range of hole sizes and better approximate an infinitely wide specimen. Daniel [5], for example, used 127-mm-wide laminates and hole diameters ranging from 6.4 to 25.4 mm. Specimen thickness is not critical and is somewhat dependent upon the specific laminate configuration to be tested. A specimen thickness on the order of 2.5 to 5 mm is commonly used. The diameter of the hole in the specimen, which is to be centered at the midlength of the specimen, can also be arbitrarily selected. However, as discussed at the beginning of this chapter, the ratio of specimen width to hole diameter influences the magnitude of the stress concentration induced. A hole diameter of 6.4 mm has become a commonly used size.

Unless a laminate with a high percentage of 0° plies is to be tested, tabs are not usually necessary. If aggressively serrated tensile wedge grips are used it may be necessary to protect the open-hole tension specimen surfaces with one or more layers of emery cloth, an (unbonded) layer of plastic sheet material (approximately 1 to 2 mm thick), or similar padding material. The open-hole compression test methods typically involve the use of some type of special fixture to prevent specimen buckling, as will be discussed. These fixtures are usually designed for use with an untabbed specimen.

Measure the cross-sectional dimensions (average six measurements) and check for parallelism of the edges and of the end-tab surfaces if used (see Chapter 4 for typical specimen tolerances).

If a series of tests are to be conducted for various hole sizes, divide the specimens into groups by hole size. Note also that one of these groups should be specimens without holes to determine the unnotched strength, σ_0. At least three specimens should be assigned to each group, although a minimum of five specimens is more common. At least three hole diameters should be investigated; for example, D = 3, 5, and 7 mm. Machine the holes as specified in Section 4.2.

13.3 Tensile Test Procedure and Data Reduction

The specimens should be mounted and tested in a properly aligned and calibrated testing machine with mechanical wedge action or hydraulic grips. Set the crosshead rate at about 0.5 to 1 mm/min. Record the load vs. crosshead displacement to detect the ultimate load and any anomalous load-displacement behavior. If a strain gage is used, place it midway between the

FIGURE 13.8
Carbon–epoxy open-hole tensile specimen tested to failure.

TABLE 13.1

Unnotched and Notched Strength Data for $[0/\pm45/90]_s$ Carbon/Epoxy Coupons

Notch Radius (mm)	Strength (MPa)
0	607 (σ_0)
1.6	437
2.5	376
3.3	348

hole and the end tab. Make sure eyes are protected in the test area. Load all specimens to failure. Figure 13.8 shows an open-hole tension carbon/epoxy specimen after testing.

Notched strength, σ_N, is calculated based on the gross cross-sectional area (A = wh). A typical set of unnotched and notched strength data for $[0/45/90]_s$ carbon/epoxy coupons is given in Table 13.1. Because the strength model discussed here is restricted to a plate with an infinite width-to-hole diameter ratio, a comparison between experimental data and the notch strength model requires correction for the finite width of the specimen. A common way to correct the data is to multiply the experimental notched strength with a correction factor, K/K_∞, where K is the stress concentration factor for an orthotropic plate of finite width; i.e.,

$$\sigma_N(\infty) = \sigma_N(w)\frac{K}{K_\infty} \tag{13.13}$$

where $\sigma_N(w)$ is the experimental strength for a plate of width w, and $\sigma_N(\infty)$ is the corresponding strength for an infinite plate. A closed-form expression

TABLE 13.2

Finite Width Correction Factors for Various Carbon/Epoxy (AS4/3501-6) Lay-ups [8] E_1 = 125 GPa, E_2 = 9.9 GPa, ν_{12} = 0.28, and G_{12} = 5.5 GPa

Lay-Up	K_∞[a]	w/D = 2	3	4	6	8	10
$[0/\pm45/90]_s$	3.00	1.4340	1.1495	1.0736	1.0260	1.0107	1.0037
$[0_2/\pm45]_s$	3.48	1.3725	1.1291	1.0632	1.0216	1.0093	1.0031
$[0_4/\pm45]_s$	4.07	1.3226	1.1109	1.0577	1.0172	1.0095	1.0041
$[0_6/\pm45]_s$	4.44	1.2992	1.1006	1.0472	1.0152	1.0102	1.0051
$[\pm45]_s$	2.06	1.6425	1.2379	1.1215	1.0442	1.0180	1.0062
Equation (13.14)		1.417	1.148	1.076	1.031	1.017	1.011

[a] Determined from Equation (13.2).

for K, however, does not exist, and K has to be determined using the boundary collocation method [6] or the finite element method [7]. Table 13.2 gives finite width correction factors as a function of width-to-hole diameter ratio (w/D) for various carbon/epoxy lay-ups [8]. Note that K/K_∞ is >1, which means that finite-width specimens exhibit larger stress concentrations than infinitely wide specimens ($w/D \geq 8$). Consequently, it is expected that a hole in a finite-width specimen will be more detrimental in terms of strength than a hole in an infinitely wide specimen. A common approximation, which is also reasonably accurate for composite laminates with $w/D > 4$ [8] (see also Table 13.2) is to use an isotropic expression [9,10] for K/K_∞

$$\frac{K}{K_\infty} = \frac{2 + \left(1 - (D/w)\right)^3}{3\left(1 - (D/w)\right)} \tag{13.14}$$

To enable comparison of the data with the PSC (Equation (13.6)), first correct the experimental data (Table 13.1) for the finite size, using the approximate expression for the stress concentration factor (Equation (13.14)). Then solve for the parameter λ in Equation (13.6) using an interactive method such as Muller's method [11] or Newton-Raphson's method [12,13]. From the definition of λ (Equation (13.12)) it is observed that only the root between zero and one is required. For illustrative purposes, the notched strength data listed in Table 13.1 were corrected according to Equation (13.14), and the corresponding λ values were determined with the Newton-Raphson method, and are listed in Table 13.3.

To obtain the parameters m and C, Equation (13.12) may be written as

$$-\log(1/\lambda - 1) = \log C + (1 - m)\log R \tag{13.15}$$

By plotting $-\log(1/\lambda - 1)$ vs. log R, the slope and the intercept at log R = 0 can be obtained by the least-squares method. The slope is equal to 1 – m, and the intercept is equal to log C. Figure 13.9 shows $-\log(1/\lambda - 1)$ plotted vs. log R for the data of Table 13.3.

TABLE 13.3

Corrected Notched Strength Data (Table 13.1) and Values of λ Determined Using the Newton-Raphson Method

R (mm)	σ_N/σ_0[a]	λ
1.6	0.73	0.5998
2.5	0.64	0.6867
3.3	0.62	0.7052

[a] Corrected using Equation (13.14).

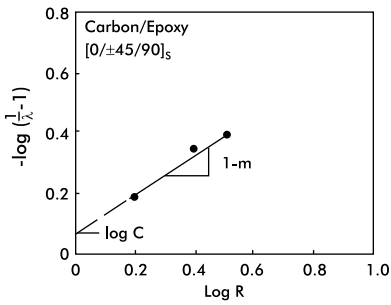

FIGURE 13.9

Determination of the parameters m and C for $[0/\pm45/90]_s$ carbon/epoxy specimens, m = 0.36, and C = 1.16 mm^{-1}.

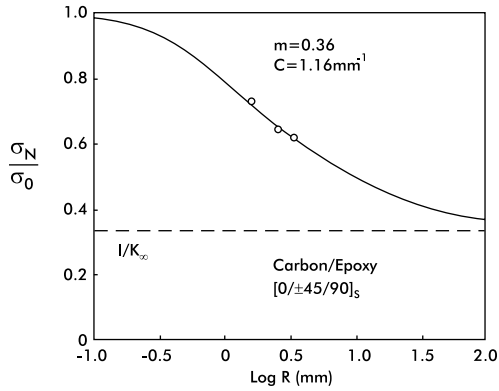

FIGURE 13.10

Theoretical and experimental notch sensitivity for $[0/\pm45/90]_s$ carbon/epoxy specimens.

As an illustration of the goodness of the fit for the parameters m and C, the theoretical curve of σ_N/σ_0 is plotted vs. log R along with the experimental values in Figure 13.10. Within the limited range of experimental data, excellent agreement is observed. Once the parameters m and C are established, it is possible to predict the notched strength for any hole size and coupon width (within reasonable limits) using the above methodology.

13.4 Standardized Open-Hole Tension Test Method

Rather than utilize the PSC and ASC developed by Whitney and Nuismer [1] discussed in the previous sections of this chapter, it has become common to simply test a specimen of one specific configuration and then use the measured strength as a comparative measure. That is, if a common specimen configuration is used, open-hole tensile strength results for different materials can be directly compared. The specimen configuration most commonly used is 305 mm long, 38 mm wide, and containing a centrally located 6.4-mm-diameter hole at the midlength of the specimen. This configuration was developed by the Boeing Company [14] and has now been standardized by both SACMA [15] and ASTM [16].

The laminate configuration and specimen thickness are somewhat arbitrary, but of course the results obtained will be dependent on these parameters as well as the type of material being tested. Although any laminate configuration can be used, most commonly a $[0/\pm45/90]_{ns}$ (quasi-isotropic) laminate is selected. Laminates with higher percentages of 0° plies are tested when of specific interest to the intended design application.

Lower strength laminate orientations such as the quasi-isotropic lay-up can normally be tested without specimen tabs. When laminates with higher percentages of 0° plies are to be tested, tabs may be necessary. However, because a strength-reducing hole is present, it may be possible to successfully test an open-hole tension specimen without tabs, whereas the corresponding laminate without a hole could not be tested.

Standard mechanical or hydraulic grips, as described in Section 13.2, can be used for this standardized test. That is, unless a laminate with a high percentage of 0° plies is to be tested, tabs are not usually necessary. If aggressively serrated tensile wedge grips are used, it may be necessary to protect the open-hole tension specimen surfaces with one or more layers of emery cloth, an (unbonded) layer of plastic sheet material (approximately 1 to 2 mm thick), or similar padding material.

Although applied load vs. crosshead displacement is usually monitored, as a means of detecting any testing anomalies, only the maximum applied load, P_{max}, to cause failure is used directly. That is, the test results are quantified for comparison purposes by calculating an open-hole tensile strength

$$\sigma_N = P_{max}/A \tag{13.16}$$

where P_{max} is the maximum load applied to fail the specimen, and A is the cross-sectional area of the specimen (A = wh), where w and h are the specimen width and thickness, respectively. Note that the open-hole strength is based on the gross cross-sectional area of the specimen (disregarding the hole) and not the net cross-sectional area.

13.5 Standardized Open-Hole Compression Test Methods

There are two standardized open-hole compression test methods in use, e.g., the so-called Boeing Open-Hole Compression [14] and the Northrop Open-Hole Compression [17] test methods. The Boeing method was first standardized by SACMA [18] and more recently by ASTM [19], as was its tensile loading counterpart. Although the Northrop method presently is still an individual company standard, it is frequently used by other groups also.

13.5.1 Boeing Open-Hole Compression Test Method

The specimen configuration is the same as that of the Boeing Open-Hole Tension test method (Section 13.4). That is, the specimen is 305 mm long and 38 mm wide, and contains a 6.4-mm-diameter hole centered at the midlength of the specimen. Again, the laminate configuration and specimen thickness are somewhat arbitrary, and the results obtained are dependent on these parameters as well as the material being tested.

A special fixture has been designed to load the specimen in compression while preventing gross (Euler) buckling, as shown in Figure 13.11. The 305-mm-long specimen is installed such that its ends are flush with the outer ends of the fixture halves. Thus, essentially the entire length of the specimen is supported against buckling, with only a small gap existing between the fixture halves themselves so that they do not come into contact when the compressive loading is applied. The standards specify that the ends of the fixture be installed in hydraulic grips. Because of the thickness (approximately 35 mm with a specimen installed) and width (76 mm) of the fixture, this requires large hydraulic wedge grips. For example, commercially available hydraulic grips of 250 kN capacity or greater are required (e.g., see Reference [19] for descriptions of such grips). There is no need for grips of this loading capacity in many testing laboratories. These large grips are

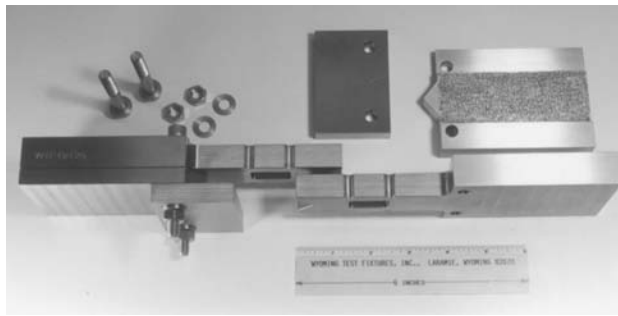

FIGURE 13.11
Boeing open-hole compression test fixture (ASTM D 6484-99). (Photograph courtesy of Wyoming Test Fixtures, Inc.)

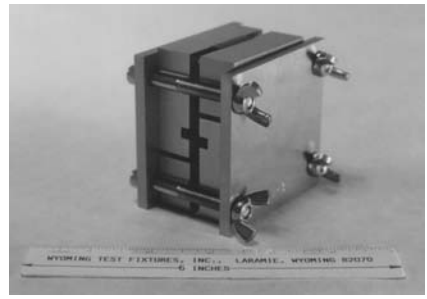

FIGURE 13.12
Northrop open-hole compression test fixture (Northrop Specification NAI-1504). (Photograph courtesy of Wyoming Test Fixtures, Inc.)

relatively expensive, and are very massive and thus difficult to handle during installation and removal from the testing machine. For example, each of the 250 kN hydraulic grips (MTS Systems Corporation, Eden Prairie, MN) weighs about 125 kg [20]. Because of this, the fixture of Figure 13.11 is often loaded directly on its ends between compression platens. The faces of the fixture in contact with the specimen are thermal-sprayed with tungsten carbide particles, as discussed in Chapters 5 and 6. Thus, if the fixture is clamped tightly to the specimen, the applied end loading will become a combined end loading and shear loading, just as for the Wyoming combined loading compression test fixture described in Section 6.3 of Chapter 6; it is hoped that end crushing of the specimen will be avoided. This success is particularly likely because, as noted above, the strength of an open-hole compression specimen is typically not very high. However, if direct end loading is to be used, care must be taken to secure the fixture so that it does not slip out from between the platens when the loading is applied and potentially cause injury to nearby personnel. For example, restraint boxes attached directly to the testing machine can be used instead of platens [21,22]; the ends of the fixture slip into these restraint boxes as shown in Figure 13.13.

Although strain gages can be used, the ASTM standard has eliminated their use because they do not provide necessary information. As for the open-hole tension testing, only the compressive strength is calculated, using Equation (13.16).

13.5.2 Northrop Open-Hole Compression Test Method

The Northrop open-hole compression test method [17] was developed at about the same time as the Boeing method. The Northrop open-hole compression test specimen is only 76 mm long and 25 mm wide, i.e., only one fourth as long and two thirds as wide as the Boeing specimen. It contains a 6.4-mm-diameter hole centered at its midlength. That is, it requires only one sixth as much material per specimen — a significant savings. However, as discussed at the beginning of this chapter, it may be desirable to use a wider

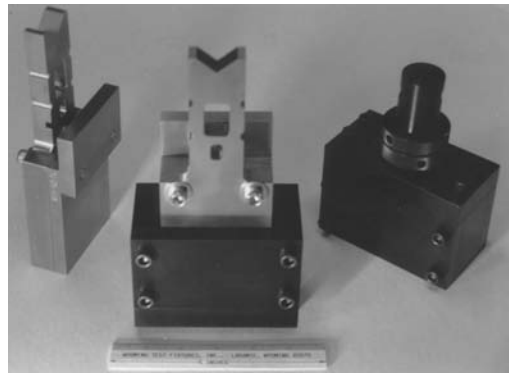

FIGURE 13.13
Restraint boxes for use with the Boeing open-hole compression test fixture when applying loading directly through the specimen ends (lower half of fixture shown in a box; both boxes to be attached directly to the testing machine). (Photograph courtesy of Wyoming Test Fixtures, Inc.)

specimen to reduce edge effects. Thus, a modification of the Northrop fixture to accommodate 38-mm-wide specimens has also been utilized [21]. It has been shown to produce compressive strengths comparable to the standard Boeing test, while reducing the volume of specimen material required to one fourth — still a significant savings.

The Northrop test fixture is shown in Figure 13.12. It is designed such that the untabbed specimen is installed flush with the ends of the fixture and is directly end loaded. Although a moderate clamping force is exerted on the specimen when the fixture screws are tightened to the recommended 6.8 N·m torque, the faces of the fixture are smooth and not intended to transfer a shear loading to the specimen. That is, the force applied to the specimen is essentially all end loading. As for the Boeing fixture, the specimen is supported over almost its full length, although a small gap is maintained between the fixture halves to prevent them from coming into contact with each other when the compressive loading is applied. Because the fixture is compact, with a base comparable in dimensions to its height, there is little danger of it being ejected from between the platens when loaded, and thus need not be constrained. The fixture has recesses machined into it to permit the use of strain gages, but as for the Boeing fixture, strain gages are not normally used. Compressive strength is calculated using Equation (13.16).

13.5.3 Comparison of the Boeing and Northrop Open-Hole Compression Test Methods

The performance of the Boeing and Northrop open-hole compression test methods and corresponding fixtures are directly compared in Reference [21]. In addition to 25-mm-wide specimens tested in the standard Northrop fixture, 38-mm-wide specimens were tested in a special fixture fabricated with this increased width capability. Although there were some minor differences

in the results, there were no distinct trends to report. This included whether the Boeing specimen was shear loaded or end loaded, and whether the Northrop specimen was 25 mm or 38 mm wide.

As previously noted in Section 13.4, the open-hole tests, whether tension or compression, are usually used as comparative tests. Thus, until additional studies such as that of Reference [21] are conducted, it is best to select one open-hole compression test method and use it consistently, knowing that the results obtained will not be significantly different from those obtained using one of the other open-hole compression test methods.

13.5.4 Filled-Hole Tension and Compression Test Methods

The discussion in this chapter addresses the influence of empty (unfilled) holes in composite laminates. An unfilled hole will deform under loading. However, often a hole is created in a laminate to accommodate a fastener of some type, e.g., a bolt, pin, or rivet. The presence of a close-fitting fastener will restrict the deformation of the hole, thus changing the state of stress in the laminate, and possibly the failure stress.

ASTM is currently preparing a standard [23] to govern the tensile and compressive testing of laminates with filled holes. The test fixtures and procedures are similar to those outlined in the previous sections for unfilled holes. However, the laminate failure modes may change because of the fastener interference. The differences in failure mode are discussed in Reference [24].

References

1. J.M. Whitney and R.J. Nuismer, Stress fracture criteria for laminated composites containing stress concentrations, *J. Compos. Mater.*, 8, 253–265, 1974.
2. R.B. Pipes, R.C. Wetherhold, and J.W. Gillespie, Jr., Notched strength of composite materials, *J. Cons. Mater.*, 13, 148–160, 1979.
3. R.F. Karlak, Hole effects in a series of symmetrical laminates, *Proceedings of a Conference on Failure Modes in Composites (III)*, American Society for Metals, Chicago, 1977.
4. H.J. Konishi and J.M. Whitney, Approximate stresses in an orthotropic plate containing a circular hole, *J. Compos. Mater.*, 9, 157–166, 1975.
5. I.M. Daniel, Failure mechanisms and fracture of composite laminates with stress concentrations, *Proceedings of the 7th International Conference on Experimental Stress Analysis*, Technion, Haifa, Israel, 1982.
6. J.M. Ogonowski, *Analytical Study of Finite Geometry Plates with Stress Concentrations*, AIAA Paper 80-0778, American Institute of Aeronautics and Astronautics, Reston, VA, 1980.
7. K.-J. Bathe, *Finite Element Procedures in Engineering Analysis*, Prentice-Hall, Englewood Cliffs, NJ, 1982.
8. J.W. Gillespie and L.A. Carlsson, Influence of finite width on notched laminate strength predictions, *Compos. Sci. Technol.*, 32, 15–30, 1988.

9. R.E. Peterson, *Stress Concentration Factors*, John Wiley & Sons, New York, 1974.
10. R.J. Nuismer and J.M. Whitney, *Uniaxial Failure of Composite Laminates Containing Stress Concentrations*, ASTM Spec. Tech. Publ. 593, American Society for Testing and Materials, West Conshohoken, PA, 1975.
11. D.E. Muller, A method for solving algebraic equations using an automatic computer, *Math. Tables Comput.*, 10, 1956.
12. R.C. Hornbeek, *Numerical Methods*, Quantum, New York, 1975.
13. S.D. Conte and C. de Boor, *Elementary Numerical Analysis: An Algorithmic Approach*, 2nd ed., McGraw-Hill, New York, 1965.
14. Boeing Specification Support Standard BSS 7260, *Advanced Composite Compression Tests*, The Boeing Company, Seattle, WA, December 1988 (originally issued February 1982).
15. SACMA Recommended Method SRM 5R-94, *Open-Hole Tensile Properties of Oriented Fiber-Resin Composites*, Suppliers of Advanced Composite Materials Association, Arlington, VA (originally issued April 1989, revised 1994).
16. ASTM D 5766-95, *Test Method for Open-Hole Tensile Strength of Polymer Matrix Composite Laminates*, American Society for Testing and Materials, West Conshohocken, PA, 2001.
17. Northrop Specification NAI-1504C, *Open-Hole Compression Test Method*, Northrop Corporation, Hawthorne, CA, Revision B, May 1988.
18. SACMA Recommended Method SRM 3R-94, *Open-Hole Compression Properties of Oriented Fiber-Resin Composites*, Suppliers of Advanced Composite Materials Association, Arlington, VA (originally issued April 1989, revised 1994).
19. ASTM D 6484-99, *Test Method for Open-Hole Compressive Strength of Polymer Matrix Composite Laminates*, American Society for Testing and Materials, West Conshohocken, PA, 2001.
20. *Material Testing Products*, Product Catalog, 7th ed., MTS Systems Corporation, Eden Prairie, MN, 1999.
21. S.L. Coguill and D.F. Adams, A Comparison of Open-Hole Compression Fixtures by Experimental Evaluation, *Proceedings of the 45th International SAMPE Symposium and Exhibition*, SAMPE, West Covina, CA, May 2000, pp. 1095–1105.
22. *High Performance Test Fixtures*, Product Catalog No. 106, Wyoming Test Fixtures, Inc., Laramie, WY, 2000 (also, www.wyomingtestfixtures.com).
23. Draft ASTM Standard, *Standard Practice for Filled-Hole Tension and Compression Testing of Polymer Matrix Composite Laminates*, American Society for Testing and Materials, West Conshohocken, PA, 2000.
24. A. Sawicki and P. Minguet, Failure mechanisms in compression-loaded composite laminates containing open and filled holes, *J. Reinf. Plast. Compos.*, 18(18), 1706–1728, 1999.

14

Characterization of Delamination Failure

The interlaminar mode of fracture (delamination) has aroused considerable attention since the early 1970s [1]. With the introduction of laminated composites into structures subjected to service loads, it has become apparent that the delamination failure mode has the potential for being the major life-limiting failure process. These delaminations are typically induced in composite laminates during service. However, delaminations may also be introduced during processing of the lay-up, for example as a result of contamination of the prepreg, leading to locally poor ply adhesion, or they may form locally in regions of high void content. Delamination may also be introduced during post-fabrication handling of the structure.

It is recognized that a delamination represents a crack-like discontinuity between the plies and that it may propagate during application of mechanical or thermal loads, or both. It thus seems appropriate to approach the delamination using fracture mechanics (Section 2.7), which indeed has evolved as a fruitful approach for material selection and assessment of structural integrity. Fracture mechanics of delaminations is commonly based on the strain energy release rate, and fracture toughness is expressed as the work of fracture. Consequently, many new fracture tests have been devised for measuring the static interlaminar fracture toughness, as well as the crack propagation rate during cyclic loading. Most such tests and standard test procedures are limited to unidirectional $[0]_n$ laminates in which a delamination propagates between the plies along the fiber direction. In laminates with multidirectional plies, the crack may have a tendency to branch through the neighboring plies, invalidating the coplanar assumption in fracture analysis [2–4]. Composites with tough resin films (called interleaves) between the plies may experience peculiar delamination resistance behavior depending on crack path selection, i.e., if the crack propagates cohesively in the tough interlayer or adhesively at the film–composite interface [5]. In woven fabric composites, a delamination crack will interact with matrix regions and interlacing yarns during its propagation, and as a result, will experience varying growth resistance [6]. Composites with through-thickness reinforcement may experience large extended regions where the reinforcements bridge the crack (bridging zones), which invalidates data reduction schemes based on linear elastic fracture mechanics [7]. Although fiber bridging is common in unidirectional (all 0° plies) composites, characterization of the delamination

resistance of such composites tends to be associated with fewer complications. Consequently, we will here limit attention to unidirectional composites.

Fracture mechanics analysis, preparation of test specimens, testing, and data reduction will be described for some contemporary interlaminar fracture test specimens, namely, the double-cantilever beam (DCB) specimen (Mode I), end-notched flexure (ENF) specimen (Mode II), four-point bend end-notched flexure (4ENF) specimen (Mode II), the mixed-mode bending (MMB) specimen, and the edge crack torsion (ECT) specimen (Mode III). The various fracture modes are defined in Figure 2.9.

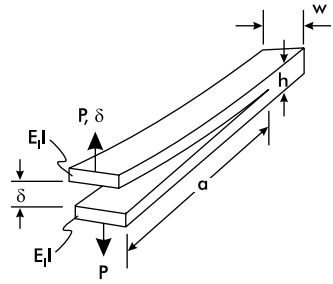

FIGURE 14.1
DCB specimen geometry.

14.1 Double-Cantilever Beam (DCB) Test

The DCB specimen for Mode I fracture testing and the test principle is shown in Figure 14.1. This specimen is a standard test method, ASTM D 5528 [8]. The purpose of the test is to determine the opening mode interlaminar fracture toughness, G_{IC}, of continuous fiber composite materials with a polymer matrix. First developed in a tapered form by Bascom, et al. [9], the straight-sided geometry proposed by Wilkins et al. [10], shown in Figure 14.1, has become standard. Although data reduction does not rely on the classical beam theory approach used by Wilkins, et al. [10], the simplicity of this theory makes it easy to examine some features of the DCB specimen.

If we assume that classical beam theory is valid, the load-point compliance, $C = \delta/P$, of the DCB specimen becomes

$$C = \frac{2a^3}{3E_1 I} \tag{14.1}$$

where P is the load applied, δ is the crack opening, a is the crack length, and E_1I is the flexural rigidity of each beam of the specimen, with E_1 being the Young's modulus of the composite in the fiber direction and I the moment

of inertia (Figure 14.1). The strain energy release rate, $G = G_I$, is obtained from Equation (2.59)

$$G = \frac{P^2}{2w}\frac{dC}{da} \tag{14.2}$$

in which w is the specimen width. Equations (14.1) and (14.2) give

$$G = \frac{P^2 a^2}{wE_1 I} \tag{14.3}$$

If G_{IC} is a true material constant, stable crack growth requires (see Section 2.7),

$$dG/da \leq 0 \tag{14.4}$$

For the DCB specimen under fixed-load conditions, dG/da is obtained from Equation (14.3) as

$$\frac{dG}{da} = \frac{2P^2 a}{wE_1 I} \tag{14.5}$$

This quantity is always positive and thus the crack growth is unstable under load-controlled testing conditions.

For fixed-grip conditions, dG/da may be obtained by substitution of $P = \delta/C$ in Equation (14.2) and differentiation

$$\frac{dG}{da} = \frac{-4\delta^2 a}{c^2 wE_1 I} \tag{14.6}$$

This quantity is always negative, and thus the crack growth is stable. Experimentally, most testing is performed under fixed-grip conditions (displacement control), which should render stable crack growth.

14.1.1 DCB Specimen Preparation and Test Procedure

The DBC specimen should be at least 125 mm long and between 20 and 25 mm wide. The number of plies, dimensions, and preparation of the panel are outlined in Appendix B. An even number of plies should be employed to achieve a thickness (h in Figure 14.1) between 3 and 5 mm. Variations in thickness should be less than 0.1 mm. Tough composites may require thicker specimens to avoid large displacements and nonlinear response. Figures 14.2 and 14.3 show the DCB specimen with hinge loading tabs prepared and

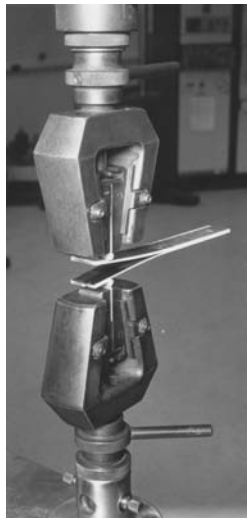

FIGURE 14.2
DCB test setup.

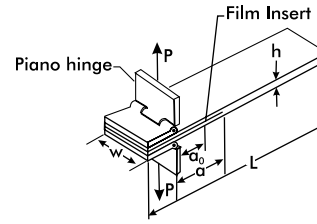

FIGURE 14.3
Hinge loading tab arrangement for the DCB specimen.

bonded as described in Chapter 4. The precrack is defined by inserting a thin film (<13 μm) at the midplane of the panel (see Appendix B). Crack length, a, is defined as the distance from the line of load application to the crack tip, Figure 14.3. The length of the film insert should be adjusted to obtain a precrack length, a_0, of approximately 50 mm (see Appendix B).

Measure thickness and width of the specimen close to each end and at the center and calculate averages. Paint the specimen edges with a thin, white, brittle coating such as typewriter correction fluid. To aid in recording of crack length, mark the first 5 mm from the insert with thin vertical lines every 1 mm. Mark the remaining 20 mm every 5 mm.

The specimen should be mounted in the grips of a properly calibrated test machine with a sufficiently sensitive load cell. A traveling optical microscope with approximately 10× magnification and a cross hair can be positioned on one side of the specimen to enable monitoring of the delamination crack tip and its extension during the fracture test within ±0.5 mm. Locate the cross hair at the delamination front without applying load to the specimen to obtain a record of the precrack length, a_o (Figure 14.3). Set the crosshead rate at 0.5 mm/min, and plot load vs. crosshead displacement for real-time visual inspection of the load-displacement response. Displacement of the loaded ends (δ in Figure 14.1) can be taken as the crosshead travel, provided the machine and load cell are stiff enough not to deform more than 2% of the total opening displacement.

Observe the delamination front as the specimen is being loaded. When the delamination begins to grow from the end of the insert, mark this incident as a_o on the chart recording as indicated in Figure 14.4. Continue to observe the front of the growing crack, and mark the chart accordingly.

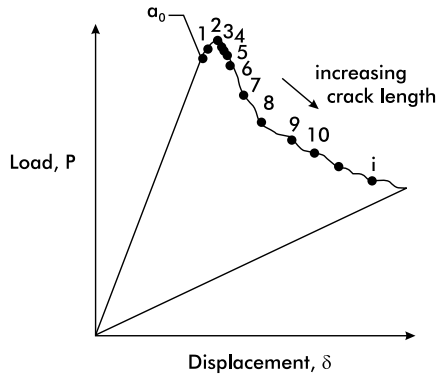

FIGURE 14.4
Schematic load-displacement record during crack growth for a DCB test.

For the first 5 mm of crack growth, each 1 mm increment should be marked. After 5 mm of crack extension, the crosshead rate may be increased. Mark every 5 mm of crack length on the graph. Observe the opposite edge to monitor deviations from uniform crack extension across the beam width. The difference in crack length between the two edges should be less than 2 mm for a valid test. When the delamination has extended about 25 mm, the specimen may be unloaded while the unloading load-displacement response (see Figure 14.4) is recorded. A common occurrence in testing unidirectional DCB specimens is fiber bridging, which refers to debonded fibers bridging the fracture surfaces, as illustrated in Figure 14.5. The fiber bridging elevates the fracture resistance as a result of the closure tractions that develop in the fibers that bridge the crack faces behind the crack tip, and the energy consumed as the bridged fibers debond from the matrix [11].

It is common to display the fracture toughness measured at various crack lengths as a resistance curve (R-curve). As discussed by Suo et al. [11], such R-curves do not represent true material behavior because they depend on specimen thickness. Fiber bridging is less likely to occur in multidirectional laminates used in composite structures because less opportunity exists for fiber wash, i.e., intermingling of wavy fibers between adjacent plies. Fiber bridging is thus likely to lead to nonconservative estimates of the actual delamination toughness. It is argued that the most meaningful, and also conservative, estimate of fracture toughness is the initiation toughness, G_{IC}(init.), associated with the initial crack propagation from the Teflon insert [8], because this value is not influenced by fiber bridging. Further discussion will follow.

14.1.2 DCB Data Reduction

Several data reduction methods for evaluating the Mode I fracture toughness, G_{IC}, have been proposed [12]. A simple, yet accurate method is the

empirical compliance method suggested originally by Berry [13], where the beam compliance, $C = \delta/P$, is expressed as a power function of crack length,

$$C = \frac{a^n}{H} \tag{14.7}$$

where a is the crack length, and n and H are parameters determined experimentally. If classical beam theory and the assumption of fixed ends are valid, $n = 3$ and $H = 3E_1I/2$. In reality, the legs of the DCB specimen are elastically built into the uncracked portion of the specimen rather than being rigidly fixed. This will cause deviations from classical beam theory.

To establish the actual values of the empirical parameters in Equation (14.7), measured load and displacement data at each crack length are evaluated from the load-displacement graph (Figure 14.4), and the stiffness, i.e., the inverse of the compliance ($1/C = P_c/\delta_c$), is plotted vs. crack length (a) in a double-logarithmic graph as shown in Figure 14.6. By fitting a straight line to the data, it is possible to establish the exponent, n, in Equation (14.7). Substitution of Equation (14.7) into (14.2) yields at fracture

$$G_{IC} = \frac{nP_c\delta_c}{2wa} \tag{14.8}$$

in which P_c and δ_c are the critical load and displacement associated with each crack length, a.

Three toughness values corresponding to crack growth from the insert may be defined. G_{IC}(NL) refers to the critical load and displacement associated with the deviation from linear response (Figure 14.4). The second definition, G_{IC}(vis.), refers to the visual observance of crack growth measured with the traveling microscope. The third definition, G_{IC}(5%), uses the load

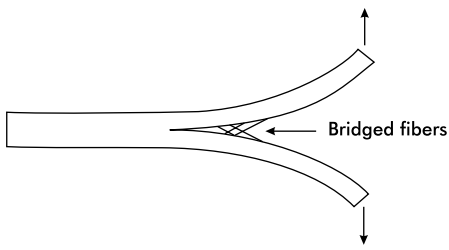

FIGURE 14.5
Fiber bridging in DCB testing.

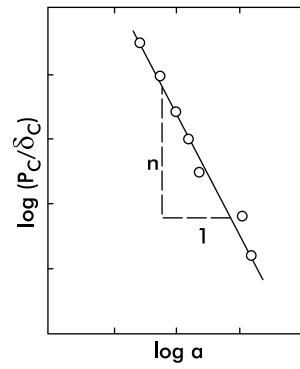

FIGURE 14.6
Log–log plot of DCB specimen stiffness vs. crack length.

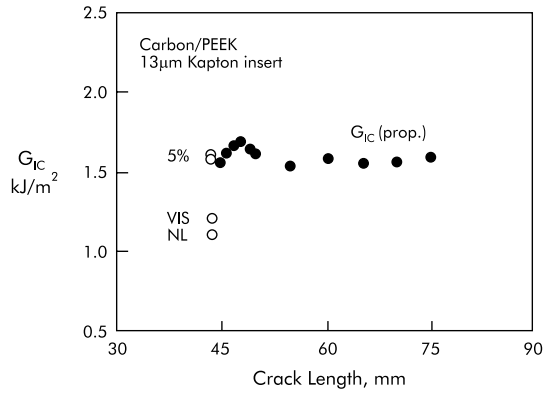

FIGURE 14.7
R-curve describing mode I interlaminar fracture resistance of carbon–PEEK with a 13 μm insert.

and displacement at a 5% increase in compliance. G_{IC}(NL) is typically the most conservative estimate of the fracture toughness and is recommended as a measure of Mode I delamination toughness. For subsequent crack growth, G_{IC} is calculated from Equation (14.8) using the recorded loads and crack lengths (Figure 14.4).

A crack growth resistance curve (R-curve) displaying G_{IC} vs. crack extension can be constructed from the fracture toughness, G_{IC}, and crack length, a, data. Figure 14.7 shows an example of an R-curve for a carbon/polyetheretherketone (PEEK) composite. At the first loading increment, the delamination grows from the tip of the thin film insert starter crack without any influence from fiber bridging. The corresponding three initiation fracture toughness values, G_{IC}(NL), G_{IC}(vis.), and G_{IC}(5%), are indicated in Figure 14.7. As the crack grows, the crack surfaces become more and more separated and bridged fibers may fracture or become pulled out from the matrix, which causes the apparent fracture toughness to increase. With further crack extension a steady-state toughness, G_{IC}(prop.), is usually reached, corresponding to an equilibrium number of bridged fibers per unit crack area. As mentioned earlier, the initial value associated with propagation of the crack from the film insert constitutes a well-defined measure of fracture toughness because it is unaffected by the fiber bridging that occurs with crack extension [11,12].

14.2 End-Notched Flexure (ENF) Test

The ENF specimen (Figure 14.8) was introduced as a pure Mode II delamination specimen for testing of composites by Russell and Street [14]. The purpose of the ENF specimen is to determine the critical strain energy release rate in pure Mode II loading of unidirectional composites [14,15]. The ENF specimen

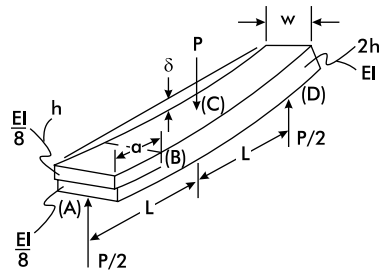

FIGURE 14.8
ENF specimen.

produces shear loading at the crack tip without introducing excessive friction between the crack surfaces [16,17]. The ENF specimen is standardized in Europe [18] and Japan [19], and has been studied extensively in the U.S. by the ASTM D-30 Committee as a candidate for ASTM standardization. As will be discussed, however, the ENF specimen is inherently unstable under displacement control, which has slowed acceptance of this specimen as a standard fracture test.

Assuming that classical beam theory is valid, an expression for the strain energy release rate, G, can be derived [14,15]:

$$G = \frac{9P^2Ca^2}{2w(2L^3 + 3a^3)} \tag{14.9}$$

where P is the applied load, C is the compliance, a is the crack length, w is the specimen width, and L is the span between the central loading cylinders and the outer support cylinders (Figure 14.8). The specimen compliance as given by beam theory [14,15] is

$$C = \frac{2L^3 + 3a^3}{8E_1wh^3} \tag{14.10}$$

where E_1 is the flexural modulus, and h is one half the total thickness of the beam, i.e., the thickness of each sub-beam of the delaminated region.

The stability of crack growth may be judged from the sign of dG/da. For fixed-load conditions, Equations (14.9) and (14.10) give

$$\frac{dG}{da} = \frac{9aP^2}{8Ew^2h^3} \tag{14.11}$$

This quantity is positive, hence the crack growth is unstable.

For fixed-grip conditions, Equations (14.9) and (14.10) give

$$\frac{dG}{da} = \frac{9\delta^2 a}{8E_1w^2h^3C^2}\left[1 - \frac{9a^3}{2L^3 + 3a^3}\right] \tag{14.12}$$

Stable crack growth requires dG/da to be less than or equal to zero. This gives

$$a \geq L/\sqrt[3]{3} \approx 0.7L \tag{14.13}$$

Consequently, for the commonly used a = L/2, the crack growth is unstable also under fixed-grip conditions. This has the consequence that only one measurement of the fracture toughness is obtained for each specimen.

14.2.1 ENF Specimen Preparation and Test Procedure

The ENF specimen is typically 120 mm long and 20 to 25 mm wide. Specimen thicknesses for unidirectional carbon- and glass-fiber composites are typically 3 and 5 mm (60% fiber volume fraction), respectively. The specimen is loaded in a three-point bend fixture (Figure 14.9) with a distance between the supports, 2L, of 100 mm. The loading and support cylinders should be about 5 mm in diameter. The crack length-to-half span ratio, a/L, should be 0.5 at propagation of the crack. Panels should be prepared with a nonadhesive Teflon or Kapton film of thickness less than 13 μm placed at the midplane to define a starter crack. Further details of specimen preparation are presented in Appendix B. After specimens have been cut from the panel, the width and thickness at the center and 1 cm from each end should be measured for all specimens. The thickness variations should not exceed 0.1 mm. Prior to testing, a brittle white coating should be applied to the specimen edges as described in Section 14.1.1.

The issue of whether precraking of the ENF specimen should be performed has long been discussed. Precracking in Mode I is likely to create the fiber-bridging discussed in Section 14.1, and is not recommended [20]. A shear precrack may be achieved by loading the specimen in the stable crack length regime, a >0.7L, according to Equation (14.13), until a short extension of the crack occurs. Unfortunately, however, it is difficult to detect the exact position and shape of the shear precrack after completion of the fracture test, and it is also difficult to obtain a straight and uniform crack front. For reasons of simplicity and consistency with the DCB procedure (Section 14.1), crack propagation from specimens with thin insert films, but without additional extension of the precrack, is advocated.

The ENF specimen is placed in a standard three-point bend fixture [21], so that a crack length, a, of 25 mm is achieved (Figures 14.9 and 14.10). To facilitate appropriate positioning of the crack tip, a low-magnification (10×) traveling microscope is useful. Mark the support location on the specimen edge for subsequent measurement of crack length. Measure the center beam deflection (load-point displacement), δ, with a linear variable differential transformer (LVDT), or from the crosshead displacement corrected for the machine compliance. Use a crosshead rate in the range of 0.5 to 1 mm/min, and monitor the load-displacement response. Record both loading and

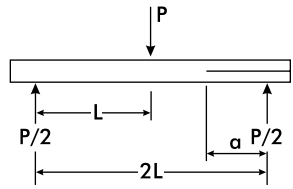

FIGURE 14.9
ENF specimen geometry parameters.

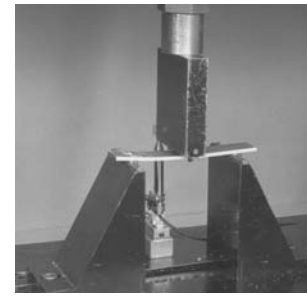

FIGURE 14.10
ENF test setup.

unloading paths. Observe the crack tip during loading (a traveling microscope is recommended) to detect any slow, stable crack propagation prior to fast fracture. Slow crack propagation preceding fast fracture is commonly observed in ductile matrix composites and leads to a nonlinear load-displacement curve (Figure 14.11 [22]). Indicate this event on the load-deflection curve. An example of a load-deflection curve for a brittle carbon/epoxy composite is shown in Figure 14.12. For this composite, fast fracture occurred without noticeable stable crack extension, and the response curve is essentially linear up to fracture.

14.2.2 ENF Data Reduction

Evaluation of the Mode II fracture toughness, G_{IIC}, requires a record of the load-displacement response, e.g., Figures 14.11 and 14.12. Toughness values G_{IIC}(NL), G_{IIC}(vis.), and G_{IIC}(max.), referring to the loads at the onset of nonlinearity, visual stable crack extension, and maximum load, respectively,

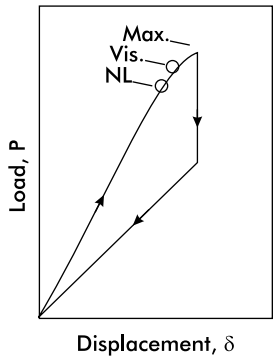

FIGURE 14.11
Schematic load-displacement curve for ENF fracture test of a ductile matrix composite. P(NL), P(vis.), and P(max.) denote loads at onset of nonlinearity, onset of visible stable crack growth, and onset of fast fracture, respectively.

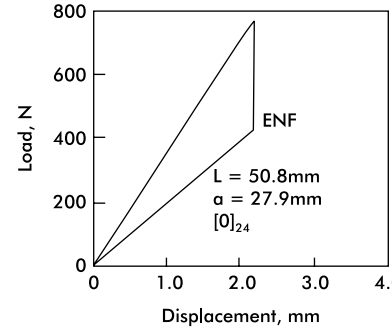

FIGURE 14.12
Load-deflection curve for a carbon/epoxy (AS4/3501-6) ENF specimen. L = 50.8 mm, w = 25.4 mm, and a = 27.9 mm.

as illustrated in Figure 14.11, can be determined. For calculation of G_{IIC}, the initial crack length is required. The initial crack length can be measured by cracking the failed specimen into two parts and measuring the distance between the support cylinders (marked on the specimen edge) and the initial crack front at three locations (each edge and center of the beam width). Commonly, the support cylinders leave imprints on the specimen surface that can be used to further verify the crack length measurements after the fracture test.

If the flexural modulus, E_1, of the specimen is not known, the fracture toughness, G_{IIC}, is calculated from the following beam theory expression using the measured compliance, C,

$$G_{IIC} = \frac{9a^2P^2\left(C - C_{SH}\right)}{4wL^3\left[1 + 1.5\left(a/L\right)^3\right]} \tag{14.14}$$

where C_{SH} is a compliance correction factor arising from interlaminar shear deformation calculated from

$$C_{SH} = \frac{6L + 3a - L^3/a^2}{20whG_{13}} \tag{14.15}$$

In the calculation of C_{SH}, the interlaminar shear modulus G_{13} is required. If G_{13} is unknown, the in-plane shear modulus, G_{12} (Chapter 7), can be used as an approximation to G_{13} for unidirectional composites. If the flexural modulus, E_1, of the ENF specimen is known, it is most straightforward to determine G_{IIC} from a beam theory expression [16],

$$G_{IIC} = \frac{9a^2\,P^2}{16w^2\,h^3\,E_1}\left[1 + 0.2\left(\frac{h}{a}\right)^2\frac{E_1}{G_{13}}\right] \tag{14.16}$$

To determine G_{IIC}(NL), G_{IIC}(vis.), and G_{IIC}(max.), the loads P(NL), P(vis.), and P(max.), defined in Figure 14.11, and the initial crack length are substituted in Equations (14.14) and (14.16). Consider, as an example, the load-displacement record shown in Figure 14.12 for a carbon/epoxy ENF specimen of dimensions L = 50.8 mm, a = 27.9 mm, 2h = 3.5 mm, w = 25.3 mm, and $G_{13} = G_{12} = 5$ GPa. The critical load was 762 N, and the specimen compliance was 2.3 μm/N. Substituting these data in Equations (14.14) and (14.15) gives $G_{IIC} = 553$ J/m^2.

Note that the experimental compliance calibration method may be used for determination of the fracture toughness of the ENF specimen [20,22]. This method requires long ENF specimens with long precrack lengths, which enable sliding of the specimen across the test fixture to cover the desired range of crack lengths. Compliance data are collected at each crack length

by loading the specimen at loads small enough not to promote crack extension. A set of compliance values at discrete crack lengths (a) is obtained, and the data set is fitted by a third-order polynomial in crack length,

$$C = C_0 + C_3a^3 \tag{14.17}$$

Differentiation of this equation with respect to crack length, and substitution into Equation (2.59), yields

$$G = \frac{3P^2C_3a^2}{2w} \tag{14.18}$$

Substitution of the corresponding critical loads, Figure 14.11, into this equation yields G_{IIC}(NL), G_{IIC}(vis.), and G_{IIC}(max.).

Overall, however, this method tends to yield highly scattered G_{IIC} data for the ENF test. Davies et al. [23] found that the coefficient of variation for G_{IIC} as determined for a carbon/epoxy composite using Equation (14.18) is 21%, whereas the corresponding value for the beam analysis method, Equation (14.16), is 14%. The reasons for the low precision are that the rate of change in the ENF specimen compliance with crack length is relatively small, and the experimental determination of compliance requires accurate measurements of crack length, load, and displacement, whereas Equation (14.16) requires load and crack length only [23].

14.3 The Four-Point Bend ENF (4ENF) Test

As indicated above, the ENF specimen suffers from unstable crack growth, which means that only one toughness value per specimen can be determined. Consequently, it is not possible to determine Mode II R-curves using this specimen. In an effort to overcome this drawback, a stable test obtained by modification of the load introduction to the ENF specimen (Figure 14.13) was recently proposed by Martin and Davidson [24]. Because of the four-point loading, the specimen is called a 4ENF specimen [24]. The 4ENF test employs a specimen similar to the ENF specimen and is currently being examined as a standard pure Mode II delamination fracture test method by the ASTM D-30 committee. As discussed by Davies et al. [23], promoting stable delamination growth has several benefits; an R-curve can be determined, which may be important for damage tolerance assessment, and an R-curve yields more significance to the measured initiation value of G_{IIC}. The data analysis for the 4ENF specimen is currently based on the experimental compliance method because this method is perceived as being more accurate

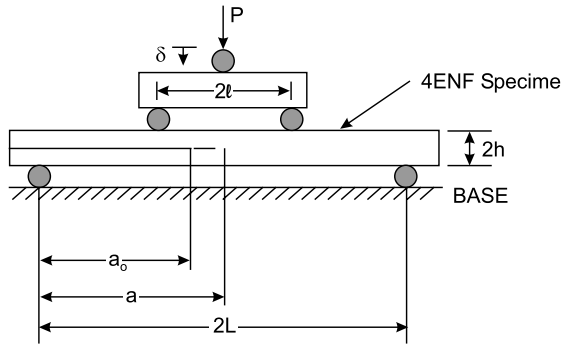

FIGURE 14.13
Principle of 4ENF test and definition of geometry parameters.

than analytically derived procedures. Presently, to the best knowledge of the authors, no beam analysis for the 4ENF specimen has been published.

14.3.1 4ENF Specimen Preparation

The 4ENF specimen is prepared in the same way as the ENF specimen, although the recommended length is 140 mm. The length of the insert film at the edge of the panel (Appendix B) should be about 50 mm. The ends of the insert should be marked on the edges of the panels before specimens are cut. After specimens are cut from the panels, measure the length of each specimen to the nearest millimeter. Measure the width and thickness of each specimen at the center and 1 cm from each end, to the nearest 0.05 mm. The variation in thickness should not exceed 0.1 mm. Similar to the DCB and ENF specimens, the edges of the specimens should be coated with a brittle white coating to aid in detection of the crack tip. Place a reference mark at the end of the insert. Its exact location is difficult to locate, but may be verified after completion of the fracture test by splitting the specimen open. Marks should be placed every mm over a distance of about 4 cm ahead of the insert tip.

14.3.2 4ENF Test Fixture

Figure 14.13 shows the pertinent geometry symbols for the 4ENF test geometry and specimen. The diameter of the loading and support cylinders are as specified for the three-point flexure test in ASTM D 790, i.e., 10 mm [21]. The lower support span, 2L, should be 10 cm, and the upper span, 2ℓ, should be 6 cm. The upper loading cylinders should be mounted on a beam that is allowed to rotate freely about a horizontal axis perpendicular to the longitudinal axis of the beam specimen to ensure equal load sharing for the two loading cylinders during loading of the (asymmetric) specimen. The upper cylinder, where load is introduced, should be centered between the upper and lower loading and support cylinders.

14.3.3 4ENF Test Procedure

The 4ENF specimen should be placed in the fixture so that the tip of the insert film, which is about 50 mm long, is 15 mm inside the left upper loading cylinder (Figure 14.13). This positioning corresponds to a 35-mm-long precrack length, $a_0 = 35$ mm. To facilitate positioning of the specimen in the test fixture at the proper crack length, it is beneficial to use a low-magnification (10×) traveling microscope. Mark the support location at the cracked end on the specimen edge to aid in subsequent crack length identification.

Load the specimen in a properly calibrated test fixture using displacement control. Set the crosshead rate between 0.1 and 0.5 mm/min and adjust the traveling microscope so that propagation of the delamination can be monitored during loading.

The displacement of the loading point, δ (Figure 14.13), can be measured using an LVDT or from the crosshead motion corrected for machine and fixture compliance, if necessary. Record the load (P) vs. displacement (δ) response on a chart recorder while observing the delamination front. At the onset of crack propagation, mark the P-δ graph as indicated by "vis" in Figure 14.14. The loading should be stopped after about 2 to 3 mm of crack growth. If possible, check the opposite edge for uniformity of growth. The difference in crack length between the two edges should be less than 2 mm for a valid test. Sometimes the crack propagates unstably from the insert. Figure 14.15 represents actual test results for an IM7/8552 carbon/epoxy 4ENF specimen [25]. For the first increment the crack "jumped" about 12 mm (Figure 4.15). Schuecker and Davidson [25] attributed this phenomenon to the higher toughness associated with propagation through the resin pocket in front of the insert film.

After 2 to 3 mm of crack growth is observed, the specimen should be completely unloaded at a crosshead rate up to 5 mm/min. The specimen should then be reloaded at the same rate as used for the first loading increment. If a significant amount of unstable growth occurs, Schuecker and Davidson [25] propose to shift the specimen to the left in the fixture so that

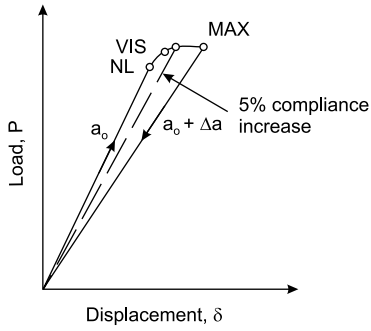

FIGURE 14.14
Schematic load-displacement record for 4ENF test.

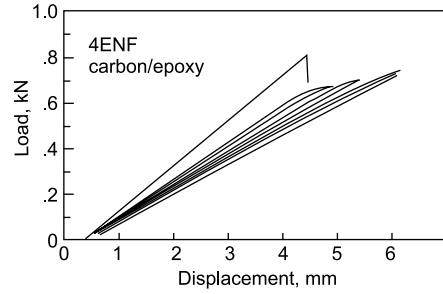

FIGURE 14.15
Load-displacement curves for a carbon–epoxy 4ENF specimen showing initial unstable growth [25].

the original initial crack length is restored. This is necessary to enable enough length for subsequent crack propagation increments (at least six). Following this procedure, subsequent propagation cycles, each with 2 to 3 mm of crack propagation, should be performed in the above-described manner (Figure 14.15) until the delamination front reaches within 10 mm of the right loading cylinder. The subsequent crack increments should occur in a stable manner without crack jumps.

After completion of the test, remove the specimen from the fixture and split it open. The length of the precrack can now be measured, which, if necessary, enables for correction of the crack length, a, measured from the marks on the specimen edge.

14.3.4 4ENF Data Reduction

Evaluation of the fracture toughness, G_{IIC}, of the 4ENF specimen is based on the experimental compliance method. Compliance, $C = \delta/P$, is determined from the linear slope of the load-displacement record. After the crack lengths are corrected (see Section 14.3.3), compliance data are graphed as shown in Figure 14.16. As indicated in Figure 14.16, the C vs. a data follow a linear relation, i.e.,

$$C = C_0 + C_1 a \tag{14.19}$$

Combining Equations (14.19) and (14.2) yields

$$G = \frac{P^2 C_1}{2w} \tag{14.20}$$

where w is the specimen width. At fracture, $P = P_c$ and $G = G_{IIC}$. The parameter C_1 in Equations (14.19) and (14.20) is identified as the slope, m, of the line fitted to the data points in Figure 14.16. It is possible to determine fracture

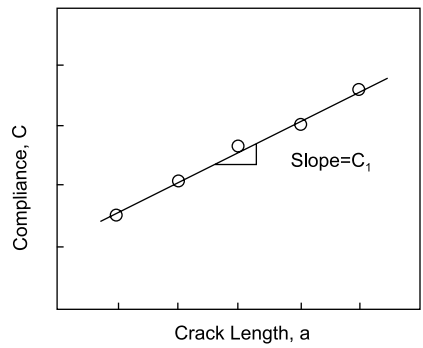

FIGURE 14.16
Schematic of compliance vs. crack length for a 4ENF specimen.

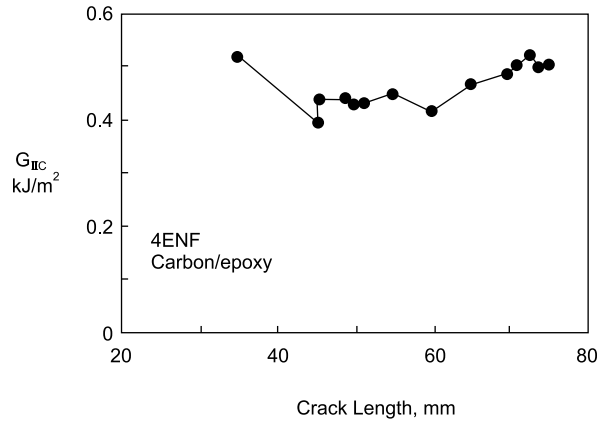

FIGURE 14.17
Mode II R-curve for a carbon/epoxy composite [23].

toughness values based on the load when the load-displacement record deviates from linearity (NL), the load when crack propagation is visually observed (vis.), and the maximum load (max.) (Figure 14.14). In case the P-δ record is highly nonlinear and there is no clear indication of an early maximum, the point on the P-δ curve where a straight line offset by a 5% increase in compliance intersects the curve may be used as the maximum load (Figure 14.15). In this manner, it is possible to establish three toughness values for each loading increment, i.e., G_{IIC}(NL), G_{IIC}(vis.), and G_{IIC}(max.). If any of these toughness values are plotted vs. crack length, a fracture resistance curve is obtained. Figure 14.17 shows an R-curve determined for a carbon/epoxy composite where G_{IIC}(max.) is plotted vs. crack extension [23]. The first data point represents (unstable) propagation from the insert. The R-curve for stable growth is quite flat, although there is a slight increase in G_{IIC} with crack extension for this composite. The initial G_{IIC} value tends to be 20 to 30% higher than those at subsequent crack increments [23,25]. Moreover, the G_{IIC} values determined using the 4ENF test are typically 10 to 20% higher than those determined using the ENF test [26]. Part of this difference has been attributed to friction between sliding crack faces, which is more a concern for the 4ENF test than the ENF test. This is because in the 4ENF test there are two contact regions where the crack faces slide (Figure 14.13), whereas in the ENF geometry (Figure 14.8) there is only one such region. Detailed analysis of the frictional effect in the 4ENF test [26], however, shows that in a typical 4ENF test, friction will increase the apparent G_{IIC} value by no more than 5%.

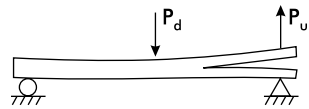

FIGURE 14.18
Principle of MMB test.

14.4 Mixed-Mode Bending (MMB) Test

In most practical situations, delaminations in composite laminates tend to grow in mixed-mode stress fields, i.e., tension and shear stresses are acting ahead of the crack front. Previous work, e.g., References [27,28], has shown that the resistance to delamination growth increases as the amount of shear loading (Mode II) increases. Consequently, delamination characterization requires mixed-mode fracture testing. Several mixed-mode fracture tests exist where various combinations of Mode I and Mode II can be generated. Most such methods, however, suffer from complicated test fixturing, a small range of mode mixities (G_{II}/G_I), and varying mode mixity as the crack grows [29].

The most promising test principle for mixed-mode delamination toughness testing is the MMB test proposed by Crews and Reeder [30–32] (Figure 14.18). The MMB test is a superposition of the DCB and ENF tests discussed previously. The MMB method has recently become an ASTM standard [33] because of simplicity of testing and the wide range of mode mixities possible.

Figure 14.19 depicts the geometry parameters and test principle of the MMB specimen. The loading lever adds an opening load to the midspan-loaded ENF specimen. The distance, c, between the point of load application and the midspan, determines the ratio of the downward force, P_d, to upward force, P_u, and hence the mode mixity. Pure Mode II corresponds to c = 0, with the ratio G_{II}/G_I decreasing with increasing distance c.

A distance of 15 mm between the point of load application and the specimen midplane (Figure 14.19) has been found to minimize geometrical nonlinearity effects [31,32]. Figure 14.20 shows various parts of the MMB assembly [34]. Detailed drawings are provided in ASTM Standard D 6671 [33]. Loading supports should be between 5 and 15 mm in diameter and should be mounted on roller bearings. The MMB specimen is loaded through roller bearings attached to the lever (Figure 14.20). Figure 14.21 shows a photograph of the MMB test setup. The loading lever is a low weight aluminum I-beam that is several orders of magnitude stiffer than the specimen.

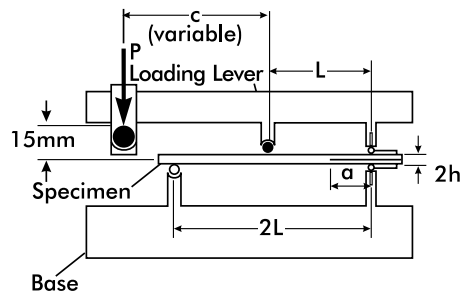

FIGURE 14.19
Definition of geometry parameters for the MMB specimen.

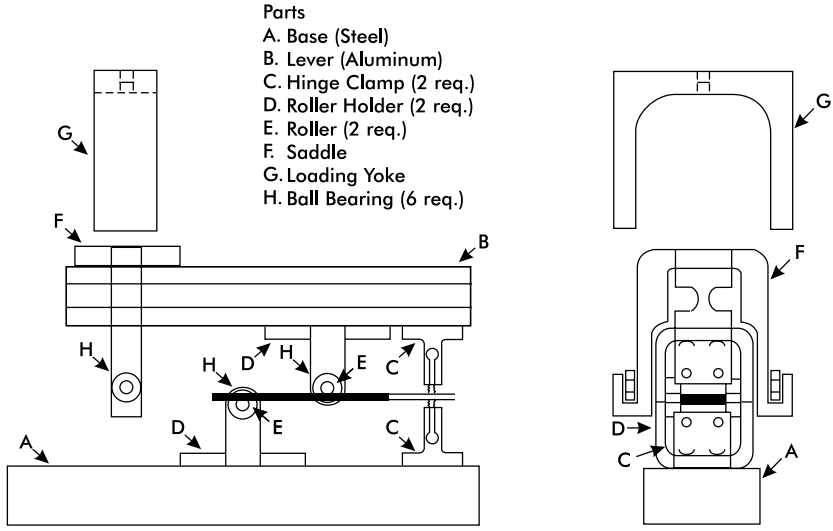

FIGURE 14.20
MMB test assembly [33].

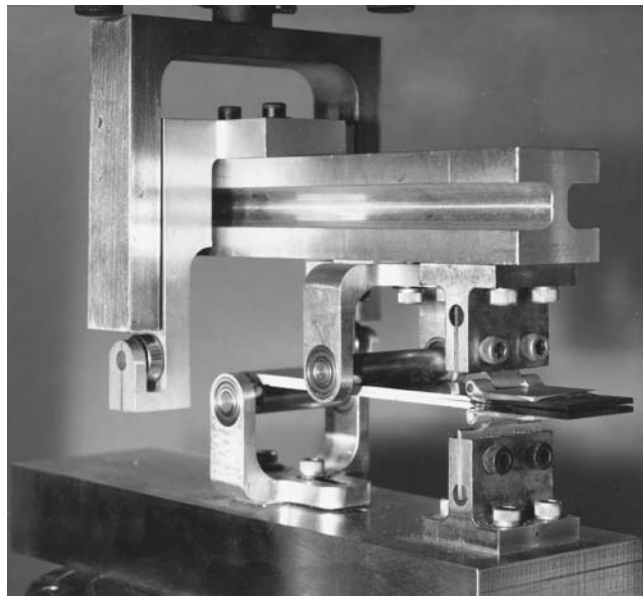

FIGURE 14.21
MMB test setup. (Courtesy of J.R. Reeder, NASA Langley Research Center.)

The lever load, the midspan load, and the left support reaction are applied through bearing-mounted rollers to reduce frictional forces. The right end of the specimen is loaded through high-quality, extruded aluminum hinges bonded to the specimen arms. The apparatus rests on a thick steel base.

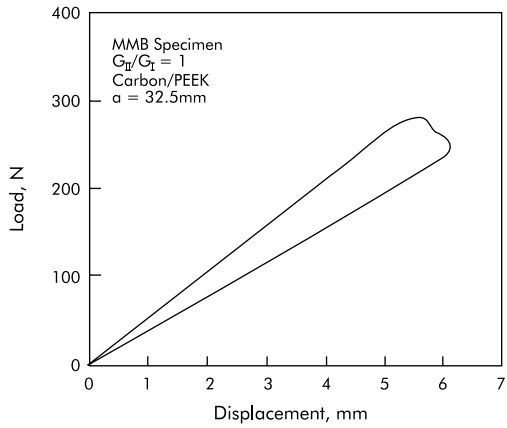

FIGURE 14.22
Load-displacement record for a carbon/PEEK MMB specimen [30].

14.4.1 MMB Test Procedure

The MMB test employs a 165-mm-long, hinged specimen prepared as the DCB specimen discussed in Section 14.1 (no precrack) (see also Appendix B). The width and thickness of each specimen is measured to the nearest 0.025 mm at the midpoint and at 1 cm from both ends. Three thickness measurements are made at each of these positions with one measurement close to each edge and one at the center. Variations in thickness should not exceed 0.1 mm. Average values of the width and thickness measurements shall be recorded. The specimen width, w, and nominal thickness, 2h, for the carbon/epoxy composite considered by Reeder and Crews [30–32] are 25 mm, and 3 to 4.4 mm, respectively. The initial delamination length, a, is 25 mm, and the half-span length, L, is 50 mm (Figure 14.19). The loading lever length, c, should be set to approximately achieve the following mode mixities: G_{II}/G_I = 0.25, 1, and 4 (using Equation (4.25) of the next section). Test a minimum of three replicate specimens at each mode mixity.

Use a crosshead rate of 0.5 mm/min for consistency with the Mode I and Mode II tests discussed above. Record the load-displacement response on an x-y recorder, while monitoring the crack tip with a low magnification traveling microscope. If slow, stable crack growth occurs, mark this event on the load-displacement curve. Figure 14.22 shows a load-displacement record for a carbon/PEEK composite [30]. It is observed that the load-displacement record is similar to that of the ENF specimen, Figure 14.11, which allows evaluation of G_C(NL), G_C(vis.), and G_C(max.).

14.4.2 MMB Data Reduction

The following empirical expressions for the Mode I and Mode II components of the strain energy release rate were suggested by Hashemi et al. [34] and Kinloch et al. [35],

$$G_I = \frac{12P_1^2(a + xh)^2}{w^2h^3E_1} \tag{14.21a}$$

$$G_{II} = \frac{9P_{II}^2(a + 0.42xh)^2}{16w^2h^3E_1} \tag{14.21b}$$

where $G = G_I + G_{II}$, and P_I and P_{II} are the opening and shearing components of the applied load given by [30],

$$P_I = P\left(\frac{3c - L}{4L}\right) \tag{14.22a}$$

$$P_{II} = \frac{P(c + L)}{L} \tag{14.22b}$$

The correction term x in Equations (14.21) was obtained by curve fitting Equations (14.21) to numerical (finite element) data [34,35],

$$x = \left[\frac{E_1}{11G_{13}}\left(3 - 2\left(\frac{\Gamma}{\Gamma + 1}\right)^2\right)\right]^{1/2} \tag{14.23}$$

with

$$\Gamma = 1.18\frac{\sqrt{E_1E_2}}{G_{13}} \tag{14.24}$$

The expressions (14.21) are considered quite accurate for commonly used MMB geometries and carbon/epoxy composites [36]. It may furthermore be verified that the ratio between the fracture modes, e.g., G_{II}/G_I, as given by Equations (14.21), is only weakly dependent on crack length.

An approximate equation for the mode mixity is obtained from the asymptotic beam analysis presented in Reference [30],

$$\frac{G_{II}}{G_I} = \frac{3}{4}\left(\frac{c + L}{3c - L}\right)^2, \qquad c \geq L/3 \tag{14.25}$$

For $c < L/3$, crack face contact may occur that corresponds to $G_1 = 0$ and invalidates the analysis above. Equation (14.25) can be used for initial (approximate) calculation of the mode mixity, which more accurately is calculated using Equations (14.21).

After testing is complete, break open the specimen and measure the crack length (the distance from the center of the hinge pin to the end of the delamination starter film). Measure the crack length at the edges and center of the specimen and obtain a mean value.

Calculations of G_I and G_{II} using Equations (14.21) require the critical load and several of the material properties, i.e., E_1, E_2, and G_{13}. The moduli E_1, E_2, and G_{13} (approximately equal to G_{12}) have to be known from previous tests (Chapters 5 and 7). The (flexural) modulus E_1 may also be calculated from the MMB compliance C [33, 37]

$$E_1 = \frac{8(3c - L)^2(a + xh)^3 + (c + L)^2\left[4L^3 + 6(a + 0.42xh)^3\right]}{16CL^2wh^3} \tag{14.26}$$

where C is the specimen compliance corrected for the load cell compliance and (lever length-dependent) fixture compliance.

As an alternative, more accurate procedure, the uncracked portion of the beam may be tested in three-point bending [21] to obtain the flexural modulus E_1 as specified in Chapter 8.

The components $(G_I, G_{II})_C$ of the mixed-mode fracture toughness are calculated using the various moduli, specimen geometry data, and measured critical load in Equations (14.21).

It has become customary to represent mixed-mode fracture toughness data in terms of the Mode II fraction, G_{II}/G, where $G = G_I + G_{II}$. Benzeggagh and Kenane [38] proposed the following type of equation for empirical description of the relation G_C vs. G_{II}/G,

$$G_C = G_{IC} + \left(G_{IIC} - G_{IC}\right)\left(G_{II}/G\right)^{\beta} \tag{14.27}$$

where β is an empirical factor determined from a fit of the experimentally determined G_C vs. G_{II}/G data. Figure 14.23 shows the relation between G_C and G_{II}/G for a range of carbon fiber, polymer matrix composites [37]. It is observed that the fracture toughness of AS4/PEEK remains fairly independent of mode ratio, while the fracture toughness of the more brittle thermoset-matrix composites shows a quite large sensitivity to the mode ratio.

14.5 Edge-Cracked Torsion (ECT) Test

The ECT test was introduced by Lee in 1993 [39] as a test method to determine the Mode III delamination toughness of composites. Figure 14.24 shows the ECT test specimen and test fixture. The test specimen is a rectangular composite plate containing an edge delamination at the midplane.

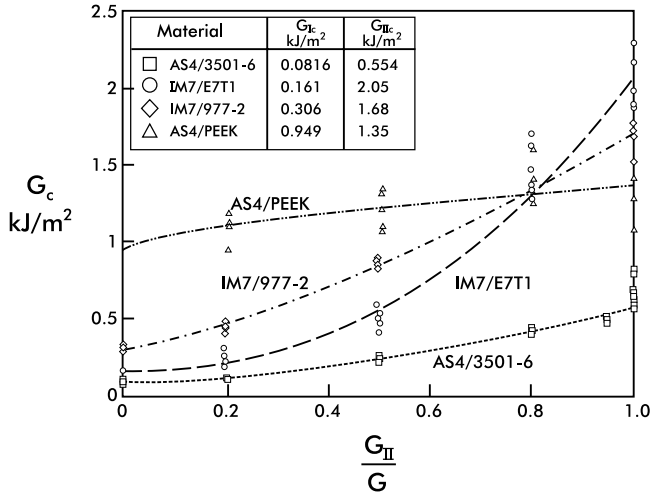

FIGURE 14.23

Mixed-mode interlaminar fracture toughness for a variety of carbon fiber, polymer matrix composites. The parameter β (Equation (14.27)) varies from 0.63 (AS4/PEEK) to 2.35 (IM7/977-2) for such composites [37].

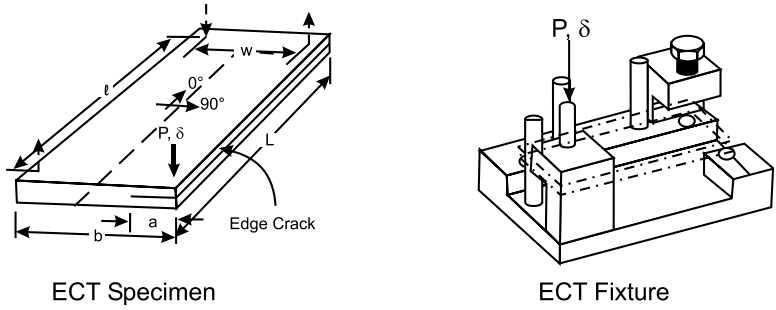

FIGURE 14.24

ECT specimen and test fixture [39]. The specimen is loaded near the right front corner and supported near the other corners. Forces at those corners are reaction forces.

For carbon/epoxy, a lay-up of $[90/(\pm 45)_n/(\mp 45)_n/90]_s$, with the longitudinal direction defining the 0° direction, is recommended. The integer n is 2 or 3, corresponding to a total of 20 or 28 unidirectional plies, respectively. A precrack is defined by inserting a strip of film of thickness less than 13 μm between the 90° plies at the midplane of the panel to define an edge crack of length a (Figure 14.24). Appendix B outlines the panel design for the ECT specimen.

The test fixture (Figure 14.24) is designed so that three corners of the panel are supported, while one corner on the cracked side is displaced normal to the panel. This loading produces a pair of couples of equal magnitude but of opposite sign that induce twisting of the plate and the characteristic Mode III deformation illustrated in Figure 2.9. Crack propagation should

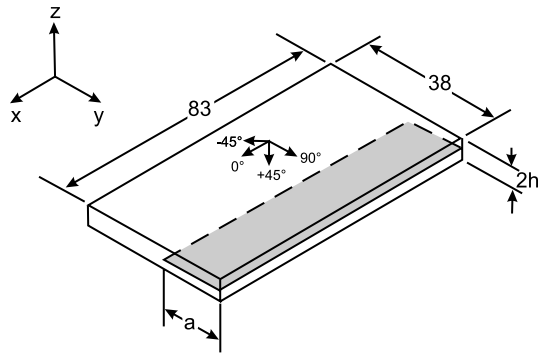

FIGURE 14.25
ECT specimen geometry and dimensions.

ideally occur uniformly in a direction perpendicular to the crack front at the midplane, i.e., parallel to the 0° fibers. In this way, a toughness value, G_{IIIC}, is determined that may be compared to those determined in the Mode I and Mode II tests outlined above.

14.5.1 ECT Specimen Preparation

The ECT specimen (Figure 14.25) is a flat, rectangular plate, 83 mm long and 38 mm wide. Lay-ups are $[90/(\pm 45)_n/(\mp 45)_n/90]_s$, where n = 2 or 3 for unidirectional carbon/epoxy and n = 3 for unidirectional glass/epoxy. Corresponding laminate thicknesses are about 2.5 and 3.6 mm. An edge crack is defined by inserting a thin strip (<13 μm) of nonstick film such as Teflon, Kapton, or polypropylene. The film is inserted between the 90° plies at the midplane to define a straight precrack of the desired length, a (Figure 14.25). Specimen details are provided in Figure 14.25. Panel design is outlined in Appendix B. Precrack lengths of 0, 8, 11, 15, 19, and 23 mm are recommended. Although testing of the uncracked specimen (a = 0) does not yield any toughness data, it provides a reference point for subsequent data reduction using the compliance calibration method. After the specimens are cut from the panel, measure the width (b) and length (L) to the nearest 0.1 mm, and thickness (2h) to the nearest 0.01 mm of each specimen. Measure the width and length near the corners and at the midlength of each side. Measure thickness at the center and near each corner. Thickness should not vary more than 0.1 mm. In a manner similar to that for the other fracture specimens, the free edges may be coated with a brittle white coating to aid in visual detection of crack extension.

14.5.2 ECT Test Fixture

The schematic in Figure 14.24 shows that the ECT specimen is constrained against lateral displacement at three corners and loaded by a concentrated

normal force at the forth corner. The distance, w, between the support–loading pins along the short edge is 31.8 mm. The distance, ℓ, between the support–loading pins along the crack front is 76.2 mm.

14.5.3 ECT Test Procedure

Place the ECT test specimen in the test fixture. Adjust the threaded support pin (Figure 14.24) so that all four support–loading pins contact the specimen. Place the fixture in a properly calibrated load frame. Set the crosshead rate at 1.3 mm/min, and load the specimen while recording the load (P) vs. displacement (δ) response on an x-y recorder. Observe the crack front and P-δ record for indications of propagation of the crack.

Figure 14.26 shows schematic load-displacement records that are typically observed for the ECT test. The curve in Figure 14.26(a) indicates stable crack propagation under increasing load, whereas the curve in Figure 14.26(b) indicates some extent of unstable growth and a clearly defined early maximum load, P_c. For the curve in Figure 14.26(a), the critical load for crack propagation, P_c, is determined by the 5% offset method. A straight line offset by a 5% increase in compliance is drawn as shown in Figure 14.26(a), and P_c is defined as the load value where this line intersects the recorded P-δ curve. Notice that if the 5% offset line intersects the P-δ curve after the maximum load is reached, as in Figure 14.26(b), P_c is defined as the maximum load.

After completion of the fracture test, unload the specimen, and remove it from the fixture. Separate the fracture specimen into two halves. This enables accurate measurements of the precrack length (Figure 14.25) at the edges and midlength of the crack front. Although the final crack length is not used in the determination of G_{IIIC}, an average crack length may be determined from crack length measurements at six or more equally spaced locations along the crack front.

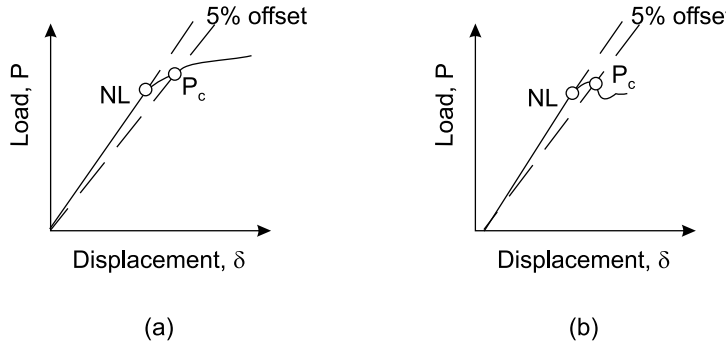

FIGURE 14.26
Schematic illustrations of load-displacement records and determination of critical load, P_c, for crack propagation in the ECT specimen: (a) stable growth, and (b) initial unstable growth.

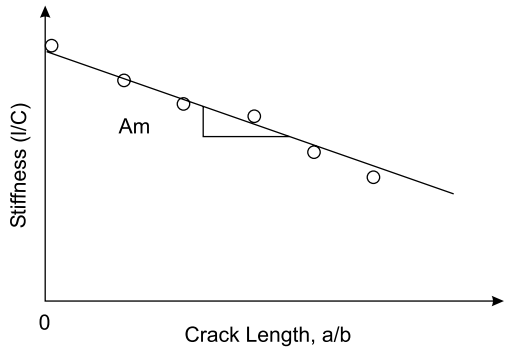

FIGURE 14.27
Stiffness (1/C) of ECT specimen plotted vs. normalized crack length (a/b) for experimental determination of mode III toughness.

14.5.4 ECT Data Reduction

Evaluation of the Mode III fracture toughness, G_{IIIC}, of the ECT specimen is based on the experimental compliance calibration method. Compliance, C, is determined from the linear slope of the load vs. displacement record (Figure 14.26), $C = \delta/P$. After correction for machine and fixture compliance, the stiffness, P/δ, i.e., the inverse of the compliance, is plotted vs. the average initial crack length, a, normalized by edge length, b, for all the specimens tested (Figure 4.27). Analysis of the ECT test [39] predicts a linear dependence of specimen stiffness on crack length, which is also observed experimentally (Figure 4.28) [40]. A linear equation in crack length is fitted to the stiffness data in Figure 14.27 using the least-squares method according to

$$\frac{1}{C} = A\left[1 - m\left(\frac{a}{b}\right)\right] \tag{14.28}$$

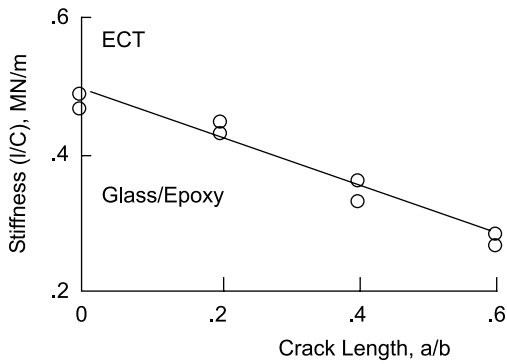

FIGURE 14.28
Stiffness vs. crack length data for glass/epoxy ECT specimen [40].

where A is the intercept of the line at the 1/C axis, and Am is the magnitude of the slope of the line. Differentiation of Equation (14.28) yields, in conjunction with (14.2), the strain energy release rate for the ECT specimen

$$G = \frac{mCP^2}{2Lb\left(1 - m\left(a/b\right)\right)} \tag{14.29}$$

where L is the distance between the two couples defined in Figure 14.24. Substitution of the critical load, P_c, into the above equation yields the Mode III delamination toughness, G_{IIIC}. Similar to the other delamination tests, G_{IIIC}(NL) and G_{IIIC}(max.) may be determined on the basis of the load-displacement record (Figure 14.26). For example, Li et al. [40] determined G_{IIIC} for a glass/epoxy composite with 56% fiber volume fraction and found G_{IIIC}(NL) = 1.23 ± 0.09 kJ/m^2 and G_{IIIC}(max.) = 1.48 ± 0.18 kJ/m^2.

References

1. R.B. Pipes and N.J. Pagano, Interlaminar stresses in composite laminates under uniform axial extension, *J. Compos. Mater.*, 4, 538–548, 1970.
2. D.J. Nicholls and J.P. Gallagher, Determination of G_{IC} in angle-ply composites using a cantilever beam test method, *J. Reinf. Plast. Compos.*, 2, 2–17, 1983.
3. P. Robinson and D.Q. Song, A modified DCB specimen for mode I testing of multidirectional laminates, *J. Compos. Mater.*, 26, 1554–1577, 1992.
4. Y.B. Shi, D. Hull, and J.N. Price, Mode II fracture of +θ/–θ angled laminate interfaces, *Compos. Sci. Technol.*, 47, 173–184, 1993.
5. F. Ozdil and L.A. Carlsson, Mode I interlaminar fracture of interleaved graphite/epoxy, *J. Compos. Mater.*, 26, 432–459, 1992.
6. N. Alif, L.A. Carlsson, and J.W. Gillespie, Jr., Mode I, mode II, and mixed mode interlaminar fracture of woven fabric carbon/epoxy, *ASTM Spec. Tech. Publ.*, 1242, 82–106, 1997.
7. B.N. Cox, R. Massabo, D.R. Mumm, A. Turrettini, and K.B. Kedward, Delamination Fracture in the Presence of Through-Thickness Reinforcement, *Proceedings of the 11th International Conference on Composite Matererials* (ICCM-11), M.L. Scott, Ed., Gold Coast, Australia, 1997, Technomic, Lancaster, PA, 1997, pp. 159–177.
8. ASTM Standard D5528-94a, *Test Method for Mode I Interlaminar Fracture Toughness of Unidirectional Fiber-Reinforced Polymer Matrix Composites*, American Society for Testing and Materials, West Conshohocken, PA, 2001.
9. W.D. Bascom, R.J. Bitner, R.J. Moulton, and A.R. Siebert, The interlaminar fracture of organic-matrix woven reinforced composites, *Composites*, 11, 9–18, 1980.
10. D.J. Wilkins, J.R. Eisenmann, R.A. Camin, W.S. Margolis, and R.A. Benson, Characterizing delamination growth in graphite-epoxy, *ASTM Spec. Tech. Publ.* 775, 168–183, 1982.
11. Z. Suo, G. Bao, and B. Fan, Delamination R-curve phenomnena due to damage, *J. Mech. Phys. Solids*, 40, 1–16, 1992.

12. T.K. O'Brien and R.H. Martin, Results of ASTM round robin testing for mode I interlaminar fracture toughness of composite materials, *J. Compos. Tech. Res.*, 15, 269–281, 1993.
13. J.P. Berry, Determination of fracture energies by the cleavage technique, *J. Appl. Phys.*, 34, 62–68, 1963.
14. A.J. Russell and K.N. Street, Factors affecting the interlaminar fracture energy of graphite/epoxy laminates, in *Progress in Science and Engineering of Composites*, T. Hayashi, K. Kawata, and S. Umekawa, Eds., ICCM-IV, ASM International, Tokyo, 1982, pp. 279–286.
15. A.J. Russell and K.N. Street, Moisture and temperature effects on the mixed-mode delamination fracture of unidirectional graphite/epoxy, *ASTM Spec. Tech. Publ.*, 876, 349–370, 1985.
16. L.A. Carlsson, J.W. Gillespie, Jr., and R.B. Pipes, On the analysis and design of the end notched flexure (ENF) specimen for mode II testing, *J. Compos. Mater.*, 20, 594–604, 1986.
17. J.W. Gillespie, Jr., L.A. Carlsson, and R.B. Pipes, Finite element analysis of the end notched flexure (ENF) specimen for measuring mode II fracture toughness, *Compos. Sci. Technol.*, 26, 177–197, 1986.
18. AECMA Aerospace Series, Carbon Fiber Reinforced Plastics: Determination of Interlaminar Fracture Toughness Energy in Mode I — G_{IC} (prEN6033) and Mode II — G_{IIC} (pr EN 6034), Association Europeene de Constructeurs de Materiel Aerospatial, Paris, France, Dec. 1995.
19. Japan Industrial Standards, JIS 7086, *Testing Methods for Interlaminar Fracture Toughness of Carbon Fiber Reinforced Plastics*, Japanese Standards Association, Tokyo, Japan, 1993.
20. T.K. O'Brien, G.B. Murri, and S.A. Salpekar, Interlaminar shear fracture toughness and fatigue thresholds for composite materials, *ASTM Spec. Tech. Publ.*, 1012, 222–250, 1989.
21. ASTM Standard D 790-00, *Test Methods for Flexural Properties of Unreinforced and Reinforced Plastics and Electrical Insulating Materials*, American Society for Testing and Materials, West Conshohocken, PA, 2002.
22. L.A. Carlsson, J.W. Gillespie, Jr., and B.R. Trethewey, Mode II interlaminar fracture of graphite/epoxy and graphite/PEEK, *J. Reinf. Plast. Compos.*, 5, 170–187, 1986.
23. P.D. Davies, G.D. Sims, B.R.K. Blackman, A.J. Brunner, K. Kageyama, M. Hojo, K. Tanaka, G. Murri, C. Rousseau, B. Gieseke, and R.H. Martin, Comparison of test configurations for determination of mode II interlaminar fracture toughness results from international collaborative test programme, *Plast. Rubber Compos.*, 28(8), 432–437, 1999.
24. R.H. Martin and B.D. Davidson, Mode II fracture toughness evaluation using a four point bend end notched flexure test, *Plast. Rubber Compos.*, 28(8), 401–406, 1999.
25. C. Shuecker and B.D. Davidson, Evaluation of the accuracy of the four-point end-notched flexure test for mode II delamination toughness determination, *Compos. Sci. Technol.*, 60, 2137–2146, 2000.
26. C. Schuecker and B.D. Davidson, Effect of friction on the perceived mode II delamination toughness from three- and four-point end-notched flexure tests, *ASTM Spec. Tech. Publ.*, 1383, 334–344, 2000.
27. W.S. Johnson and P.D. Mangalgiri, Influence of the resin on interlaminar mixed mode fracture, *ASTM Spec. Tech. Publ.*, 937, 295–315, 1987.

28. S. Hashemi, A.J. Kinloch, and J.G. Williams, The effects of geometry, rate, and temperature on the mode I, mode II, and mixed mode I/II interlaminar fracture of carbon-fiber/poly (ether-ether ketone) composites, *J. Compos. Mater.*, 24, 918–956, 1990.
29. L.A. Carlsson, Fracture of fiber composites, in *Structure and Properties of Composites*, T.-W. Chou, Ed., VCH Publishers, Weinheim, Germany, 1993, pp. 533–582.
30. J.R. Reeder and J.H. Crews, Jr., Mixed mode bending method for delamination testing, *AIAA J.*, 28(7), 1270–1276, 1990.
31. J.R. Reeder and J.H. Crews, Jr., Redesign of the mixed mode bending test for delamination toughness, S.W. Tsai and G.S. Springer, Eds., *Proceedings of the 8th International Conference on Composite Matererials*, Honolulu, HI, July 1991, Society for the Advancement of Materials and Process Engineering (SAMPE), Covina, CA.
32. J.R. Reeder and J.H. Crews, Jr., Redesign of the mixed mode bending delamination test to reduce nonlinear effects, *J. Compos. Technol. Res.*, 14(1), 12–19, 1992.
33. ASTM Standard D 6671-01, *Test Method for Mixed Mode I-Mode II Interlaminar Fracture Toughness of Unidirectional Fiber Reinforced Polymer Matrix Composites*, American Society for Testing and Materials, West Conshohocken, PA, 2001.
34. S. Hashemi, A.J. Kinloch, and J.G. Williams, The analysis of the interlaminar fracture in uniaxial fiber-polymer composites, *Proc. Math. Phys. Sci.*, 427, 173–199, 1990.
35. A.J. Kinloch et al., The mixed-mode delamination of fiber composite materials, *Compos. Sci. Tech.*, 47, 225–237, 1993.
36. S. Bhashyan and B.D. Davidson, An evaluation of data reduction methods for the mixed-mode bending test, *Proc. 37th Struct., Struct. Dyn. and Mater. Conf.*, AIAA-96-1419-CP, 1996.
37. J.R. Reeder, personal communication.
38. M.L. Benzeggagh and M. Kenane, Measurement of mixed-mode delamination fracture toughness of unidirectional glass/epoxy composites with mixed-mode bending apparatus, *Compos. Sci. Tech.*, 56, 439–449, 1996.
39. S.M. Lee, An edge crack torsion method for mode III delamination fracture testing, *Compos. Technol. Res.*, 15(3), 193–201, 1993.
40. X. Li, P. Davies, and L.A. Carlsson, Influence of fiber volume fraction on mode III interlaminar toughness of glass/epoxy, to be published.

Appendix A

Compliance and Stiffness Transformations and Matrix Operations

Transformation of plane stress compliance (S_{ij}) and stiffness (Q_{ij}) elements:

$$\begin{aligned}
\bar{S}_{11} &= m^4 S_{11} + m^2 n^2 (2S_{12} + S_{66}) + n^4 S_{22} \\
\bar{S}_{12} &= m^2 n^2 (S_{11} + S_{22} - S_{66}) + S_{12}(m^4 + n^4) \\
\bar{S}_{22} &= n^4 S_{11} + m^2 n^2 (2S_{12} + S_{66}) + m^4 S_{22} \\
\bar{S}_{16} &= 2m^3 n(S_{11} - S_{12}) + 2mn^3 (S_{12} - S_{22}) - mn(m^2 - n^2) S_{66} \\
\bar{S}_{26} &= 2mn^3 (S_{11} - S_{12}) + 2m^3 n(S_{12} - S_{22}) + mn(m^2 - n^2) S_{66} \\
\bar{S}_{66} &= 4m^2 n^2 (S_{11} - S_{12}) - 4m^2 n^2 (S_{12} - S_{22}) + (m^2 - n^2) S_{66}
\end{aligned} \tag{A.1}$$

$$\begin{aligned}
\bar{Q}_{11} &= m^4 Q_{11} + 2m^2 n^2 (Q_{12} + 2Q_{66}) + n^4 Q_{22} \\
\bar{Q}_{12} &= m^2 n^2 (Q_{11} + Q_{22} - 4Q_{66}) + (m^4 + n^4) Q_{12} \\
\bar{Q}_{22} &= n^4 Q_{11} + 2m^2 n^2 (Q_{12} + 2Q_{66}) + m^4 Q_{22} \\
\bar{Q}_{16} &= m^3 n(Q_{11} - Q_{12}) + mn^3 (Q_{12} - Q_{22}) - 2mn(m^2 - n^2) Q_{66} \\
\bar{Q}_{26} &= mn^3 (Q_{11} - Q_{12}) + m^3 n(Q_{12} - Q_{22}) + 2mn(m^2 - n^2) Q_{66} \\
\bar{Q}_{66} &= m^2 n^2 (Q_{11} + Q_{22} - 2Q_{12} - 2Q_{66}) + (m^4 + n^4) Q_{66}
\end{aligned} \tag{A.2}$$

The matrices [A′], [B′], and [D′] may be determined from

$$\begin{aligned}
[A'] &= [A^*] - [B^*][D^*]^{-1}[C^*] \\
[B'] &= [B^*][D^*]^{-1} \\
[D'] &= [D^*]^{-1}
\end{aligned} \tag{A.3}$$

where

$$[A^*] = [A]^{-1}$$

$$[B^*] = -[A]^{-1}[B] \tag{A.4}$$

$$[C^*] = [B][A]^{-1}$$

$$[D^*] = [D] - [B][A]^{-1}[B]$$

For symmetric laminates, [B] = [0]. For that case,

$$[A'] = [A]^{-1}$$

$$[B'] = [0] \tag{A.5}$$

$$[D'] = [D]^{-1}$$

Appendix B

Preparation of Test Specimens and Panels

In this appendix, specimen geometries will be summarized and suggestions for geometries and dimensions of panels for the various tests discussed in Chapters 5–14 will be presented. Note that there are many ways in which the panels could be designed. The dimensions of the panels herein should be appropriate for a laboratory-size autoclave. Dimensions of each and every test specimen and panel will not be specified. Rather, the examples provided here can be adapted to, or easily modified for, preparation of those types of specimens that are not specifically included here.

The illustrations that follow detail the specimen geometries and dimensions and show suggested panel lay-ups and dimensions (in millimeters). The lay-ups shown for the delamination beam specimens are all unidirectional $[0]_{24}$ laminates that should be appropriate for carbon/epoxy composites. Ductile-matrix composites or composites with lower modulus fibers require thicker specimens (more plies). The delamination fracture specimens (Chapter 14) incorporate a thin film at the laminate midplane to define an initial delamination. Panels for delamination testing should therefore contain an even number of plies and be manufactured with a nonadhesive Teflon or Kapton film at the laminate midplane. The film thickness should be less than 13 μm, and the film may be sprayed with a mold-release agent before it is inserted between the plies. The insert length should extend an appropriate distance from the front edge of the specimen to achieve the correct precrack length, as illustrated in the figures that follow. It is difficult to detect the thin insert film when viewed from the edge of a cut specimen. Therefore, the area covered by the insert should carefully be marked on the panel before the specimens are cut.

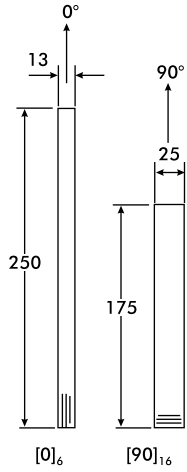

FIGURE B.1
Specimen geometries, dimensions (millimeters), and lay-ups for lamina tension experiment.

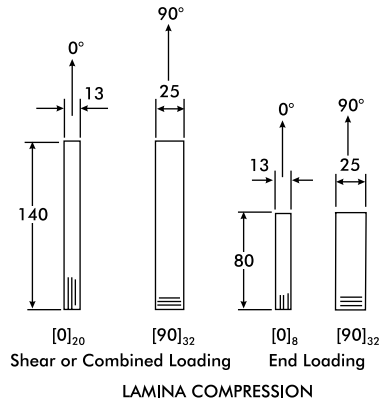

FIGURE B.2
Specimen geometries, dimensions (millimeters), and lay-ups for lamina compression experiment.

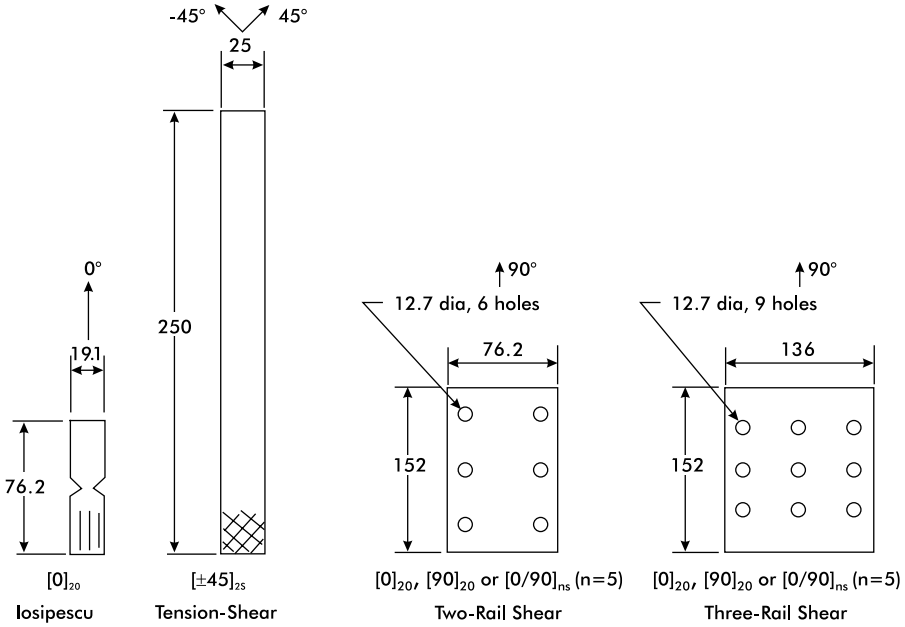

FIGURE B.3
Specimen geometries, dimensions (millimeters), and lay-ups for lamina shear experiment.

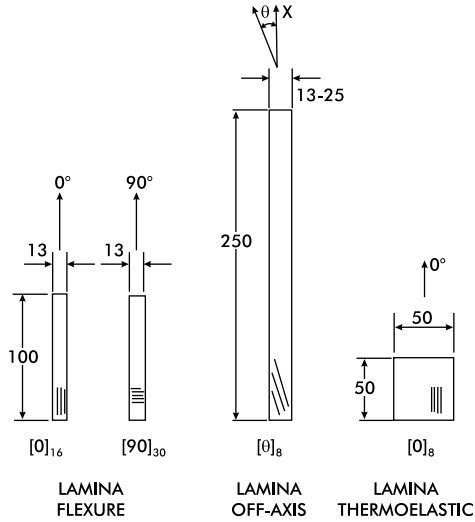

FIGURE B.4
Specimen geometries, dimensions (millimeters), and lay-ups for lamina flexure, lamina off-axis, and lamina thermoelastic experiments.

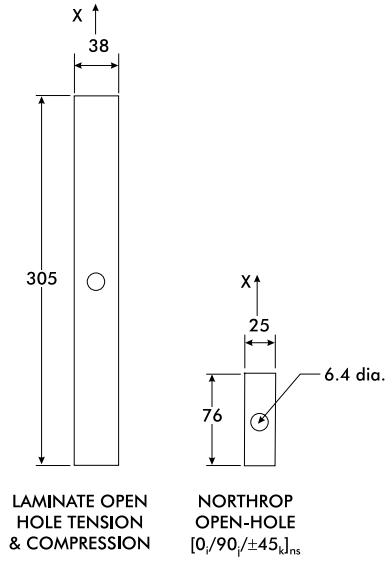

FIGURE B.5
Specimen geometries and dimensions (millimeters) for laminate open-hole tension and compression experiments.

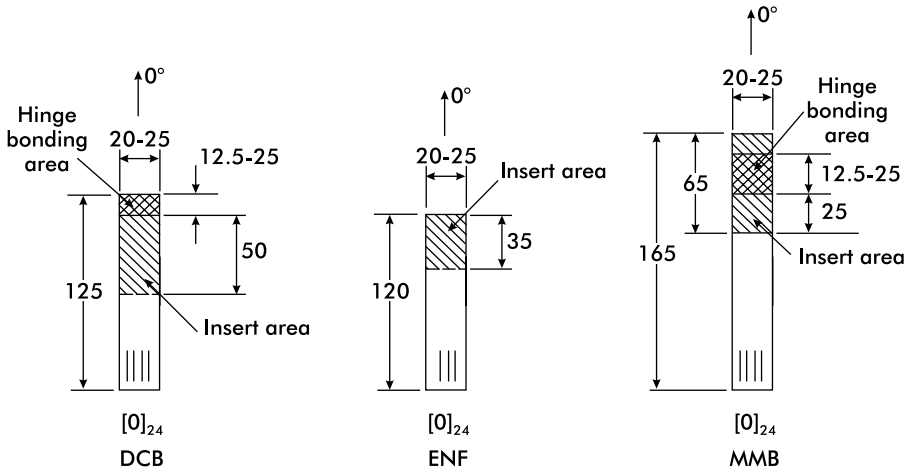

FIGURE B.6
Geometries, dimensions (millimeters), and lay-ups for DCB, ENF, and MMB specimens.

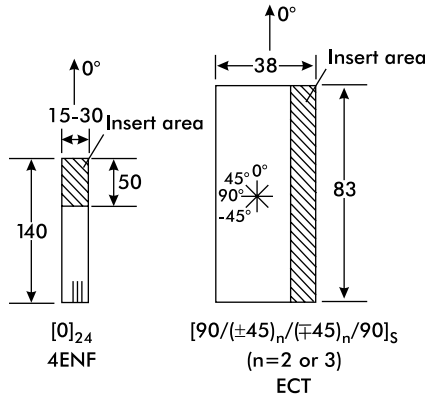

FIGURE B.7
Geometries, dimensions (millimeters), and lay-ups for 4ENF and ECT specimens.

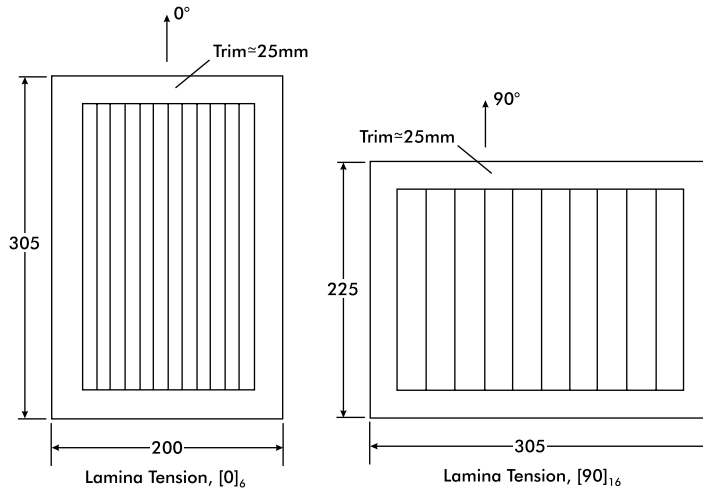

FIGURE B.8
Suggested panel dimensions (millimeters) for 0° and 90° lamina tension experiment.

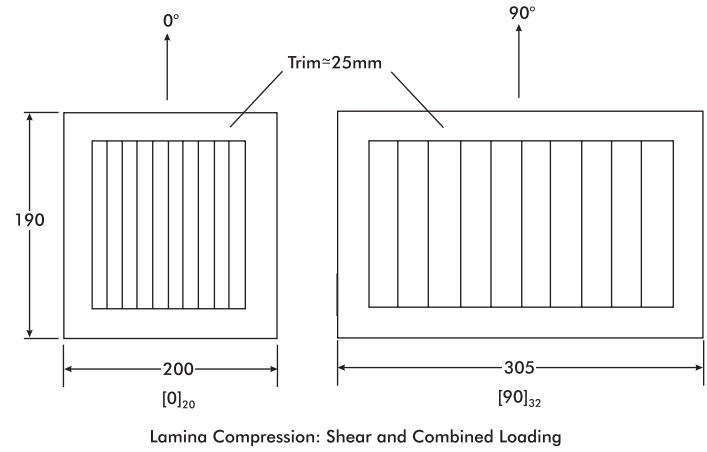

FIGURE B.9
Suggested panel dimensions (millimeters) for lamina compression experiment (shear and combined loading).

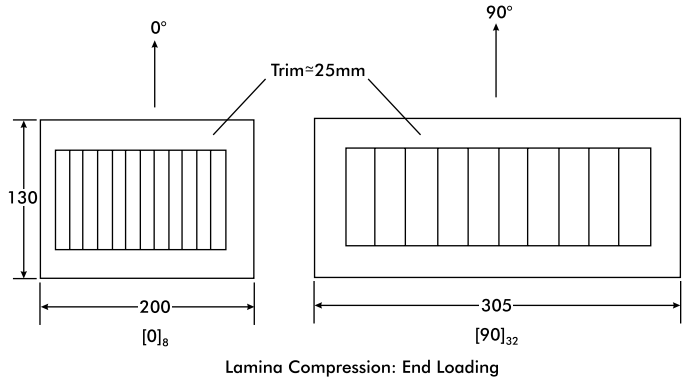

FIGURE B.10
Suggested panel dimensions (millimeters) for lamina compression experiment (end loading).

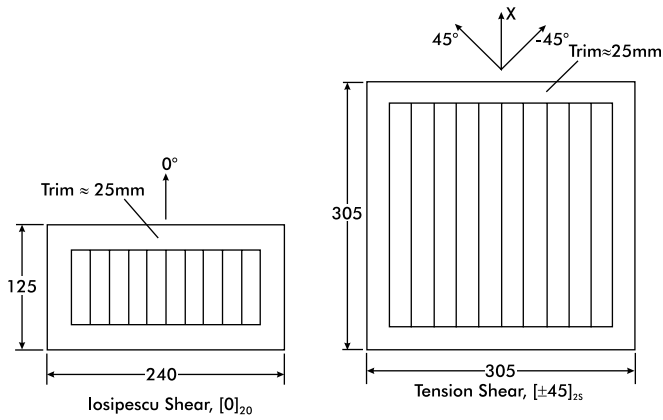

FIGURE B.11
Suggested panel dimensions (millimeters) for Iosipescu and tensile shear experiments.

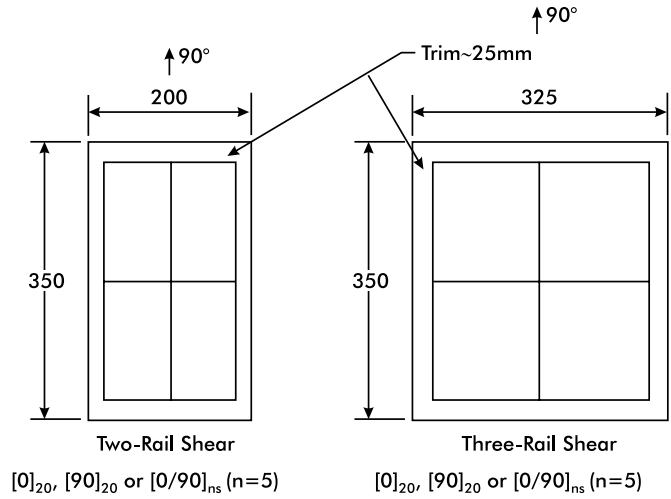

FIGURE B.12
Suggested panel dimensions (millimeters) for two-rail and three-rail shear experiments.

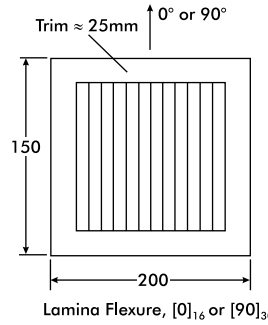

FIGURE B.13
Suggested panel dimensions (millimeters) for lamina flexure experiment.

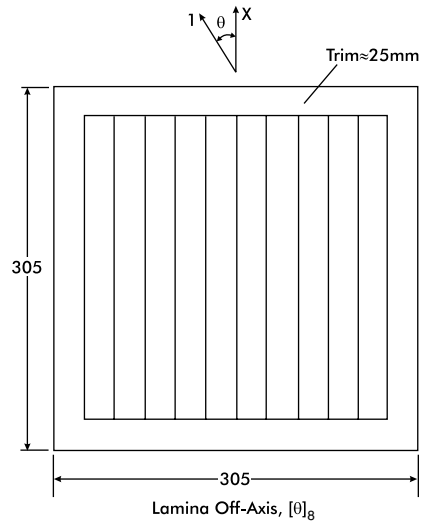

FIGURE B.14
Suggested panel dimensions (millimeters) for lamina off-axis experiment.

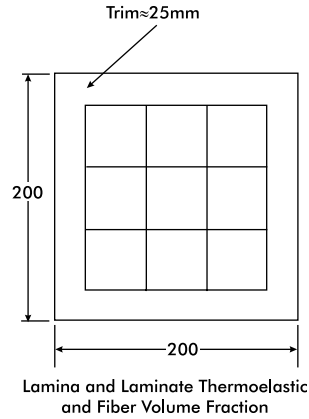

FIGURE B.15
Suggested panel dimensions (millimeters) for lamina and laminate thermoelastic and fiber volume fraction experiments.

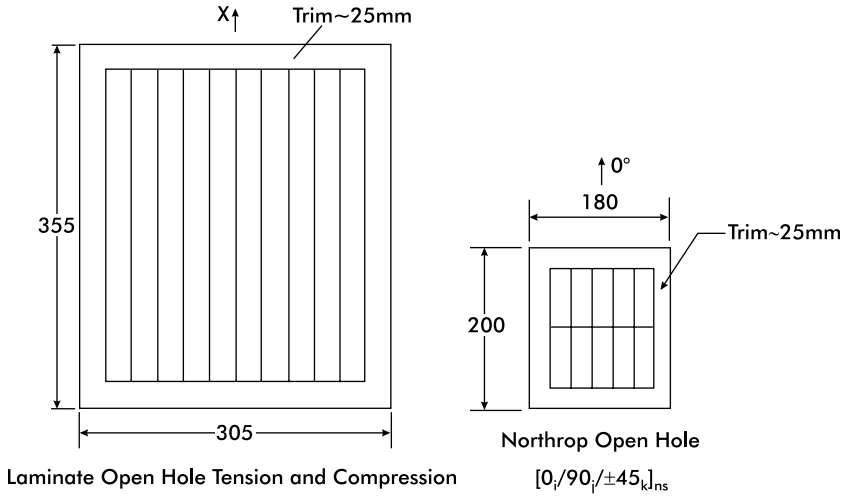

FIGURE B.16
Suggested panel dimensions (millimeters) for laminate and Northrop open-hole experiments.

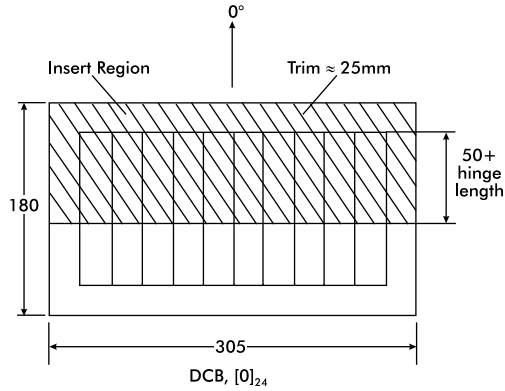

FIGURE B.17
Suggested panel dimensions (millimeters) for DCB specimen. Insert film should be placed at midplane.

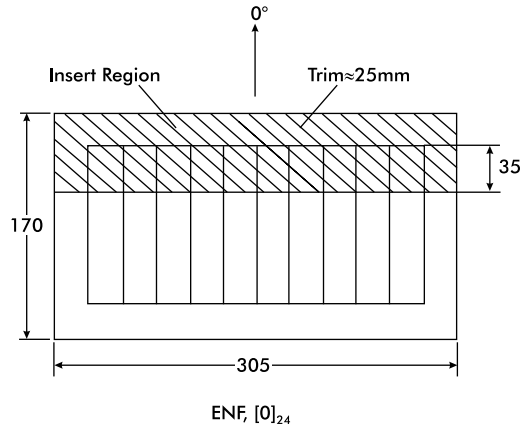

FIGURE B.18
Suggested panel dimensions (millimeters) for ENF specimen. Insert film should be placed at midplane.

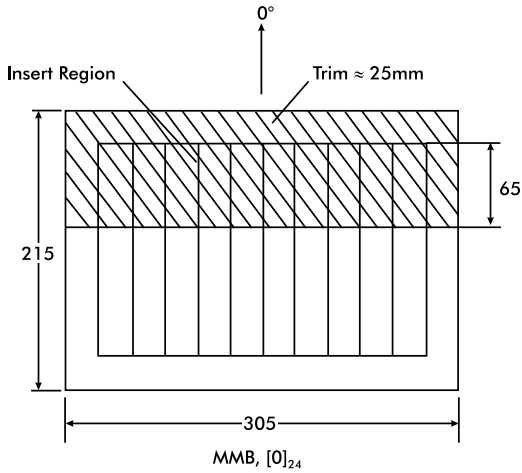

FIGURE B.19
Suggested panel dimensions (millimeters) for MMB specimen. Insert film should be placed at midplane.

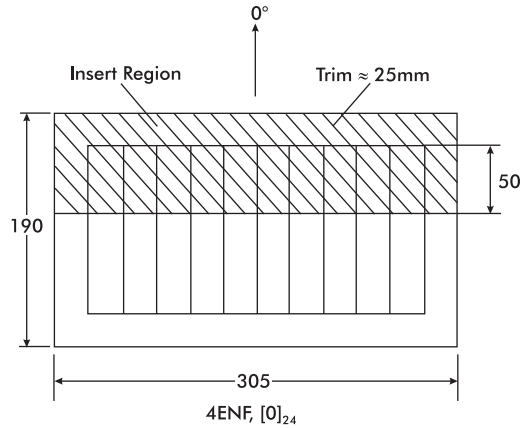

FIGURE B.20
Suggested panel dimensions (millimeters) for 4ENF specimen. Insert film should be placed at midplane.

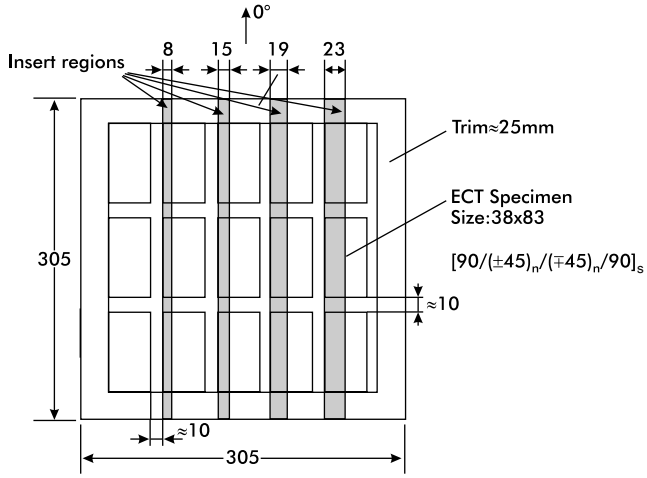

FIGURE B.21
Suggested panel dimensions (millimeters) for ECT specimen. Insert film should be placed at midplane.

Appendix C

Sample Laboratory Report

Lamina Tensile Response

The lamina tensile response of a carbon–fiber, epoxy–matrix composite was examined experimentally to establish the intrinsic mechanical properties. The test specimen geometries were chosen according to the outline presented in Chapter 5, in accordance with ASTM standards. The specimens were loaded to failure in a tensile testing machine utilizing serrated wedge grips. Average test results and standard deviations were as follows:

Elastic modulus in the fiber direction		$E_1 = 126 \pm 2$ GPa
Elastic modulus transverse to the fiber direction		$E_2 = 10.2 \pm 0.4$ GPa
Poisson's ratios:	Major	$\nu_{12} = 0.30 \pm 0.01$
	Minor	$\nu_{21} = 0.024$
Ultimate tensile stress in the fiber direction		$X_1^T = 2037 \pm 85$ MPa
Ultimate tensile stress in the transverse direction		$X_2^T = 53 \pm 8$ MPa
Ultimate tensile strain in the fiber direction		$e_1^T = 0.015$
Ultimate tensile strain in the transverse direction		$e_2^T = 0.0057$

Procedure

The procedure for this experiment is detailed in Chapter 5. Briefly, unidirectional panels were configured for achieving test specimens with 0 and 90° orientation as shown in Appendix B. After the edges of the panels were trimmed, tabs made from a glass–fabric epoxy laminate were adhesively bonded to both surfaces at two opposite edges of the panels. Four specimens of each orientation were machined to the appropriate widths using procedures detailed in Chapter 4. The 0° specimens were nominally 12.7 mm wide, whereas the 90° specimens were 25.4 mm wide. The 0° specimens were 8 plies thick, whereas the 90° specimens were 16 plies thick. To establish the axial stiffness (E_1), Poisson's ratio (ν_{12}), and the overall stress–strain response of the 0° specimens, a bidirectional (0°/90°) strain gage rosette was bonded at the geometric center on one surface of each specimen. In addition, an axial gage was bonded on the opposite surface of the specimen. For the 90°

specimens, a single-element strain gage oriented along the length of the specimen was bonded to each surface of the specimen in the gage section to determine the axial stress–strain response. No strain gages transverse to the specimen loading axis were used because the minor Poisson's ratio (ν_{21}) may be determined from E_1, E_2, and ν_{12}. Each specimen was tested in a general-purpose testing machine at a crosshead rate of 2 mm/min. Specimen load and strains were sampled throughout the test using a PC-driven data acquisition system. The specimens were loaded to failure.

Specimen Dimensions

Specimen cross-sectional dimensions were recorded as follows:

Specimen	Orientation (deg)	Width (w) (mm)	Thickness (t) (mm)
1	0	12.78	1.067
2	0	12.78	1.067
3	0	12.65	1.067
4	0	12.75	1.067
5	90	25.40	2.184
6	90	25.35	2.185
7	90	25.45	2.134
8	90	25.53	2.236

Stress–Strain Data

The load readings were converted to axial stress readings using the cross-sectional dimensions reported above. Examples of stress and strain data recorded using the data acquisition system are tabulated below.

Stress-Strain Data for Specimen 2 ($[0]_8$) (Reduced Set from Original Record)
The last two columns are strain readings from the same strain gage rosette.

σ_1 (MPa)	ε_1 (μstrain)	ε_1 (μstrain)	$-\varepsilon_2$ (μstrain)
0	0	10	0
36	310	320	120
72	590	600	200
108	860	870	280
144	1,140	1,160	340
180	1,420	1,440	420
252	2,010	2,000	570
395	3,050	3,030	880
647	4,900	4,850	1,380
1,006	7,490	7,430	2,040
1,294	9,470	9,420	2,540
1,617	11,640	11,590	3,070
1,977[a]	14,060	13,990	3,610

[a] Ultimate stress.

Stress-Strain Data for Specimen 6 ($[90]_{16}$)
(Reduced Set from Original Record)

σ_2 (MPa)	ε_2 (μstrain)	ε_2 (μstrain)
0	0	0
1.77	180	200
3.54	350	380
5.31	520	550
10.6	1040	1120
17.7	1750	1860
23.0	2290	2410
30.1	2990	3130
35.4	3520	3690
40.7	4120	4330
49.6	5050	5280
60.2	6220	6510
63.4[a]	6580	6879

[a] Ultimate stress.

Test Results

Test results for three representative 0° test specimens are presented in graphical form in Figures C.1–C.3. The linear response region in the fiber direction is bounded by a strain of about 0.004. It is noteworthy that the stress–strain response exhibits strain hardening characteristics — a reflection of the strain hardening behavior of carbon fibers. Results for three representative 90° specimens are shown in Figures C.4–C.6. Here only a modest nonlinearity in the stress–strain response is observed. The strain softening is due to the nonlinear response of the epoxy matrix.

Reduced Data

The mechanical properties were reduced from the measured data using procedures and equations provided in Chapter 5. The following equations were employed:

$$E_1 = \frac{\sigma_1}{\varepsilon_1} \tag{C.1}$$

$$\upsilon_{12} = \frac{-\varepsilon_2}{\varepsilon_1} \tag{C.2}$$

$$X_1^T = \sigma_1^{ult} \tag{C.3}$$

$$E_2 = \frac{\sigma_2}{\varepsilon_2} \tag{C.4}$$

$$X_2^T = \sigma_2^{ult} \tag{C.5}$$

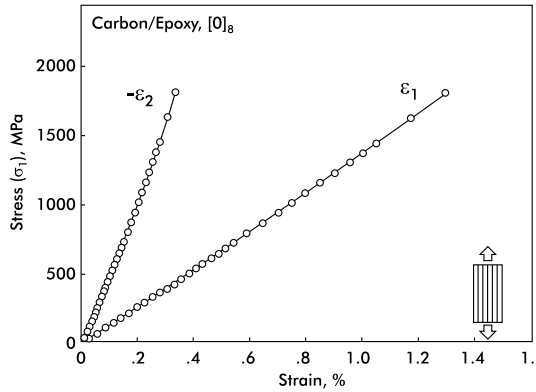

FIGURE C.1
Stress–strain results for specimen 1 (0°).

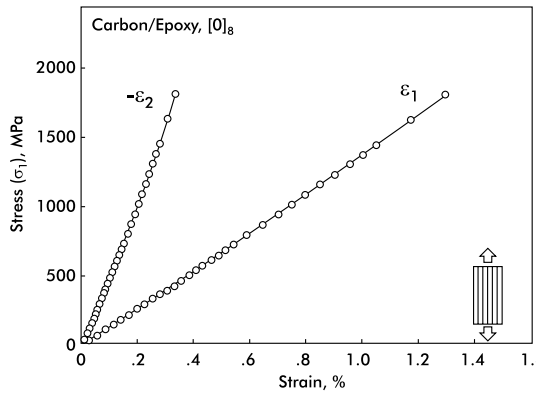

FIGURE C.2
Stress–strain results for specimen 2 (0°).

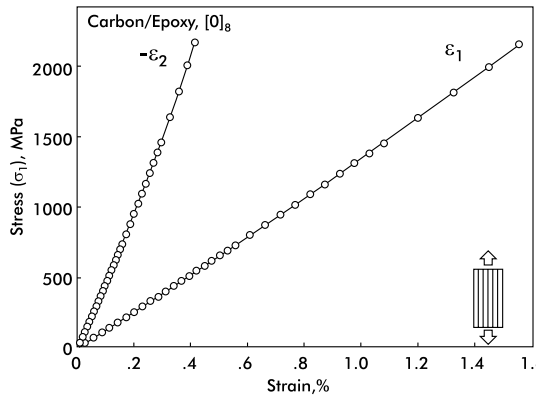

FIGURE C.3
Stress–strain results for specimen 3 (0°).

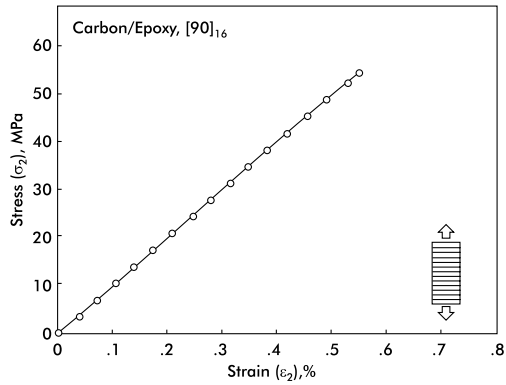

FIGURE C.4
Stress–strain results for specimen 5 (90°).

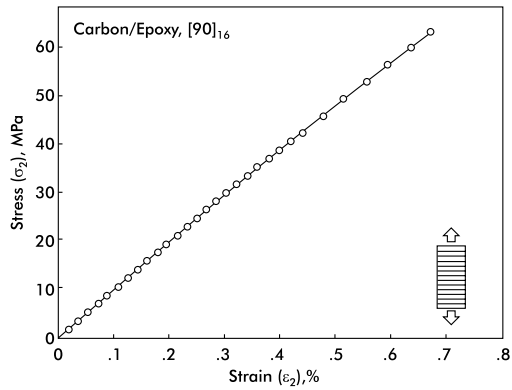

FIGURE C.5
Stress–strain results for specimen 6 (90°).

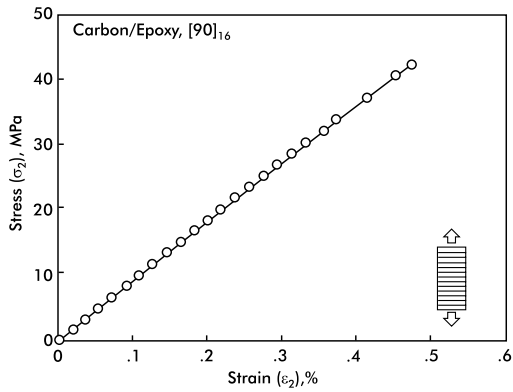

FIGURE C.6
Stress–strain results for specimen 7 (90°).

where σ_1 and σ_2 refer to the load per unit cross-sectional area ($\sigma = P/(wt)$) for the 0 and 90° tests, respectively. Note that it was not possible to evaluate experimentally the minor Poisson's ratio, ν_{21}, because the 90° specimens were not instrumented with a transversely oriented strain gage. The reduced data are summarized below.

	E_1 (GPa)	ν_{12}	X_1^T (MPa)	e_1^T	E_2 (GPa)	X_2^T (MPa)	e_2^T
	128	0.295	2034	0.015	9.92	54.5	0.0056
	127	0.292	1800	0.013	9.79	63.4	0.0067
	124	0.299	2158	0.016	10.5	45.6	0.0046
	125	0.319	1979	0.014	10.4	48.3	0.0049
Avg.	126	0.301	1993	0.015	10.2	53.0	0.0055
STD[a]	2	0.012	149	0.001	0.4	7.9	0.0010

[a] STD = standard deviation.

Using the reciprocal relations between the elastic moduli and Poisson's ratios given in Chapter 2, the minor Poisson's ratio was determined as

$$\nu_{21} = \nu_{12}E_2/E_1 = 0.301 \times 10.2/126 = 0.024$$

Uncertainty Analysis

An uncertainty analysis was performed to estimate the possible scatter range in the mechanical properties as a result of uncertainties in the primary measurements of force, strain, and specimen dimensions. Procedures for such estimation are outlined in the text by Holman and Gajda [1]. Here, we will perform a simple, conservative propagation of error analysis [1] on the governing Equations (C.1–C.5) used for data reduction and property determination. Such an analysis yields

$$\Delta E_i = E_i\left[\frac{\Delta P}{P} + \frac{\Delta w}{w} + \frac{\Delta t}{t} + \frac{\Delta \varepsilon}{\varepsilon}\right] \qquad i = 1,2 \tag{C.6}$$

$$\Delta \upsilon_{12} = \upsilon_{12}\left[\frac{\Delta \varepsilon_1}{\varepsilon_1} + \frac{\Delta \varepsilon_2}{\varepsilon_2}\right] \tag{C.7}$$

$$\Delta X_i^T = X_i^T\left[\frac{\Delta P}{P} + \frac{\Delta w}{w} + \frac{\Delta t}{t}\right] \qquad i = 1,2 \tag{C.8}$$

Consider the uncertainties in measuring the load (P), strain (ε), and dimensions (w and t):

$$\Delta P = \pm 10N$$

$$\Delta \varepsilon = \pm 5 \times 10^{-6}$$

$$\Delta w = \pm 0.025 \text{ mm}$$

$$\Delta t = \pm 0.025 \text{ mm}$$

With the above uncertainties in the load and strain data and in the cross-sectional dimensions, load and strain values were inserted into Equations (C.6)-(C.8) to yield the uncertainties in the reduced mechanical properties. When considering uncertainties in the elastic moduli (E_i) and Poisson's ratio (ν_{12}), the load and strains in the middle of the linear response region (Figures C.1–C.6) were used. For uncertainty analysis of the strengths (X_i^T), the ultimate loads were used. The calculations yield the following uncertainties:

$$\Delta E_1 = 3.2 \text{ GPa}$$

$$\Delta \nu_{12} = 0.002$$

$$\Delta X_1^T = 52 \text{ MPa}$$

$$\Delta E_2 = 0.3 \text{ GPa}$$

$$\Delta X_2^T = 1.0 \text{ MPa}$$

The uncertainties are all below 4% of the corresponding average values, which indicates that the measuring accuracy was reasonable. For several of the mechanical properties the standard deviation exceeds the above-estimated uncertainties, which indicates that the variability of the material properties contributes to the scatter.

Micromechanics Predictions

It is useful to compare the measured properties to those predicted by the micromechanics analyses discussed in Chapter 2. Previous laboratory experiments using an AS4/3501-6 carbon/epoxy composite gave a fiber volume fraction of 0.55 (see Chapter 3). Application of the micromechanics relations for E_1, ν_{12}, and E_2 given in Chapter 2, i.e., Equations (2.25a), (2.25c), and (2.26), together with the following data for AS4 carbon fibers and 3501-6 epoxy obtained from References [2–4]:

Fiber Data [2,3]	Matrix Data [3,4]
Axial modulus (E_L), 235 GPa	Young's modulus (E), 4.28 GPa
Transverse modulus (E_T), 13.8 GPa	Poisson's ratio (ν), 0.35
Axial Poisson's ratio (ν_{LT}), 0.20	

yields the following estimate of the mechanical properties of the composite

$$E_1 = 131 \text{ GPa}$$

$$\nu_{12} = 0.27$$

$$E_2 = 8.3 \text{ GPa}$$

The estimated properties agree reasonably well with the measured data. The differences may be due to variations in fiber volume fraction.

References

1. J.P. Holman and W.J. Gajda, Jr., *Experimental Methods for Engineers*, 5th ed., McGraw-Hill, New York, 1993.
2. Product Data, Number 841-4, Hercules Inc., Wilmington, DE, 1987.
3. J. Aboudi, *Mechanics of Composite Materials — A Unified Micromechanical Approach*, Studies in Applied Mechanics - 29, Elsevier, Amsterdam, 1991.
4. N.J. Johnston, T.W. Towell, and P.M. Hergenrother, Physical and mechanical properties of high-performance thermoplastic polymers and their composite materials, in *Thermoplastic Composite Materials*, L.A. Carlsson, ed., Elsevier, Amsterdam, 1991, pp. 27–71.

Appendix D

Unit Conversions

Quantity	SI to English	English to SI
Length	1 m = 39.4 in.	1 in. = 0.0254 m
	1 cm = 0.394 in.	1 in. = 2.54 cm
	1 mm = 0.0394 in.	1 in. = 25.4 mm
Force	1 N = 0.225 lb	1 lb = 4.445 N
Stress	1 MPa = 145 psi	1 psi = 6.895 kPa
Work	1 J = 1 N·m = 8.86 in.-lb	1 in.-lb = 0.113 J
Surface energy	$1\ J/m^2 = 5.71 \times 10^{-3}$ in. lb/in.^{2}	1 in.-lb/in.^{2} = 175 J/m^2
Temperature	°F = 1.8°C + 32	°C = 0.56°F – 17.8
Coefficient of thermal expansion	α[1/°F] = 0.55α[1/°C]	α[1/°C] = 1.8α[1/°F]

Index

Coefficients of thermal expansion:
  lamina, 143
  laminate, 164
Compliance matrix, 11, 213
Compressive testing:
  back-out factor, 101
  combined loading compression (CLC) test method, 91, 96
  cross-ply laminate testing, 100
  data reduction, 98, 152
  end-loading test methods, 88
  failure modes, 85, 97
  IITRI test fixture, 87, 95
  indirect determination of lamina strength, 100
  lamina, 85
  laminate, 158
  modified ASTM D 695 test method, 88, 96
  open hole, 169
  shear loading test methods, 87
  test procedure, 93
  Wyoming CLC test fixture, 92, 96
Deformation measurement:
  linear variable differential transformer (LVDT), 68
Delamination testing:
  mixed mode MMB specimen, 201
  mode I DCB specimen, 186
  mode II 4ENF specimen, 196
  mode II ENF specimen, 191
  mode III ECT specimen, 205
Double cantilever beam (DCB) specimen:
  beam analysis, 186
  compliance, 190
  data reduction, 189
  fiber bridging, 189
  hinge attachment, 64
  resistance curve (R-curve), 189
  specimen geometry, 186
  specimen preparation, 187
  test procedure, 187
Edge-cracked torsion (ECT) specimen:
  data reduction, 209
  specimen geometry, 207
  specimen preparation, 207
  test fixture, 206, 207
  test procedure, 208
End-notched-flexure (ENF) specimen:
  compliance, 192
  crack stability, 193
  data reduction, 194
  specimen preparation, 193
  test procedure, 193
Fiber and resin properties, 51, 233
Filled-hole test methods, 183
Flexure testing:
  data reduction, 127, 154
  four-point loading, 123
  lamina, 121
  laminate, 158
  test procedure, 126
  test specimen, 126
  three-point loading, 122
Four-point bend ENF (4ENF) specimen:
  compliance, 199
  data reduction, 199
  specimen preparation, 197
  test fixture, 197
  test procedure, 198
Fracture mechanics:
  compliance, 31
  fracture modes, 29, 32
  fracture toughness, 185
  strain energy release rate, 29, 185
Hygrothermal strains, 15
Lamina:
  compressive response, 85, 99
  constitutive relations, 11
  engineering constants, 12
  flexure response, 121, 128
  moisture expansion coefficients, 17
  off-axis tensile response, 131
  principal material coordinate axes, 6, 12
  property data, 9
  property symbols, 9
  shear response, 105, 110, 116
  stiffnesses, 14
  strength analysis, 24
  tensile response, 75, 81
  thermal expansion coefficients, 17
  thermoelastic response, 143, 149
Laminate:
  basic condensed code, 5
  bending stiffnesses, 21
  constitutive relationships, 21
  coordinate system, 20
  coupling stiffnesses, 21
  delamination testing, 185

extensional stiffnesses, 21
filled-hole testing, 183
mechanical response, 151, 160
notched strength, 32
open-hole testing, 169
orientation code, 3
plate theory, 20
ply coordinates, 22
processing, 37
property symbols, 159
specific condensed code, 6
standard laminate code, 4
strength analysis, 27, 156
tensile response, 151
thermal force resultants, 22
thermal moment resultants, 22
thermoelastic response, 163, 165
Micromechanics
expansion coefficients, 19
stiffness properties, 18
Mixed-mode bending (MMB) specimen:
data reduction, 203
hinge attachment, 64
test procedure, 203
Off-axis tensile test:
data reduction, 138
test procedure, 138
Open-hole laminate testing:
Boeing open-hole test compression method, 180
data reduction, 175
Northrop open-hole compression test method, 181
tensile test procedure, 175, 179
Orthotropic material, 11
Plane stress, 11
Poisson's ratio, 7, 12
Processing:
autoclave molding, 41, 48
autoclave, 38
cure cycle, 40, 43
degree of cure, 38
prepreg, 37
resin transfer molding (RTM), 37, 44
thermoplastic composites, 48
thermoset composites, 38
vacuum-assisted resin transfer molding (VARTM), 45
Reduced stiffness, 14, 213
Shear coupling ratio, 133
Shear modulus, 7, 13
Shear testing:
$[\pm 45]_{ns}$ tensile test method, 115
data reduction, 154
failure modes, 110
Iosipescu test method
lamina, 105
laminate, 158
short-beam test method, 117
three-rail test method, 114
two-rail test method, 111
St. Venant's principle, 23
Strain measurements:
electrical resistance strain gage, 66
extensometer, 67
Strength analysis:
average stress criterion (ASC), 172
first-ply failure, 27
lamina, 24
laminate, 27, 156
matrix cracking, 27
maximum strain criterion, 26
maximum stress criterion, 25
modified PSC, 173
notches, 28
off-axis tensile strength, 137, 141
point stress criterion (PSC), 171
Tsai-Wu criterion, 26
Stress concentration, 33, 169
Tensile testing:
clamps, 77
data reduction, 80, 152
lamina, 75, 79, 131
laminate, 157
load introduction, 76
off-axis testing, 131
open hole, 175
specimen geometries, 77, 79
tabbed specimen, 77
untabbed specimens, 79
wedge grips, 79
Test specimen preparation:
conditioning, 65
hinge attachment, 64
machining, 57
panel and specimen dimensions, 215
tabbing, 60, 61
Testing machines, 69
Thermoelastic testing:
data reduction, 148, 165
lamina, 143
laminate, 163
measurement of thermal expansion, 147
temperature compensation, 145
temperature sensor, 145
Transformation:
compliance matrix, 213
matrix, 15
stiffness matrix, 213
strain, 14
stress, 14
Uncertainty analysis, 232
Unit conversions, 235
Volume fractions:
chemical matrix digestion method, 50
photomicrographic method, 52
void content, 51
Young's modulus, 7, 12